Ove Undheim

# The non-linear microscale flow solver 3DWind

## Developments and validation

Doctoral thesis
for the degree of doktor ingeniør

Trondheim, May 2005

Norwegian University of
Science and Technology
Faculty of Engineering Science and Technology
Department of Energy and Process Engineering

NTNU
Innovation and Creativity

**NTNU**
Norwegian University of
Science and Technology

Doctoral thesis
for the degree of doktor ingeniør

Faculty of Engineering Science and Technology
Department of Energy and Process Engineering

ISBN 82-471-7056-6 (printed ver.)
ISBN 82-471-7055-8 (electronic ver.)

Doctoral Theses at NTNU, 2005:90

Printed by Tapir Uttrykk

# Abstract

This PhD thesis describes the implementation of a Reynolds Stress Model in the RANS microscale solver 3DWind, which is developed to model wind flow in complex terrain. The solver is also calibrated and validated with the two-dimensional channel flow test case C18 from the ERCOFTAC Classic database and the full-scale atmospheric flow case of the Askervein hill.

The implemented equations calculate both flow cases in good accordance with available experimental and numerical results. Still, the simulation experience and obtained results show that modelling of recirculation is a difficult task. The calculated flow field is very sensitive to the separation point, which is sensitive to several other factors. One important factor is the wall functions, which cause the separation zone to depend on the thickness of the first grid cell.

Compared to the k-ε model, results from simulations with the Reynolds Stress Model gave improvements in the calculated turbulence upstream the C18 hill. There were also differences in the solutions in the wake of both the C18 and the Askervein hills; still, the differences are too small to make any conclusions about the quality of the models. The disadvantages of decreased stability, more wiggles in the solution and increased computational effort are considered larger than the advantages of accounting for anisotropy and historical effects in the Reynolds stresses.

The solver is further used to quantify the effects of roughness and topography by generalized two-dimensional investigations of atmospheric flow. Hills and ridges are in this analysis found to increase wind velocities at 80m by up to 38%, and wind velocities above the ocean at 80m are 14% higher than corresponding open land velocities. Finally, a full wind resource assessment has been carried out at Eldsfjellet at the Norwegian island Hitra. Results were compared with measured data and simulation results from the linearized model WAsP. WAsP was found to estimate higher velocities in the valleys and near terrain edges, and WAsP is supposed to overestimate the velocities in these areas.

## Preface

This thesis is submitted in partial fulfilment of the requirements for the degree of doktor ingeniør from the Norwegian University of Science and Technology (NTNU). The research work was conducted during the period from May 2001 to May 2005 at NTNU and Institute for Energy Technology (IFE). The main fields of this thesis are Wind Engineering and Computational Fluid Dynamics (CFD). CFD-models are powerful tools with the ability to predict complex flows. This is an interesting and advanced topic, which was new to me at the beginning of this work. During the first year, I went into fundamental and more advanced topics related to this field, and through the work with this thesis I achieved practical experience with CFD modelling. Looking backwards, I am satisfied with the direction of my educational specialization.

Even though the possibilities with CFD-models are huge, the complexity often causes several problems. I think it is a well-known feeling among programmers, searching over and over again, for months, knowing that something is wrong, but being unable to locate the error. Throughout the work I have continually been delayed because of the dissatisfaction with the model performance. One main focus has been to get the model to a level where I was able to believe in the results myself. Maybe this focus limited the results of this thesis, but I still believe it was the right choice.

I would like to express my special gratitude to my supervisors Prof. Helge I. Andersson, Department of Energy and Process Engineering at NTNU, Dr. Erik Berge, Kjeller Vindteknikk (KVT), and Dr. Andreas Knauer, IFE. I am grateful for their follow-up through the entire process. They have all contributed to this thesis with good general advice and feedback. In addition, they have provided me with expert advice in different fields. Prof. Helge I. Andersson had the administrative responsibility, and has secured all processes to walk on smoothly. He has also given particularly good advice and feedback related to the field of turbulence modelling. Dr. Erik Berge contributed through the writing process, with particularly good backup the last few weeks. His meteorological knowledge has also been of great help. Dr. Andreas Knauer had earlier experience with 3DWind, and helped me with the initial simulations. His experience with wind tunnel simulations has also been helpful in discussions.

I want to thank The Norwegian Research Council (NFR) and Statkraft SF, which have funded this work through the KMB project “Development of Norwegian wind power technology”. This is a co-operative research project between NTNU, IFE and SINTEF. I want to thank Prof. Tor Anders Nygaard, for kindly answering model related questions. I also want to thank my opponents, whose fast feedback made the defence of this thesis possible before the summer holiday 2005. I want to thank my colleagues at IFE and NTNU. Many have contributed in different manners. I am also very grateful to my family and friends, who have supported me through the entire work. I want to thank my friends Kjetil Mosesen and Aanund Storhaug for constructing technical discussions, and I want to thank my friend John Gravdal, for proofreading the thesis. I also want to thank my good friends and neighbours that have contributed with delightful dinners, particularly during the last busy weeks.

Finally, I want to remember my beloved wife Solfrid. She died suddenly and unexpected early in the period of my doctoral studies. This caused later technical problems to become secondary, even though they intertwined with the loss. Many a day I was reminded of some words from the Bible in Matthew 6:34: “Therefore do not worry about tomorrow, for tomorrow will worry about itself. Each day has enough trouble of its own.”

Ove Undheim

Kjeller, 04th Mai 2005

# Contents

## Attached papers:

*IFE report:*

**Paper 1: Description and validation of 3DWind**

*Article:*

**Paper 2: The Askervein hill case; Some new aspects**

*Conference articles:*

**Paper 3: 2D simulations of terrain effects on atmospheric flow**

**Paper 4: Comparison of turbulence models for wind evaluation in complex terrain**

# 1 Introduction

The white paper[1] on Norwegian energy policy states that wind power should contribute by 3TWh energy production in Norway within 2010. To achieve this goal, annual installations of 100MW at an expected annual cost of 800MNOK are needed. A successful exploitation of the Norwegian wind resources requires simultaneous development of the Norwegian wind engineering competence. Knowledge of the wind conditions is important in order to optimally design and locate the wind farms.

The terrain of the Norwegian coast is complex, and not fully described by methods developed to estimate the wind conditions in flat terrain. Steep terrain demands detailed flow solvers to map the wind resources. Such models are available, but they can be developed and validated to reduce the uncertainty level of the results. If three percent increased energy production had been achieved by optimized park design, the 55MW wind farm at Hitra[2] would have annual savings of about 1MNOK. These results are based on an expected annual power production of 150GWh and mean annual spot prizes in 2004 from Nord Pool[3]. In complex terrain three percent production increase is achievable solely from model improvements.

Based on this fact the goal of this PhD study has been to develop and to validate a model for simulation of microscale flow in complex terrain. The field of Computational Wind Engineering is complicated and model improvements together with increasing computational power cause continuous progress within the field. There are lots of difficulties in applying Computational Fluid Dynamics (CFD) to wind engineering problems. According to Murakami (1998) main problems are caused by the large Reynolds number, impinging at the front wall, sharp edges of the bluff body and remaining effect of flow obstacle at outflow boundary.

Improved performance alone is worthless in a commercial view. Large projects need low uncertainties to make the credit risks as low as possible. Thorough validation increases the model knowledge. This corresponds to decreased uncertainties. Validation is important in order to ensure that the model results are both qualitatively and quantitatively reasonable. The validation focus is in accordance with resent research activities. The 11th ERCOFTAC/IAHR Workshop on Refined Turbulence Modelling was held at Chalmers University of Technology April 7-8, 2005[4]. The aim of this workshop was to validate flow solvers, and one of the test cases contained flow over an axisymmetric three-dimensional hill described by Simpson et al. (2002).

---

[1] Report to the Storting No. 29 (1998-99)

[2] http://www.statkraft.no/wbch3.exe?p=2566

[3] http://www.nordpool.com/

[4] http://www.tfd.chalmers.se/~gujo/WS11_2005/

In this PhD thesis the flow solver 3DWind has been chosen as basis for the CFD-model studies. The model is developed at Institute for Energy Technology[5] (IFE), and is therefore a natural choice since the PhD study was performed at IFE. The first version, which is described by Alm and Nygaard (1995), was based on the general purpose CFD code PHOENICS, developed by Cham Ltd[6]. The connection to PHOENICS was removed, and a new solver was built in through 1999-2001. This new version was validated and calibrated (Nygaard, 2000) and tested at a potential Norwegian wind farm site at Vikna (Knauer and Nyhammer, 2002), prior to the work presented in this thesis.

A Reynolds Stress Model (RSM) was the main implementation of this PhD study. RSM is known to improve impinging at the front wall. This causes improved turbulence estimates upstream of a hill. The RSM is also a more detailed description allowing history effects and anisotropy in the Reynolds stresses. This is expected to give improved results in the wake of a hill, where turbulence quantities are large. The RSM approach is generally a more physical representation expected to give improved results. Case C18 from the ERCOFTAC Classic database[7] (Almeida et al., 1993) is a chosen test case. This case was considered at the 4th ERCOFTAC/IAHR Workshop on Refined Flow Modelling, held at Karlsruhe in 1995. The channel flow is well documented containing both available experimental results and reference simulations (Laurence et al., 2003). The Askervein hill case is a full-scale atmospheric flow (Taylor and Teunissen, 1987). This hill is representative to real potential wind power sites, and is therefore within the application range of 3DWind and a chosen test case. Several other simulation results are also available for this case (Walmsley and Taylor, 1996).

This PhD study is funded by the Norwegian Research Council and Statkraft SF, and a part of the KMB[8] project “Development of Norwegian wind power technology”. This project was initialized in 2001 and continues until the end of 2005. The project includes two doctoral studies. Those works are expected to contribute to a long-term development of the Norwegian wind power technology.

# 2 Overview of related studies and CFD-models

In order to relate the work to existing solvers with similar purposes, some publications and websites are summarized in the following. It is difficult to separate research codes and pure commercial codes, so they are presented together. Before this summary, basic theory and modelling terms are defined.

The atmospheric flows are often divided into three scales. The largest scale is the macroscale. This scale contains global motions and interactions between synoptic scale high and low pressure systems. The phenomena’s average sizes are larger than 200km (Ahrens, 1994). This scale is not further discussed in this thesis. The microscale is the

---

[5] http://www.ife.no/

[6] http://www.cham.co.uk/

[7] http://cfd.me.umist.ac.uk/cgi-bin/cfddb/ezdb.cgi?ercdb+search+retrieve+&&&*%%%%dm=Line

[8] Competence project with user participation

smallest scale with sizes of motion up to 1km (Ahrens, 1994). At this scale, local effects like friction, topography, buoyancy, evaporation and condensation are important. The mesoscale is the middle scale, with average sizes of the phenomena ranging from 1 to 200km (Ahrens, 1994). At this scale both macro scale terms and micro scale terms are important. This is an important scale in weather forecasting, and the vertical distributions of motion, temperature and humidity are extracted from simulations on this scale. The planetary boundary layer is developed on the mesoscale. This is the part of the flow influenced by the ground surface. It varies in thickness from 20m to 5km, depending on the weather conditions, but a typical thickness on a day with moderate winds is 1km (Arya, 1988).

It is important to note the difference between the mesoscale meteorological models and the microscale CFD-models. Mesoscale models like HIRLAM[9], MM5[10] and WRF[11] solve coupled equations for all important physical processes in the atmosphere based on real-time observations and analysis of meteorological variables (Erik Berge, per. comm.), whereas CFD-models normally solve the flow field only for a steady state situation. This is often done to simplify the model and instead focus on the resolution. The advantage of the mesoscale models is a more realistic physical description of the atmosphere, and thereby the wind field, but due to poor resolution, they are often used in connection with microscale models (Eidsvik, 2004). Another way to account for low resolution is to use statistical downscaling (Martí et al., 2001). In addition to the above mentioned mesoscale models, MASS[12], MIUU[13] (Bergström and Källstrand, 2001) (Bergström, 2004i, ii) and GESIMA[14] (Heinemann et al., 1999) have also been used in connection with wind power assessments.

Mathematically, the atmospheric flow is described by the continuity equation, the *Navier-Stokes* (NS) equations, the temperature equation and the equation of state (Versteeg and Malalasekera, 1995). This equation set is generally not solvable analytically, and numerical solutions have to be obtained. For low Reynolds numbers, the equation set can be resolved on a fine grid by *Direct Numerical Simulation* (DNS). Atmospheric flow has large Reynolds number, and is not resolvable with computer resources available today. In order to obtain a numerical solution, the small-scale motions have to be modelled. The numerical approach used to solve the equations, depends on the information that is needed, the size of the computational domain, necessary accuracy, available computational power and time.

Different numerical approaches are available to solve the equation set. In the following, three different approaches are presented. The descriptions are extracted from Ferziger and Perić (2002). All methods use a grid that covers the solution domain. In the *finite*

---

[9] http://hirlam.knmi.nl/

[10] http://www.mmm.ucar.edu/mm5/

[11] http://www.wrf-model.org/index.php

[12] http://www.meso.com/

[13] http://www.met.uu.se/cirrus/wind/windenergy.html

[14] http://w3g.gkss.de/staff/kapitza/gesima/

*difference approach*, the differential equation is approximated by replacing the partial derivatives by approximations in terms of the nodal values of the functions at each grid point. The result is one algebraic equation per grid node, in which the variable value at that and a certain number of neighbour nodes appear as unknown. The main problem with this approach is that the conservation is not enforced unless special care is taken (Ferziger and Perić, 2002).

Conservation is more naturally accounted for in the *finite volume approach*. In this method the solution domain is subdivided into a finite number of contiguous *control volumes* (CVs), and the conservation equations are applied to each CV. The values of the variables are calculated at the centroid of each CV, and interpolation is used to express variable values at the CV surface in terms of the nodal values. Surface and volume integrals are approximated to obtain an algebraic equation for each CV. Compared to a finite difference model, it is more difficult to develop higher order methods in three dimensons (3D) (Ferziger and Perić, 2002).

In the *finite element method* the domain is broken into a set of discrete volumes, most often tetrahedra or hexahedra. In the simplest finite element approach the solution is approximated by a linear shape function within each element in a way that guarantees continuity of the solution across element boundaries. Such a function can be constructed from its values at the corners of the elements. The method finds the best solution within the set of allowed functions. The result is a set of non-linear algebraic equations (Ferziger and Perić, 2002).

The most detailed information about the atmospheric flow field today is found with *Large Eddy Simulations* (LES). These simulations are similar to DNS, except from small-scale motions which are modelled. This is a rational approach since small-scale motions have a high degree of isotropy, meaning motions being equally distributed in all directions. Increasing computational power causes these methods to become interesting in connection with microscale flow. Chow and Street (2004) performed LES at the Askervein hill. Another LES operated on the microscale is RIAM-COMPACT (Uchida and Ohya, 2003).

LES provides fully transient solutions. This is often not necessary, particularly not in wind resource estimations, which often are based on annual mean values. In such cases the *Reynolds Averaged Navier-Stokes* (RANS) can provide sufficient information. In Reynolds averaging, the variables are split in mean values and fluctuating values. This splitting introduces some new variables, and the equation set is no longer closed. These new variables are correlations between fluctuating quantities. In the momentum equations these correlations are called Reynolds stresses. To close the new equation set, the Reynolds stresses can be modelled. This is a first order closure, and turbulence models like the mixing length model and the k-ε model are two commonly used models with this approach. An alternative approach is to develop transport equations for the Reynolds stresses. This is a second order approach where the closure problem is removed from the momentum equations to the Reynolds stress equations. This approach is called Reynolds Stress Modelling (RSM).

Some CFD-models solve the entire equation set, where the energy equation is included. This allows buoyancy effects, which are essential to estimate the effects of atmospheric stability. The energy equation is included in the 3D Galerkin finite element method SIMRA[15]. This is a model developed at NTNU[16] and SINTEF[17] (Eidsvik and Utnes, 1997) and lately also in collaboration with met.no[18] and UiB[19]. This model is connected to the mesoscale through the models HIRLAM and MC2 (Eidsvik, 2004). If a solver is used to evaluate dispersion and transformation of pollutants, the atmospheric stability and specific humidity are particularly important quantities. Examples of CFD-models with this purpose are the microscale model MIMO coupled with the mesoscale model MEMO[20] (Ehrhard et al., 2000), the finite volume solver SWIFT (Apsley and Castro, 1997) and the finite difference solver described by Dawson et al. (1991).

Still, it is more common to ignore the temperature equation and assume a neutrally stratified atmosphere. This is often a good approximation in situations of wind speeds of moderate to high magnitude, and in cases where annual mean conditions are evaluated, the stability parameter has to be ignored. Among these microscale CFD-solvers the finite volume method is most commonly used. An early finite volume simulation on atmospheric flow was performed by Raithby et al. (1987). Other finite volume models are VENTOS[21] (Castro et al., 2003) (Castro and Palma, 2002), CANYON (Lopes, 2003), a Korean solver (Kim et al., 1997) (Kim and Patel, 2000) (Kim et al., 2000) and MASCOT (Ishihara et al., 2003), which is connected to the mesoscale model RAMS (Yamaguchi et al., 2003). ARIA Local[22] is based on the MERCURE model, and is a combination of finite difference and finite volume (Noel et al., 2001). Ayotte has developed the non-linear time-dependent finite difference gridpoint model RaptorNL at CSIRO[23] (Ayotte, 2002). Wind energy services with this model are now offered commercially through the company WindLab Systems Pty Ltd.

EllipSys3D[24] is a general purpose finite volume solver, which has been jointly developed by Risø and the Technical University of Denmark (DTU) (Michelsen (1992 and 1994) and Sørensen (1995), referred in Jørgensen et al. (2004)). The solver is used both for wind turbine aerodynamics and micro-siting in complex terrain. Different turbulence closures are available in the solver and Jørgensen et al. (2004) described results with *Detached Eddy Simulation* (DES) (Johansen et al., 2002), a combination of LES and RANS. Compared to a pure RANS showing mean values, the results from DES are transient. According to Jørgensen et al. (2004), this DES model holds promise

---

[15] http://balder.ntnu.no/ttp/

[16] http://www.ntnu.no/

[17] http://www.sintef.no/content/page3____149.aspx

[18] http://met.no/index.shtml

[19] http://www.uib.no/

[20] http://www2.dmu.dk/AtmosphericEnvironment/trapos/data_and_models.htm

[21] http://paginas.fe.up.pt/ventos/

[22] http://www.aria-net.it/eng/theme_6.htm

[23] http://www.csiro.au/

[24] http://www.afm.dtu.dk/Publications/PhD/RobertMikkelsen2003.pdf

of more accurate predictions in addition to providing the unsteady flow field needed for dynamic load calculations.

Some micro scale models are also based on commercially available multi-purpose finite volume based CFD codes. The commercial model WindSim[25] (Gravdahl, 1998) (Leroy and Gravdahl, 1999) is based on PHOENICS. At Renewable Energy Systems[26] in the UK, FLUENT[27] has been used to predict the wind speeds for an existing wind farm at Coal Clough, Lancashire (Lam, 2002). Microscale simulations performed with FLUENT were also described by Gasset et al. (2003) and Mandas et al. (2004). The CFX-4[28] model was first used in a simulation of the site of Mt-Crosin East (Montavon et al., 1999) (Montavon, 2003), but this model has later on been used in several simulations and it is part of services offered by Meteotest[29] (Toomer et al., 2001, 2002) (Watson and Montavon, 2003). Another example of a general-purpose CFD-solver is the STAR-CD[30], which was used together with the mesoscale model HIRLAM (Magnusson and Wern, 2001).

The RANS equations are a complicated set of non-linear equations. Non-linear equations are considerably more difficult to solve than linear equations, and if the flow condition is simple, a linear approach can be sufficient. In those cases a constant velocity linearizes the non-linear advection terms. If the solution is close to this preset value, the assumption causes minor errors. Iterative methods are often used to optimize this value. Linear models are characterized by good spatial resolution at a low computational cost, but the predictions are often inaccurate in areas dominated by non-linear effects, like a separation zone (Beljaars et al. 1987).

The two dominating systems of linear solvers can be represented by the two models MS3DJH/3R (Walmsley et al., 1982) and BZ (Troen and Petersen, 1988i, ii). Both models are based on the theory by Jackson and Hunt (1975). The main difference is that MS3DJH/3R uses a standard Cartesian coordinate system and solves the wind speed at each point in the modelling domain, while BZ employs a polar coordinate system, and the wind speed is only calculated in the origin of this system (Barnard, 1991). According to Troen and Petersen (1988) this polar distribution gives the BZ model higher resolution.

Among the linear models WAsP[31] is the best known (Troen and Petersen, 1988i, ii). WAsP is based on the BZ model, and it was developed at Risø[32]. Due to long experience with the model, empirical adjustments are available to improve the results.

---

[25] http://windsim.com/

[26] http://www.res-ltd.com/

[27] http://www.fluent.com/

[28] http://www.ansys.com/products/cfx-4.asp

[29] http://www.meteotest.ch/en/meteowind_dl?w=ber

[30] http://www.cd-adapco.com/products/star_overview.htm

[31] http://www.wasp.dk/Products/Index.htm

[32] http://www.risoe.dk/

The ruggedness index (RIX) is used to compensate for recirculation in complex terrain areas (Mortensen and Petersen, 1997) (Berge et al., 2004) (Pinto et al., 2004) and forests are expressed by both the roughness and the displacement length (Dellwik et al., 2004). WAsP has been established as an industrial standard, and the model is available in most wind modelling groups. Therefore, the results from many other models have been compared to results from WAsP. Undheim (2003) describes a comparison between WAsP and 3DWind. Other comparison analyses have been performed between WAsP, CFX-4 and WindSim (Schaffner and Gravdahl, 2003), between WAsP and WindSim (Moreno et al., 2003) (Watson et al., 2004), and between WAsP and WindFarm (Alé et al., 2004).

Atmospheric Environment Service of Canada[33] and Zephyr North[34] developed the other commonly used linear models. The first model MS3DJH was further developed to MSFD (Beljaars et al. 1987), a model with the finite difference approach in the vertical direction. The non-linear terms were further included in the source term in the model NLMSFD (Xu and Taylor, 1992) (Walmsley and Taylor, 1996) (Taylor, 1998). Other linear models are FLOWSTAR[35], LINCOM[36]; a part of the collection of programs called WAsP Engineering[37] (Mann, 1999), and a similar 3D integral boundary layer solver in use at CRES[38] in Greece (Douvikas and Chaviaropoulos, 1997, 1999).

The large commercial wind park design tools are mainly based on the linear models. WindFarm[39] estimates the flow across the terrain by means of MS-Micro/MS3DJH. GH Windfarmer[40] is most commonly based on WAsP. WindPro[41] is based on WAsP and WindSim. AWS Truewind's micrositing tool SiteWind[42] couples the mesoscale model MASS with the linear model MSFD (Reed et al., 2004)

The simplest methods used in connection with wind resource estimations are the mass-conservative models. In this approach the momentum equations are ignored. According to Barnard (1991), it is perhaps best to consider this model as an intelligent interpolation/extrapolation scheme that begins with knowledge of the wind at specific points – the wind observations. After an initial guess of the velocities is constructed, this flow field is adjusted as little as possible to satisfy the equation of mass conservation (Barnard, 1991). Barnard (1991) compared three different linear models at Askervein hill. As a mean of 6 cases, the prediction errors between the calculated and

---

[33] http://www.ec.gc.ca/envhome.html

[34] http://www.zephyrnorth.com/

[35] http://www.cerc.co.uk/software/flowstar.htm

[36] http://www.risoe.dk/vea-atu/atm_disp/lincomT.htm

[37] http://www.waspengineering.dk/

[38] http://www.cres.gr/kape/present/labs/aiolikwn_uk.htm

[39] http://www.resoft.co.uk/html/windflow.htm

[40] http://www.garradhassan.com/

[41] http://www.emd.dk/WindPRO/

[42] http://www.awstruewind.com/inner/services/windmapping/sitewind/sitewind.htm

observed winds were 8.4% for the MS3DJH/3R, 7.9% for the BZ and 9.1% for the NOABL model, which is a mass-conservative model. The article concluded with similar performances. Two other mass consistent models are Aiolos (Focken et al., 1999) and Minerve, which is the basis for ARIA Wind (Noel and Chevallaz-Perrier, 2001).

# 3 Modifications of 3DWind

3DWind was originally an operational finite volume method operated on a non-orthogonal grid. There was a three-stage explicit Runge-Kutta solver, and the pressure field was solved by Chorin's method. The implemented turbulence models were a mixing length model, a k-l model and a k-ε model, though a small modification had to be done to make the k-ε model run.

Explicit solvers are slow due to a time step restriction. To make the code more efficient "inlining" of routines were tried. This means to avoid calls to subroutines from within a loop. This caused minor changes in the computational effort and showed that the Fortran compiler handles this automatically. Another way to increase the speed is to save a value in the memory instead of computing it each time it is called. The wall distance was computed each time needed, but are now instead saved in the memory. There were no significant improvements seen from this change, because it is a very small fraction of the total simulation effort.

One main task throughout the study has been to reduce spatial wiggle, ocillations in time and the divergence of the simulation. The velocity pressure coupling in conjunction with collocated grid is the main reason for the odd-even pattern. In order to suppress this wiggle, the artificial viscosity has been modified through the entire study, but has never really reached satisfactory performance. Main changes in today's version are a removed anisotropy choice due to grid dependence and decreased vertical diffusion toward the wall. This is an area with strong natural diffusion and large gradients, causing the artificial diffusion to have large influence on the flow in an area where it is unnecessary. The advection subroutine was modified due to instabilities and divergence in the area of the separation zone.

Special attention was also given to the pressure development with Chorin's method, without any particular modification. The integration order and method have though been modified to avoid odd-even oscillations that appeared in an area of adverse pressure gradient. These were overcompensations caused by the integration in time of the pressure and the vertical velocity.

The simple two-dimensional C18 simulation caused large convergence problems and unphysical solutions. To figure out if the problems were connected to the density difference between water and air, the computational domain was enlarged to form a simulation with the same Reynolds number in airflow. This gave reasonable results, and indicated problems connected to the density implementation. The density of air is 1.22kg/m$^3$, and this is too close to one for errors to appear in simulations. In total, three terms influensed by wrong estimates related to the density were corrected.

A Reynolds Stresses Model was implemented. One problem with this method is the wall functions of the Reynolds stresses. The diffusion of the velocities is calculated from the derivatives of the Reynolds stresses, and a wall function seldom gives good estimates of the derivatives. To minimize this problem, two different methods to calculate the diffusion terms were compared and a combined method between the k-ε model and the Reynolds stress model was implemented.

In the Hitra simulations there were found some grid dependence in the solution caused by coordinate axes not parallel to the grid axes, and new routines were made to both turn the grid and the coordinate axes according to the wind direction. The grid generator was also modified to have the possibility of making a larger central area with good spatial resolution.

Most of the post processing routines were developed throughout the work. This is mainly done in Matlab. The model has been upgraded with several new facilities, and some of them are listed in the following. The residual smoothing algorithm is speeding the simulation and smoothing the solution. It is possible to adjust the inflow condition to fit the wind direction in one given point. The RNG k-ε model is implemented, and standard values of the k-ε model are available. A new wall function approach is also implemented. Upwinding is possible instead of adding artificial viscosity. It is possible to read a detailed roughness map, and the simulations have become more flexible, since it is possible to run based on a script, and to save and to stop the simulation during operation.

# 4 Summaries of the papers

## 4.1 Paper 1: Description and validation of 3DWind

This is a central work of this thesis (Undheim, 2005i). The theoretical and the numerical background for 3DWind are described in detail. The solution techniques for the continuity equation and the Navier-Stokes equations are presented. In order to validate and calibrate the model, two very different flow cases are investigated by means of model simulations and measurements.

Test case C18 from the ERCOFTAC Classic database is a water channel flow simulation described by Almeida et al. (1993). The simulation set-up and results were later on basis of a test case considered at the 4th ERCOFTAC/IAHR Workshop on Refined Flow Modelling, held in Karlsruhe in 1995. The flow is well documented containing both available experimental results and reference simulations (Laurence et al., 2003). 3DWind had not been tested on a scale different from the atmospheric scale, and a flow medium different from air. Thus the C18 case study is a test to ensure that the general governing equations are correctly implemented.

Based on this case different parameter studies are performed. The pseudo velocity of sound is a numerical constant which influences the coupling between the velocity and the pressure. Simulations with different values are carried out to optimize the constant. The artificial viscosity is an additional term in the equation to smooth numerical oscillations. The levelling of this term is important. If the level is too low, this will cause the simulation to diverge or poor convergence will result. If the level is too high the numerical diffusion reaches the same order as natural diffusion, and thus has a significant influence on the flow field. By optimizing of the residual smoothing algorithm, the maximum timestep length was allowed to be doubled. This method adds some implicit character to the equations, enabling larger time steps. This method also has a smoothing influence, but the term does not influence the final solution.

A grid dependence test is performed. This analysis indicates that the major grid influence is caused by the thickness of the first gridcell. If the thickness of the first gridcell is increased, the estimated separation zone is decreased. This is related to the wallfunctions. The results from the indirect wallfunction approach (named conventional in Craft et al. (2002)) were particularly sensitive to the thickness of the first gridcell. The wallfunction approach described by Versteeg and Malalasekera (1995) was therefore chosen for future simulations. There are also found differences in the estimated recirculation zone between 0.order and 1.order pressure extrapolation at the wall. The recirculation bubble became a little larger with the 0.order approach. This difference is probably a result of this flow being highly dependent on the estimated recirculation point.

The main analysis compares different turbulence models. The simulation results based on both the k-ε model and the RSM show relatively good accordance with both the reference solution and the measurements. Still, the RSM results seem to have more diffusion than the RSM reference solution. This is particularly visible in the shear layer between the separation zone and the free stream. The k-l model was found to depart some in the simulated recirculation bubble. It is difficult to distinguish between the quality of the performances of the other models, but the RSM is seen to improve the profile of the turbulence in front of the hill. On the other hand wiggle is seen in the velocity at the hilltop. The conclusion is that the RSM is considerably more complex, without a corresponding gain in increased details and accuracy.

The Askervein hill is located at the west coast of the Outer Hebrides island chain in Scotland. This is a full-scale atmospheric flow, and measurements used in this work were conducted in the afternoon 3 October 1983. The current period contained steady, moderate-to-strong winds from southwest (Taylor and Teunissen, 1987). This hill is representative to real potential wind power sites, and therefore within the application range of 3DWind.

The Askervein hill flow is solved with good resolution, and good accordance with measurements is found without any parameter tuning. Terrain details in the hill region are seen to influence the solution in a similar way as high-resolution linear simulations by Beljaars et al. (1987). Results show almost no differences when the horizontal resolution is reduced. This indicates that a limit is reached where minor improvements are expected by increased horizontal resolution. Simulated speed-up factors upstream the hill and at the top of the hill are almost equal to measurement data for all the different turbulence models and grids. In the wake of the hill there are differences indicating the difficulty of predicting high turbulence separation areas.

The turbulence estimates in front of the hill from the RNG k-ε model are in level with measurements, while k-l model estimates of the turbulence are almost twice the measurement level. This turbulence level distribution is similar to corresponding velocity values in the wake. This can be a coincidence, but indicates a connection between estimated upstream turbulence and the velocity in the wake. The RNG k-ε model was chosen for further analysis of the grid dependence and the roughness influence.

The solution is found to be more sensitive to decreased vertical grid resolution than decreased horizontal grid resolution. This is attributed to the wallfunctions and the thickness of the first grid cell. The consequences of reduced resolution in the vertical direction are increased speed and decreased turbulence in the wake.

The implementation of a detailed roughness representation influences the solution of both speed-ups and turbulence. The speed-ups along the hilltop are higher with detailed roughness and in better accordance with measurements. Generally the speed-ups in the wake became higher. This is probably caused by the low roughness at the hilltop. This roughness reduction is also found to improve the vertical speed-up profile at the hilltop. The new speed-up results near the ground at the hilltop are almost equal to measurements. Even though some aspects were improved, others were worsened, and it is difficult to conclude with improved overall results. One possible reason for the results not being significantly improved is that the true roughness is not correctly represented by the manual roughness digitizing.

## 4.2 Paper 2: The Askervein hill case; Some new aspects

3DWind is, in this paper (Undheim et al., 2005), applied to new aspects of the Askervein hill flow. In previous publications dependencies concerning grid, inflow boundary profile, roughness length and turbulence model are treated. There have also been comparisons of linear and non-linear models, and several models have been validated by means of the Askervein hill case. This analysis is the continuation of the Askervein hill analysis presented in the report “Description and validation of 3DWind” (Undheim, 2005i). The article focuses on the dependency on the inflow direction and the contour intervals of the map, in addition to the regular grid dependence test also presented in the report (Undheim, 2005i), and summarized in the previous subsection 4.1.

The direction dependence test was performed since there are large uncertainties in the direction measurements. The simulated direction estimates along a line through the hilltop also contain a bias. This indicates that the inflow direction in the simulation could be incorrect. In complex terrain small differences in incident flow direction can cause large differences in the flow field. This was still not expected in this case, since Askervein hill is quite regular and the surrounding terrain is quite homogeneous.

The direction simulations show that a better correspondence between measurements and simulations are found if the flow is rotated to come 10° more from the South. At this 200° direction the estimated speed-ups in all locations are close to be within the uncertainty levels of the measurements. There is almost no bias in the simulated direction along the line through the hilltop, and the direction variation along this line is 24.4°. Since the corresponding direction variation was 29° from the measurement data, 24.4° is a considerable improvement compared to 15.8° direction variation simulated from the original 210° direction. Still the modified direction is not able to entirely describe the differences seen in the direction variation from measurements, and a slightly stable atmosphere may be causing this. For further analyses it would be interesting to evaluate this possible stratification effect in a non-hydrostatic 3DWind simulation.

Simulations with different contour intervals of the map show large differences close to the ground on the top of the hill. In 10m height along the hilltop velocities are decreased by up to about 10%. This was expected, since this is where the speed-up is most important, at the same time as the 10m contour interval causes a hill height of 120m instead of 126m. The top of the hill has therefore been cut off in the model. The differences are decreasing with the height from the ground. At higher levels the speed-ups are smaller and caused by terrain formations with larger scales. There are also areas where the results are practically equal, since the different contour intervals do not cause any difference in the grid.

## 4.3 Paper 3: 2D simulations of terrain effects on atmospheric flow

The study presented in this paper (Undheim, 2005ii) was initialized to visualize some terrain effects in a presentation at a wind power seminar at Lindesnes in 2004. Some new results where added and this final work is prepared for MekIT'05, a conference in computational mechanics held in Trondheim May 2005.

In this analysis 3DWind is a tool for 2D simulations to investigate effects of the topography and the roughness on the wind flow field. This is an important issue in order to know where to locate wind turbines. The simulations are meant to give some interpretations of the atmospheric flow that is available without detailed simulations, some rules of thumb describing the simplest flow situations.

Firstly, the roughness aspect is discussed, and it is seen that the influence of a roughness change spreads upwards in the boundary layer by 1m pr 13-30m downstream from the roughness change. In this simulation the roughness changes from sea to land. The corresponding boundary layer development with an empirical equation is found to be 1m pr 10-20m. 4km from the shore, the wind conditions are found to be 13% better in 80m than a similar location far from the coast. An estimate from the empirical equation predicts wind conditions to be improved up to 20-50km from the shore. It is also seen that a 2km long forest in open land with few trees, decreases the mean wind speed 4km downstream from the forest with about 2% in 80m.

2D simulations were also performed to visualize topographical effects. Four different sine shaped slopes (8.4°, 12°, 24° and 42°) were used in conjunction with the representation of escarpments and ridges. In the escarpment cases the profiles development downstream the escarpment plateaus are visualized. At the escarpment top the largest speed-ups were found for the steepest slope, but all speed-ups are at the same order, and the speed-up for the 12° slope was 29% in 80m, 4km downwind at the plateau the speed-up in this height is 8%. Corresponding values with the empirical approach are 30% and 1%. The speed-up difference in 4km is large. A possible reason is that 4km is outside the optimum range of the empirical formula.

For the ridge cases both the speed-ups at the top of the ridges and the reconstructions of the boundary layer profiles in the wakes of the ridges are visualized. In 80m at the hill summit the largest speed-up of 38% was found for the 12° slope. This is lower than the 53% speed-up found from the empirical equation. One possible explanation is that 2D separations generally are larger than similar 3D results (Arya, 1988). Large separation causes decreased speed-up at the hilltop. This is also the reason for larger speed-up with the 12° slope than 24° and 42°, which have a larger separation zone. In the wake of the hill 4km from the hilltop, only the gentlest slope has a fully reconstructed flow field. For the steepest slope the velocity is still reduced by 42%. This analysis shows large terrain influence on the flow field and the mean wind conditions. To predict the sum of these non-linear effects, simulations performed by a non-linear flow solver are recommended to supplement measurements.

## 4.4 Paper 4: Comparison of turbulence models for wind evaluation in complex terrain

This is an analysis (Undheim, 2003) of the wind conditions at the island Hitra, located at the west coast of central Norway. This particular study was of special interest for Statkraft SF, which has participated in the funding of the doctoral study. During 2003-2004 a wind farm with 55MW installed capacity, producing 150 GWh energy yearly, was located in this area. This is sufficient energy for about 7500 households[43]. The article was published in conjunction with the European Wind Energy Conference in Madrid 2003.

This article presents a full analysis of a potential windfarm location. The annual mean wind, turbulence and direction distribution were calculated from measurements at 3 locations within the area collected during one year, starting October 1998. Simulations with 3DWind were carried out with three different turbulence models, the mixing length, a k-l and a k-ε model, for each of twelve directions. These results were scaled by measurements and combined to form annual mean maps for the horizontal velocity, the vertical angle of the velocity and the turbulence intensity. For comparison, simulations results were also found with the linearized model WAsP.

To compare the models, their ability to predict the annual mean wind in one measurement location based on another is compared. The mean deviations are found to be 2.6% with the k-ε model, 1.9% with the k-l method and 2.4% with the mixing length model. WAsP simulations gave a mean deviation of 4.1%. Qualitatively the different turbulence models in 3DWind show similar results in all variables, but there is a difference in turbulence level between the k-ε model and the two other turbulence models. Mean turbulence intensities are found to be 0.16 from the k-ε model, 0.10 from the k-l model and 0.09 from measurements. There were not found any particular reason for this difference between the k-l model and the k-ε model in this analysis, and it seems strange since the opposite tendency was found at the Askervein hill. The differences are maybe caused by model changes in between the simulations.

---

[43] http://www.statkraft.no/wbch3.exe?p=2566

Compared to simulation results from WAsP, which only contain estimates of the horizontal mean wind velocity, the mean flow pattern seems to differ especially in the vicinity of steep edges and in valleys. The differences are probably caused by an overestimation in WAsP. High mean wind values in the valleys are connected to the linearity of WAsP. These areas have large turbulence and are more influenced by non-linear effects. This is also found to be the main disadvantage of linear models in the simulation of Askervein hill (Beljaars et al., 1987). WAsP estimates high wind conditions close to edges of steep terrain. These are areas of large flow inclination, and turbine positioning in these areas should be avoided. The article concludes that the differences in mean wind fields are large enough to result in differences in optimal wind turbine positioning.

# 5 Conclusions and further improvements

The overall conclusions regarding the validation of 3DWind and some further improvements are summarized in this section. One major task of this study has been the implementation and testing of a Reynolds Stress Model. Results from *Description and validation of 3DWind* (Undheim, 2005i) gave improvements in the calculated upstream turbulence from simulations with this Reynolds Stress Model. There were also differences in the solutions in the wake of the hill, but no conclusion about which model that has the best performance is drawn. The disadvantages of decreased stability, more wiggle in the solution and increased computational effort are considered larger than the advantages of accounting for anisotropy and historical effects in the Reynolds stresses.

The grid dependence analyses showed that the wall functions cause the solution to depend on the thickness of the first grid cell. Increased thickness of the first grid cell caused a reduced separation zone and increased velocities in the wake. This is a problem present in both the simulation from C18 and Askervein hill. According to Murakami (1998) the development of accurate wall boundary conditions of macroscopic type is one of the most important targets in computational wind engineering research. It is therefore recommended to implement a generalized wall function approach, in order to reduce this problem.

The topic of atmospheric stratification has an increasing actuality with increasing computational power. The effect of buoyancy has earlier been implemented in 3DWind, and it is recommended that this parameter is re-included in the simulations. This is feasible by full inclusion of the temperature equation, or simpler by a preset vertical temperature gradient causing buoyancy effects. This would give additional information in a test case like the Askervein hill case, but would also improve the results when non-neutral boundary profiles are taken from mesoscale models as inflow boundary condition. A possible test case is the strongly stratified flow at Cinder Cone Butte (Apsley and Castro, 1997).

3DWind still has divergence problems in certain complex flow situations. This could be improved by orthogonal grids, an option not yet available in the grid generator (grid3d) connected to 3DWind. Improvement of the artificial viscosity is also recommended. Chorin's method may not be the optimal method to calculate the pressure. A possible improvement could be the SIMPLE method for collocated grids (Rahman and Siikonen, 2000). However, the collocated approach is seen to cause problems in the velocity pressure coupling. This may be improved by changing to a staggered grid, or the common used Rhie and Chow pressure weighted interpolation method (Rhie and Chow, 1983).

## References

Ahrens, C. D. (1994). *Meteorology Today. An introduction to weather, climate, and the environment.* Fifth edition. West Publishing Company, Minneapolis.

Alé, J. A. V., Azambuja, G. G., Paula, A. V. & Adegas, F. D. (2004). Wind farm assessment: Comparative tools results in Rio Grande do Sul. *Conference Proceedings European Wind Energy Conference*, London, Great Britain.

Alm, L. K. & Nygaard, T. A. (1995). Flow over complex terrain estimated by a general purpose Navier-Stokes solver. *Modelling, identification and control*, 16: 169 – 176.

Almeida, G. P., Durao, D. F. G. & Heitor, M. V. (1993). Wake flows behind two-dimensional model hills. *Experimental Thermal and Fluid Science*, 7:87 – 101.

Apsley, D. D. & Castro, I. P. (1997). Flow and dispertion over hills: Comparison between numerical predictions and experimental data. *Journal of Wind Engineering and Industrial Aerodynamics*, 67&68: 375 – 386.

Arya, S. P. (1988). *Introduction to Micrometeorology*. International Geophysics Series, Volume 42. Academic Press, Inc, San Diego, California.

Ayotte, K. (2002). A nonlinear wind flow model for wind energy resource assessment in steep terrain. *Conference proceedings Global Windpower 2002*, Paris, France.

Barnard, J.C. (1991). An evaluation of three models designed for siting wind turbines in areas of complex terrain. *Solar Energy*, 46: 283 – 294.

Beljaars, A. C. M., Walmsley, J. L. & Taylor, P. A. (1987). A mixed spectral finite-difference model for neutrally stratified boundary-layer flow over roughness changes and topography. *Boundary-Layer Meteorology*, 38: 273 – 303.

Berge, E., Nyhammer, F., Tallhaug, L. & Jakobsen, Ø. (2004). An evaluation of the WAsP model at a coastal mountainous site in Norway. *Scientific paper. Conference Proceedings European Wind Energy Conference*, London, Great Britain.

Bergström, H. & Källstrand, B. (2001). Estimating wind potential in a complex terrain artic mountain valley. *Conference Proceedings European Wind Energy Conference*, Copenhagen, Denmark.

Bergström, H. (2004i). A study of valley winds using the MIUU meso-scale model. *Scientific paper. Conference Proceedings European Wind Energy Conference*, London, Great Britain.

Bergström, H. (2004ii). Higher-order closure meso-scale modelling for wind resource estimates in Sweden. *Conference Proceedings European Wind Energy Conference*, London, Great Britain.

Castro, F. A., Palma J. M. L. M. & Lopes A. S. (2003). Simulation of the Askervein flow. Part 1: Reynolds averaged Navier-Stokes equations (k-epsilon turbulence model). *Boundary-Layer Meteorology*, 107: 501 – 530.

Castro, F. A. & Palma J. M. L. M. (2002). The wind over complex terrain, or why simpler models do not work. *Conference proceedings Global Windpower 2002*, Paris, France.

Chow, F. K. & Street, R. L. (2004). Evaluation of turbulence models for Large-Eddy simulations of flow over Askervein hill. Paper 7.11, *16th Symposium on Boundary Layers and Turbulence*, American Meteorological Society.

Craft, T. J., Gerasimov, A. V., Iacovides, H. & Launder, B. E. (2002). Progress in the generalization of wall-function treatments. *International Journal of Heat and Fluid Flow*, 23: 148 – 160.

Dawson, P., Stock, D. E. & Lamb, B. (1991). The Numerical Simulation of Airflow and Dispersion in Three-Dimensional Atmospheric Recirculation Zones. *Journal of applied meteorology*. 30: 1005 – 1024.

Dellwik, E., Landberg, L. & Jensen, N. O. (2004). WAsP in the forest. *Scientific paper. Conference Proceedings European Wind Energy Conference*, London, Great Britain.

Douvikas, D. I. & Chaviaropoulos, P. K. (1997). 3D viscous computation over complex terrain using integral boundary layer method. *Conference Proceedings European Wind Energy Conference*, Dublin Castle, Ireland.

Douvikas, D. I. & Chaviaropoulos, P. K. (1999). CRES' 3-D boundary layer method for complex terrain micrositing. Application examples. *Conference Proceedings European Wind Energy Conference*, Nice, France.

Ehrhard, J., Khatib, I. A., Winkler, C., Kunz, R., Moussiopoulos, N. & Ernst, G. (2000). The microscale model MIMO: development and assessment. *Journal of Wind Engineering and Industrial Aerodynamics*, 74 – 76: 25 – 47.

Eidsvik, K. J. & Utnes, T. (1997). Flow separation and hydraulic transitions over hills modelled by the Reynolds equations. *Journal of Wind Engineering and Industrial Aerodynamics*, 67 – 68: 403 – 413.

Eidsvik, K. J. (2004). A System for Wind Power Estimation in Mountainous Terrain. Prediction of Askervein Hill Data. Research Article in press at *Wind Energy*.

Ferziger, J. H. & Perić, M. (2002). *Computational Methods for Fluid Dynamics*. 3rd Edition. Springer-Verlag, Berlin Heidelberg, Germany.

Focken, U., Heinemann, D. & Waldl, H. P. (1999). Wind assessment in complex terrain with the numeric model Aiolos – implementation of the influence of roughness changes and stability.*Conference Proceedings European Wind Energy Conference*, Nice, France.

Gasset, N., Poitras, G. J., Gagnon, Y. & Brothers, C. (2003). Atmospheric boundary layer over a coastal cliff. *Conference proceedings European Wind Energy Conference*, Madrid, Spain.

Gravdahl, A. R. (1998). Meso scale modeling with a Reynolds Averaged Navier-Stokes Solver. *31th IEA Experts Meeting - State of the Art of Wind Resource Estimation.* Risø, Denmark.

Heinemann, D., Mengelkamp, H. T., Strack, M. & Waldl, H. P. (1999). Experiences with the Application of the Non-Hydrostatic Mesoscale Model GESIMA for assessing Wind Potential in Complex Terrain. *Conference Proceedings European Wind Energy Conference*, Nice, France.

Ishihara, T., Yamaguchi, A. & Fujino, Y. (2003). A Nonlinear Model MASCOT: Development and Application. *Conference proceedings European Wind Energy Conference*, Madrid, Spain.

Jackson, P. S. & Hunt, J. C. R. (1975). Turbulent flow over a low hill. *Quart. J. Roy. Meteorol. Soc.,* 101: 925 – 955.

Johansen, J., Sørensen, N. N., Michelsen, J. A. & Schreck, S. (2002). Detached-Eddy Simulation of Flow Around the NREL Phase VI Blade. *Wind energy*, 5: 185 – 197.

Jørgensen, B. H., Hansen, A., Myllerup, L., Sørensen, N. N., Mann, J., Ott, S. & Badger, J. (2004). Computational wind power meteorology in complex terrain compared to measurements. *Conference Proceedings European Wind Energy Conference*, London, Great Britain.

Kim, H. G., Lee, C. M., Lim, H. C. & Kyong, N. H. (1997). An experimental and numerical study of the flow over two-dimensional hills. *Journal of Wind Engineering and Industrial Aerodynamics*, 87: 45 – 60.

Kim, H. G. & Patel V. C. (2000). Test of turbulence models for wind flow over terrain with separation and recirculation. *Boundary-Layer Meteorology*, 94: 5 – 21.

Kim, H. G., Patel, V. C. & Lee, C.M. (2000). Numerical simulation of wind flow over hilly terrain. *Journal of Wind Engineering and Industrial Aerodynamics*, 87: 45 – 60.

Lam, J. K. W. (2002). Mapping a Wind Farm. *Fluent news.* Vol XI Issue I, Spring 2002 page 8. (http://www.fluent.com/about/news/newsletters/02v11i1/a3.htm)

Laurence et al. (2003) (EU project G1RT-CT-2000-05003). www.qnet-cfd.net. Thematic Area 3, Underlying Flow Regime: Flow separation behind a 2D hill.

Leroy, J. & Gravdahl, A. R. (1999). *Wind field simulations at Askervein hill.* Vector, Tønsberg, Norway.

Lopes, A. M. G. (2003). WindStation – a software for the simulation of atmospheric flows over complex topography. *Environmental Modelling & Software,* 18: 81 – 96.

Magnusson, M. & Wern, L. (2001). Wind energy predictions using CFD and HIRLAM forecast. *Conference Proceedings European Wind Energy Conference*, Copenhagen, Denmark.

Mandas, N., Cambuli, F., Crasto, G. & Cau, G. (2004). Numerical Simulation of the Atmospheric Boundary Layer (ABL) over complex terrains. *Conference Proceedings European Wind Energy Conference*, London, Great Britain.

Mann, J. (1999). Turbulence in complex terrain. *Conference Proceedings European Wind Energy Conference*, Nice, France.

Martí, I., Nielsen, T. S., Madsen, H., Navarro, J., Roldán, A., Cabezón, D. & Berquero, C. G. (2001). Prediction models in complex terrain. *Conference Proceedings European Wind Energy Conference*, Copenhagen, Denmark.

Michelsen, J. A. (1992). *Basis3D – a platform for development of multiblock PDE solvers*. Technical Report AFM 92-05, Technical University of Denmark, Lyngby.

Michelsen, J. A. (1994). *Block structured multigrid solution of 2D and 3D elliptic PDEs*. Technical Report AFM 94-06, Technical University of Denmark, Lyngby.

Montavon, C., Hertig, J. A. & Sarlos, G. (1999). Wind power potential assessment over complex terrain using a modified version of the turbulent flow solver CFX-4. *Conference Proceedings European Wind Energy Conference*, Nice, France.

Montavon, C. (2003). Assessing the wind power potential of a site. *CFX Update.* No 23 Summer 2003, page 16. (http://www-waterloo.ansys.com/cfx/pdf/pdf0379.pdf)

Moreno, P., Gravdahl, A. R. & Romero, M. (2003). Wind Flow over Complex Terrain: Application of Linear and CFD Models. *Conference proceedings European Wind Energy Conference*, Madrid, Spain.

Mortensen, N. G., & Petersen, E. L. (1997). Influence of topographical input data on the accuracy of wind flow modelling in complex terrain. *Conference Proceedings European Wind Energy Conference*, Dublin Castle, Ireland.

Murakami, S. (1998). Overview of turbulence models applied in CWE-1997. *Journal of Wind Engineering and Industrial Aerodynamics.* 74 – 76: 1 – 24.

Noel, J. M. & Chevallaz-Perrier, R. (2001). Wind resource assessment with ARIA Wind in a complex site. *Conference Proceedings European Wind Energy Conference*, Copenhagen, Denmark.

Noel, J. M., Chevallaz-Perrier, R. & Albergel, A. (2001). Solving the problems of wind turbines in complex terrain with a complete atmospheric tool. *Conference Proceedings European Wind Energy Conference*, Copenhagen, Denmark.

Nygaard, T. A. (2000). *Application of a Navier-Stokes solver to the siting of wind turbines in complex terrain.* Limited technical report IFE-KR/F-2000/086. Institute for Energy Technology, Norway.

Pinto, P., Guedes, R., Ferrieira, M. & Rodrigues, Á. (2004). Wind prediction deviations in complex terrain. *Conference Proceedings European Wind Energy Conference*, London, Great Britain.

Rahman, M. M. & Siikonen, T. (2000). An improved simple method on a collocated grid. *Numerical Heat Transfer*, 38: 177 – 201.

Raithby, G. D., Stubley, G. D. & Taylor, P. A. (1987). The Askervein Hill project: A finite control volume prediction of three-dimensional flows over the hill. *Boundary-Layer Meteorology*, 39: 247 – 267.

Reed, R., Brower, M. & Kreiselman, J. (2004). Comparing SiteWind with standard models for energy output estimation. *Conference Proceedings European Wind Energy Conference*, London, Great Britain.

Rhie, C. M. & Chow, W. L. (1983). Numerical study of the turbulent ow past an airfoil with trailing edge separation. *AIAA Journal*, 21: 1525 – 1532.

Schaffner, B. & Gravdahl, A. R. (2003). Wind Modeling in Mountains: Intercomparison and Validation of Models. *Conference proceedings European Wind Energy Conference*, Madrid, Spain.

Simpson, R. L., Long, C. H. & Byun, G. (2002). Study of vortical separation from an axisymmetric hill. *Int. J. Heat and Fluid Flow*, 23: 582 – 591.

Sørensen, N. N. (1995). *General Purpose Flow Solver Applied to Flow over Hills*. PhD Thesis, Risø-R-827(EN), Risø National Laboratory, Roskilde, Denmark.

Taylor, P. A. & Teunissen, H. W. (1987). The Askervein Hill project: Overview and background data. *Boundary-Layer Meteorology*, 39: 15 – 39.

Taylor, P. A. (1998). Turbulent boundary-layer flow over low and moderate slope hills. *Journal of Wind Engineering and Industrial Aerodynamics*, 74 – 76: 25 – 47.

Toomer, C. A., Sander, J. & Kunz, S. (2001). A study of wind potential in complex terrain. *Conference Proceedings European Wind Energy Conference*, Copenhagen, Denmark.

Toomer, C. A., Sander, J., Kunz, S. & Buzzi, M. (2002). Wind-potential estimation over complex terrains and the effects of topography and large-scale wind profile data. *Conference proceedings Global Windpower 2002*, Paris, France.

Troen, I. & Petersen, E. L. (1988i). Siting of wind turbines. *European Community Wind Energy Conference*, Herning, Denmark.

Troen, I. & Petersen, E. L. (1988ii). *European Wind Atlas.* Risø National Laboratory, Roskilde, Denmark.

Uchida, T. & Ohya, Y. (2003). Large-eddy simulation of turbulent airflow over complex terrain. *Journal of Wind Engineering and Industrial Aerodynamics.* 91: 219 – 229.

Undheim, O. (2003). Comparison of turbulence models for wind evaluation in complex terrain. *Conference proceedings European Wind Energy Conference*, Madrid, Spain.

Undheim, O. (2005i). *Description and validation of 3DWind.* Internal report IFE/KR/F-2005/062, Part of PhD thesis, Kjeller, Norway.

Undheim, O. (2005ii). 2D simulations of terrain effects on atmospheric flow. *Conference proceedings MekIT'05*, Trondheim, Norway.

Undheim, O., Andersson, H. I. & Berge, E. (2005). *The Askervein hill case; Some new aspects*. Paper submitted for journal publication, Part of PhD thesis, Kjeller, Norway.

Versteeg, H. K. & Malalasekera, W. (1995). *An introduction to Computational Fluid Dynamics; The Finite Volume Method*. Prentice Hall, London.

Walmsley, J. L. & Taylor, P. A. (1996). Boundary-layer flow over topography: Impacts of the Askervein study. *Boundary-Layer Meteorology*, 78: 291 – 320.

Walmsley, J. L., Salmon, J. R. & Taylor, P. A. (1992). On the application of a model of boundary-layer flow over low hills to real terrain. *Boundary-Layer Meteorology*, 23: 17 – 46.

Watson, S. J. & Montavon, C. (2003). CFD Modelling of the Wind Climatology at a Potential Offshore Wind Farm Site. *Conference proceedings European Wind Energy Conference*, Madrid, Spain.

Watson, G., Douglas, N. & Hall, S. (2004). Comparison of wind flow models in complex terrain. *Conference Proceedings European Wind Energy Conference*, London, Great Britain.

Xu, D. & Taylor, P. A. (1992). A non-linear extension of the Mixed Spectral Finite Difference model for neutrally stratified boundary-layer flow over topography. *Boundary-Layer Meteorology*, 59: 177 – 186.

Yamaguchi, A., Ishihara, T. & Fujino, Y. (2003). A Dynamical Statistical Downscaling Procedure for Local Wind Climate Assessment. *Conference proceedings European Wind Energy Conference*, Madrid, Spain.

# Paper 1

## Description and validation of 3DWind

*IFE Report*

Institute for Energy Technology

|  | KJELLER | HALDEN | Availability |
|---|---|---|---|
| Address | NO-2027 Kjeller, Norway | NO-1751 Halden, Norway | Limited |
| Telephone | +47 63 80 60 00 | +47 69 21 22 00 |  |
| Telefax | +47 63 81 29 05 | +47 69 21 22 01 |  |

| Report number | Date |
|---|---|
| IFE/KR/F-2005/062 | 2005-05-04 |
| Report title<br>Description and validation of 3DWind |  |
|  | Number of pages<br>87 |

**Summary**

For the RANS solver 3DWind, the governing physical equations and numerical methods are described and discussed. The model is further validated with simulations of two different flow cases.

Test case C18 from the ERCOFTAC Classic database is a channel flow containing both experimental results and reference simulations. Based on this case the pseudo speed of sound and the artificial viscosity term are calibrated, in addition to a grid dependence study and a turbulence model analysis. Relatively good accordance is found between the 3DWind simulation results and both the reference solution and the measurements.

The Askervein hill case is a full-scale atmospheric flow, equal to real or potential windpower sites in complex terrain. This flow is solved with good resolution and good accordance is again found with measurements. Comparing a k-l model, two k-ε models and a RSM, best correspondence to measurements is found with the k-ε turbulence models. The RNG k-ε model was chosen for a further analysis of the grid dependence and the influence of a detailed roughness representation.

**Keywords:** Microscale flow, Navier-Stokes simulation, complex terrain wind, turbulence model comparison, C18 ERCOFTAC, Askervein hill

## Contents

## Abbreviations

| | |
|---|---|
| CFD | Computational Fluid Dynamics |
| RANS | Reynolds Averaged Navier-Stokes |
| RSM | Reynolds Stress Modelling |
| SIMPLE | Semi-Implicit Method for Pressure-Linked Equations |
| RK | Runge-Kutta |
| KMB | Kompetanseprosjekt med brukermedvirkning<br>(Competence project with user participation) |
| SODAR | Sound Detection and Ranging |
| WAsP | Wind Atlas Analysis and Application Program |
| ERCOFTAC | European Research Community on Flow, Turbulence and Combustion |
| IAHR | International Association for Hydraulic Research |
| NTNU | Norges Tekniske Naturvitenskaplige Universitet<br>(Norwegian University of Science and Technology) |
| CFL | Courant-Friedrichs-Lewy |
| TKE | Turbulent kinetic energy |
| EPS | Dissipation rate of turbulent kinetic energy |

# 1 Introduction

Power extraction from wind is growing fast, and so is the wind power industry. Around 8200 MW of new wind power capacity was installed worldwide in 2003. This is 21% higher than in 2002 and corresponds to an annual growth rate of 26%, which is slightly less than the mean annual growth rate of 30% for the last decade. At the end of 2003 the global installed capacity was about 40GW (Windpower, 2004).

The Norwegian government has realized that energy from wind is both clean and competitive to other energy sources. There has been a decision to increase the energy production from new renewable energy sources to 10 TWh per year within 2010. The fraction of wind power should be at least 3 TWh. 10 TWh is well within reach only from windpower. This energy amount corresponds to large exploitation and causes high activity within the Norwegian wind energy market (Windpower, 2004).

The wind power production is proportional to the third power of the wind speed. To secure an optimal usage of the wind resources, it is therefore important with detailed information on the wind conditions. To be able to evaluate the wind condition in an area, it is important to have reliable measurements. These measurements should be as close to the area of interest as possible. This is particularly important in areas of complex topography. The western coast of Norway is dominated by steep mountains and long fjords. This causes the wind conditions to be highly dependent on the terrain formations. Measurements are expensive, and it takes some time to gain results. Therefore, a numerical model that has the ability to simulate the wind conditions accurately is a good supplementary tool.

WAsP is a model that has become an industrial standard for wind simulations. It is a linear spectral model consisting of a roughness change model, a shelter model and an orographic model (Troen and Petersen, 1988). WAsP is developed at RISØ in Denmark, and gives accurate climatological predictions over low, smooth hills of small to moderate dimensions with sufficiently gentle slopes and attached flows (Bowen and Mortensen, 1996). The model is not able to predict flow detachment, which occurs on the lee side of a steep hill, and causes the flow to recirculate. WAsP results should therefore be used with care in areas with complex terrain. Slopes exceeding $17^{o}$ are critical (Bowen and Mortensen, 1996).

To be able to predict flow detachment, the numerical model should contain most of the physical equations describing the flow. These equations are the Navier-Stokes equations, which cannot be solved in full for atmospheric flow. The typical range of eddy sizes is $10^{-3}$ to $10^{3}$ m (Arya, 1988), where the fastest events take place with a frequency on the order of 10kHz (Versteeg and Malalasekera, 1995). To resolve the motions on all scales, the gridcells have to be of the size $10^{-4}$ m, with a timestep of $10^{-4}$ s. Resolving 1 $km^{3}$ corresponds to 10 million cells in each space direction, which corresponds to $10^{21}$ gridcells in total. To reduce the computational needs, the Navier-Stokes equations are averaged in both time and space. The highest frequencies and smallest scales in space are assumed to contain some regularity, and are solved by turbulence models.

3DWind is a Reynolds Averaged Navier-Stokes (RANS) solver developed to simulate the wind field over complex terrain. The first version described by Alm and Nygaard (1995) was based on the general purpose CFD solver PHOENICS, developed by Cham Ltd[1]. 3DWind was developed as wind flow solver through 1999-2001, and has been evaluated on potential Norwegian wind farm sites at Vikna (Knauer and Nyhammer, 2002) and Hitra (Undheim, 2003). In short, this model solves the incompressible Reynolds Averaged Navier-Stokes equations by the finite volume method on a non-orthogonal terrain-following grid. A three stage explicit Runge-Kutta time stepping is used to solve the time derivative.

In meteorology the atmospheric flow is divided in microscale, mesoscale and macroscale (Utaaker, 1991)(Ahrens, 1994). The horizontal extension of the microscale is in the range 0.01 to 1000 m, the mesoscale is in the range 1 to 200 km and macroscale is above 200km. In short, the flow field on the macroscale is dominated by the Coriolis force and horizontal pressure gradients caused by sun radiation. This is the scale of the weather map and the global wind patterns. The mesoscale is the middle scale, connecting the microscale and the macroscale. The planetary boundary layer is developed on the mesoscale, and the vertical distribution of motion, temperature and humidity is extracted from simulations on this scale. Both the macro scale terms, and the micro scale terms are important on this scale. The micro scale terms mostly depend on local effects like friction, topography, buoyancy, evaporation and condensation.

For wind power projects, the areas of interest vary typically from 1 – 20 km$^2$, giving simulation domains up to 400 km$^2$. At this scale, mesoscale terms influence the flowfield and should preferably be taken into account. Still, the topography and the roughness, which act on the microscale, are assumed to have the largest influence on the wind velocity distributions near the ground.

The validation of a flow solver aimed to model atmospheric flow is however difficult. A validation case should preferably contain information on the entire flow field and detailed information regarding surface roughness and elevation. Today measurements are either point measurements (anemometers) or profiles (SODAR). Anemometers are accurate, but it is impossible to decide if the entire wind field from the simulation is correctly estimated, even if the calculation coincides at one measurement point. Measurements at different heights and locations are able to correct some of these sources of error. The SODAR profiles contain more information, but those data have a larger uncertainty.

For validation, it is convenient to compare numerical results with wind tunnel test results. In wind tunnels the flow conditions are controlled, and the number of unknown variables are set to a minimum. There exist accurate methods of collecting data without interfering with the flow.

The structure of the report is the following: Chapter 2 gives a detailed description of the model, chapter 3 describes the validation and parameter tuning with testcase C18 from

---

[1] http://www.cham.co.uk/

the ERCOFTAC Classic database. Chapter 4 describes the validation based on the Askervein hill study. In chapter 5 the conclusions are presented.

This report is a documentation and validation of the wind flow solver 3DWind. It is a part of the Dr.ing thesis of Ove Undheim to be submitted to NTNU. The work is also a part of the KMB "Development of Norwegian windpower technology", which is funded by the Norwegian Research Council and Statkraft SF.

# 2 Model description

## 2.1 Physical description and governing equations

3DWind solves the flow field on a meteorological microscale. The flow field can be regarded as incompressible if the Mach number[2] is below 0.3 (Ferziger and Perić, 2002). At the temperature 273K and one atmosphere pressure the speed of sound of dry air is 331m/s (Seinfeld and Pandis, 1998), which allows velocities up to 100m/s in an incompressible approach. Dealing mainly with windspeeds up to 25m/s, this assumption gives negligible errors. The sizes of the areas that are considered in each simulation are in the order 1 km$^2$-400 km$^2$. Some models working on this range choose to ignore the Coriolis force (Lopes, 2003) and others do not (Kim et al., 2000). In 3DWind the Coriolis force term is implemented to improve results. Note that most simulations are performed at sizes larger than 1 km$^2$, which is regarded mesoscale.

### 2.1.1 RANS equations

The model solves the incompressible Reynolds Averaged Navier-Stokes equations (RANS), where the averaged mass balance is given by:

$$\frac{\partial U_i}{\partial x_i} = 0 \tag{1}$$

$U_1$, $U_2$ and $U_3$ are the time averaged velocity components. $U_1$ and $U_2$ are the horizontal components, and $U_3$ is the vertical component.

Averaged momentum equations are given by:

$$\frac{\partial U_1}{\partial t} + U_j \frac{\partial U_1}{\partial x_j} - \frac{\partial}{\partial x_j}\left( -\overline{u_1 u_j} + \nu_t \frac{\partial U_1}{\partial x_j} \right) + \frac{1}{\rho}\frac{\partial P}{\partial x_1} - fU_2 = 0 \tag{2}$$

$$\frac{\partial U_2}{\partial t} + U_j \frac{\partial U_2}{\partial x_j} - \frac{\partial}{\partial x_j}\left( -\overline{u_2 u_j} + \nu_t \frac{\partial U_2}{\partial x_j} \right) + \frac{1}{\rho}\frac{\partial P}{\partial x_2} + fU_1 = 0 \tag{3}$$

---

[2] Fluid velocity divided by speed of sound

$$\frac{\partial U_3}{\partial t}+U_j\frac{\partial U_3}{\partial x_j}-\frac{\partial}{\partial x_j}\left(-\overline{u_3 u_j}+\nu_l\frac{\partial U_3}{\partial x_j}\right)+\frac{1}{\rho}\frac{\partial P}{\partial x_3}=0 \qquad (4)$$

The equations use summation over repeated indices. $u_1$, $u_2$ and $u_3$ are velocity fluctuations, $\nu_l$ is the kinematic viscosity, $P$ is the averaged pressure and $f$ is a factor that depends on the rotational speed of the reference frame. This term represents the Coriolis force, a fictive force acting perpendicular to the velocity vector. Compared to the velocity vector, the Coriolis force is rotated 90º in the clockwise direction at the northern hemisphere. All accelerated frames of reference cause fictive forces to appear, to compensate the acceleration of the frame of reference. The factor $f$ on the surface of the earth is given by equation (5).

$$f = 2\Omega\sin\phi \qquad (5)$$

$\Omega$ is the earth's rate of rotation (7.29x10$^{-5}$ sec$^{-1}$) and $\phi$ is the latitude (Panofsky and Dutton, 1984). At Norwegian latitudes from Lindesnes in the South (58º) to Nord Kapp in the North (71º) this corresponds to $f$ = 0.00012-0.00014s$^{-1}$.

The correlations of the deviation from the mean wind speed $-\overline{u_i u_j}$ are called the Reynolds stresses or second moments. This is a second-order symmetrical tensor that must be parameterized to close the equations.

Even though the time derivative is included in the equations, transient solutions are not achievable with the model. This is caused by the numerical approaches used to solve the equations. This is both connected to variable time step length described in subsection 2.2.7, and a non-physical solution of the pressure field described in subsection 2.2.2

## 2.2 Numerical aspects

The Reynolds Averaged Navier-Stokes equations can in general not be solved analytically. The equations have to be discretized and solved by a numerical method. The 3D finite volume method (Versteeg and Malalasekera, 1995) is used in 3DWind. This method divides the solution domain in a finite number of cubes, in which the values inside each cube is assumed to be constant. The Reynolds Averaged Navier-Stokes equations describe the interaction between the cubes. This collection of cubes is called a grid, and the grid generator Grid3d makes grids for use in 3DWind. Formally, this collection of cubes is named a mesh, while a grid is the collection of points used in the finite difference approach. Still, grid is generally the most used expression, and also often used instead of mesh.

To describe the numerical aspects, some terms have to be defined. This is a short summary of the definitions from Ferziger and Perić (2002). The *truncation error* is the difference between the discretized and the exact equation. For a method to be *consistent*, the truncation error must approach zero when the mesh spacing approaches zero. In order to get a solution, the numerical method has to be *stable*. A stable method does not magnify the errors that appear in the solution process. The contrary is a *diverging* method. The coupling of a consistent and stable solution gives *convergence*. This is difficult to demonstrate, and therefore convergence is usually checked by numerical experiments where all approximations used in the discretization process are consistent and the solution approaches grid independency.

Three other aspects to be aware of in this type of modelling are the *conservation*, the *boundedness* and the *realizability* (Ferziger and Perić, 2002). The equations to be solved are conservation laws, and the numerical scheme should respect this both on a local and global basis. For the finite volume method, the conservation on each cell secures conservation on global basis. Boundedness means that the numerical solutions should lie within the physical bounds, like density and turbulent energy never turning negative. Some phenomena are too complex to be treated directly, and thus have to be modelled. Realizability is the aspect of those models being designed to guarantee physically realistic solutions (Ferziger and Perić, 2002). The turbulence is an important quantity that has to be realizable to avoid divergence and unphysical solutions.

### 2.2.1 Grid generation

There has been little focus on grid generation in conjunction with micro scale modelling, and there exist no general rules to apply. The different approaches to the grid generation are discussed in the following. The important task of the grid generator is to produce a grid that represents the topography's influence on the flow as accurate as possible, given a finite number of grid cells. This is one of the most important issues of the discretization process. The grid should further secure a convergent and cost effective solution.

In order to make a grid, digitized topography information is needed. 3DWind is presently using the WAsP map format as input. This is a contour format. The extraction of the height information can be done in different ways. One way is to extract the height value at the point of interest directly from interpolation between the contours. This is one of the choices in Grid3d, and recommended if the grid is able to resolve the information in the available digitized map.

On the other hand, if the digitized map contains information on a sub grid scale, picking the height information based on one point can be a source of error. The point height may not be representative of the area surrounding the point. In this case an area averaging is preferred, giving the point a height value representative of the area it represents. The drawback of this procedure is that it reduces large absolute values of the second derivative of the surface, generating a generally undesired terrain smoothing.

A series of one-dimensional visualisations are given in *Figures 1-4* to illustrate these two effects. Different map resolutions and different grids are used on a series of sine hills (*Figure 1*). *Figure 1* illustrates the phenomenon that can occur if the map contains sub grid scale information. Without area averaging (black) the two geometrically identical series of hills come out with totally different information. The first is believed to be a long hill of height 60m, the second is not captured at all. With area averaging the result of the two series are almost predicted identical, as a long hill of height 30m. In this case the latter is the best prediction. The remaining information is sub grid scale, and should be accounted for by the roughness. The main problem without area averaging is the unpredictable result.

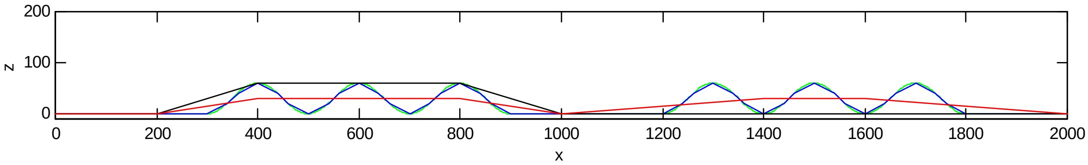

*Figure 1: The grid resolution is 200m and the equidistance is 20m. (●) is real topography, (●) is the map info with an equidistance of 20m, (●) is grid surface with area averaging and (●) is grid surface without area averaging.*

*Figure 2* illustrates the smoothing effect of the area averaging in areas of nonzero second derivative of the surface. The equidistance of the map is set to 0.1m to isolate the averaging effect. The effective hill height is in this case lowered by 0.6m.

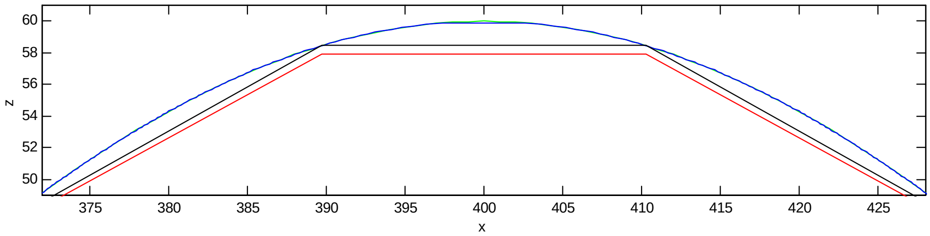

*Figure 2: The grid resolution is 20m and the equidistance is 0.1m. (●) is real topography, (●) is the map info with an equidistance of 0.1m, (●) is grid surface with area averaging and (●) is grid surface without area averaging.*

*Figures 3-4* illustrate the smoothing effect of the area averaging and the interpolation with a grid and a map resolution commonly used in real simulations. The equidistance of the map is set to 5m, and the grid cells are 20m. The figures show that the resolutions are of equal size. *Figure 3* shows the error emerging from a linear interpolation of the map information. This is actually lowering the hill height with more than one metre. This problem would have been improved with quadratic map interpolation. The last 2m are connected to the grid resolution. This could also have been improved by a least square fit of the entire surface.

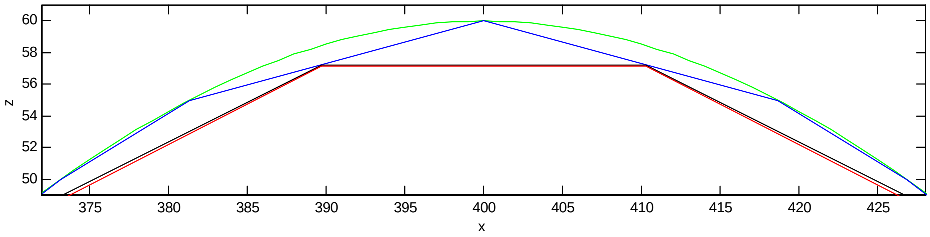

*Figure 3: The grid resolution is 20m and the equidistance is 5m. (●) is real topography, (●) is the map info with an equidistance of 5m, (●) is grid surface with area averaging and (●) is grid surface without area averaging.*

In *Figure 3* the differences with and without area averaging are small. Because of linear interpolation of the map, the second derivative of the area used in the area averaging is practically equal to zero. In *Figure 4* the grid coincides with points containing height information in the map. In this case the gain of quadratic map interpolation would be negligible, but the difference from area-averaged solution is larger because the area used in the area averaging contains a kink in the curve, corresponding to nonzero second derivative. As a conclusion, non-area averaging generally fits the terrain best, but the grid dependency is higher than with area averaging. This would partly be accounted for by quadratic map interpolation.

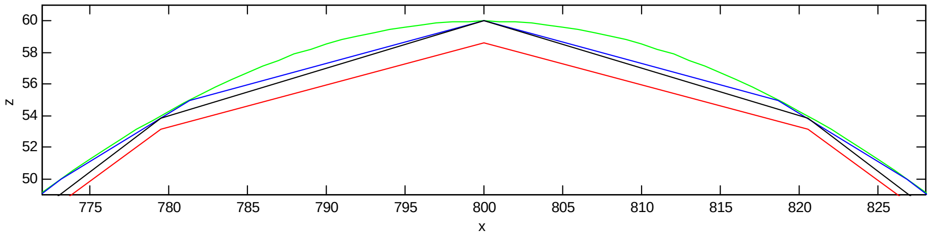

*Figure 4: The grid resolution is 20m and the equidistance is 5m. (●) is real topography, (●) is the map info with an equidistance of 5m, (●) is grid surface with area averaging and (●) is grid surface without area averaging.*

Grid3d makes grids that are non-orthogonal and terrain following. In steep terrain, this causes highly deformed grid cells. Ferziger and Perić (2002) state that the angle $\theta$ between the line, connecting neighbouring CV centres, and the cell-face normal $\vec{n}$ is a measure of deformation (see angle $\theta$ in *Figure 5*). An angle $\theta$ that is far from 0° can lead to large errors and convergence problems and should be avoided (Ferziger and Perić, 2002). In these cases the terrain is smoothed with the area averaging described in the previous section, until it is possible to achieve a stable solution.

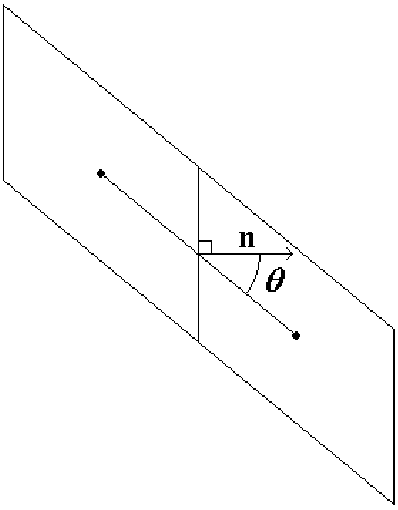

*Figure 5: An example of grid non-orthogonality.*

The smallest elevation information captured in the grid is of wavelength $2*\Delta x$. This wavelength is not resolved by the model, but can, if sufficiently large, cause numerical instability. To remove this frequency, a high frequency filter is used. This smoother-desmoother procedure is another feature adopted from mesoscale modelling (Dudhia et al., 2005).

Terrain elevations force the flow up and around the formation. This causes the vertical and the transverse velocity to become nonzero, and gives an increased vertical shear to the flow. Speed-up effects are present at the top of the formation, causing a pressure minimum. These effects are undesired at the boundaries, where it is difficult to capture those effects in the boundary condition. To ensure small gradients near the side boundaries, the elevation is gradually decreased to zero some distance from the outer bounds of the domain (*Figure* 6). This is not absolutely necessary, but helps to stabilize the solution.

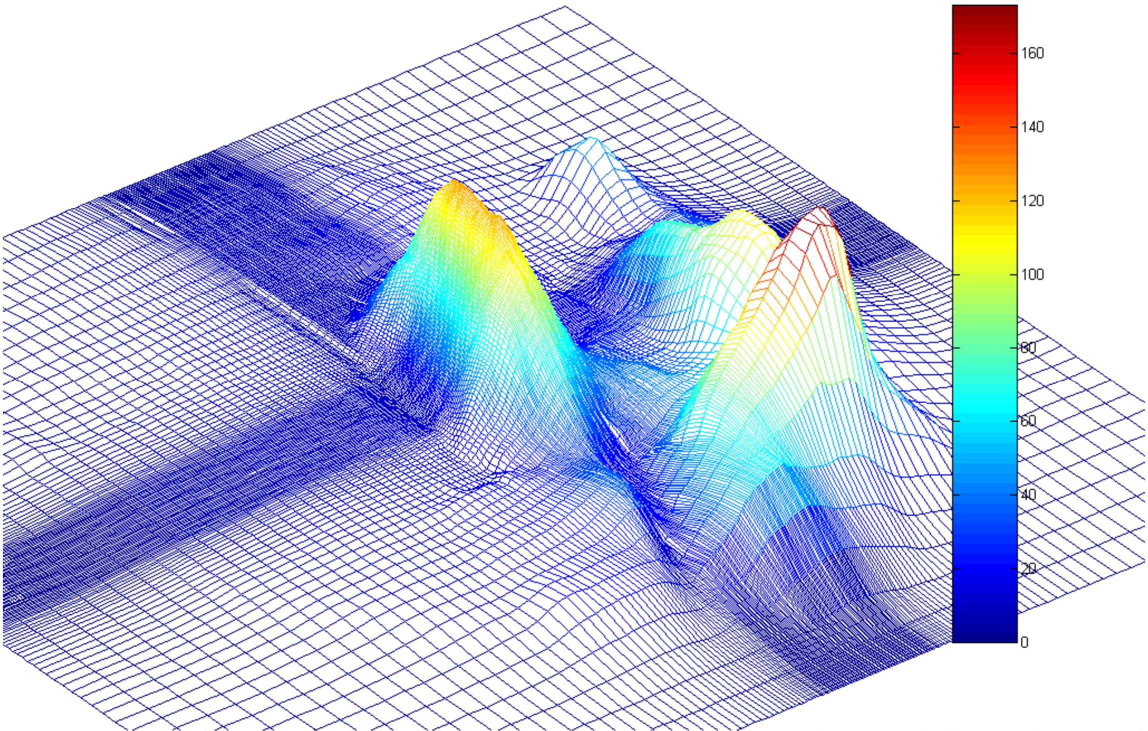

*Figure 6: The figure visualizes the horizontal grid from the Askervein hill simulation of chapter 4. The vertical scale is almost increased ten times to better show the terrain. The smoothing towards the boundaries is visible. The figure also illustrates the grid stretching with good resolution in the centre, and the large cell aspect ratios occurring in the centre of each side boundary.*

Another task of the grid generator is to focus the computational effort to areas of special interest or with high gradients (*Figure 6*). Computational costs are still a limiting factor in computational fluid dynamics. Minimizing the output data will also speed the post processing. Linear grid cell stretching is available in all directions. As a rule of thumb this stretching should be less than 20%, to ensure that the predictions are not corrupted by negligence of higher order terms in the estimation of gradients (Bredberg, 2002).

Typically, there are many grid cells near the ground where the gradients are high. In atmospheric flow the cell thickness ratio can be one hundred between the upper and lower boundary. The area of interest is usually placed in the centre of the domain with maximum resolution, and linear cell stretching towards the boundaries. A typical ratio between the horizontal spacing in the centre and near the boundary is twenty to forty. This causes cells with large aspect ratios in some areas (*Figure 6*), which should be avoided (Ferziger and Perić, 2002). Large aspect ratios can cause oscillations in one velocity component, which the pressure-velocity coupling may not be able to remove. This effect is minimized by the addition of artificial viscosity described is subsection 2.2.5. The largest aspect ratios are located near the boundaries, where the terrain is smoothed. This minimizes the combination of grid non-orthogonality and large aspect ratios

### 2.2.2 Pressure field calculation

The pressure field is only indirectly present in the incompressible flow equations (1)-(4). There is no obvious way to calculate the pressure, but when the correct pressure field is substituted into the momentum equations, the resulting velocity field satisfies the continuity equation (Patankar, 1980). A common way to solve the problem is by iteration, and several methods apply. One of the most used iterative methods using pressure and velocity correction is SIMPLE (Semi-Implicit Method for Pressure-Linked Equations) (Patankar, 1980).

In 3DWind the pressure field is calculated with Chorin's method (Chorin, 1967) (Hirsch, 1990). The average mass balance (1), is replaced by a pseudo compressibility equation:

$$\frac{1}{\beta^2}\frac{\partial P}{\partial t}+\frac{\partial U_i}{\partial x_i}=0 \tag{6}$$

The method converts the incompressible continuity equation into a time dependent equation that can be solved by Runge-Kutta time stepping, in an equal manner as the momentum equation. This gives the equations a hyperbolic character, with pseudo-pressure waves propagating with finite speed. For stationary solutions, equation (6) becomes equal to the incompressible continuity equation, and the pseudo speed of sound ($\beta$) can numerically be regarded as a relaxation. This method cannot be used to achieve transient or periodic solutions, since the solution is non-physical until steady state is reached.

### 2.2.3 Turbulence modelling

Turbulence is difficult to define precisely and is most often described by its properties. The first property of turbulence described in Panofsky and Dutton (1984), states that the fluid velocity is a chaotic and apparently random function of both space and time. This means that the turbulent information is contained in the velocity fluctuations. In the Reynolds Averaged Navier-Stokes equations (1)-(4), the only expression containing the velocity fluctuations is the Reynolds stresses, which therefore represent the turbulence of the flow. Another property of the turbulence is non-linearity. The Reynolds stresses are also non-linear terms, in accordance with this property.

In 3DWind the Reynolds stresses can be calculated by four different approaches. The simplest approaches are based on the eddy-viscosity assumption, and the advanced approach follow the Reynolds stress equation model (RSM) (Versteeg and Malalasekera, 1995).

In the eddy-viscosity assumption the Reynolds stresses are expressed by:

$$\overline{u_i u_j} = \frac{2}{3} k \delta_{ij} - \nu_T \left( \frac{\partial U_i}{\partial x_j} + \frac{\partial U_j}{\partial x_i} \right) \tag{7}$$

This is a first order closure, in meteorological literature called K-theory (Panofsky and Dutton, 1984), and in general turbulence literature called the Boussinesq eddy-viscosity approximation (Wilcox, 2000). $\nu_T$ is the turbulent viscosity and $k$ is the turbulent kinetic energy. The assumption relates directly to the diffusive property of a turbulent flow. Available turbulence models for the estimation of the turbulent viscosity in 3DWind are a zero-equation model, a one-equation k-l model and a two-equation k-ε model.

#### 2.2.3.1 A zero-equation model and the k-l model

A zero-equation model means that no additional differential equation is used to close the set of equations. This is a simple approach since the turbulence quantities are known to be flow dependent. A calibrated model in areas of homogeneous flow, can still give a fairly good approximation of the flow field. The turbulent viscosity is calculated from the algebraic expression:

$$\nu_T = \kappa \cdot u_\tau \cdot \min(z, z_{limit}) \tag{8}$$

$\kappa$ is von Karmans constant (0.41), $z$ is the height above the ground, and $z_{limit}$ is a maximum value of the length. In atmospheric flow, $z_{limit}$ is set to 100m. This is roughly one tenth of the planetary boundary layer depth. $u_\tau$ is friction velocity, defined as:

$$u_\tau = \sqrt{\frac{\tau_w}{\rho}} \tag{9}$$

In this equation $\tau_w$ is the wall shear stress. The model assumes a linear behaviour of turbulent viscosity in the logarithmic layer. This is in good accordance with experimental data from a turbulent boundary layer at zero pressure gradient (Anderson, 1988). Outside the logarithmic layer, the gradients are small, which means less dependence on the eddy-viscosity. A constant eddy-viscosity assumption is therefore sufficient in this area.

This model is only used in the initial phase of the generation of boundary condition data. The accuracy of the model will accordingly not influence the final results.

The k-l method is a one-equation method, with

$$\nu_T = c_0 \cdot \sqrt{k} \cdot l_m \tag{10}$$

In this equation $c_0$ is 0.4, $l_m$ is the mixing length given by equation (11), and $k$ is the turbulent kinetic energy given by the differential equation (12). Calculating the turbulent kinetic energy from a transport equation, incorporates non-local and flow history effects in the eddy viscosity (Wilcox, 2000).

$$l_m = \frac{\kappa \cdot z}{1 + \dfrac{\kappa \cdot z}{lmmax}} \tag{11}$$

*lmmax* is a constant that depends on the geometry surrounding the flow.

$$\frac{Dk}{Dt} = \frac{\partial}{\partial x_m}\left(\frac{\nu_T}{\sigma_k}\frac{\partial k}{\partial x_m}\right) + 2 \cdot \nu_T \cdot E_{ij} \cdot E_{ij} - \frac{c_e \cdot (k)^{3/2}}{l_m} \tag{12}$$

$E_{ij}$ is the mean strain-rate tensor (Versteeg and Malalasekera, 1995). This is a measure of the mean flow rate of deformation, which causes energy to be transferred from the mean flow to the turbulence.

$$E_{ij} = \frac{1}{2}\left(\frac{\partial U_i}{\partial x_j} + \frac{\partial U_j}{\partial x_i}\right) \tag{13}$$

$\sigma_k$ is 1.4 and $c_e$ is 0.064. The constants of this model are adjusted to give the same solution as the k-ε model for an atmospheric flow under homogeneous conditions (Nygaard, per.com., 2004).

This model is principally equal to a one-equation model described in Wilcox (2000), but the constants are different. One model applied to several flows with some degree of success used the values $\sigma_k$ equal to 1, $c_e$ ranging between 0.07 and 0.09 and $c_0$ equal to 1. The length scale distribution in that model is similar to those used in the mixing-length model (Wilcox, 2000).

Both the zero-equation model and the k-l model are incomplete. Incomplete means that there are flow dependent sizes that have to be specified in advance. In the zero-equation model, the entire turbulent viscosity is specified in advance, while in the k-l method the turbulent length scale $l_m$ has to be specified based on some geometrical length scale *lmmax*.

The advantage of zero- and one-equation models is that the numerical solution is simple and well behaved (Wilcox, 2000). The next two subsections will describe some two-equation models and a higher order model. Those models are complete, and generally need no flow information in advance. This makes the methods more general, and able to describe a wider range of flows without adjustments of parameters. The major disadvantages of these methods are that they need more computational effort to be solved and they can be difficult to solve (Wilcox, 2000).

#### 2.2.3.2 The k-ε model

This model is defined by the equations (14), (15) and (16).

$$\frac{Dk}{Dt} = \frac{\partial}{\partial x_m}\left(\frac{\nu_T}{\sigma_k}\frac{\partial k}{\partial x_m}\right) + 2 \cdot \nu_T \cdot E_{ij} \cdot E_{ij} - \varepsilon \tag{14}$$

$$\frac{D\varepsilon}{Dt} = \frac{\partial}{\partial x_m}\left(\frac{\nu_T}{\sigma_\varepsilon}\frac{\partial \varepsilon}{\partial x_m}\right) + C_{1\varepsilon}\frac{\varepsilon}{k}2\nu_T E_{ij}\cdot E_{ij} - C_{2\varepsilon}\frac{\varepsilon^2}{k} \tag{15}$$

$$\nu_T = C_\mu \frac{k^2}{\varepsilon} \tag{16}$$

ε is the dissipation rate of the turbulent kinetic energy, and is in this method described by a separate transport equation. Standard values of the constants in these equations are $C_\mu$=0.09, $\sigma_k$=1.00, $\sigma_\varepsilon$=1.30, $C_{1\varepsilon}$=1.44 and $C_{2\varepsilon}$=1.92 (Launder and Spalding, 1974). These values are used in the simulation of a channel flow experiment described by Almeida et al. (1993), which are described in Chapter 2.

In conjunction with atmospheric flow, there is no general agreement on the magnitude of these constants. According to Panofsky and Dutton (1984) the standard values are found to give too large values of the turbulent viscosity. Experimental values at the Askervein experiment indicate $C_\mu$ somewhere in the interval 0.03-0.06 (Raithby et al., 1987). Therefore, two constants are often changed in atmospheric flow. The value of $C_\mu$ is then about 0.03 and $\sigma_\varepsilon$ is 1.85 (Raithby et al, 1987)(Alm and Nygaard, 1995)(Castro et al., 2003). According to Kim and Patel (2000), the RNG k-ε method is found to have the best performance in atmospheric flow simulations. This leads to the following values of the constants in these equations; $C_\mu$=0.085, $\sigma_k$=0.7179, $\sigma_\varepsilon$=0.7179, $C_{1\varepsilon}$=1.42-$C_{1R}$ and $C_{2\varepsilon}$=1.68. Where the $C_{1R}$ and the corresponding $\eta$ are defined in equations (17) and (18).

$$C_{1R} = \frac{\eta\left(1-\dfrac{\eta}{4.38}\right)}{\left(1+0.015\eta^3\right)} \tag{17}$$

$$\eta = \sqrt{2E_{ij}E_{ij}}\,\frac{k}{\varepsilon} \tag{18}$$

According to Bonnin et al. (1995), the RNG k-ε model also gave more realistic recirculation region than the k-ε model in the C18 flow case, but this is not tested in this analysis.

#### 2.2.3.3 The Reynolds Stress Model

Instead of the assumption of a turbulent viscosity (7) that is proportional to the mean strain-rate tensor, the RSM calculates each of the Reynolds stresses with a separate transport equation (Versteeg and Malalasekera, 1995). The Reynolds stress tensor is a 2.order tensor, containing 9 elements. Because the Reynolds stress tensor is a symmetric tensor, six, instead of nine, equations appear. Compared to the k-ε model, with which totally 6 equations are solved, the RSM gives a total of 11 equations.

This allows flow history effects on the Reynolds stresses. The Boussinesq eddy-viscosity assumption (7) is known to be inaccurate for flows with sudden changes in mean strain rate and for flows with extra rates of strain (Wilcox, 2000). Practical situations in atmospheric flow, where the Boussinesq approximation fails, are flow over curved surfaces, three-dimensional flows and flows with boundary-layer separation (Wilcox, 2000). Disadvantages of the RSM model are that the computational effort is increased, and it can also be difficult to reach a convergent solution. The numerical scheme has to be sufficient accurate and stable to take advantage of the increased accuracy of the Reynolds stresses.

The increased accuracy of the Reynolds stresses may also be at a lower level than the general accuracy of the numerical method used to solve the equations.

$$\frac{D\overline{u_i u_j}}{Dt} = P_{ij} + \frac{\partial}{\partial x_m}\left(\frac{\nu_T}{\sigma_k}\frac{\partial \overline{u_i u_j}}{\partial x_m}\right) - \frac{2}{3}\varepsilon\delta_{ij} - C_1\frac{\varepsilon}{k}\left(\overline{u_i u_j} - \frac{2}{3}k\delta_{ij}\right) - C_2\left(P_{ij} - \frac{2}{3}P\delta_{ij}\right) \qquad (19)$$

Where $P_{ij} = -\left(\overline{u_i u_m}\frac{\partial U_j}{\partial x_m} + \overline{u_j u_m}\frac{\partial U_i}{\partial x_m}\right)$ and $P = \frac{1}{2}P_{kk}$

The values of the constants are $C_1$=1.8 and $C_2$=0.6. The value of $\varepsilon$ is found from (15), and the value of k is calculated from relation (20).

$$k = \frac{1}{2}\left(\overline{u_1^2} + \overline{u_2^2} + \overline{u_3^2}\right) \qquad (20)$$

### 2.2.4 Boundary treatment

An important numerical issue of the flow modelling is the boundary treatment. If the flow through and along the boundaries differs from the real conditions, so will the flow inside the domain. The boundary influence on the flow decreases with distance to the boundary. A non-physical boundary condition can therefore partly be accounted for by increasing the distance to the boundary. It is also preferred to operate with boundary conditions that are as flow independent as possible. Then general rules will apply.

The boundary conditions depend on the flow case, and there are several different possibilities. In the following the standard routines used in the two case studies presented in Chapter 3 and 4 are described.

Simulations with 3DWind require fully defined (Dirichlet) vertical profiles at the inflow boundary for all variables except the pressure, which is discussed separately at the end of this subsection. On the outflow boundary, there is a Neumann (zero gradient) condition. Periodic conditions are enforced at the side boundaries. This means that what goes out of one side, comes into the other. This ensures no leak of mass, momentum and energy.

The ground surface boundary is probably the most important boundary to evaluate accurately. In atmospheric flow this is the only solid boundary. It is not possible to remove the boundary to reduce the influence. The nacelle of wind turbines is located 50-100 m above the surface boundary, while the distances of the other boundaries are at least a factor 10 larger. Because of the no-slip boundary condition on the ground, this is also the part with the highest gradients. The boundary condition is expressed by wall functions.

3DWind have implemented two different methods to handle the influence of the wall. Both methods are based on wall functions. The simplest method (Versteeg and Malalasekera, 1995) calculates the values of the velocity, the turbulent kinetic energy and the dissipation directly from the wall functions. The velocity of the first cell follows the logarithmic law

$$U = \frac{u_\tau}{\kappa} \ln\left(\frac{z}{z_0}\right) \tag{21}$$

In this equation $z_0$ is the roughness length. This is a dimensional constant depending on the friction caused by the ground. The equation is only valid if $z_0 << z$. In atmospheric flow the roughness length typically ranges from $10^{-4}$m for calm open sea to 1m for forests and city centres (Arya, 1988).

One source of error in the direct wall function approach for the three velocities is that the continuity equation will generally not be fulfilled in the first grid cell. This will cause the modified continuity equation to continuously try to increase or lower the pressure in the first grid cell. This gives oscillations in the pressure field near the ground.

To account for this problem, it is possible to adjust the vertical velocity in the first grid cell to fulfil the continuity equation. This flow field adjustment will destroy the equation dynamics, since the pressure is calculated from the pseudo compressibility method described in subsection 2.2.2. To ensure a smooth pressure through the first grid cell, additional numerical diffusion is added to the continuity equation calculating the pressure.

The expressions of the turbulent kinetic energy and the dissipation ε are given by equation (22) and (23), respectively

$$k = \frac{u_\tau^2}{\sqrt{C_\mu}} \tag{22}$$

$$\varepsilon = \frac{u_\tau^3}{\kappa y} \tag{23}$$

An alternative approach is described in the first part of Craft et al. (2002), and is in that article named the conventional wall-function approach. The motivation for the introduction of a second wall function is twofold. Firstly, the velocity-pressure coupling works properly, and the continuity equation will have the opportunity to be fulfilled. This gives a smooth pressure field in the near wall area. Secondly the logarithmic connection between the first and the second cell sometimes causes errors. In areas of flow separation the pressure gradients sometimes cause the profile to physically differ a lot from the logarithmic profile (21) that is enforced.

Only the value of ε in the first cell is calculated directly from the wall function.

$$\varepsilon = \frac{k_P^{2/3}}{c_l y} \tag{24}$$

To calculate the velocities, the shear force $\tau_w$ from the wall is calculated from the wall function expression of the velocity (21) and the turbulent kinetic energy (22). Combining these together with the expression of the friction velocity (9) give (25)

$$\tau_w = \frac{\kappa c_\mu^{1/4} \rho k_P^{1/2} U_P}{\ln\left(\frac{z}{z_0}\right)} \tag{25}$$

The turbulent kinetic energy is calculated by assuming that the diffusion of turbulent kinetic energy through the wall is zero. The production and the dissipation of the turbulent kinetic energy within the first cell are evaluated through analytical integration, due to the high gradients within the cell.

The top boundary is evaluated using different approaches, depending on the flow. The channel case uses wall functions equal to the bottom surface. In the atmospheric flow, there is a forced physical boundary following the flow. The horizontal velocity is unchanged through the boundary, but the vertical velocity is forced to be zero at the boundary. This can be compared to a stably stratified layer in the atmosphere, which also will suppress vertical motions. To minimize the errors caused by over speeding, the terrain height on the ground must be small compared to the total height of the computational domain. As a rule of thumb, the total domain height in 3DWind is at least 10 times the maximum height of the topography.

A zero gradient approach equal to the outflow boundary is also possible at the top boundary, though mass flow budgets through the boundaries should here be used to avoid changes in the total momentum (Ferziger and Perić, 2002).

The pressure boundary condition is extrapolated from the inside on all boundaries. On the inflow and the outflow, a first order pressure extrapolation is used. There are periodic boundary conditions at the sidewalls. The bottom and the top are calculated by a zero order extrapolation. This is because the pressure isobars are mainly normal to the boundary, but also because of the pressure oscillations. These will cause larger errors with a first order approach.

To maintain a pressure field that does not drift in level, a method calibrates the pressure to be zero in one specified cell.

#### 2.2.4.1 Initial conditions

The initial condition should not influence the final steady state solution, but the chosen flow field influences the computing time. A flow field that differs much from the final solution can also cause the model to diverge.

The one-dimensional profiles from the inflow boundary condition are usually also used as the initial condition all over the domain. There is no initial condition for the pressure, so the pressure is set to zero over the entire domain.

### 2.2.5 Artificial viscosity

The artificial viscosity term is partly following the description of Jameson's artificial dissipation (Hirsch, 1990). It is isotropic in character. It is a fourth order expression added to the flux in each differential equation. It can be gradually switched off, or be set to zero if there is no need for additional diffusion.

The method ensures conservation of momentum through the cell faces. At a uniform grid the effect of the artificial viscosity at the mean horizontal velocity in the horizontal direction at one time step would be according to equation (26)

$$art\_visc = art\_fac \cdot \left(-U_{i-2} + 4 \cdot U_{i-1} - 6 \cdot U_i + 4 \cdot U_{i+1} - U_{i+2}\right) \tag{26}$$

The indices i are the cell number in the x-coordinate direction. The equation in the y-direction (j) is equal, but the z-direction (k) contains an additional multiplication factor. This is a reduction towards the wall. The reduction follows the square root of the normalized wall distance, and is introduced to avoid too high a level of smoothing in the near wall area, where gradients are high, but natural diffusion is also high.

### 2.2.6 Residual smoothing

The differential equations are discretized by the finite volume method, and the residuals of the entire flow field are calculated algebraically based on the previous time step values. This procedure causes limitations of the maximum allowable time step, and is further described in the next subsection. To be able to increase the time step limit, some implicit character has to be given to the solution method. This is done by an interconnection between all the residual values $R_{ijk}$.

$$\left(1-\varepsilon\delta_x^2\right)\left(1-\varepsilon\delta_y^2\right)\left(1-\varepsilon\delta_z^2\right)\overline{R}_{ijk} = R_{ijk} \tag{27}$$

In this equation $\delta_x$, $\delta_y$ and $\delta_z$ are the derivative in the x, y and z direction. $\varepsilon$ is not the dissipation described in the subsection covering the turbulence models, but a value greater than zero, depending on the level of residual smoothing. The maximum allowed time step increases with increased $\varepsilon$. $R_{ijk}$ are the residual values before smoothing, and $\overline{R}_{ijk}$ are the values after smoothing. This residual smoothing will also have a smoothing effect on the high-frequency variations (Hirsch, 1990).

To solve equation (27), the equation is split in one equation for each direction. One possible set of equations is

$$\begin{aligned}\left(1-\varepsilon\delta_x^2\right)R_{ijk}^{*} &= R_{ijk}\\ \left(1-\varepsilon\delta_y^2\right)R_{ijk}^{**} &= R_{ijk}^{*}\\ \left(1-\varepsilon\delta_z^2\right)\overline{R}_{ijk} &= R_{ijk}^{**}\end{aligned} \tag{28}$$

Written in a discrete way:

$$\begin{aligned}
-\varepsilon R^{*}_{i+1,j,k} + (1+2\varepsilon)R^{*}_{i,j,k} - \varepsilon R^{*}_{i-1,j,k} &= R_{i,j,k} \\
-\varepsilon R^{**}_{i,j+1,k} + (1+2\varepsilon)R^{**}_{i,j,k} - \varepsilon R^{**}_{i,j-1,k} &= R^{*}_{i,j,k} \\
-\varepsilon \overline{R}_{i,j,k+1} + (1+2\varepsilon)\overline{R}_{i,j,k} - \varepsilon \overline{R}_{i,j,k-1} &= R^{**}_{i,j,k}
\end{aligned} \tag{29}$$

The tridiagonal matrix algorithm is used to solve these equations one by one. Each value in the resulting residual field is now dependent on all values in the initial residual. It is sufficient to apply the smoothing at alternate stages, provided the smoothing parameter $\varepsilon$ is sufficiently increased (Hirsch, 1990).

### 2.2.7 Integration of time

After Jameson et al. (1981) first proposed an explicit Runge-Kutta method for the solution of the Euler equations, several Runge-Kutta methods have become available. In 3DWind the time integration is solved by an explicit, three-stage Runge-Kutta method (Eriksson (1987), referred in Øye (1996)).

$$\begin{aligned}
U^{(0)} &= U^{n} \\
U^{(1)} &= U^{(0)} + \Delta t \cdot R\left(U^{(0)}\right) \\
U^{(0)} &= \frac{1}{2}\left(U^{(0)} + U^{(1)}\right) \\
U^{(2)} &= U^{(0)} + \frac{1}{2}\Delta t \cdot R\left(U^{(1)}\right) \\
U^{n+1} &= U^{(0)} + \frac{1}{2}\Delta t \cdot R\left(U^{(2)}\right)
\end{aligned} \tag{30}$$

To evaluate the accuracy and the stability of the scheme, according to Hirsch (1988), the linear case of the model problem *R(U)=ΩU* is inserted. This gives

$$U^{n+1} = \left[1 + \Omega\Delta t + \frac{(\Omega\Delta t)^2}{2} + \frac{(\Omega\Delta t)^3}{4}\right]U^{n} \equiv zU^{n} \tag{31}$$

In this equation z is the root of the characteristic polynomial. It is seen from equation (31) that the scheme is second-order accurate, since z is the Taylor expansion of the exact amplification *exp(ΩΔt)* up to second order. The stability region is also found from the characteristic polynomial. The method is unconditionally stable if the complex length of the characteristic polynomial is less than one, i.e.

$$\left|1 + z + \frac{1}{2}z^{2} + \frac{1}{4}z^{3}\right| \le 1 \tag{32}$$

where

$$z = x + yi\,. \tag{33}$$

This gives the stability zone on the real axis range from -2 to 0. This is equal to a regular second-order scheme (Hirsch, 1988). On the imaginary axis, the zone ranges between ±2. This is larger than the regular third-order, which has the range between $\pm\sqrt{3}$. This means that the scheme will be conditionally stable for central differenced convection equations, in contrast to a standard second-order method, which does not include any portion of the imaginary axis (Hirsch, 1988). This is a result of the fact that the convection equation has imaginary eigenvalues. It is the non-linear convection expression that causes the main stability problem in the Navier-Stokes equation.

The CFL (Courant-Friedrichs-Lewy) stability restriction is an inequality equation telling which fraction between the resolution in space and time that will give a stable solution. In the simple one-dimensional situation this is expressed as

$$\frac{U\Delta t}{\Delta x} < C \tag{34}$$

The maximum value of the inequality is the Courant number *C*. In this second-order RK scheme the Courant number is found to be equal to 2, and the time step restriction of the problem is given in equation (35) (Øye, 1996). The equation is expressed in finite volume formulation.

$$\Delta t \le \frac{C \cdot Vol}{\left|U \cdot SI\right| + \left|U \cdot SJ\right| + \left|U \cdot SK\right| + \beta\left|SI + SJ + SK\right|} \tag{35}$$

In this equation *C* is the Courant number, *Vol* is the cell volume, *SI* is area in i-direction, *SJ* is area in j-direction and *SK* is area in k-direction. $\beta$ is the pseudo speed of sound and *U* is the velocity vector.

The accuracy is at the same level as a standard second-order scheme, the memory usage the same as a second-order scheme, the computational effort of each time step is on the same level as a third-order scheme, and the time step restriction lies in between a third-order and a forth-order scheme. The Runge-Kutta schemes are found to be both effective and robust, and this particular scheme has good damping properties (Øye, 1996).

The length of the time step is not uniform for the entire domain. It is calculated for each cell to follow the CFL restriction. This will only allow stationary solutions.

# 3 Testcase C18 ERCOFTAC

3DWind is tested on testcase C18 in the ERCOFTAC Classic database described in Almeida et al. (1993). The experiment represents some effects related to flow in complex terrain, and aims to help “to provide the necessary details to allow the evaluation of mathematical models of the flow over complex terrain. The scaling laws for flows over practical hills are not obeyed, but the analysis is still valid in discussing the nature of turbulence within the internal layer that dominates the practical flows. The results should therefore be treated with caution if they are to be compared to those obtained in either properly simulated model experiments or field results".

One important aspect is the testing of a solver's ability to reproduce recirculation. "The extent and strength of the recirculation zones established in the lee of the obstacles change the wind field not only in the separation region itself but over the entire hill, so that defining its limits becomes a prerequisite of establishing the overall flow field" (Almeida et al., 1993). Another interesting aspect that is also connected to the previous is the mean velocity speed-up on the hilltop (Almeida et al., 1993).

The experiment by Almeida et al. was one of the cases considered at the 4th ERCOFTAC/IAHR Workshop on Refined Flow Modelling, held at Karlsruhe in 1995. At this event 38 different results were submitted for this case (Bonnin et al., 1995).

### 3.1 Experimental description

The C18 test case describes a channel flow. The flow medium is water, and the kinematic viscosity of water is $v = 1\text{x}10^{-6}\text{m}^2/\text{s}$ at 20ºC. The channel flow is fully developed with a Reynolds number based on the centreline velocity and the hill height of 60 000 ($Re=hU_0/v$). The test case is chosen both because the experimental results are regarded to be good, and because the test case is used in a workshop and contains reference simulation results.

The flow medium in atmospheric flow is air, and the choice of a validation simulation with a different medium has both advantages and disadvantages. The large difference in density is a way to check that the density is correctly implemented. It is also a way to check the generality of the model. The disadvantage is the fact that the model is validated with a case that is far from the condition the model is calibrated to simulate. This case alone would therefore be insufficient for the evaluation of the model.

The channel height is 0.170m and the width of the channel is 0.2m. The centreline velocity at the inlet is 2.147 m/s, and the flow is recirculating in the wake of a two-dimensional, polynomial-shaped obstacle that is symmetrical about a vertical plane through the hilltop. The height of the hill is 0.028m, and the test section is shown in *Figure 7*. The centreline turbulence intensity is about 3%, and the friction factor is $C_f = 0.0026$ and the wall friction velocity is $u_\tau = 0.0689$ m/s (Almeida et al., 1993). A Laser-Doppler Velocimeter collects the flow data. Measurement errors from the Laser-Doppler measurements for a 95% confidence level are estimated to 0.5% for the mean values, and 3% for the Reynolds stresses.

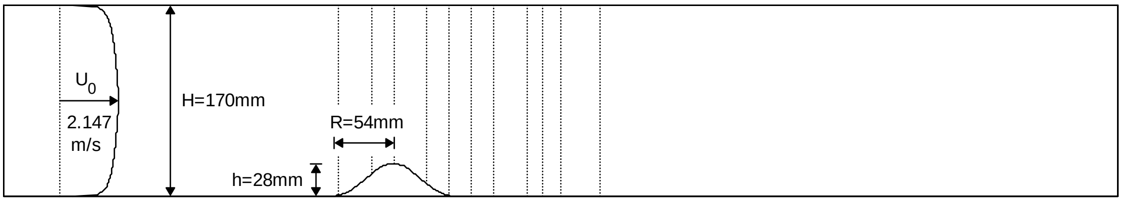

*Figure 7: The part of the tunnel containing the test section. The section shown is 1m long while the total length is 7m. The section is located about 6m downstream of the tunnel inlet. Dashed lines indicate locations of the measurement profiles.*

## 3.2 Reference solutions

A dataset of reference solutions for both the k-ε and the RSM turbulence models has been established (Laurence et al., 2004). The reference solution is established as a result of simulations executed by different users and different codes. The codes are not named in the analysis, but both large commercial and "in house" codes have been used. Grid refinement tests are performed to ensure that the results are grid independent. Different inflow conditions have also been tested to check the code's inflow dependency.

In the validation of a flow model, the results should rather fit the respective reference solution than the experimental results. One physical parameter that differs from the experimental results is the wall friction velocity $u_\tau = 0.079$ m/s (Laurence et al., 2004). The reference solutions are plotted together with experimental profiles and simulation results throughout the figures.

The cell number of the reference solution is 64 000, and the computational domain consists of 400 grid cells in the horizontal direction, and 160 grid cells in the vertical direction. The simulation is two-dimensional.

## 3.3 Grid

If an optimal grid is chosen, the model should be able to accurately describe the flow field at a low computational cost. To achieve this, the boundaries of the simulation domain are located in an optimal way to let the inflow and outflow boundary have a minor effect on the flow field around the hill and the recirculation zone. At both the inflow and the outflow boundary, the flow is assumed not to have gradients in the flow direction (x). This is not physical, but the boundaries should be placed far enough from the hill that the error is negligible. Errors caused by flow oscillations in space at inflow, should also be damped to not influence the flow in the hill vicinity. This is also taken into account in the reference simulation, and to be able to compare the results with the reference solution, a natural choice is to use the same domain.

The simulation channel section starts 0.3m before the hilltop and ends 0.8m behind the hilltop. The grid contains 140 grid cells in the horizontal direction (x) and 100 grid cells in the vertical direction (z), with a variable spacing in both directions. The cell sizes in the x-direction differ from 1.8mm at the hilltop, to 21mm and 27mm in the inflow and outflow. In the vertical direction, the stretching factor is 1.02, with the cell heights varying from 1.0mm at the boundaries, to 2.7mm in the centre. Due to terrain following features, the first cell at the hilltop is 0.6mm. The grid of the lower half of the section around the hill is shown in *Figure* 8.

The wall function assumption used in the modelling assumes logarithmic profiles; those are normally expected in the overlap layer. By definition, this layer covers the distance $35 \leq z^+ \leq 350$ (White, 1991)($z^+ = zu_\tau/\nu$), which corresponds to $4.43 \text{x} 10^{-4}\text{m} \leq z \leq 4.43 \text{x} 10^{-3}\text{m}$ in this particular case. To ensure that the assumption of logarithmic profiles is valid, both the first and the second grid point are within this distance.

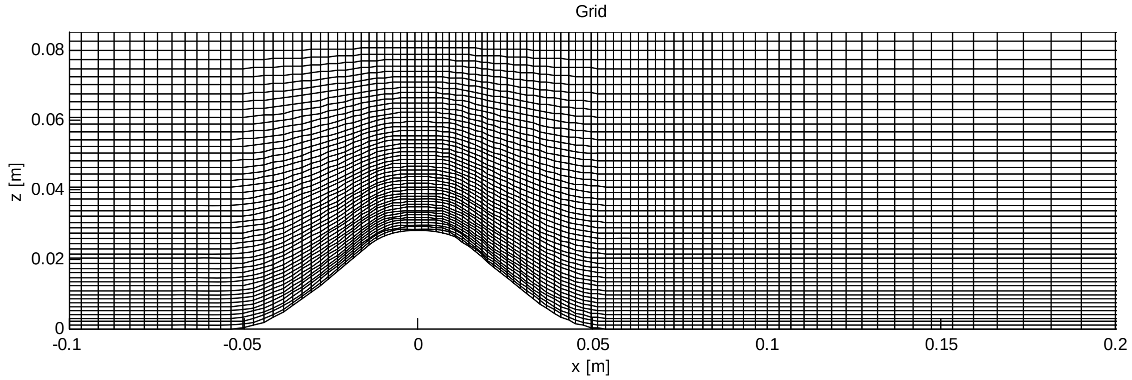

*Figure 8: The grid used in the present simulation.*

## 3.4 Simulation

The inflow profile of the reference solution is used as an inflow profile of the simulation. The wall functions are dependent on the wall friction velocity, which is given as 0.0689m/s (Almeida et al., 1993). A preliminary report by Almeida et al., available at the ERCOFTAC website, gives the friction velocity 0.079m/s. This is also the value used in the reference simulation. To be able to easily compare the modelling results with the reference solution, 0.079m/s is the chosen friction velocity in the 3DWind simulations. A separate simulation, without the hill, estimates the roughness $z_0$ corresponding to this friction velocity. The roughness is adjusted in small steps until the friction velocity in the position of the hill is $u_\tau$=0.0790m/s +/- 0.0001m/s. This method and the results of the simulation are described in subsection 3.5.2.

This simulation is a 2D simulation in the xz-plane, so the differential equation of the transverse velocity (y-direction) is not solved. This simplifies the flow field, and there is no need for additional artificial viscosity together with the k-l or k-ε turbulence model. The eddy-viscosity formulation secures sufficient damping. This gives the opportunity to test the sensitivity of the flow field to the artificial viscosity. The simulation with the RSM turbulence model is not able to damp oscillations produced by the advection term. This causes general results to have an artificial viscosity of 0.001 in the k-ε and the k-l turbulence model results, while the RSM approach uses an artificial viscosity of 0.003. The dimensions of the experimental set up given in *Figure 7* are also implemented in the modelling set up.

## 3.5 Results

### 3.5.1 Pseudo-sonic speed evaluation

The pseudo-sonic speed is an important quantity to measure the convergence rate and the stability of the numerical scheme (Hirsch, 1990). To find a reasonable value to use in the simulation, a parameter study of this quantity is performed. The value optimization is a compromise between fast convergence and small oscillations about the converged value. Hirsch (1990) indicated optimal convergence if $\beta^2 / u_{ref}^2$ is in the range 5 to 10, with divergence occurring around 100. This corresponds to a value of $\beta$ between 5 and 7, with a maximum of 21 for this particular case. Rogers and Kwak

(1991) simulated laminar flow in a square duct with bend. They found excellent convergence for values of $\beta$ ranging from 1.0 to 100, with an optimum for $\beta$ equal to 10. Based on this, evaluations are done with $\beta$ equal to 1, 5, 10, 20, 40, 80 and 150. The analysis is done with both the k-l and the k-ε turbulence models. k-l is the most stable model, and usually used from the start of the simulation. In this case, the 2D condition makes the flow simpler, and the k-ε turbulence model can therefore be used from start instead of the k-l model.

The chosen value of $\beta$ is a compromise between stability and convergence rate. If as fast a convergence as possible is desired, the value of residual smoothing is set to two, and the CFL number is set to 30. With this starting point, the k-l turbulence model gave divergence for the pseudo sonic speed values of 1, 5, 10 and 20, and the k-ε turbulence model also diverged with the value 40. On the other hand, the value of the pseudo speed should be chosen as low as possible. If the solution is stable, the low values give the fastest convergence. Due to diverged solution with the value 40, 50 is used in the k-ε simulation. The results are given in *Figures 9-14*.

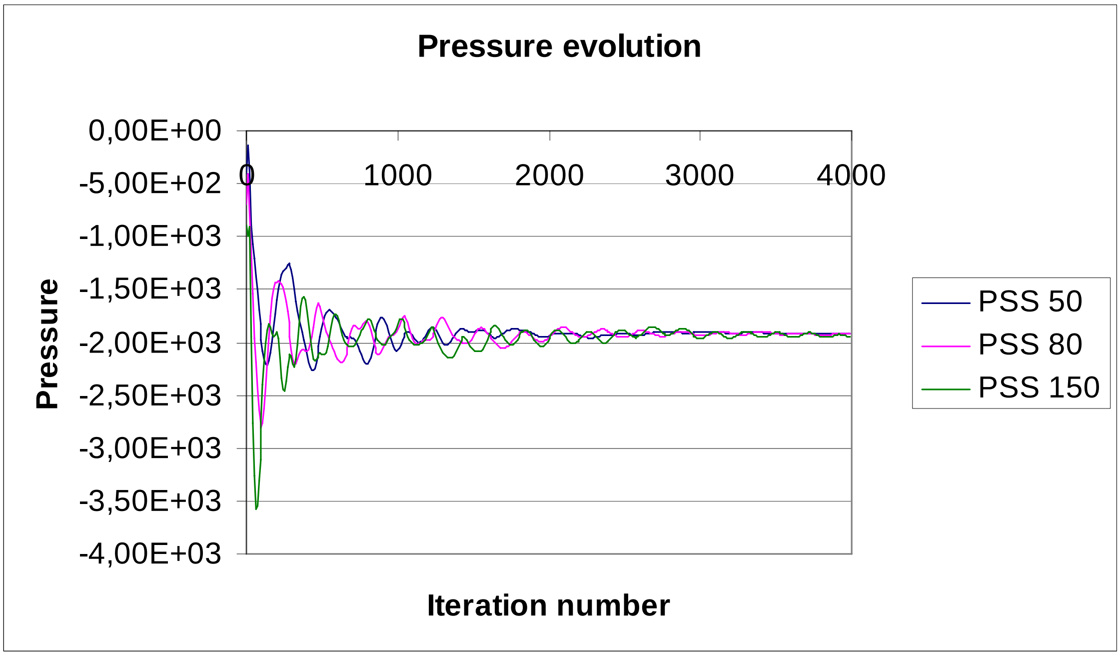

*Figure 9: The converging pressure with the three different pseudo-sonic speeds. Sufficient convergence is found after about 4000 iterations. Values are collected from cell number i=50 and j=12. This is about 1 cm above ground level in the area of flow separation, 1.3cm downwind from hill summit.*

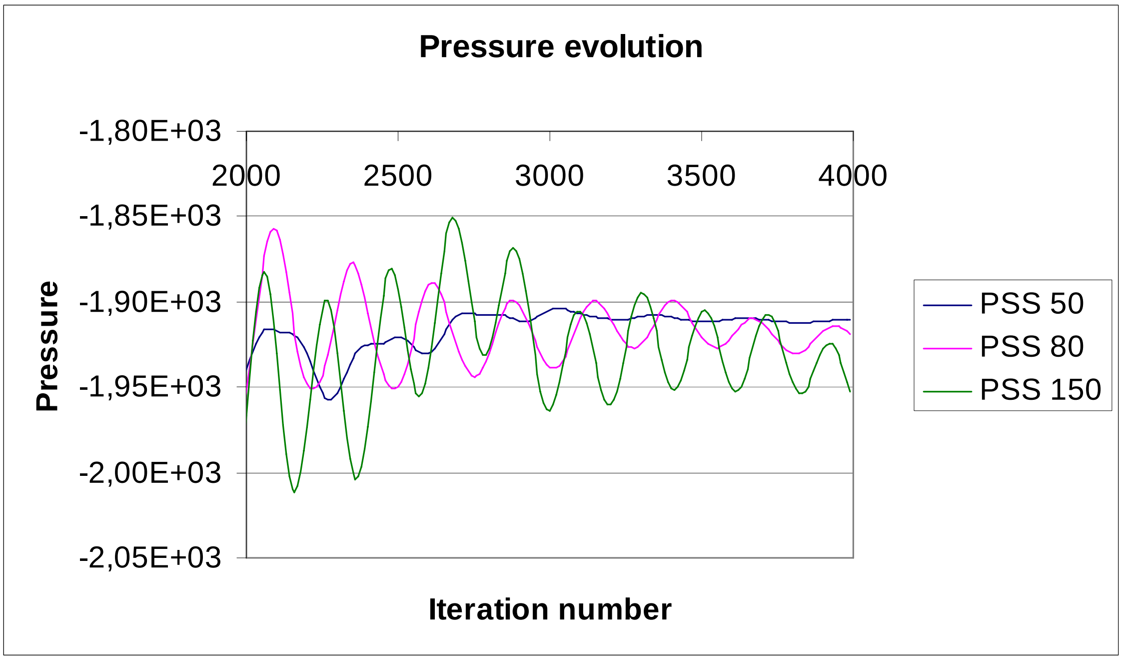

*Figure 10: Close-up of Figure 9, a detailed view of the converging pressure the last 2000 iterations. The best convergence is found for the pseudo-sonic speed equal to 50m/s. Values are collected from cell number i=50 and j=12. This is about 1 cm above ground level in the area of flow separation, 1.3cm downwind from hill summit.*

*Figure 11: The convergence of velocity with the three different pseudo-sonic speeds. Sufficient convergence is found after about 4000 iterations. Values are collected from cell number i=50 and j=12. This is about 1 cm above ground level in the area of flow separation, 1.3cm downwind from hill summit.*

*Figure 12: Close-up of Figure 11, a detailed view of the converging velocity the last 2000 iterations. The best convergence is found for the pseudo-sonic speed equal to 50m/s. Values are collected from cell number i=50 and j=12. This is about 1 cm above ground level in the area of flow separation, 1.3cm downwind from hill summit.*

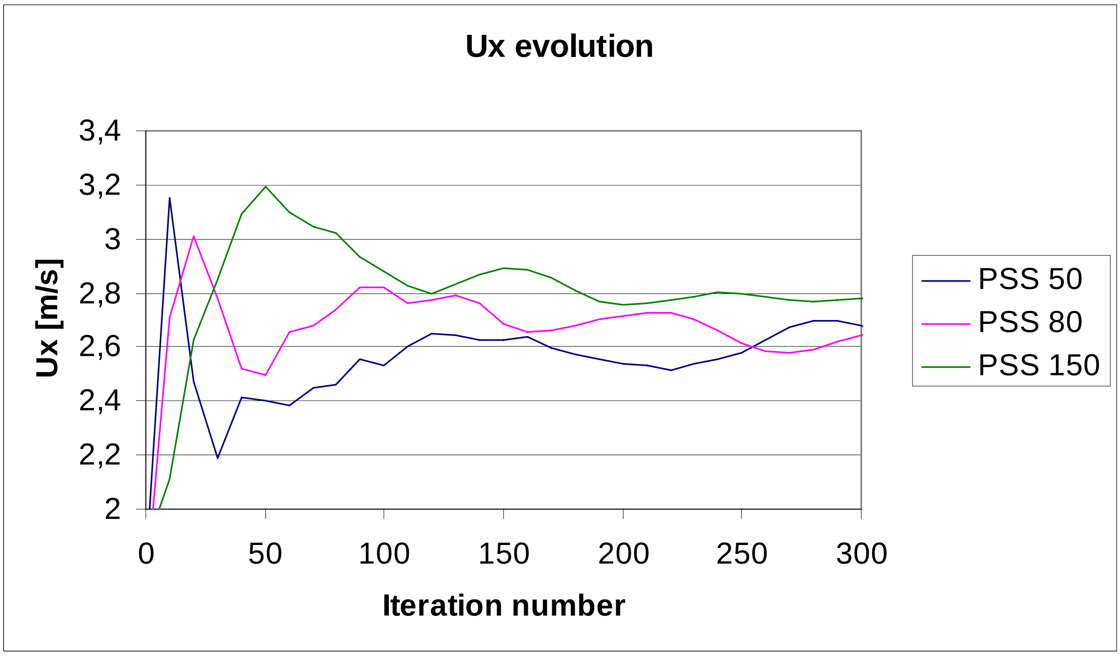

*Figure 13: Close-up of Figure 11, a detailed view of the converging velocity the first 300 iterations. The early peak for the pseudo-sonic speed equal to 50m/s shows the critical point for low values of the pseudo-sonic speed. Values are collected from cell number i=50 and j=12. This is about 1 cm above ground level in the area of flow separation, 1.3cm downwind from hill summit.*

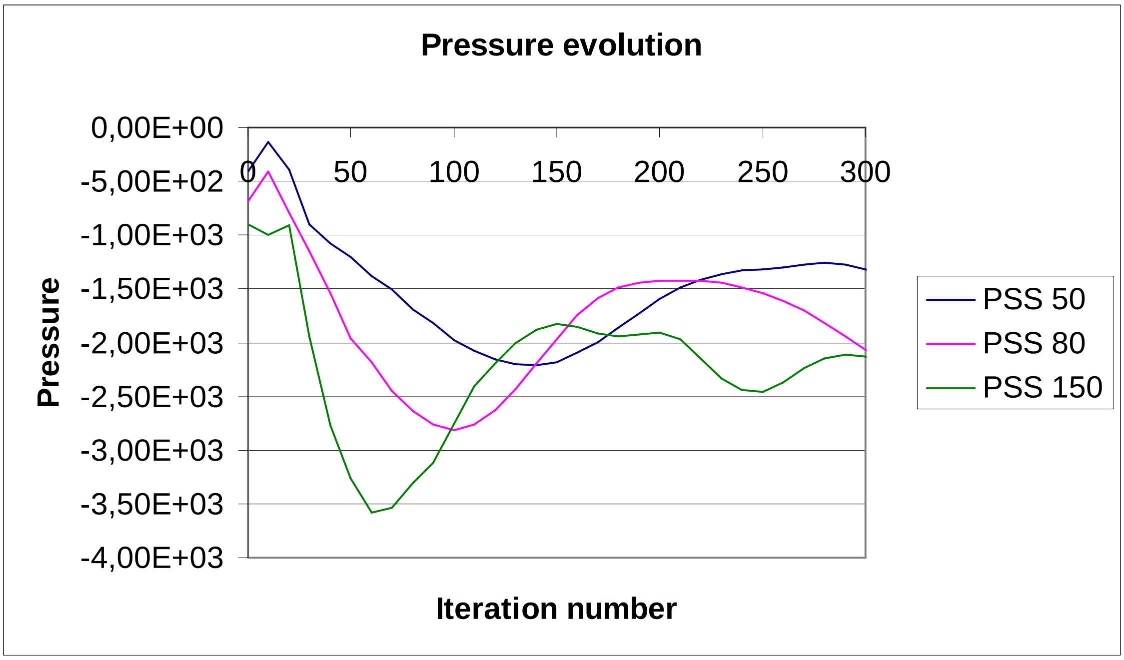

*Figure 14: Close-up of Figure 9, a detailed view of the converging pressure the first 300 iterations. The pressure effect is slower for low values of pseudo-sonic speed. Values are collected from cell number i=50 and j=12. This is about 1 cm above ground level in the area of flow separation, 1.3cm downwind from hill summit.*

*Figure 10* shows that the time oscillations at 4000 iterations are increasing with increasing pseudo-sonic speed. The conclusion is that the pseudo-sonic speed should be as low as possible, but a diverging solution must be avoided. The pseudo-sonic speed is chosen equal to 50m/s in this simulation.

### 3.5.2 Roughness estimation

In the experiment, the evaluation of the friction velocity is performed without the hill, at the location of the hilltop. The same is done in the simulation. The flow domain equals the hill case, but the channel is flat, and the estimation of the roughness is done at the x-location of the hilltop. The initial value of the roughness is estimated from the reference solution and the log law as in equation (36).

$$z_0 = \frac{z}{e^{\frac{\kappa \cdot U}{u_\tau}}} \tag{36}$$

$z_0$ is the roughness height, $z$ is the centre height of the first grid cell in the reference solution (1.404E-3m), $U$ is the velocity in this cell (1.343m/s), $u_\tau$ is the friction velocity of 0.079m/s and $\kappa$ is constant 0.4. This gives the initial $z_0$ value of 1.6E-6m.

The roughness is adjusted until the calculated friction velocity in the centre in the absence of the hill is 0.079m/s. In the method used, the value of the roughness stabilized at the value 2.485E-6m after about 2000 iterations. Another 2000 iterations are done to check that this value is not altered. Based on this analysis, the value $z_0$ = 2.5E-6m is used in the simulations.

### 3.5.3 Evaluation of artificial viscosity

All results considered in this report are calculated with an artificial viscosity factor 0.001. This is small enough to have minor effects on mean values, but still large enough to smooth out the strongest oscillations. Spatial oscillations at the size 2Δx are present in the flow because of central differences in the advection term. To evaluate the effect of the artificial viscosity, the results are compared to solutions with no artificial viscosity, and with an artificial viscosity factor of 0.005. At this level, the artificial viscosity is expected to have a visible influence on the solution.

The results are visualized in *Figure 15*, where the horizontal and the vertical velocity and the turbulent kinetic energy are evaluated at two different locations. The first line is from the top of the hill, and the second is from the recirculation zone 90mm behind the hilltop. To be able to see the differences, the figures are zoomed to view the most critical area near the bottom surface. The figures show that all the different values of the artificial viscosity could actually have been used with a minor loss of accuracy, though care should be taken before raising the artificial viscosity further on. From these results the best alternative seems to be the chosen artificial viscosity factor 0.001.

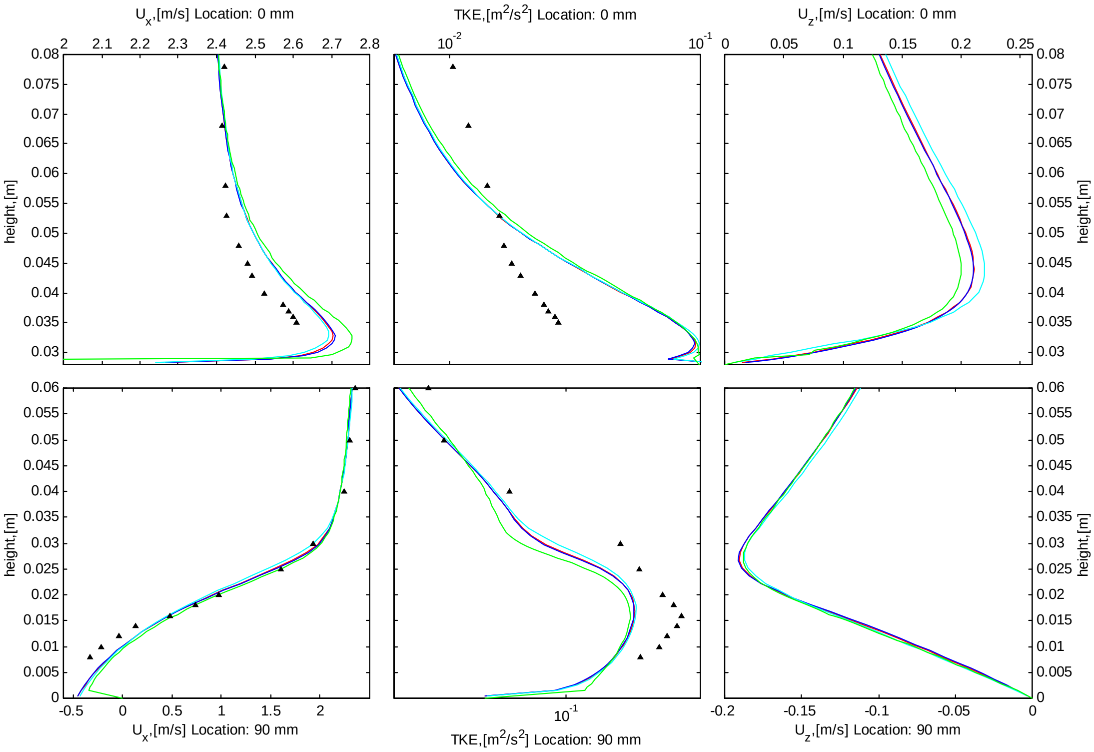

*Figure 15: The figure shows the differences between the reference k-ε solution (●), k-ε artificial viscosity 0.005(●), k-ε no artificial viscosity(●), k-ε artificial viscosity 0.001(●). (▲) are experimental values.*

### 3.5.4 Significance of wall treatments

The solution is also sensitive to the treatment of the wall. This is visible in the differences between the two different wall function approaches for the k-ε model. The wall treatment of the pressure also affects the solution. Here a 0.order treatment is compared to a 1.order treatment for the conventional wall function approach of the k-ε model.

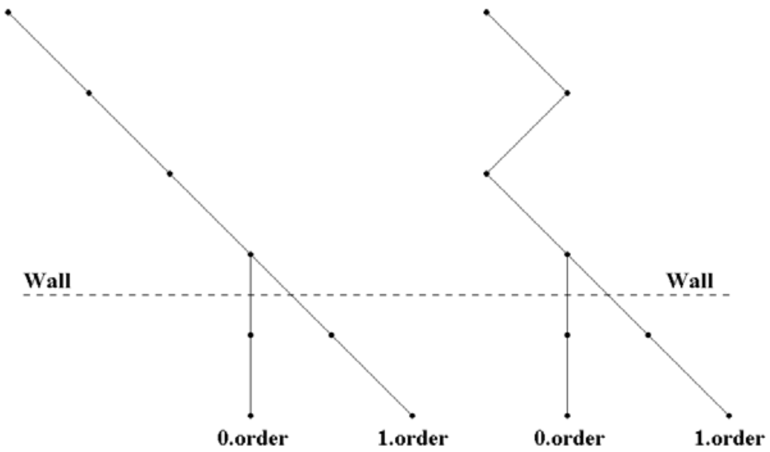

*Figure 16: The figure shows the effect of 0.order and 1.order pressure extrapolation to ghost cells. In the case of smooth pressure towards ground, the 1.order is preferred. When the pressure contains wiggles in the first cells, the 0.order is preferred.*

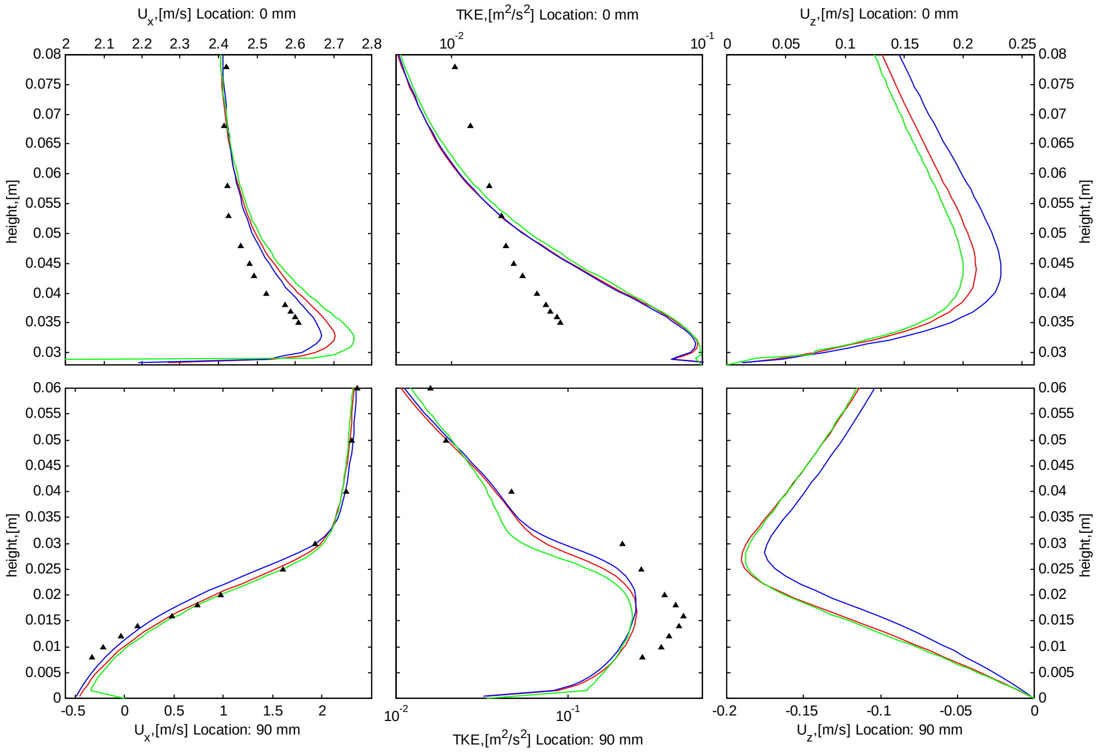

*Figure 17: The figure shows the differences between the reference k-ε solution (●), k-ε with 0.order wall treatment for the pressure(●), k-ε with 1.order wall treatment for the pressure (●). (▲) are experimental values. This effect has a greater impact on the solution than raising the artificial viscosity to 0.005.*

In 3DWind the 1.order approach is default. This causes a smooth pressure field, with isobars vertical to the ground. The 0.order approach causes some more wiggles, because the grid is not orthogonal. The effect of these small oscillations causes the separation to occur a little closer to the hilltop, and this affects the whole recirculation zone. Some results are shown in *Figure 17*. The change in wall treatment on the pressure causes changes of the same order as increasing the artificial diffusion from 0.001 to 0.005. A similar result with the two different wall function approaches is given in *Figure 18*.

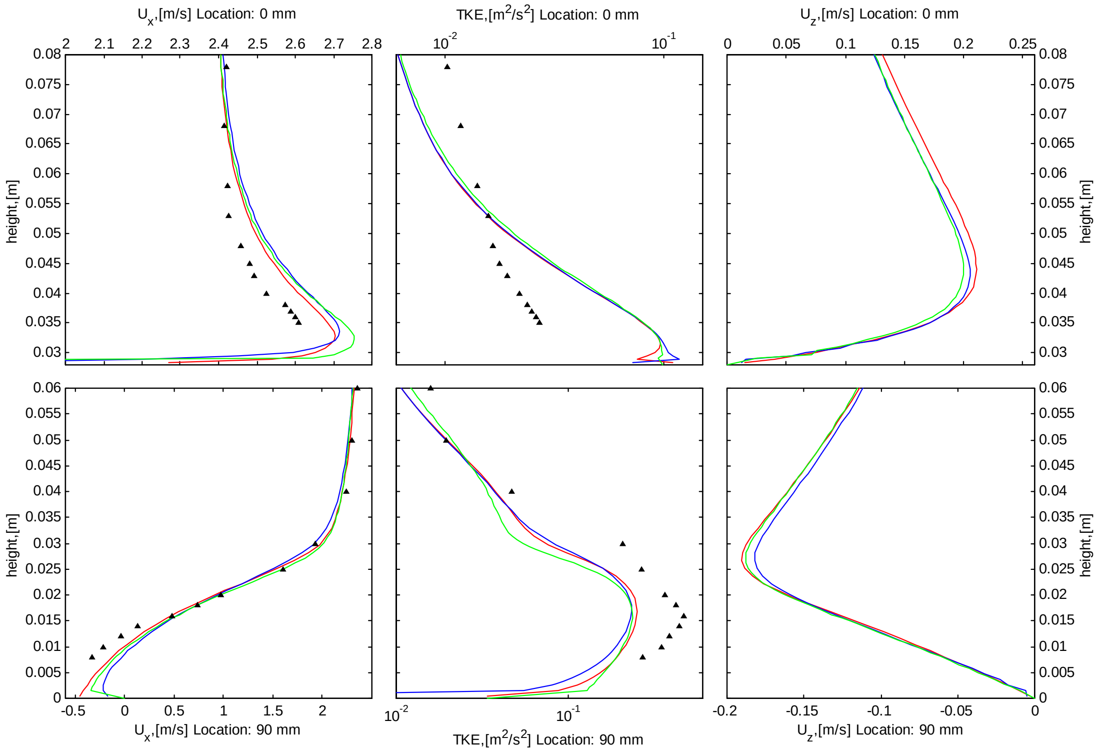

*Figure 18: The figure shows the differences between the reference k-ε solution (●), k-ε with direct wall function treatment(●), k-ε with indirect wall function treatment(●). (▲) are experimental values.*

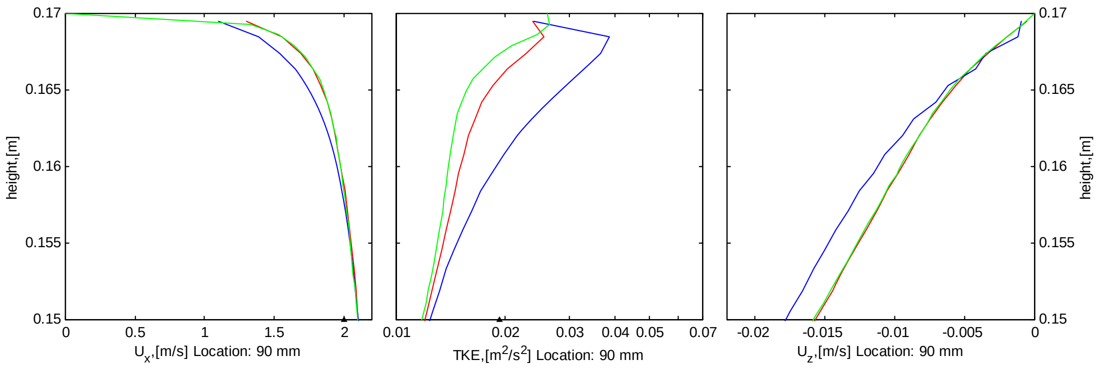

*Figure 19: The figure shows the top wall differences between the reference k-ε solution (●), k-ε with direct wall function treatment (●), k-ε with indirect wall function treatment (●).*

Still, the difference seems to have a larger impact on the upper wall. The velocity and the turbulent kinetic energy at one location on the top wall is visualized in *Figure 19*.

### 3.5.5 Grid dependence

Three different grids described in *Table 1* and visualized in *Figure 20* are used to test the grid dependence. The non-dimensionalized wall distance $z^+$ is defined by equation (37).

$$z^+ = \frac{z \cdot u_\tau}{\nu} \tag{37}$$

*Table 1: Essential sizes of the grid dependence test.*

| | **Coarse** | **Medium 1** | **Medium 2** | **Fine** |
|---|---|---|---|---|
| Number of cells | 6 300 | 14 000 | 14 000 | 28 800 |
| Dimensions | 90x70 | 140x100 | 140x100 | 240x120 |
| $z^+$ (at inlet) | 67 | 55 | 40 | 55 |

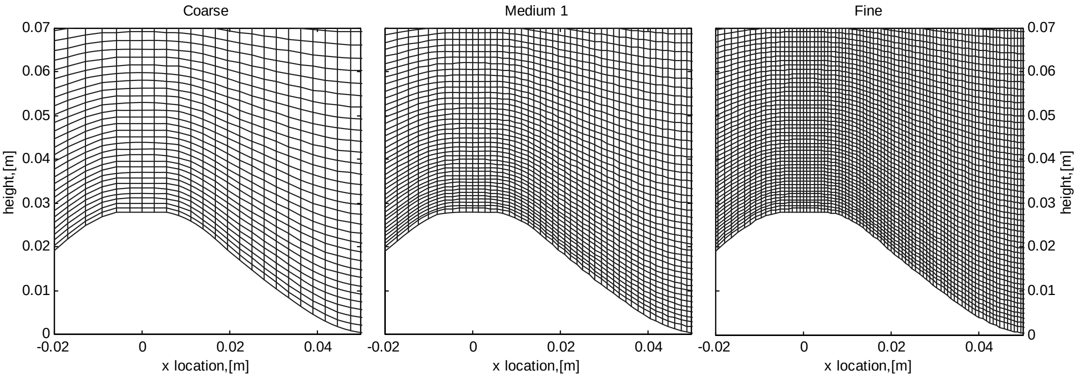

*Figure 20: Grid visualization. View of the area surrounding the separation point. Medium 2 is almost equal to Medium 1, except for the first cell enlargement.*

In the Medium 1 and the Fine grid, the first grid cell is larger than the second, in order to ensure that the first cell centre is inside the logarithmic layer for all wall cells. The smallest cells are on the top of the hill, but the velocities are larger here causing the friction velocity to become larger. The normalized distance is $z^+=55$ for the medium and fine grid with enlarged first cell. In the second medium grid, where the first cell is not enlarged, the normalized distance is $z^+=40$. In the coarse grid $z^+=67$. All results are above the lower limit of $z^+=35$.

The results of this analysis show small differences between the grids (*Figure 21*). However, the results are found to differ significantly from the reference solution. This was surprising since preliminary results coincided well with the reference solution. Laurence et al. (2003) indicate that the solution is dependent on the thickness of the first cell. To test first cell thickness sensitivity, simulations were performed with the medium grid (Medium 2), without thickness enlargement. This gave a very different flow pattern compared to the simulation with the enlarged first grid cell (*Figure 22*). The charts show that the separation point sensitivity to the thickness of the first cell is huge.

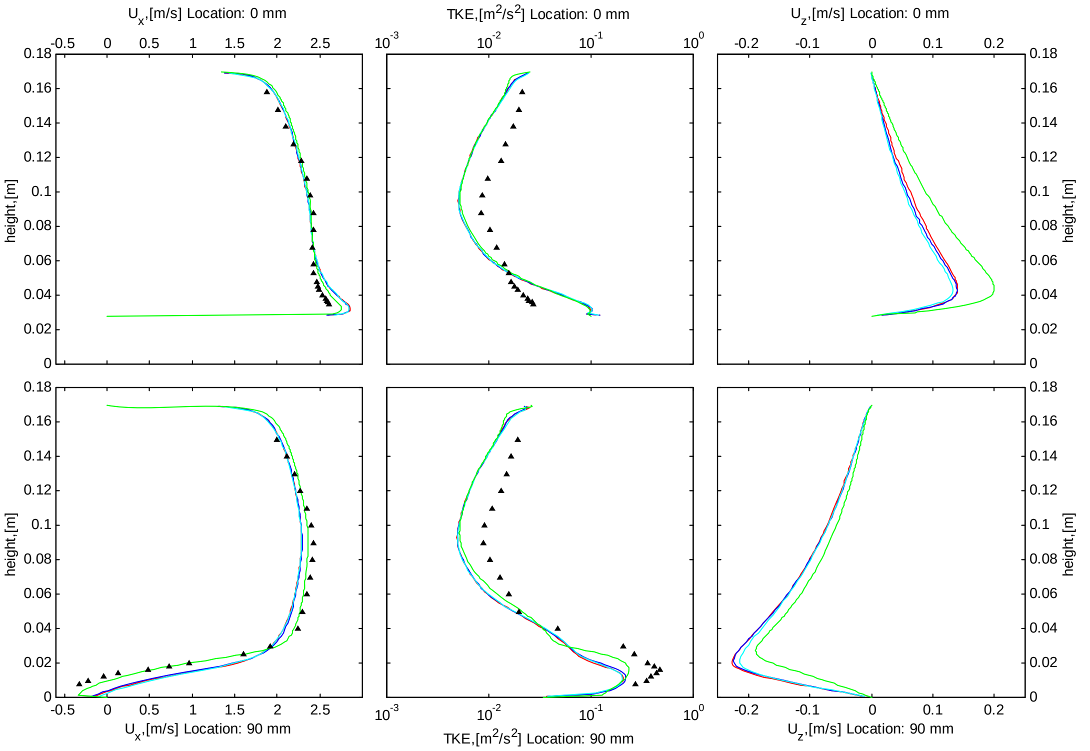

*Figure 21: The figure illustrates the grid resolution sensitivity. Reference solution(●), coarse grid(●), medium grid(●) and fine grid(●). (▲) are experimental values.*

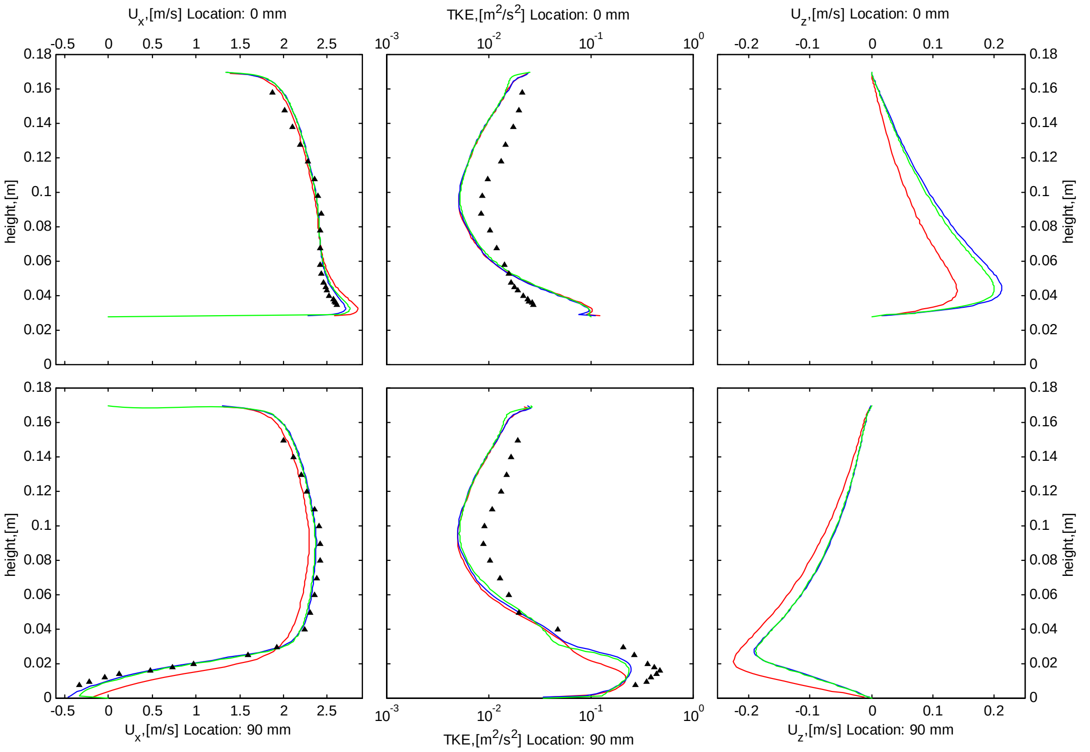

*Figure 22: The charts show the separation point sensitivity to the thickness of the first cell. Reference solution(●), first grid cell not enlarged(●) and enlarged first grid cell(●). (▲) are experimental values.*

Generally, the medium grid gave almost the same result as the fine grid, but the extra computational effort of the fine grid was considerable. The coarse grid lost some details, and the separation and the reattachment point had a larger grid dependency.

The sensitivity is found to be particular strong for the indirect wall function approach. In this approach, the results without enlarged thickness of the first cell are almost identical to the reference k-ε simulation. On the other hand the simulation with the enlarged first cell differs considerably from the reference k-ε simulation. The recirculation zone is shorter and thinner. This is mainly caused by changed separation point. Before separation, the results are almost identical.

Because of this sensitivity to the thickness of the first cell, the simulations are also performed with direct wall functions (*Figure 23*). The results are not equally good compared to the reference simulation, but the separation point sensitivity to the thickness of the first grid cell is not that large. Both results also match the separation zone better than the medium grid with enlarged thickness of the first grid cell.

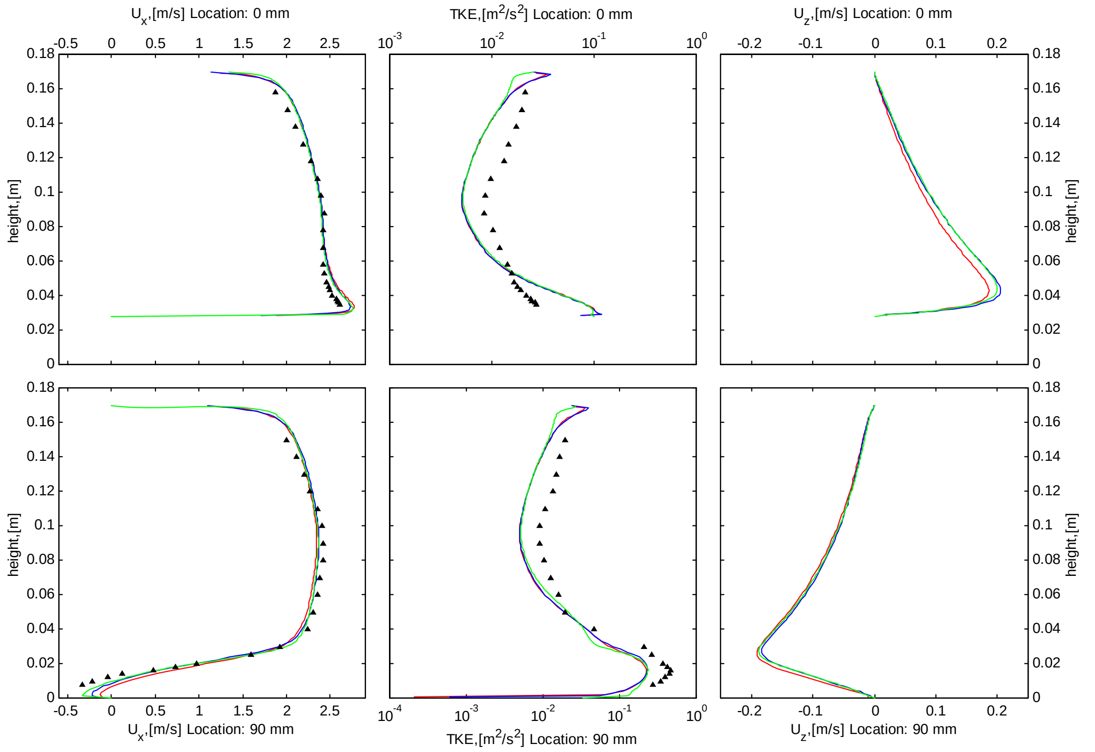

*Figure 23: The charts show the separation point sensitivity to the thickness of the first cell with the direct wall function approach. Reference solution (●), first grid cell not enlarged (●) and enlarged first grid cell (●). (▲) are experimental values.*

### 3.5.6 General results and discussion

Based on these tests the final results are given and discussed for each of the turbulence models. All these results are based on the grid without enlarged first grid cell. The art_fac of equation (26) is 0.003 for the RSM model, and 0.001 for the others. The residual smoothing factor ε is set to 0.08 in all cases. This has no influence on the final solution, but helps to speed the convergence.

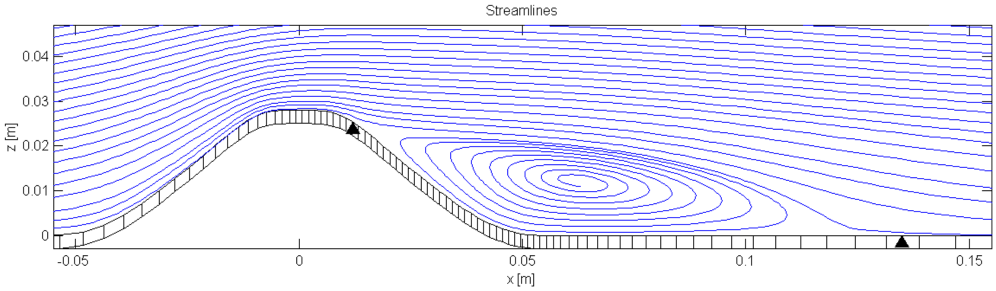

*Figure 24: Streamline plot with the k-ε turbulence model with the direct wall function approach. ▲indicates the separation and reattachment point from the experimental results.*

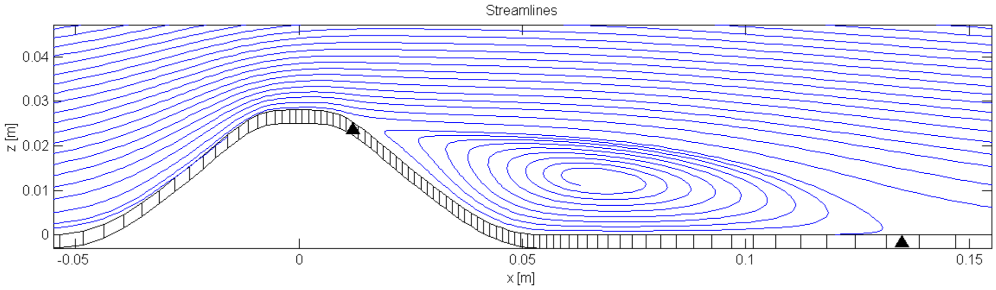

*Figure 25: Streamline plot with the k-ε turbulence model with the indirect wall function approach. ▲indicates the separation and reattachment point from the experimental results.*

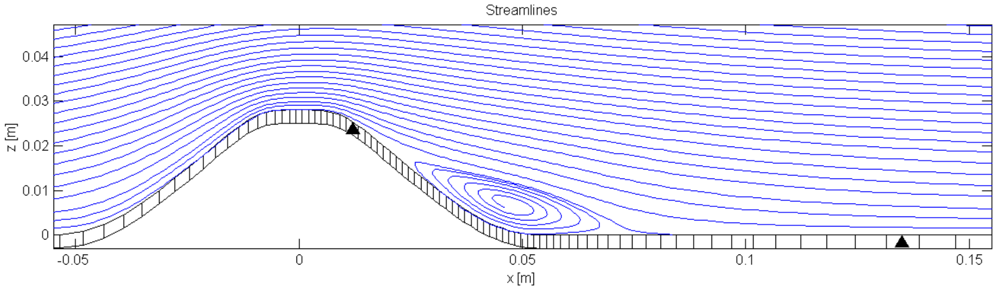

*Figure 26: Streamline plot with the k-l turbulence model with the direct wall function approach. ▲indicates the separation and reattachment point from the experimental results.*

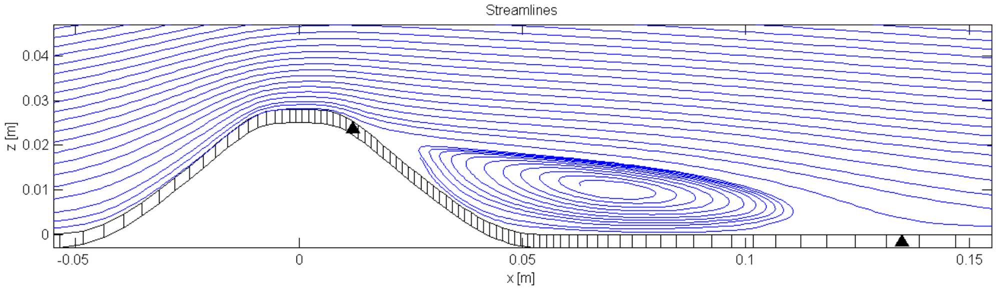

*Figure 27: Streamline plot with the RSM turbulence model with the direct wall function approach. ▲indicates the separation and reattachment point from the experimental results.*

*Figures 24-27* show the streamline plot of all the methods discussed in this chapter. Both versions of the k-ε model, and the RSM are quite close to the experimental results with respect to the separation and reattachment point. The k-l model on the other hand, estimates a creased recirculation bubble.

The 3DWind results with the three different turbulence models are plotted together with the reference solution and the experimental results for some profiles. The profiles of the horizontal velocities are plotted in *Figures 28-29*. These show all the profiles from existing experimental results and reference solutions. The full results of the vertical velocity, the turbulent kinetic energy, and the dissipation of turbulent kinetic energy are given in Appendix A. Only profiles that show some particular behaviour worthy of discussion are shown in the following. Most of these plots are magnified to better illustrate the aspects that are discussed. In those cases, the area that is magnified is marked in the full profile figures in *Figures 28-29* and Appendix A. Appendix B contains filled contour plots of the pressure fields, velocities and turbulent quantities with the different turbulence models.

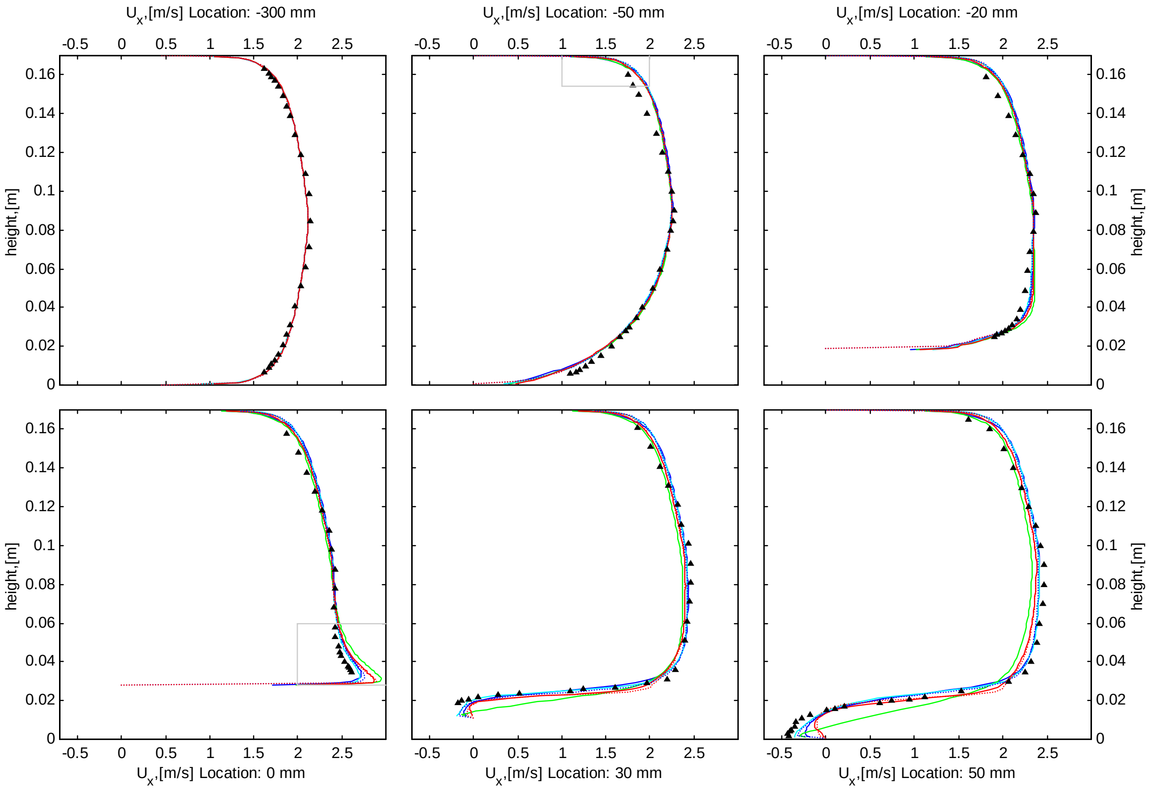

*Figure 28: The charts show the horizontal velocity of the first six profiles. The colour coding is: the k-l model(●),the k-ε model with the indirect wall function approach(●), the k-ε model(●) and the RSM(●). Dashed lines are reference values that correspond to the method of the colour they wear, (▲) are experimental values.*

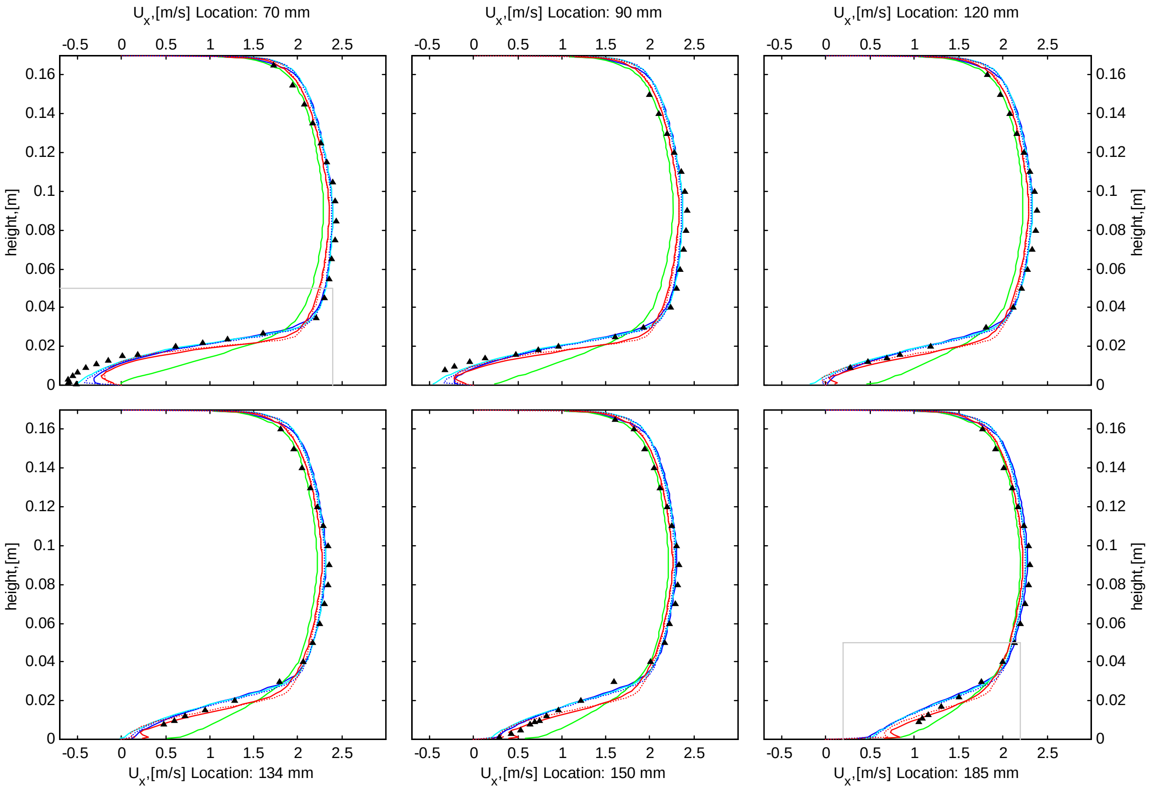

*Figure 29: The charts show the horizontal velocity of the last six profiles. The colour coding is the following: the k-l model(●),the k-ε model with the indirect wall function approach(●), the k-ε model(●) and the RSM(●). Dashed lines are reference values that correspond to the method of the colour they wear, (▲) are experimental values.*

From the overview results seen in *Figures 28-29*, it is seen that the modelling results are generally close to both the experimental results and the reference solutions. Both methods with the k-ε model are following the reference solution of the k-ε model, and the RSM solution follows the reference solution of the RSM method. As seen in the streamline plot in *Figure 26*, the only method that is significantly different is the k-l method.

The k-l method is an incomplete method. The modelling constants are tuned to fit atmospheric flow. The entire set of constants should preferably have been adjusted to fit this flow, but this method is only fit to this channel flow by changing the mixing length. This is clearly a disadvantage compared to the other methods that are complete, and not that dependent on flow tuning.

The results in *Figures 28-29* are overview results, and it is difficult to really distinguish between the different methods and watch local effects. The near wall flow at the hill summit at 0mm and the recirculating flow at 70mm, as well as the reconstruction of the boundary layer at 185mm, are magnified and plotted in *Figure 30.*

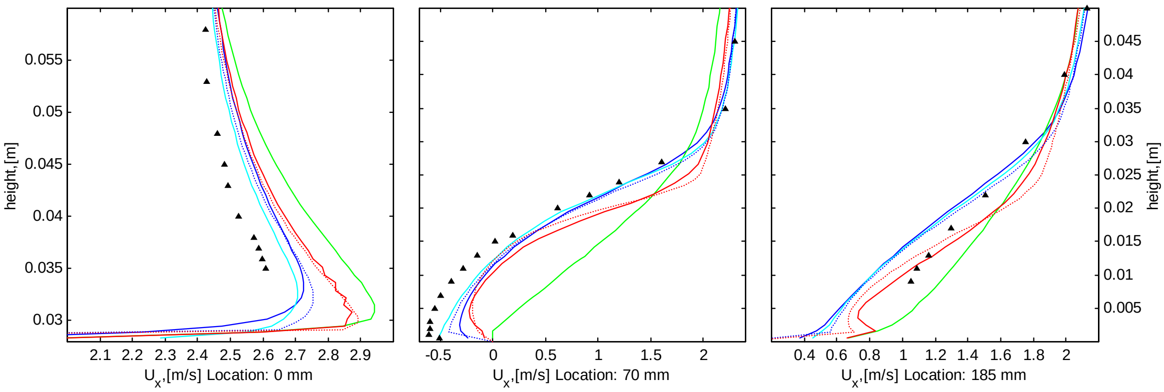

*Figure 30: The charts show the horizontal velocity in the near surface area. The colour coding is the following: the k-l model(●), the k-ε model with the indirect wall function approach(●), the k-ε model(●) and the RSM(●). Dashed lines are reference values that correspond to the method of the colour they wear, (▲) are experimental values.*

From *Figure 30*, it is seen that all methods overestimate the speed-up effect compared to experimental results at the hill summit. In the recirculating area at location 70mm, no model predicts as large negative values of the horizontal velocity as the experimental results. Moving over to 185mm, it seems like none of the numerical methods have the ability to rebuild the boundary layer as fast as seen in the experiments. It seems like the diffusion in nature is larger than the modelled one.

The speed-up seems to depend on the separation point location. A late separation is connected to larger pressure gradients and increased velocity at the hill summit. The k-l method estimates the smallest recirculation bubble, as seen in *Figure 26*. From *Figure 30* this method also estimates the largest speed-up. This strong flow dependency on the recirculation bubble is also a problem in conjunction with model validation for flow cases with recirculating flow. The separation point estimation becomes the main parameter that describes the methods ability to predict the flow, and this can be quite random. This is clearly seen in conjunction with the k-ε model with the indirect wall function approach, which is found to depend largely on the thickness of the surface cell (*Figure 22*). This is also one of the conclusions to be drawn from Bonnin et al. (1995), where highly differing recirculation zones were found with different turbulence models, but also within groups of equal turbulence models.

Regarding both the RSM method and the k-ε method, there is good accordance between the reference solution and the 3DWind results. The two turbulence models are also clearly differing from each other. The RSM results from 3DWind have maybe some more numerical diffusion than the RSM reference solution. The velocity shear between the free stream flow and the recirculation zone is higher in the reference solution. This is probably both connected to the addition of artificial viscosity, and the fact that an eddy viscosity is used to calculate the diffusion of both ε and the Reynolds stresses according to equation (15) and (19).

Another effect that is seen in *Figure 30* is the wiggle in the RSM results at the hill summit. This is connected to both large advection connected to large speed and a large pressure gradient. This is the well-known problem caused by the velocity-pressure coupling connected to collocated grid.

To further evaluate the set of equations, the solutions have been plotted together with the residual values of each term of the differential equation. This gives the ability to better understand the physics and to evaluate possible errors in the evaluation of each term. This analysis also shows which terms are oscillating and which terms oppose oscillations.

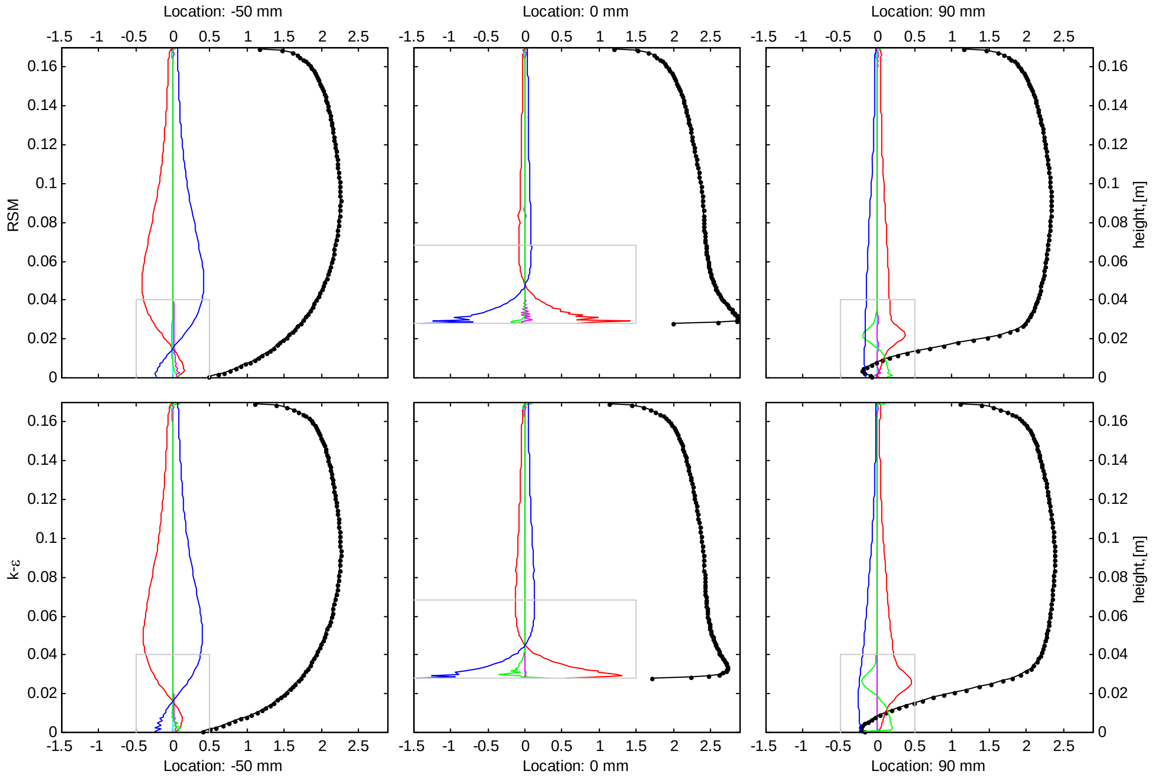

*Figure 31: The charts show the residual fraction of the different terms of the differential equation for the horizontal velocity (equation (2)). The upper line show some profiles calculated with RSM, the lower line shows the corresponding profiles with the k-ε model. The areas framed by grey lines are magnified and plotted in Figure 32. The colour coding is the following: the diffusion term (●), the artificial viscosity term (●), the pressure term (●) and the advection(●). (●) are the modelled velocities. The horizontal axis is connected to the modelled velocities. There is no axis connected to the residuals, since they are evaluated qualitatively only.*

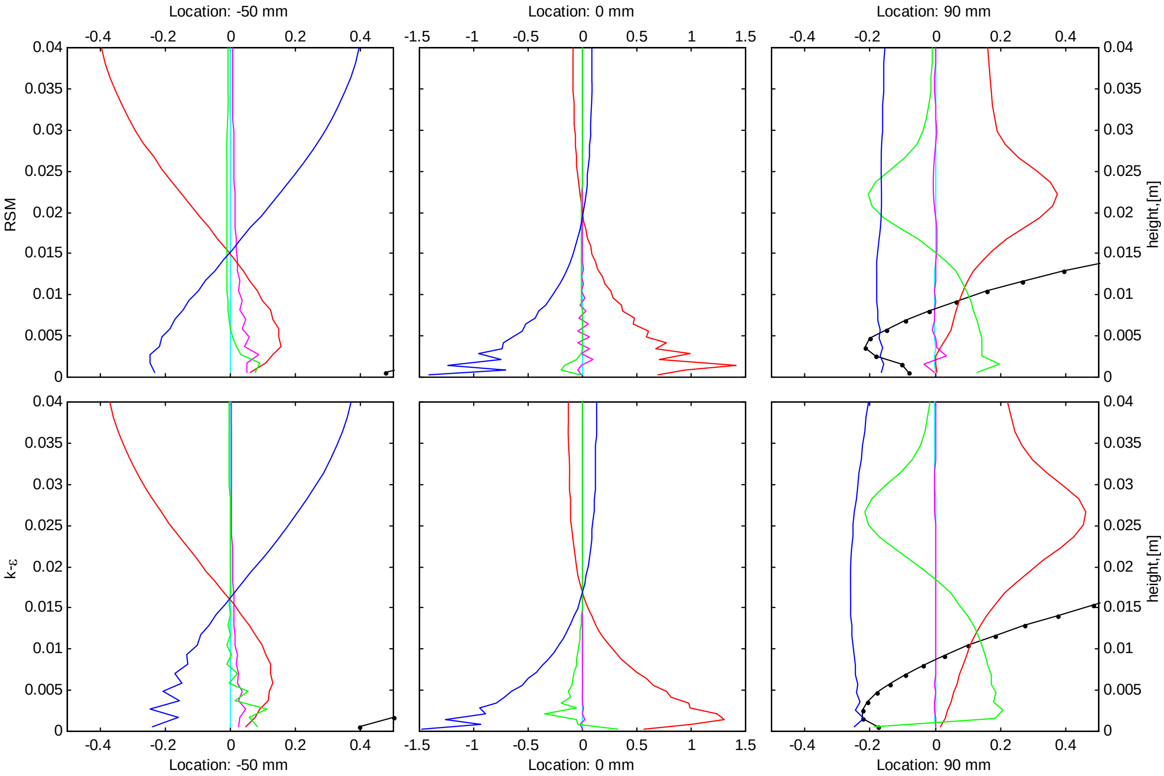

*Figure 32: The charts show the residual fraction of the different terms of the differential equation for the horizontal velocity. The upper line shows some profiles calculated with RSM, the lower line shows the corresponding profiles with the k-ε model. The areas are magnified pictures of areas framed by grey lines in Figure 31. The colour coding is the following: the diffusion term(●), the artificial viscosity term(●), the pressure term(●) and the advection(●). (●) are the modelled velocities. The horizontal axis is described in Figure 31.*

*Figure 32* illustrates some differences between the RSM approach and the k-ε approach. The turbulence model has only direct influence on the diffusion term, which is plotted with green. In modelling of the wind field, the velocities are the most interesting aspect. A smooth velocity field is more desirable than a smooth pressure field. *Figure 32* shows that the diffusion term of the k-ε model has a smoothing effect on the solution. The diffusion term of the RSM has a limited possibility to smooth oscillations. This means more artificial diffusion has to be added, and more oscillations are seen in the advection term. This means wiggles in the velocity field, which is visible in *Figure 30*.

The advantages of both methods can be combined by a combination of the RSM diffusion and the k-ε model diffusion. Good smoothing properties are found by a combination of 80% of the total diffusion calculated from the RSM approach, and the final 20% calculated from a k-ε approach. This gave good smoothing properties with minor altering of the RSM properties. Because of limited testing, and to limit the amount of information, those results are not shown in this report.

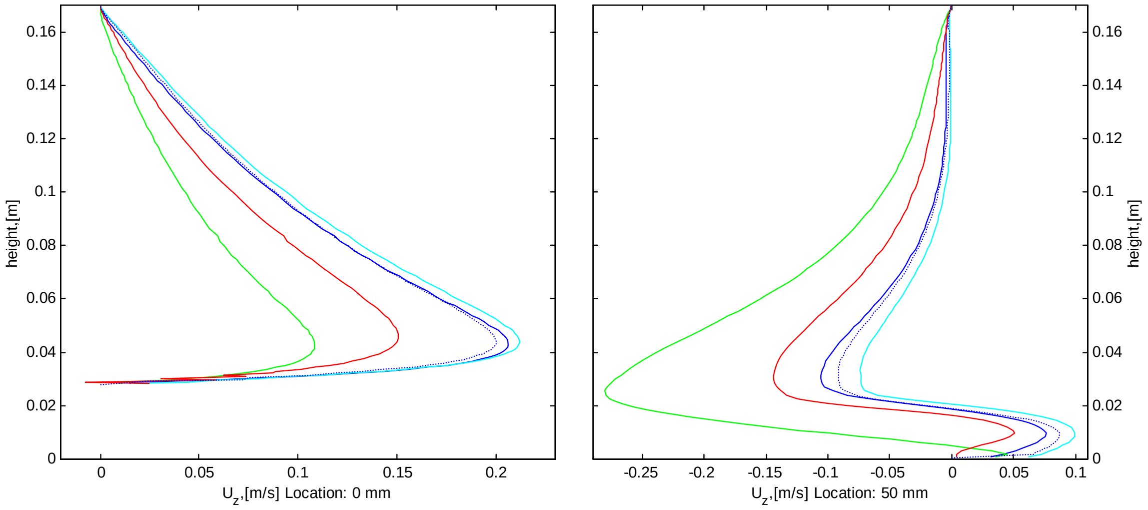

*Figure 33: The charts show the vertical velocity at the hill summit, and 50mmmm behind in the recirculation zone. The colour coding is the following: the k-l model(●), the k-ε model with the indirect wall function approach(●), the k-ε model(●) and the RSM(●). Dashed line is the reference values from the k-ε model.*

*Figure 33* shows the vertical velocity at the locations 0mm and 50mm. The vertical velocity in the entire domain is mainly depending on the estimated recirculation bubble. If the recirculation bubbles are comparable, so is the vertical velocity. Both simulated results from the k-ε model follow the reference solution quite well, while the k-l method results show a different pattern. At the hill summit, all methods give a positive vertical velocity all the way from bottom wall to the top wall. The upward velocity is caused by the non-linearity. The increased turbulence takes energy from the mean flow, and also the separation bubble causes the point where the vertical velocity turns to move down stream from the hill summit.

*Figures 34-35* show magnified charts of the turbulent kinetic energy and the dissipation rate of the turbulent energy at the locations 0mm and 90mm. The k-ε results are found to follow the reference solution quite well. One difference is however the near wall value of ε at 90mm. The indirect wall function approach follows the reference solution with a large value of ε near the wall, and the direct wall function approach gives a much lower value near the surface. Estimated k values with the k-l method are quite close to the k-ε values. These methods tend to overestimate the k values at the hill summit. This is a known problem of the k-ε method. The RSM calculates lower values of k at the hill summit. Both the k and the ε values from the RSM are also following the reference solution quite well.

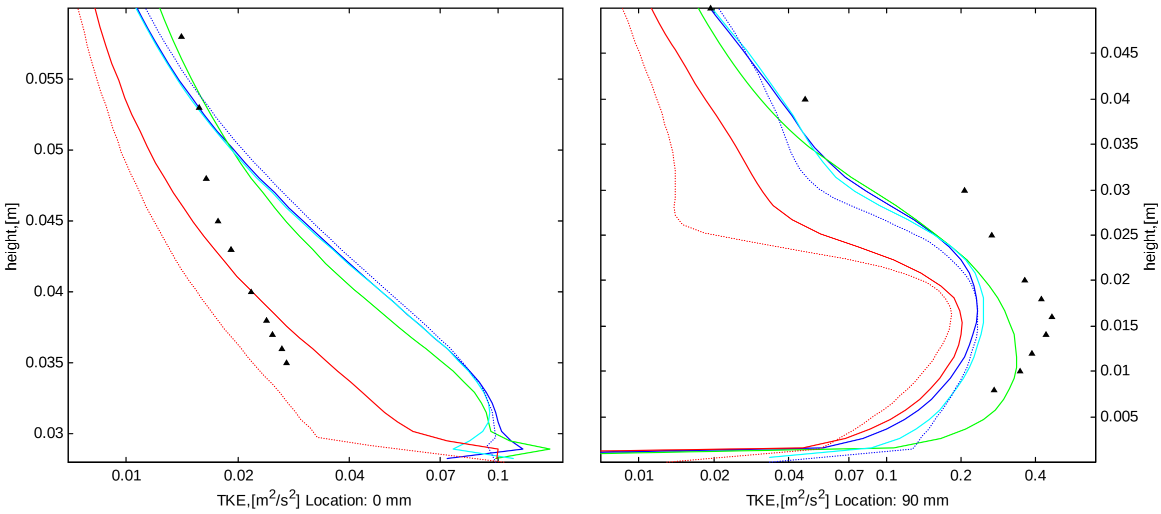

*Figure 34: The charts show the turbulent kinetic energy in the near surface area. The colour coding is the following: the k-l model(●), the k-ε model with the indirect wall function approach(●), the k-ε model(●) and the RSM(●). Dashed lines are reference values that correspond to the method of the colour they wear, (▲) are experimental values.*

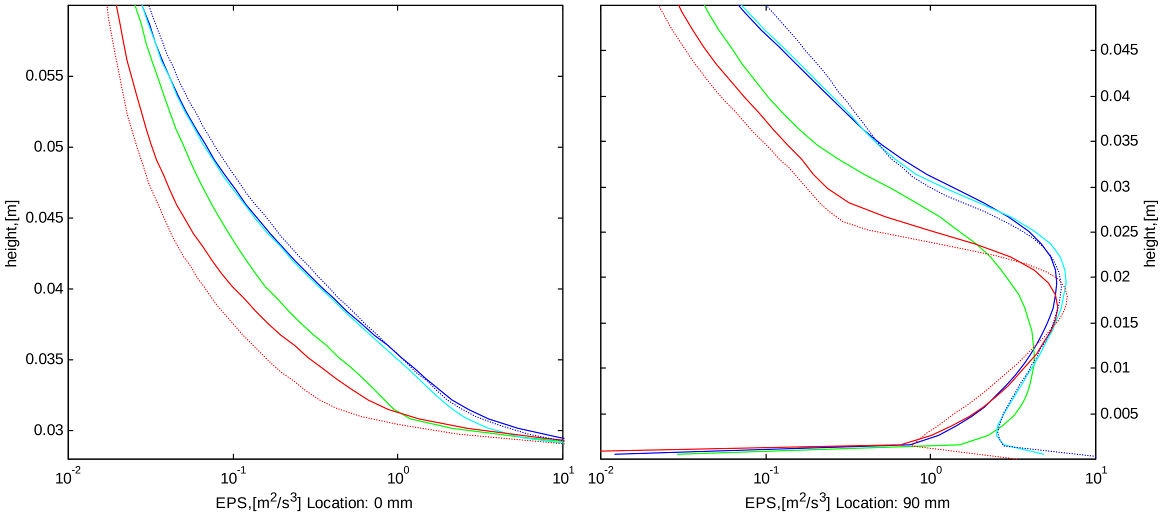

*Figure 35: The charts show the dissipation rate ε of turbulent energy in the near surface area. The colour coding is the following: the k-l model(●), the k-ε model with the indirect wall function approach(●), the k-ε model(●) and the RSM(●). Dashed lines are reference values that correspond to the method of the colour they wear.*

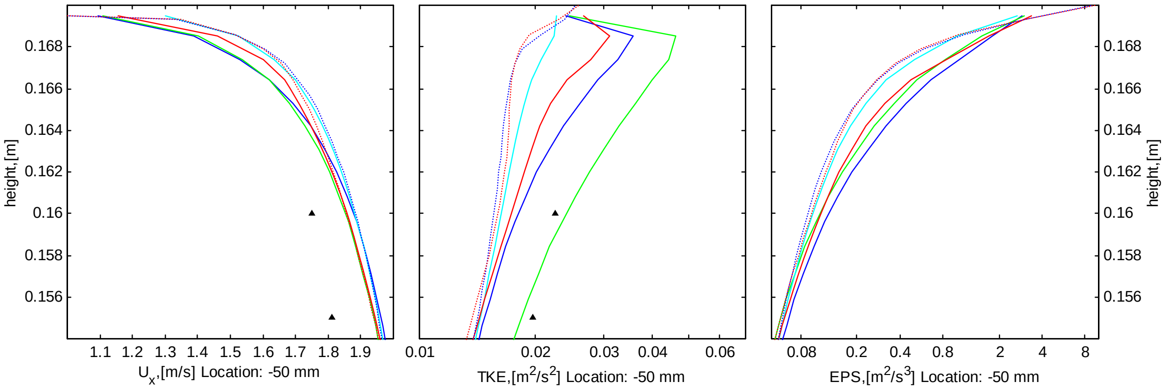

*Figure 36: The charts show the horizontal velocity, the turbulent kinetic energy k and the dissipation rate ε of turbulent energy in the near surface area at location –50mm. The colour coding is the following: the k-l model(●), the k-ε model with the indirect wall function approach(●), the k-ε model(●) and the RSM(●). Dashed lines are reference values that correspond to the method of the colour they wear, (▲) are experimental values.*

The main focus of this analysis has been on the lower wall, the surface where the obstruction is located. It is seen that the flow above the lower wall depends on the separation point. An analysis of the undisturbed boundary profile can give some additional information. *Figure 36* shows the profile of the horizontal velocity, the turbulent kinetic energy k and the dissipation rate ε. There are no measurements in the near wall area, so results are only compared to the reference solution. The direct wall function approach seems to give too much diffusion in the near wall area. Both the turbulent kinetic energy, and the dissipation rate of turbulent kinetic energy are high, and the velocity is low. With the indirect wall function, the profiles are much closer, but still with the same tendency.

The reason for the estimation of too large values for the turbulence quantities and too small values for the horizontal velocities are found to be related to the velocity wall function in the direct wall function approach. With this wall function, the velocity in the first cell is estimated from a logarithmic profile up to the first cell face, plus a linear profile between the first and the second cell centre. The method causes a velocity decrease in the first grid cell compared to the assumption of a logarithmic velocity profile up to the second grid cell centre. The decreased velocities in the first cells cause a larger shear region that gives further larger values of the turbulent quantities.

A modified velocity wall function was developed and used throughout the investigation of Askervein Hill. However, some tests of the modified wall function carried out with the C18 case, indicate more corresponding results between the two wall functions at the upper wall, while the separation zone behind the wall at the lower wall tends to decrease.

# 4 Askervein hill

Askervein hill is located at the southern end of the Outer Hebrides island chain near the west coast of South Uist, see *Figure 37*. *Figure 38* and *Figure 39* show that the hill is essentially elliptical in plan form with a 1 km minor axis, and a 2 km major axis. The terrain between the sea and the hill on the west side of the hill is fairly plane with few obstacles. The most interesting flow direction seems to be from the southwest. This wind is perpendicular to the long axis of the hill, and is one of the prevailing directions of the site. The distance to the sea in this direction is 3-4 km.

*Figure 37: The map shows the location of the Askervein hill in Scotland. Reproduced from Ordnance Survey map data by permission of Ordnance Survey, © Crown copyright.*

The measurement campaigns at Askervein hill were performed through the autumns of 1982 and 1983 (Taylor and Teunissen, 1987). This was an international project that is described in detail by Taylor and Teunissen (1983, 1985). Several aspects of the results are also described in a series of publications in Boundary- Layer Meteorology in the years 1987 and 1988 (Taylor and Teunissen, 1987) (Beljaars et al., 1987) (Raithby et al., 1987) (Teunissen et al., 1987) (Mickle et al., 1988) (Salmon et al., 1988).

The Askervein Hill case has become a standard case in testing of models used for micrositing of wind turbines. This was also one of the intensions of the experiment, and the first model testing was part of the Askervein project (Beljaars et al., 1987) (Raithby et al., 1987). Some other publications using Askervein hill as a model validation case are Troen and Petersen (1988), Barnard (1991), Alm and Nygaard (1995), Ayotte (1997), Leroy and Gravdahl (1999), Kim and Patel (2000), Kim et al. (2000), Lopes (2002), Castro et al. (2003), Chow and Street (2004) and Eidsvik (2004).

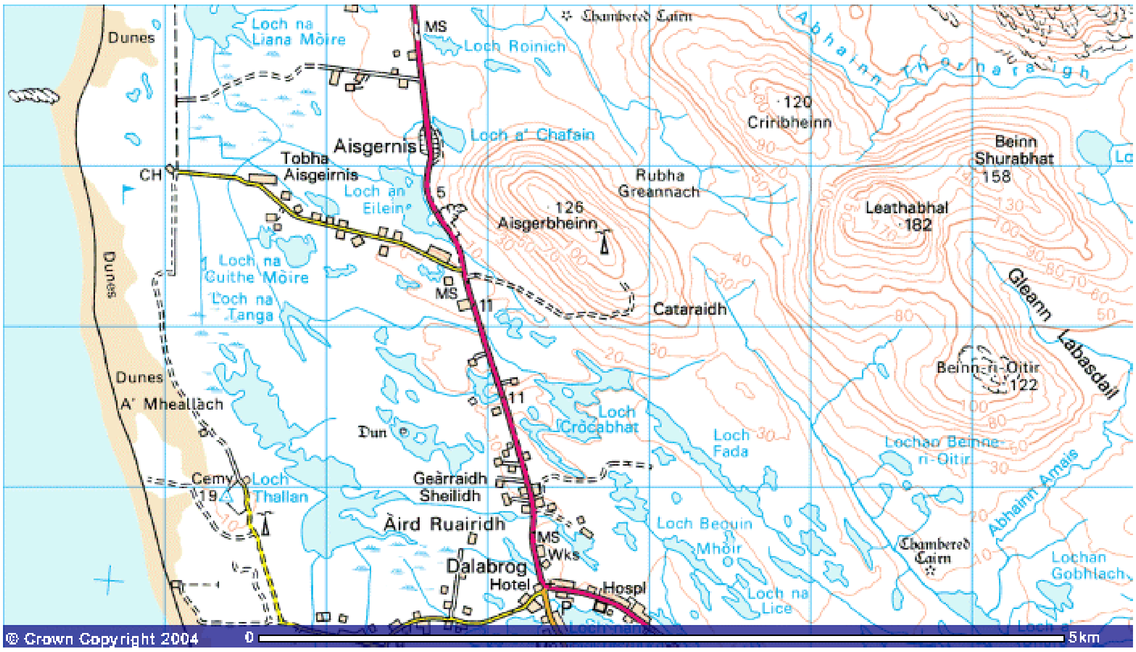

*Figure 38: The map shows the location of the Askervein hill (at the map named Aisgerbheinn) at the Outer Hebrides. Reproduced from Ordnance Survey map data by permission of Ordnance Survey, © Crown copyright.*

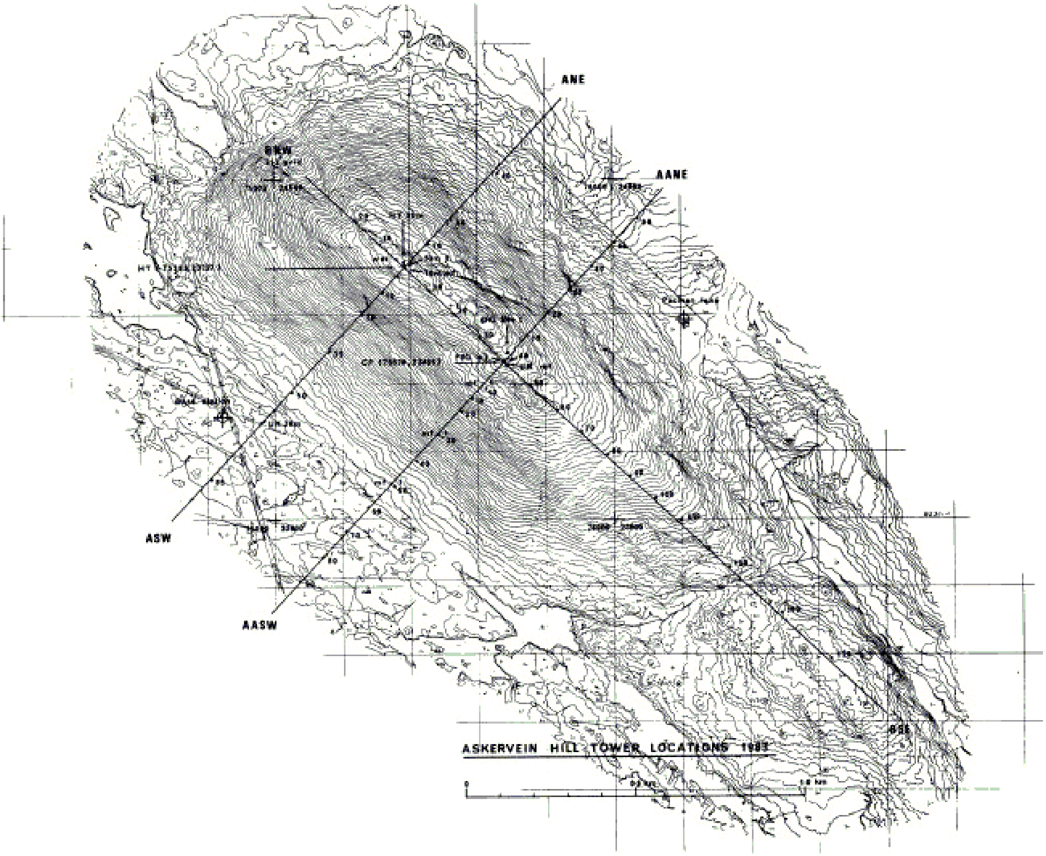

*Figure 39: 2m contours from Askervein hill (Taylor and Teunissen, 1985).*

The case chosen in this analysis was measured 3 October 1983. This is a commonly used dataset, and is generally regarded as the "best" day for data collection of the entire campaign. There were steady, moderate-to-strong winds from 210° blowing most of the day (Taylor and Teunissen, 1987). The main data from the mean flow run were collected from 1400 to 1700. The mean wind speed at the reference station was 8.9m/s, and the Richardson number $Ri^+$=-0.0110. This is a measure of the stability of the flow, and $|Ri|<0.015$ can be regarded as neutrally stratified (Taylor and Teunissen, 1987). 210° is almost vertical to the long axis of the hill, and the direction is from the undisturbed seaside.

Results are compared to a mean flow run (MF03-D 1400-1700), a turbulence run (TU03-B 1400-1700) and a TALA kite run (TK03 1500-1700). In the mean flow run measurement data are collected from cup anemometers in 10m heights along the three lines A, AA and B, sketched in *Figure 39*. Those datasets are compared with the simulation results along the same lines. All values are relative speed-up factors normalised with the speed on the reference station RS. This station is located about 1km from the shore a little south of the area contained in the map in *Figure 38*. The location is marked in the roughness map in *Figure 40*.

Turbulence results from TU03-B are collected from Gill UVW 3-component propeller anemometers along line A. The turbulence run also contains vertical profiles at both the hilltop and the reference station. At the present time interval, corresponding results are available at 3m, 5m, 8m, 15m, 24m and 34m. The TALA kite run gives the simultaneous velocity at six different heights at the coast, about 1km west of the reference station. Measurement heights are 30m, 48m, 70m, 116m, 178m and 267m. The measurement technique calculates both the velocity and the height where the kite is flown based on the line force, the line angle and the line length.

## 4.1 Grid

The digital terrain data are bought from Ordnance Survey in Great Britain. This dataset has an equidistance of ten meters. This is a little rough, and is therefore additionally manually digitized from *Figure 39* to have an equidistance of two meter for the uppermost 70m of the hill. To watch the effect of detailed height information, numerical results are given for a case without this manual digitizing.

The simulation domain is chosen to contain the neighbouring hills behind the hill. Kim and Patel (2000) found that these hills had a blocking effect, and therefore caused flow separation. On the other hand Castro et al. (2003) concluded that these hills had no influence at the top or downstream of the Askervein hill. The effect of the roughness change on the shore is assumed not to influence either the measurements at the reference station, or the measurements at the hill (Mickle et al., 1988). The shore is therefore not totally included in the simulations, but simulations are also done with a more detailed roughness map (*Figure 40*).

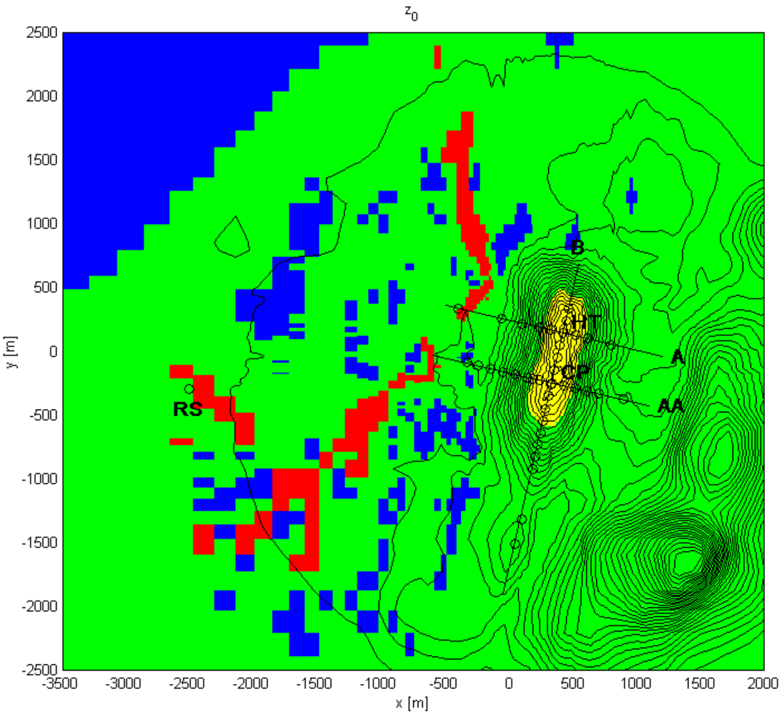

*Figure 40: The roughness map from central areas of the simulation domain. The colour coding is* 🔵 $z_0$*=0.0002m,* 🟡 $z_0$*=0.01m,* 🟢 $z_0$*=0.03m and* 🔴 $z_0$*=0.2m.*

The grid used in the simulations has a horizontal extension from 4km in front of the hilltop, to 3km behind the hilltop. The width of the domain is about 6km, and the height of the domain is 2000m. The horizontal distribution of the grid cells is visualized in *Figure 41*. The resolution in the centre is dx=10m and dy=12m. This is constant in a central square of 700mx500m, with a linear increase of 7% in the x-direction and 9% in the y-direction. The largest cell is 240m in the x-direction and 267m in the y-direction. The height of the first grid cell is 1.0m. With a vertical stretching of 12.1%, the largest vertical extension is 217m. The total amount of grid cells is 162x111x48.

The height information is first converted to .map format with the WAsP map editor, and the height of the lower vertices of the first cell is interpolated from the contours. The high frequency oscillations of wavelength 2*Δx are then removed by a high frequency filter. The height is also gradually smoothed to zero from 2.3km to 3km from the centre of the simulation.

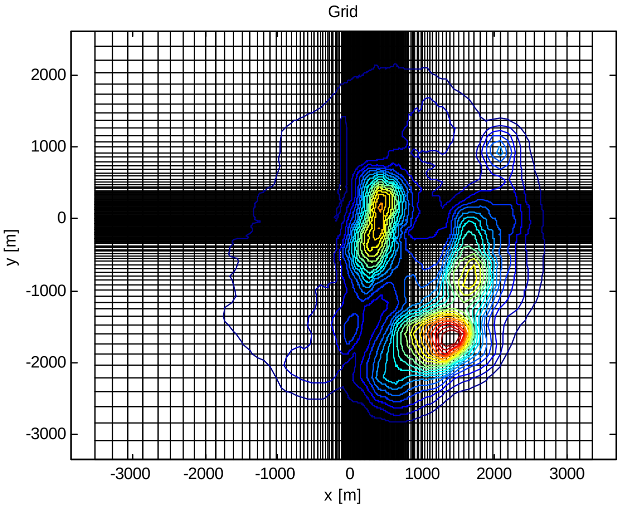

*Figure 41: The horizontal distribution of the grid cells used in the simulation.*

## 4.2 Boundary conditions and simulation

A one-dimensional simulation is done to establish a profile over homogeneous conditions. With the roughness length $z_0$=0.03m and the velocity 17m/s in 2000m, the simulated velocity 10m above ground level becomes 8.95m/s. The Coriolis term is present in the equations, and causes $10^o$ turning up to 530m and $20^o$ turning up to 2000m. This profile is used as both inflow boundary condition and initial condition for the entire domain. At the side boundaries there are periodic boundary conditions, and at the outflow boundary there is a zero-gradient (i.e. Neumann) condition. The surface boundary condition is expressed by wall functions, connecting the velocity in the first cell to the roughness and the log law assumption. The top boundary is as a zero-gradient surface in all variables except the vertical velocity, which is defined not to allow any material transport through the boundary. This means a vertical velocity equal to zero at the top boundary.

From this basis a convergent solution is obtained after about 5000 iterations. This corresponds to about 120 hours on a 2.5 GHz processor. The ε value in the residual smoothing algorithm is set to 0.05, from simulation start, but removed for the last 2000 iterations. The artificial viscosity factor is 0.003. This converged solution is the basis of a further simulation with non-uniform roughness, and different turbulence models.

## 4.3 Results and discussion

To visualize the results, the x-component of the wind speed is plotted in 10m heights for the entire hill and some of the surroundings (*Figure 42*). The corresponding plots of the y- and z-component of the speed, the effective pressure perturbation, the turbulent kinetic energy and the dissipation rate ε of the turbulent kinetic energy are found in Appendix C. Appendix C also contains streamline plots from 1m above ground level.

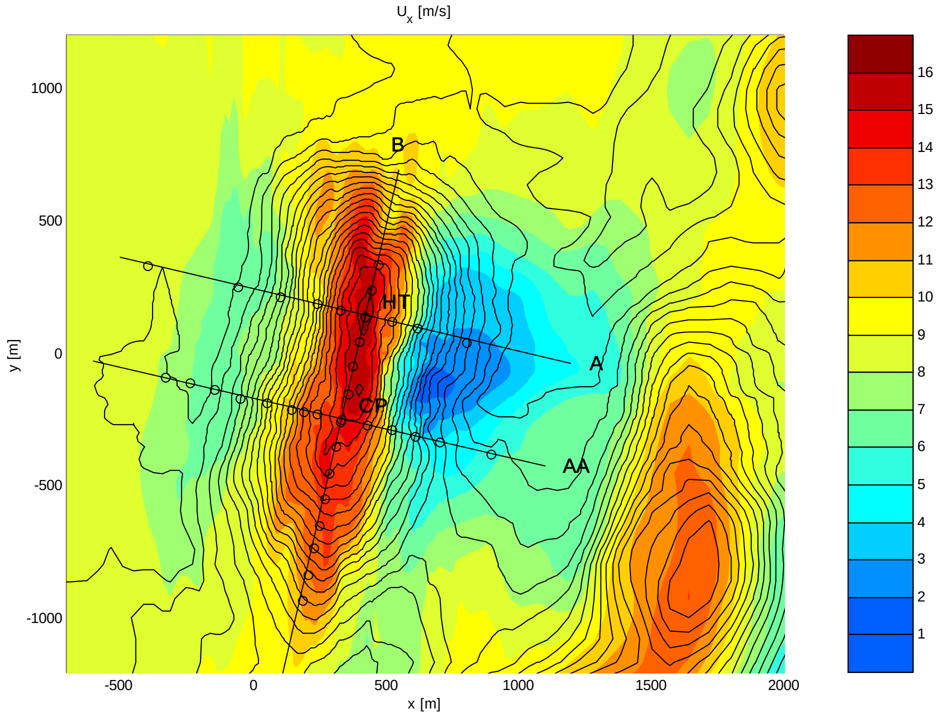

*Figure 42: The x-component of the velocity using the RNG k-ε turbulence model. The direction is from 210°.*

Qualitatively, the distribution of the velocity seems to be reasonable. It is still difficult to evaluate the level of the modeled wind speed based on *Figure 42*. To evaluate the relative values of the velocity within the domain, the horizontal velocity is interpolated along the three lines A, AA and B (*Figure 42*). The simulated and measured values are normalized with the horizontal speed in 10m at the reference station. In *Figures 43-45* these values are subtracted by one to give the relative speed-up factors caused by the hill. The plotted turbulence kinetic energies along line A are normalized by the squared horizontal velocity at the reference station $\left(normtke = tke/\left(u_x^2 + u_y^2\right)_{ref}\right)$, while vertical turbulence intensity profiles are defined as: $TI = \sqrt{\left(4 \cdot tke/3\right)/\left(u_x^2 + u_y^2\right)}$.

### 4.3.1 Turbulence model dependence

The different turbulence models give qualitatively similar results, but quantitatively there are some differences; particularly in turbulence levels, but also in the velocities in the wake of the hill. From the speed-up profiles through lines A and AA given in *Figures 43-44*, the upstream value is seen to be a little higher in the RSM case. This is probably connected to the fact that all turbulence models use the same inflow boundary profile. This profile is developed with the RNG turbulence model and is not the equilibrium state of the other turbulence models. As seen in *Figure 46* the four profiles at RS are no longer equal. The RSM value in 10m is quite low, but close to the ground the RSM has the largest values. This indicates that the RSM acts similarly to a lower friction, and the increased velocity propagates up in the boundary layer, in the same manner as a roughness change from high to low roughness length (Undheim, 2005).

This difference could have been accounted for by adjusting the reference value. *Figures 43-45* show that this overestimation is present in most of the area.

The two k-ε models are seen to be quite equal in the evaluated speed-ups along line A, AA and B (*Figures 43-45*). The k-l model differs most from the other methods. As seen from *Figure 45,* this method gives low values in the lower parts of the hill edge along line B, and increased speed-up at the hilltop, compared to the k-ε based methods. The k-l method calculates the highest speed-up values in the wake along line A, where only the RNG method is within the uncertainty limit. Along line AA, both k-ε methods underestimate the speed-up in the wake, while the RSM and the k-l method are within the uncertainty limit. No numerical results capture the large difference from the points 300m and 500m from the hilltop along line B. This is probably caused by subgrid topographic effects, measurement errors or a data treatment error.

Beljaars et al. (1987) argued that the linear method had a better spatial resolution at a much lower computational cost compared to non-linear 3D simulations. This is still true, but with increased computer power, the non-linear 3D simulation in *Figures 43-44* are seen to have the same details as the linear simulation in the area ±500m from the hilltop and the centre point. This method is also able to capture the low velocities in the wake of the hill.

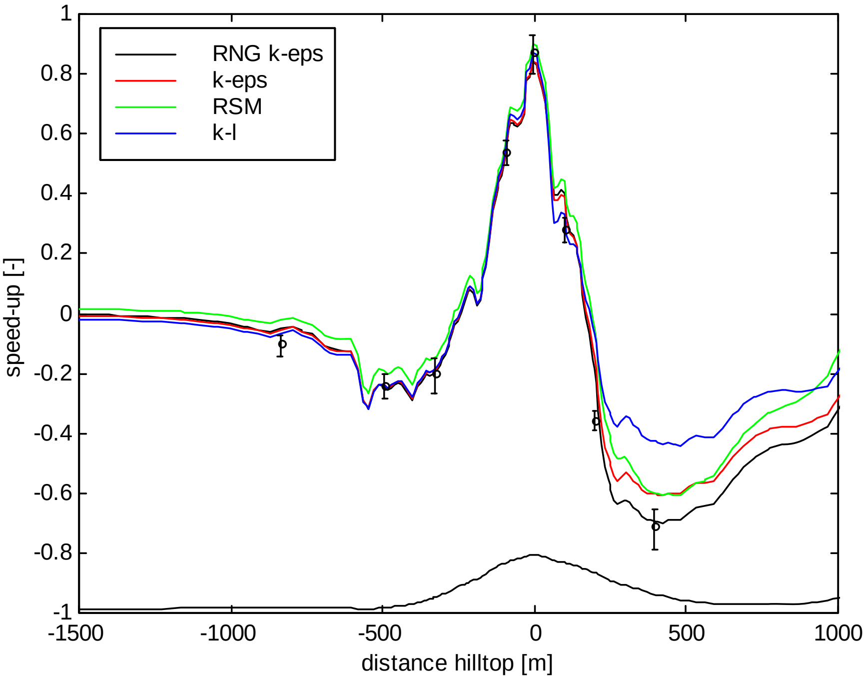

*Figure 43: Relative speed-up along line A. Symbols are measurements with uncertainty limits (Taylor and Teunissen, 1985). Different turbulence models are compared.*

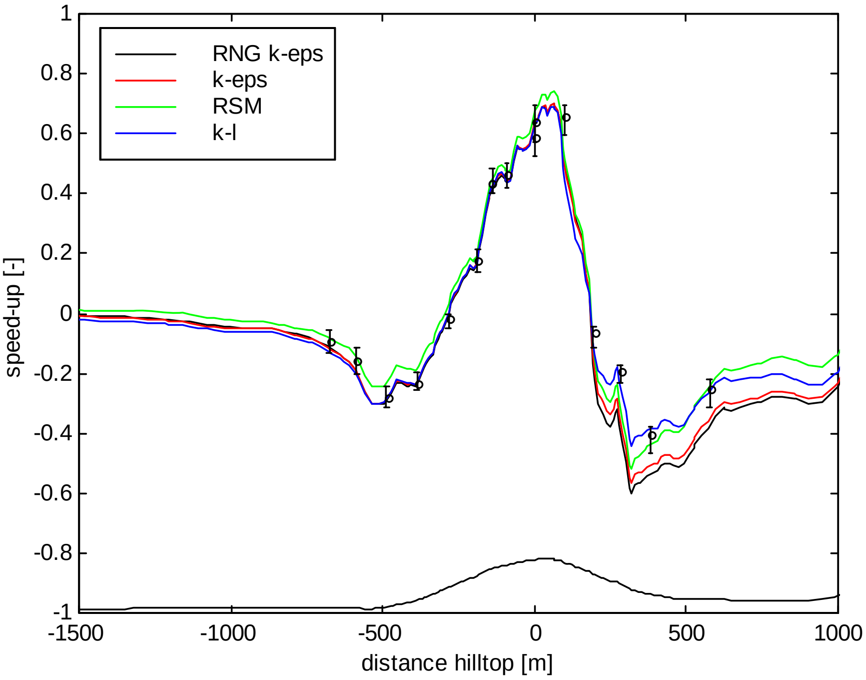

*Figure 44: Relative speed-up along line AA. Symbols are measurements with uncertainty limits (Taylor and Teunissen, 1985). Different turbulence models are compared.*

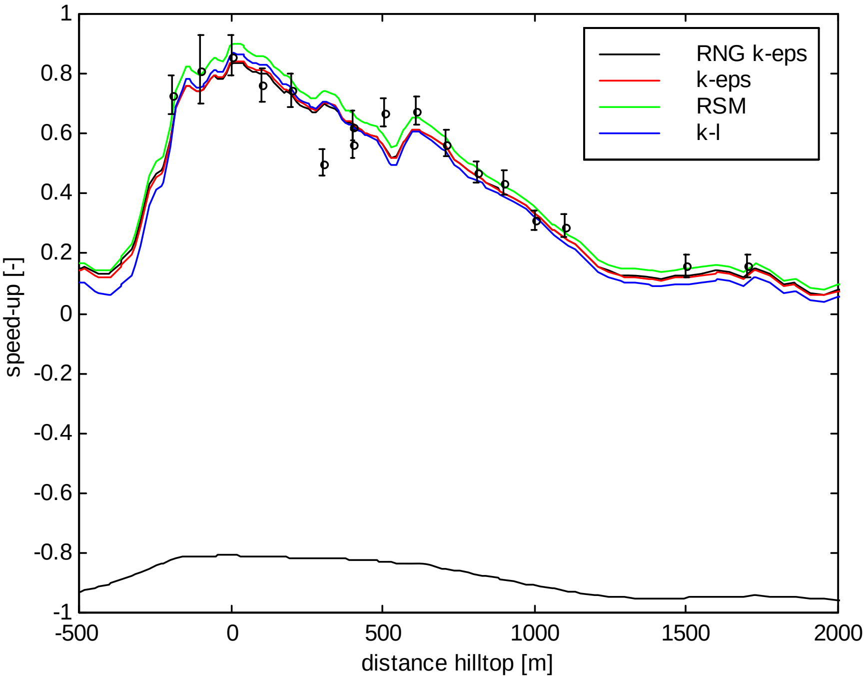

*Figure 45: Relative speed-up along line B. Symbols are measurements with uncertainty limits (Taylor and Teunissen, 1985). Different turbulence models are compared.*

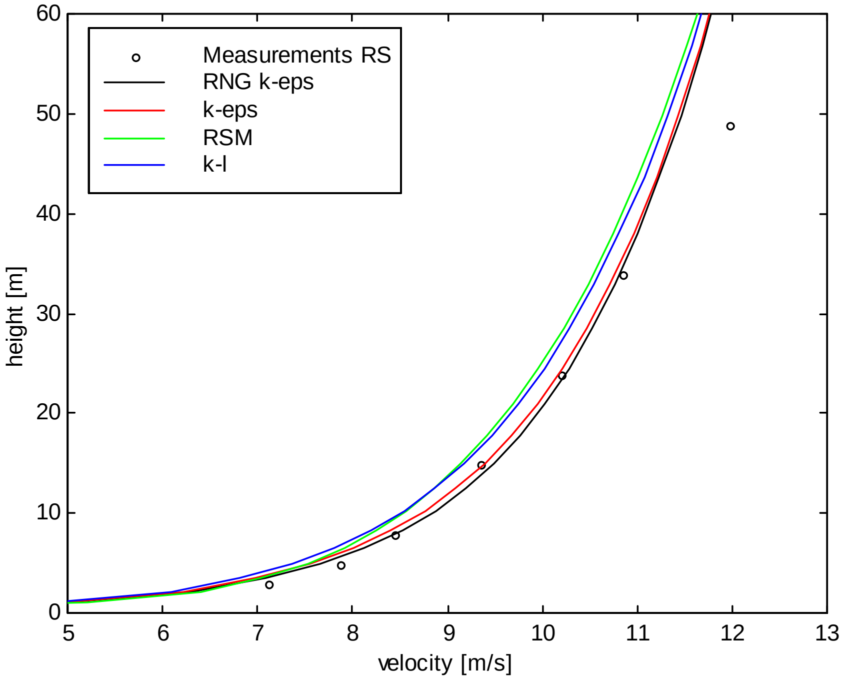

*Figure 46: Simulated velocity profiles at the reference station from different turbulence models. Results are compared to measurements (○)(Taylor and Teunissen, 1985).*

Through the turbulence run TU03-B the direction, the vertical velocity and the turbulent kinetic energy were collected along line A. These results are compared with the simulation results from the four turbulence models. According to Taylor and Teunissen (1985), the wind direction measurements from the TU runs at the hilltop are strongly suspected to have an alignment error, and are therefore in the direction plots replaced by the direction data extracted from the HT Wind monitor strip chart.

*Figure 47* show that the simulation results are not able to capture the large wind direction variation seen along line A, and the mean direction also tends to be a little higher than the measurements. This is mainly connected to the inflow direction, as discussed in Undheim et al. (2005). Besides this, the four turbulence models calculate almost identical estimates of the direction distribution. The angles between the wind velocity and the horizontal plane follow the measurements quite accurately for all turbulence models (*Figure 48*).

Turbulent kinetic energies along line A show large variations (*Figure 49*). The RNG results are found to correspond with the measurements upstream the hilltop. The k-ε model and the RSM calculate similar values, which are a little higher. This similarity is not surprising since the RSM is based on the k-ε model, and therefore has equal expressions for the production and the dissipation of the turbulent energy. The k-l method is a level higher than the other turbulence models. Estimated turbulent kinetic energy is almost twice the measurement level at the upstream side. One reason for the differences is that a one-equation model should be optimized to fit a more complex model in some standard flow situations. There have been some changes in 3DWind without a calibration of the k-l model.

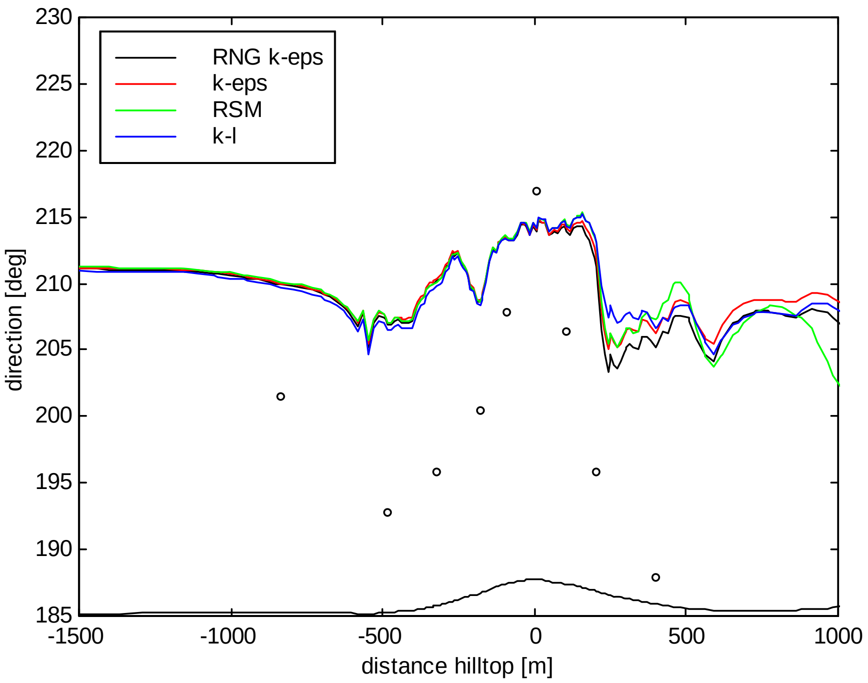

*Figure 47: Direction distributions along line A. Symbols are measurements (Taylor and Teunissen, 1985). Different turbulence models are compared.*

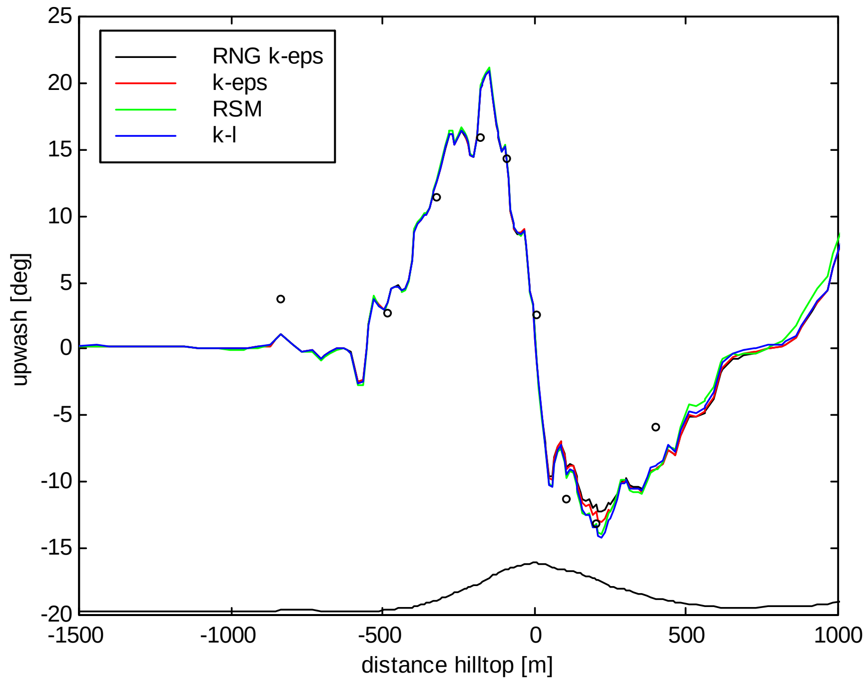

*Figure 48: The angles between the wind velocity and the horizontal plane along line A. Symbols are measurements (Taylor and Teunissen, 1985). Different turbulence models are compared.*

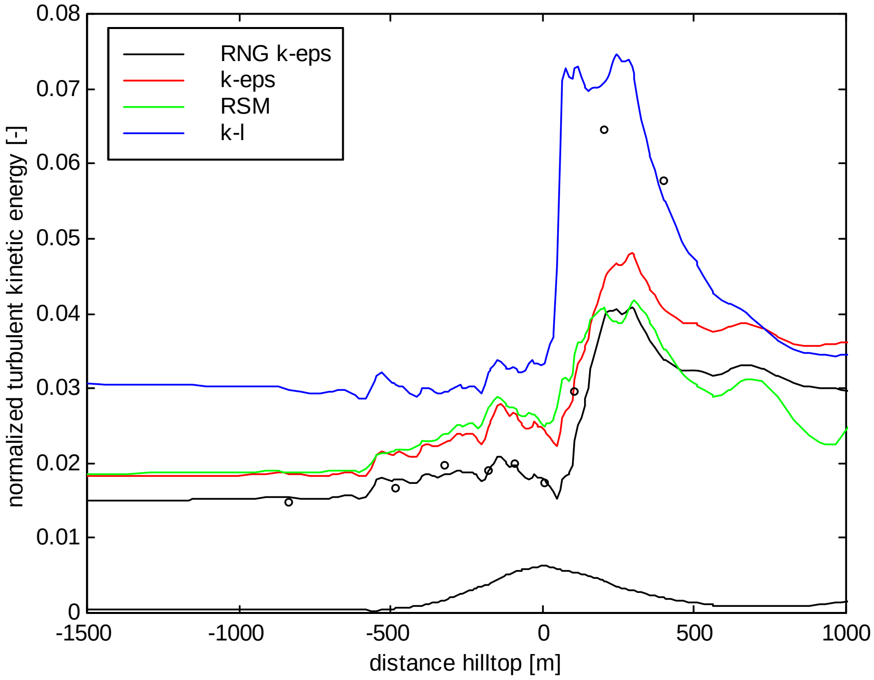

*Figure 49: The normalized turbulent kinetic energies along line A. Symbols are measurements (Taylor and Teunissen, 1985). Different turbulence models are compared.*

Raithby et al. (1987) and Castro et al. (2003) found turbulence values upstream of the hill that were higher than experimental values. The level was in the middle between the k-l results and the k-ε results from 3DWind, and Castro et al. (2003) related it to a possible bias in the Gill anemometers, but stated also that rapid-distortion and streamline curvature effects might reduce the turbulence kinetic energy. Kim and Patel (2000) related this to the turbulence closure with modified constants. A 3DWind simulation was initialized with modified constants, but this turbulence model caused the simulation to diverge, so no results are available for comparison.

From *Figure 49* the simulated turbulence levels in the wake of the hill are underestimated for all turbulence models, except for the k-l model, which actually overpredicts it. Underprediction is in accordance with other similar models (Raithby et al., 1987) (Kim and Patel, 2000) (Castro et al., 2003) (Eidsvik, 2004). As discussed by Raithby et al. (1987) and Castro et al. (2003), this might be caused by non-stationary effects not accounted for in the model. Castro et al. (2003) found turbulence values in the wake that were closer to experimental values, but this is maybe caused by high upstream values in the same manner as the k-l method.

One interesting finding, seen if the turbulence profile along line A is compared with the speed-up profile along line A, is the connection between high estimated turbulence values upstream the separation point and the speed-up values in the wake. High turbulence levels cause high speed-up levels in the wake. One possible explanation is that higher turbulence gives better mixing, and therefore increased velocities in the wake and less tendency to separate. Another factor, though small, is that the high turbulence level causes decreased velocity values at the reference station, and thereby influences estimated speed-up values in the wake.

The results discussed above illustrate the CFD model's ability to predict wind variations in the horizontal plane. An aspect that also is important in the field of wind engineering is the model's ability to predict the vertical profiles within the area. Measurement profiles exist both at the hilltop and at the reference station. The simulated profiles of both the horizontal wind speed and the turbulence intensities are compared to these profiles.

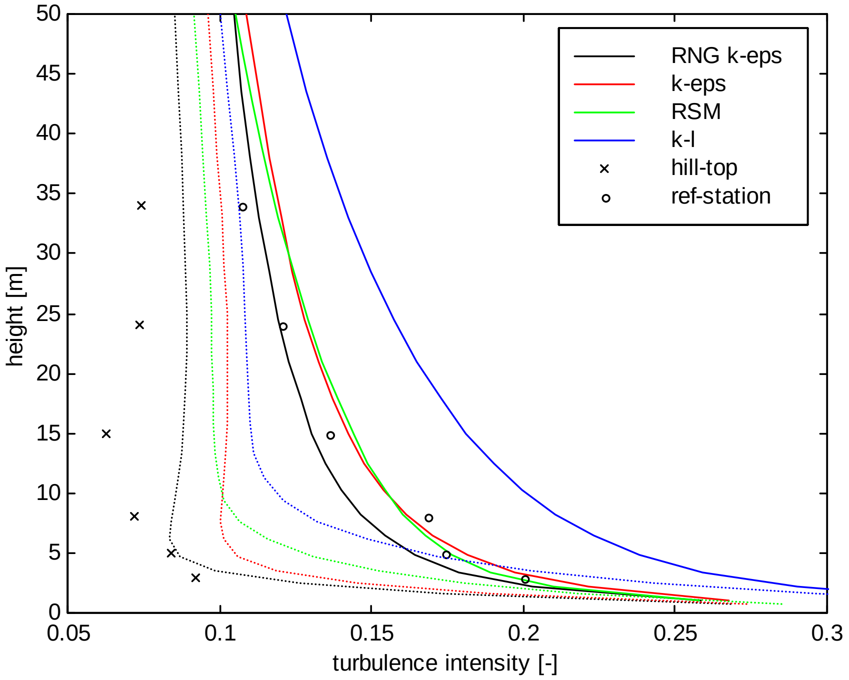

*Figure 50: Simulated turbulence intensity profiles at the hilltop and the reference station from different turbulence models. Results are compared to measurements at the hilltop (x) and measurements at the reference station (○) (Taylor and Teunissen, 1985).*

Simulated vertical profiles of the turbulence intensities seen in *Figure 50* are pretty much the same as the turbulent kinetic energy along line A. Turbulence intensity levels are overpredicted with the k-l method; the other methods give good predictions at the reference station, but values are overpredicted at the hilltop. Best turbulence intensity estimates at the hilltop are found with the RNG model.

*Figure 51* shows that the vertical speed-up profile at the hilltop is almost equally predicted by the two k-ε models. Results in all heights are within the uncertainty limits, but there is a tendency to overpredict the speed-ups above about 30m, and an underprediction below 30m height. In the k-l case and the RSM case this limit is decreased to about 20m, and the underestimation near the ground is larger; simulated speed-ups in the height of the lowermost measurement are not within the uncertainty limits. In accordance with the findings in the roughness dependence subsection 4.3.3, the maximum speed-up is not found at the surface, but at about 5m with the RSM and about 3m with the other turbulence models.

Both the general differences between simulation results and measurements seen in *Figure 51* and the tendency to underpredict the wind veering seen in *Figure 56*, are maybe connected to the slight stability discussed by Undheim et al. (2005). The atmosphere tends to avoid vertical motions, and this causes higher speed-ups near the ground, and more of the flow going around the hill. Another possible reason for differences that are indirectly dependent on the stability, is the inflow profile represented by the profile at the Reference station (see *Figure 52*). Near the ground the profile is almost logarithmic, and there is good accordance between the measurements and the simulated results, but above 30m there is a kink, not present in the simulation results. Ayotte (1997) found improved results when the inflow profile was fitted to measurements.

It is difficult to arrange the performance of the turbulence models, but generally best accordance between simulation results and measurements is found with the two k-ε models. The RNG-method was initially used to establish the one-dimensional profile based on findings from Kim and Patel (2000). This model is therefore preferred for the grid dependence test and the roughness dependence test in the following sections.

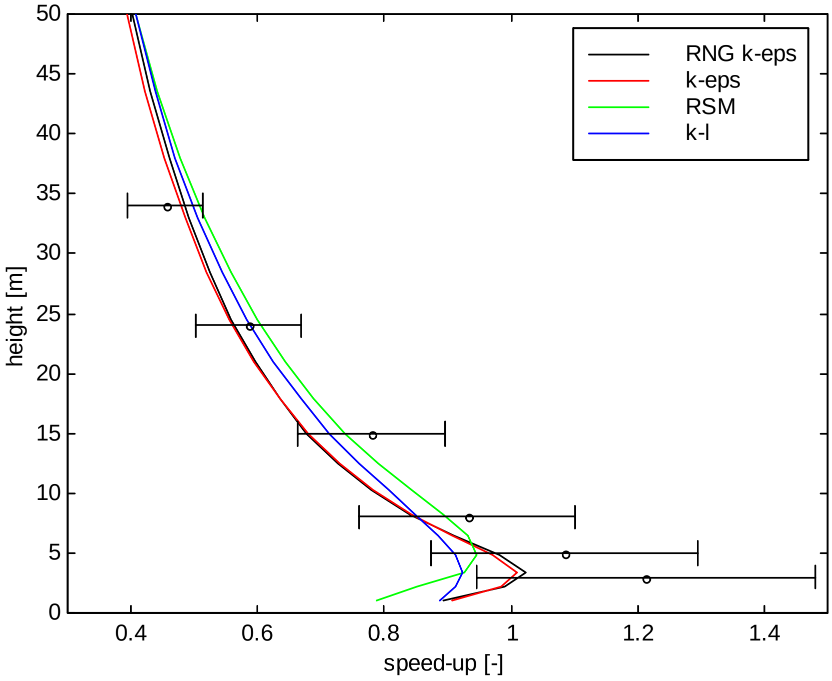

*Figure 51: Comparison of speed-ups at HT relative to RS in different heights agl. with different turbulence models. Symbols are measurements with uncertainty limits (Taylor and Teunissen, 1985).*

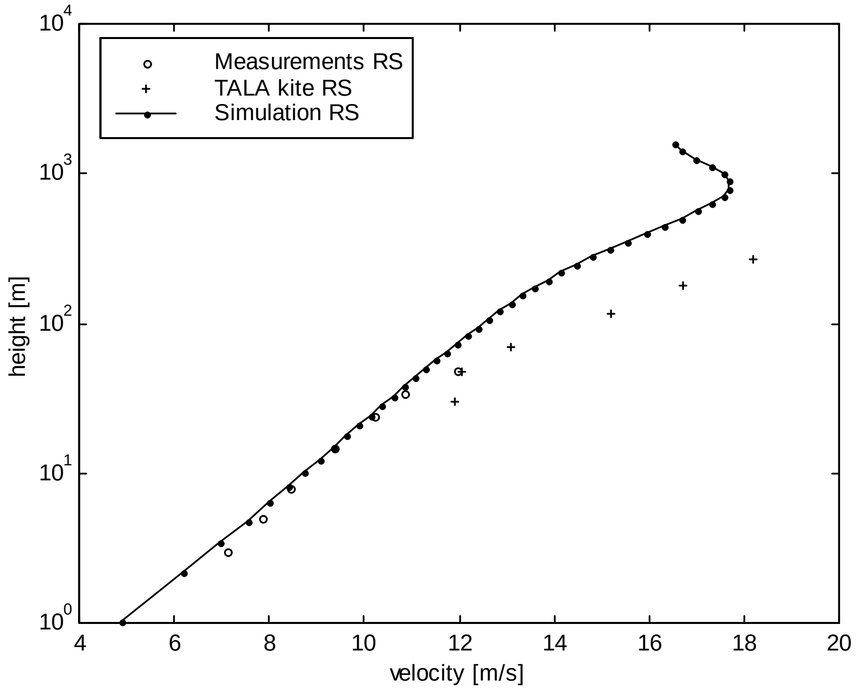

*Figure 52: Semi logarithmic plot of the horizontal velocity profile at RS from the RNG simulation. ○ are measurements from met mast at RS, + are TALA kite measurements, 1km west of RS (Taylor and Teunissen, 1985).*

### 4.3.2 Grid dependence

Main results of this analysis are obtained from the grid denoted by 'fine'. This is the grid described in the set up section. In order to evaluate the grid dependence of the solution, results are compared to three coarser grids. In the coarse ij grid, every second node is removed in the x and y direction in the horizontal plane. The vertical resolution is unchanged. In the coarse k grid, every second node is removed in the vertical direction (z), while the horizontal resolution remains unchanged. In the coarse ijk grid, every second node is removed in all three directions. This is done to separate grid dependences caused by the horizontal and the vertical resolution.

*Figures 53-55* show that the largest impact is caused by decreased vertical grid resolution. When the vertical resolution is decreased, the speed-up at the hilltop is slightly increased, and the speed-ups behind the hill are higher. The ability to estimate the speed-up values at the two leftmost points of line B (see *Figure 42*), is related to the horizontal resolution. Good resolution causes the speed-up on this low hill to be captured.

The different grids caused small differences in the vertical velocities along line A. The simulated direction along line A also had small differences, as illustrated in *Figure 56.*

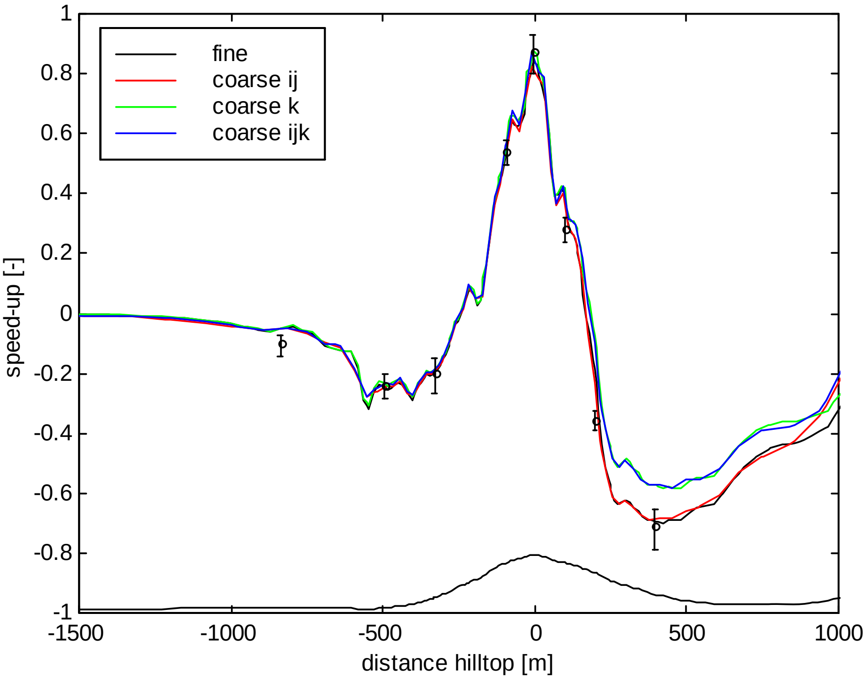

*Figure 53: A grid dependence comparison of relative speed-up along line A. Symbols are measurements with uncertainty limits (Taylor and Teunissen, 1985).*

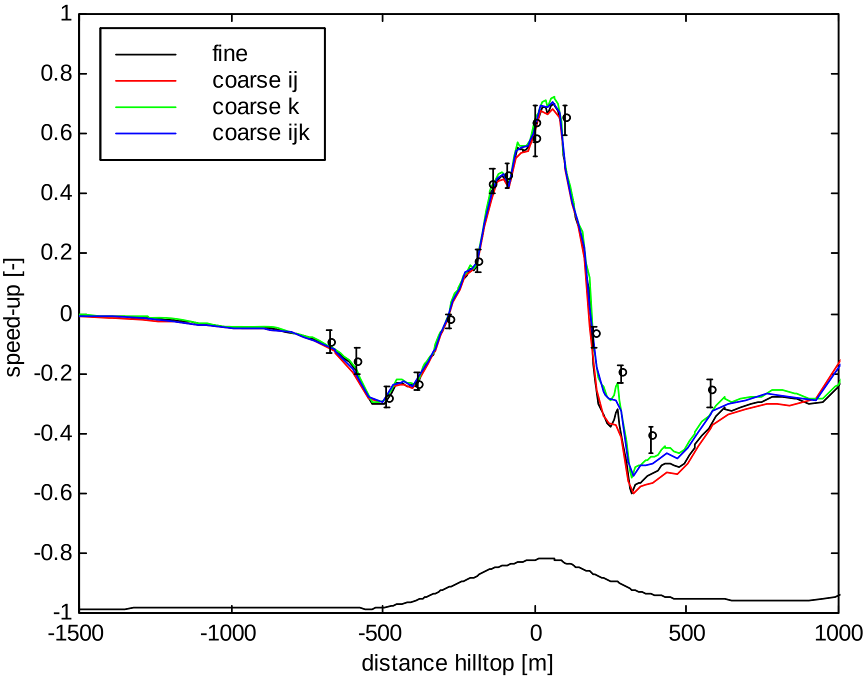

*Figure 54: A grid dependence comparison of relative speed-up along line AA. Symbols are measurements with uncertainty limits (Taylor and Teunissen, 1985).*

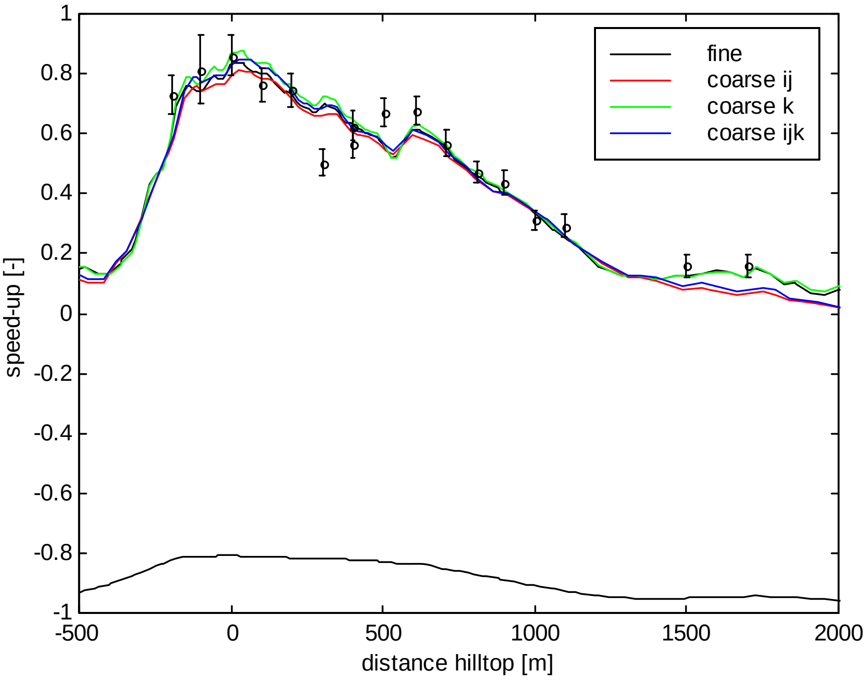

*Figure 55: A grid dependence comparison of relative speed-up along line B. Symbols are measurements with uncertainty limits (Taylor and Teunissen, 1985).*

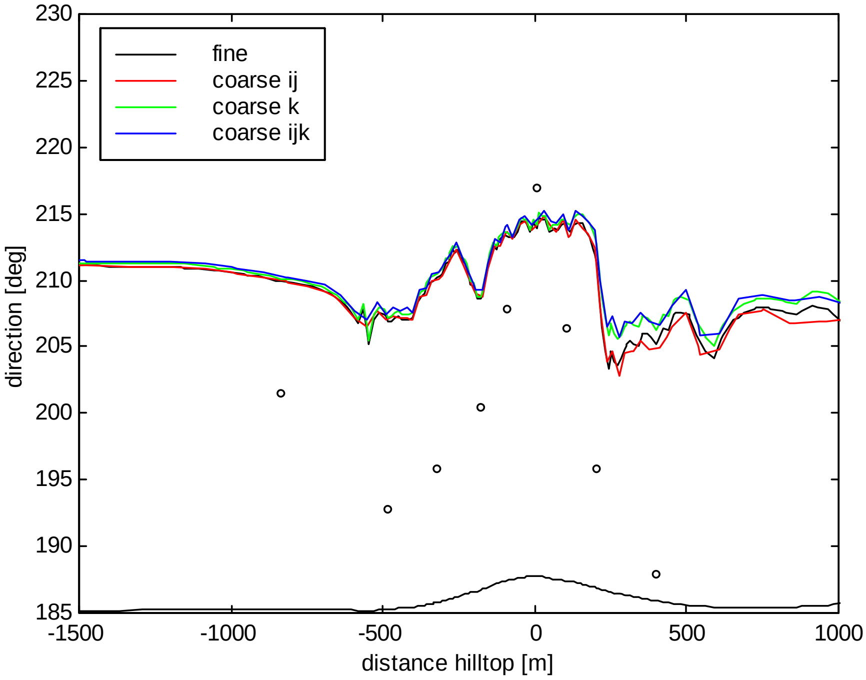

*Figure 56: A grid dependence comparison of direction distributions along line A. Symbols are measurements (Taylor and Teunissen, 1985).*

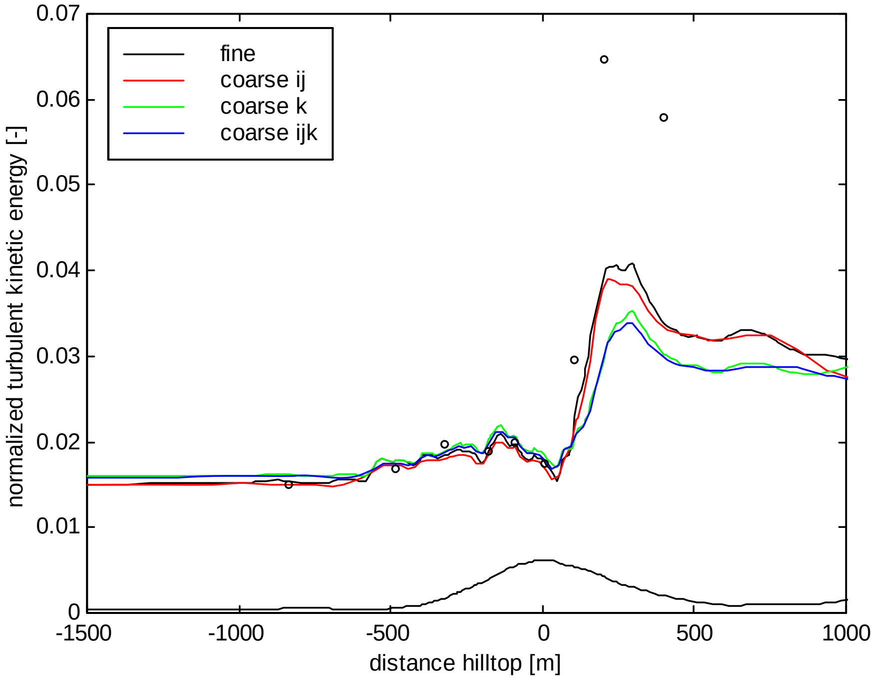

*Figure 57: A grid dependence comparison of the normalized turbulent kinetic energies along line A. Symbols are measurements (Taylor and Teunissen, 1985).*

The fact that the turbulence in the wake from *Figure 57* is higher than similar results from Kim and Patel (2000), which used the same turbulence model, is maybe connected to the different thickness of the first grid cell. Diminished vertical resolution tends to give a little larger turbulence upstream of the hill, but underestimates the turbulence in the wake of the hill some more than the high vertical resolution grids.

From *Figure 58* it is seen that decreased resolution in the horizontal plane causes an underestimation of windspeed above heights of about 7m and an overestimation below, compared to the fine grid. Decreased resolution along the vertical axis causes the opposite. Those two effects are seen to align each other, and the results from the pure coarse grid are following the results from the fine grid quite well.

The turbulence intensity profiles in *Figure 59* are found to depend somewhat on the vertical resolution. High resolution causes lower turbulence values, particularly near the ground. Compared to measurements, the turbulence profile at the reference station is quite accurate, while the turbulence profile at the hilltop follows the measurements near the ground and up to a minimum in heights of about 5m. The measured turbulence data continue to decrease, and have a minimum in approximate 15m heights.

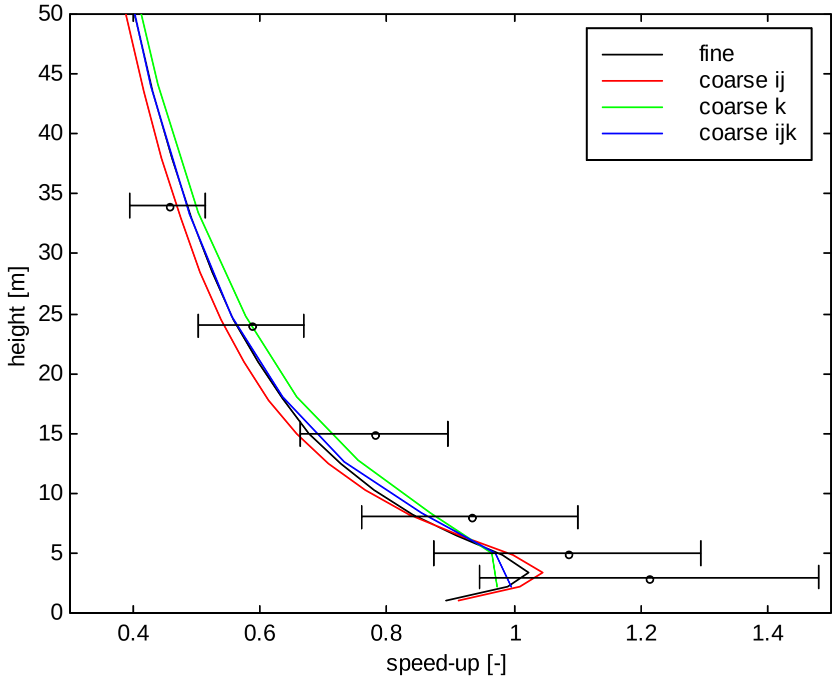

*Figure 58: A grid dependence comparison of the speed-up at the hilltop (HT) relative to the reference station (RS) in different heights above ground. Symbols are measurements with uncertainty limits (Taylor and Teunissen, 1985).*

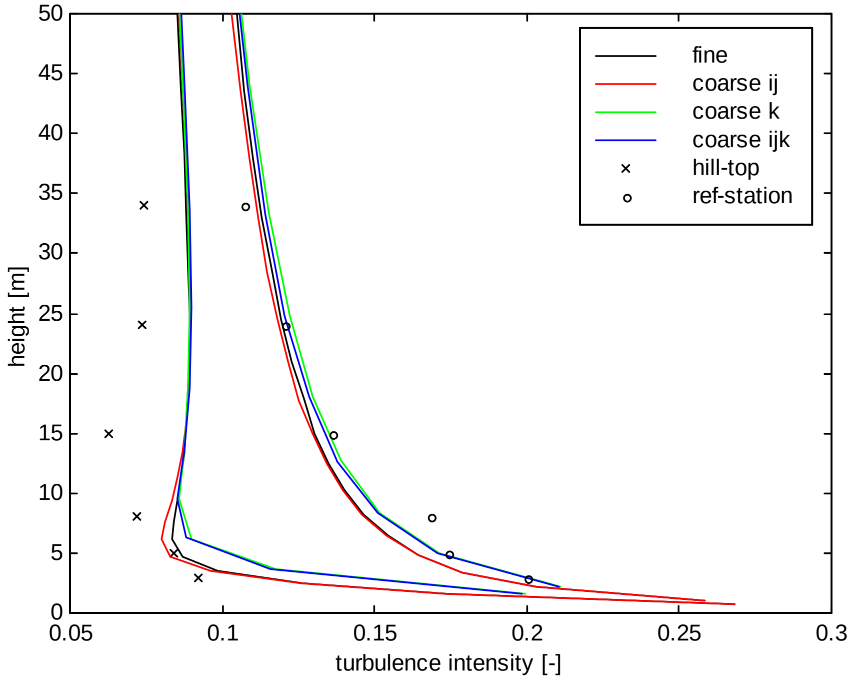

*Figure 59: A grid dependence comparison of the turbulence intensities with different meshes. x is the turbulence intensity measurements at the hilltop (HT) and ○ is the turbulence intensity measurements at the reference station (RS) (Taylor and Teunissen, 1985).*

### 4.3.3 Roughness dependence

The detailed roughness description seems to improve some aspects of the flow and worsen others. The profile along line A in *Figure 60* is best matched with uniform roughness, while the profile along line AA in *Figure 61* is best matched with non-uniform roughness. Along both profiles, non-uniform roughness causes increased upstream speed-ups. This is mainly caused by the high roughness just behind the reference station seen in *Figure 40*, which causes decreased values at the reference station. This difference is aligned by increased roughness in the area 500-1000m before the hilltop. This is caused by some buildings along a road as seen in *Figure 38*.

Low roughness on the hilltop causes increased speed-ups for the non-uniform roughness, both at the hilltop and in the wake. This causes wake values along line A to be overestimated, while wake values along line AA are within the uncertainty level. Speed-up values along line B in *Figure 62* is increased in the non-uniform roughness case. This is partly attributed to low roughness on the hilltop, but the values are also increased in areas without low roughness. This indicates that the reduced velocity at the reference station is maybe most important to the speed-up differences along line B.

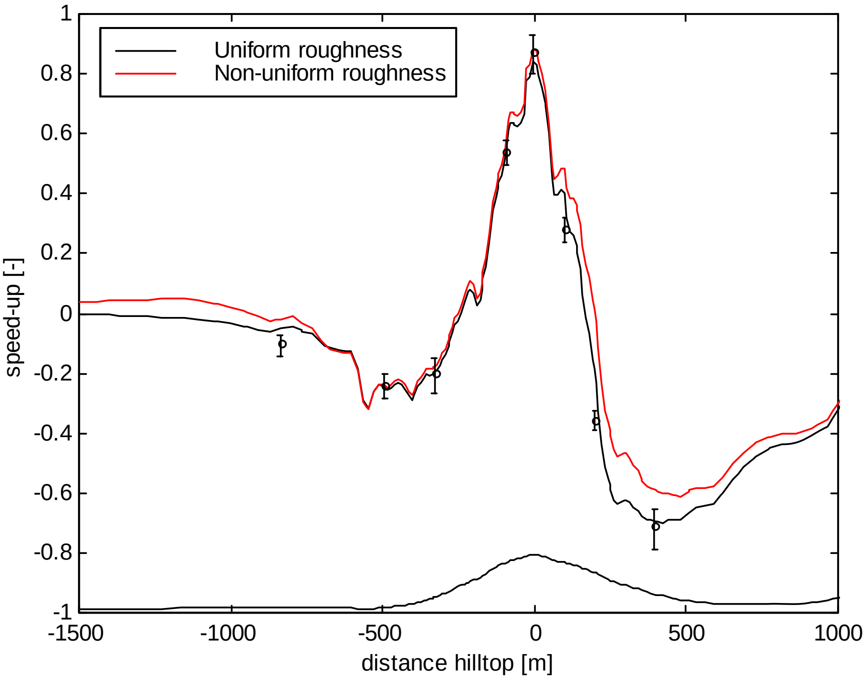

*Figure 60: Relative speed-up along line A. Symbols are measurements with uncertainty limits (Taylor and Teunissen, 1985). Non-uniform roughness length simulations (Figure 40) are compared to uniform roughness length simulations ($z_0$=0.03m).*

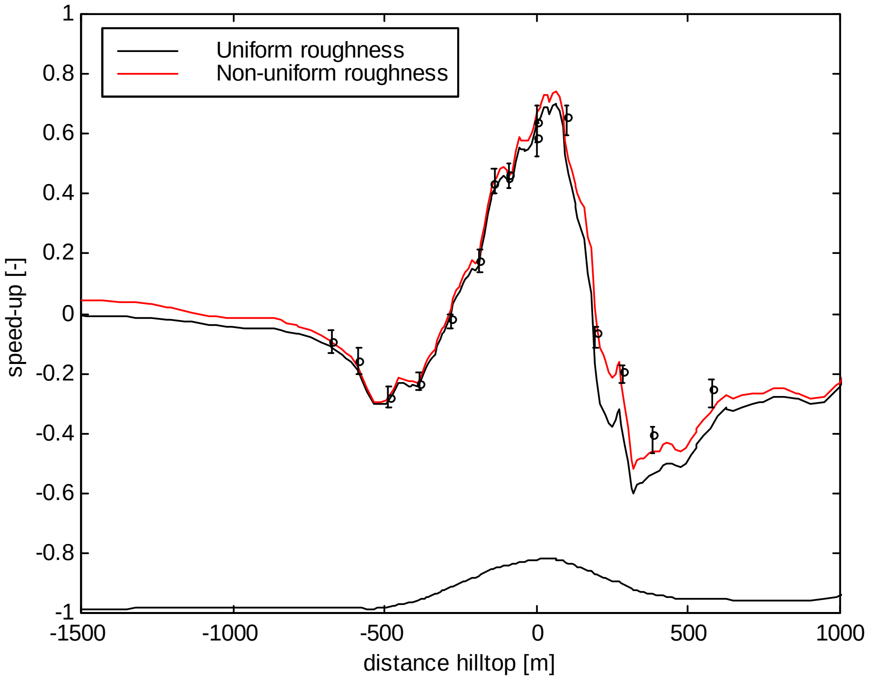

*Figure 61: Relative speed-up along line AA. Symbols are measurements with uncertainty limits (Taylor and Teunissen, 1985). Non-uniform roughness length simulations (Figure 40) are compared to uniform roughness length simulations ($z_0$=0.03m).*

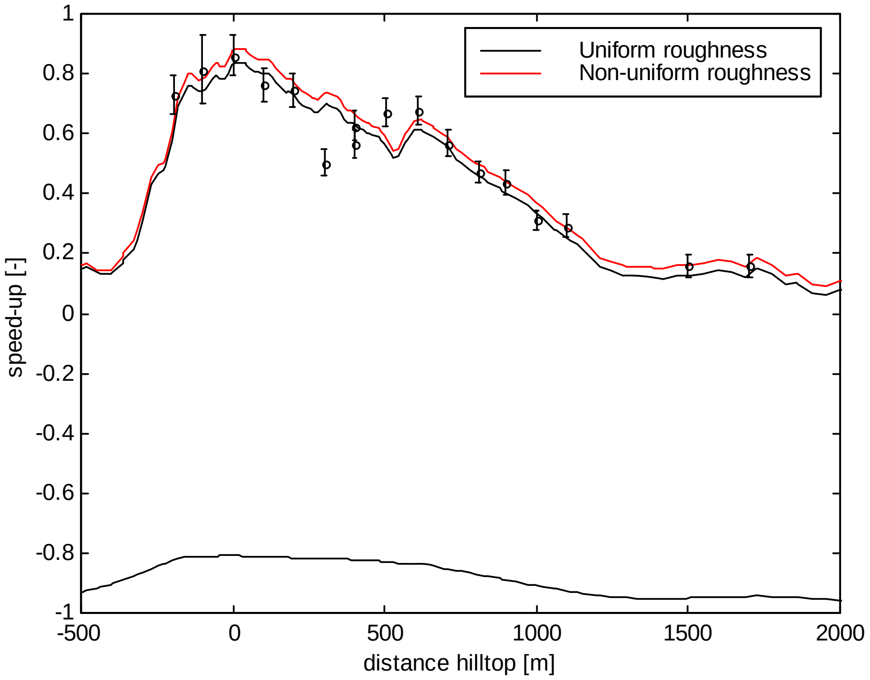

*Figure 62: Relative speed-up along line B. Symbols are measurements with uncertainty limits (Taylor and Teunissen, 1985). Non-uniform roughness length simulations (Figure 40) are compared to uniform roughness length simulations ($z_0$=0.03m).*

The direction plots in *Figure 63* show less turning. This is maybe caused by the low roughness at the hilltop. The angles between the wind velocity and the horizontal plane along line A show minor differences, and are not joined in the results. The turbulent kinetic energy profile in *Figure 64* indicates that the low hilltop roughness causes the turbulence increase in the wake to start later, and have a less increase. The calculated turbulence intensity profiles at the reference station and the hilltop (*Figure 65*) are improved. Turbulence intensity values are slightly increased at the reference station. This is partly due to increased turbulence level, and partly to decreased velocity. The opposite effect is seen at the hilltop. The turbulence intensity is slightly decreased due to decreased turbulence level and increased velocities.

*Figure 66* shows the effect of decreased roughness at the hilltop. Uniform roughness causes a speed-up maximum in 3m agl. This departs from the theoretical considerations suggesting that these maxima should occur at the surface (Teunissen et al., 1987), which is in accordance with full-scale measurements. Mickle et al. (1988) suggested possible reasons for the underprediction. One of the possibilities is that it is related to variations in the surface roughness on the hill; there is suspicion that the hilltop area could have been slightly smoother than the upstream terrain. Castro et al. (2003) performed simulations with decreased roughness on the top of the hill, and found improved relative speed-up profiles between the hilltop and the reference station. This effect is also seen in *Figure 66*, where the maximum speed-up is found on the ground, and where a good accordance to measured speed-up values is present.

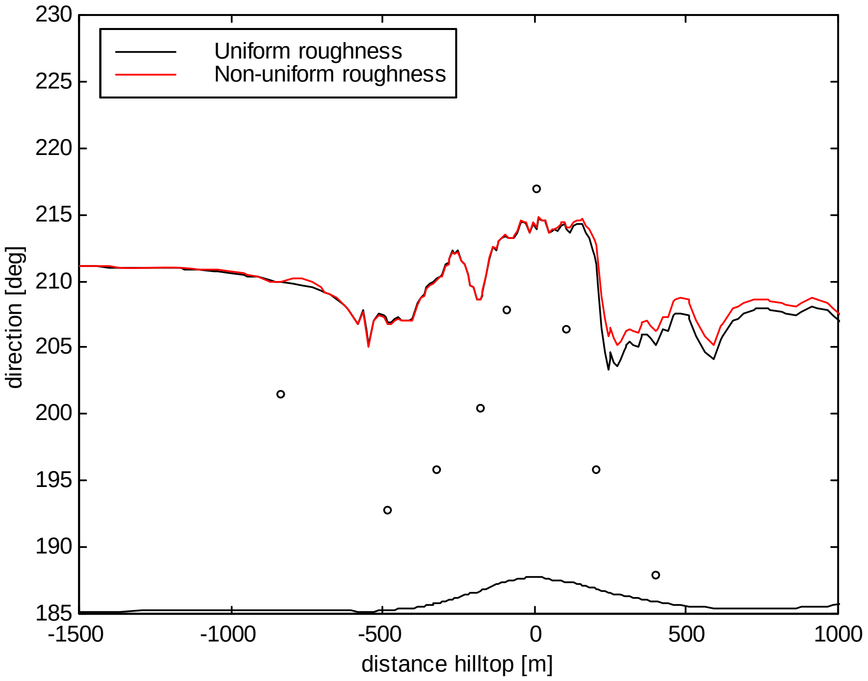

*Figure 63: Direction distributions along line A. Symbols are measurements (Taylor and Teunissen, 1985). Non-uniform roughness length simulations (Figure 40) are compared to uniform roughness length simulations ($z_0$=0.03m).*

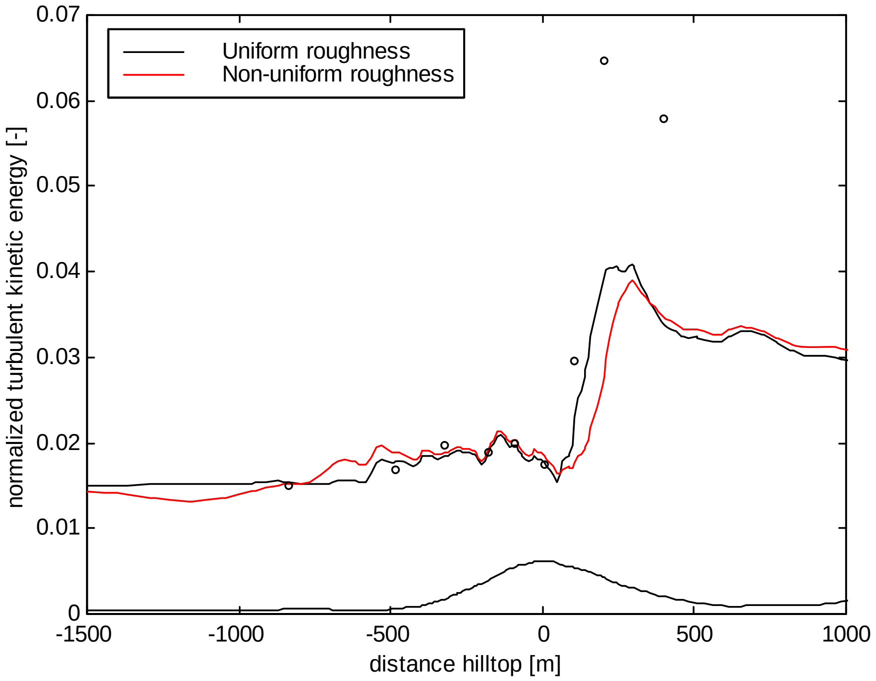

*Figure 64: The normalized turbulent kinetic energies along line A. Symbols are measurements (Taylor and Teunissen, 1985). Non-uniform roughness length simulations (Figure 40) are compared to uniform roughness length simulations ($z_0$=0.03m).*

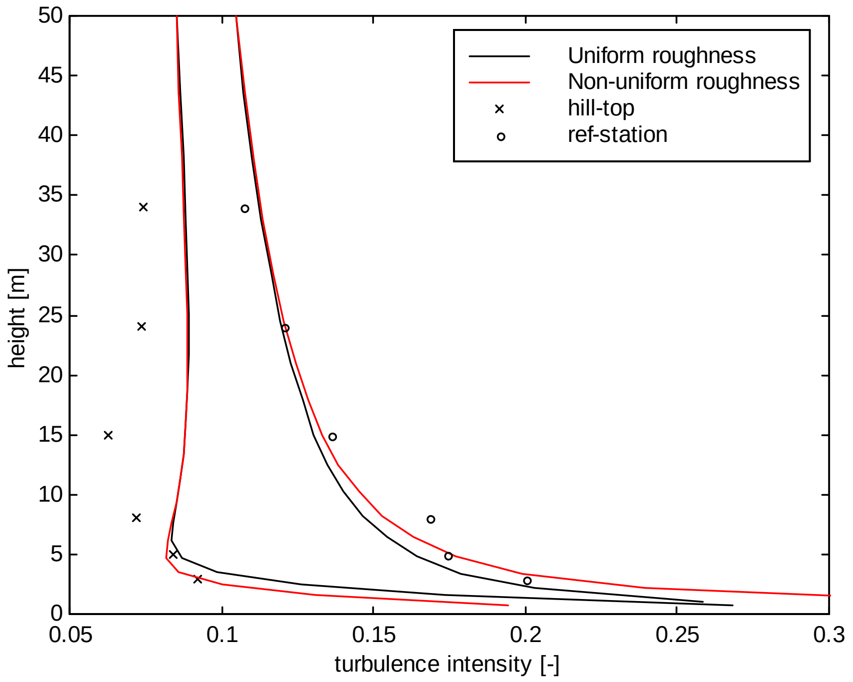

*Figure 65: Simulated turbulence intensity profiles at the hilltop and the reference station with uniform ($z_0$=0.03m) and non-uniform (Figure 40) roughness length. Results are compared to measurements at the hilltop (X) and at the reference station (○) (Taylor and Teunissen, 1985).*

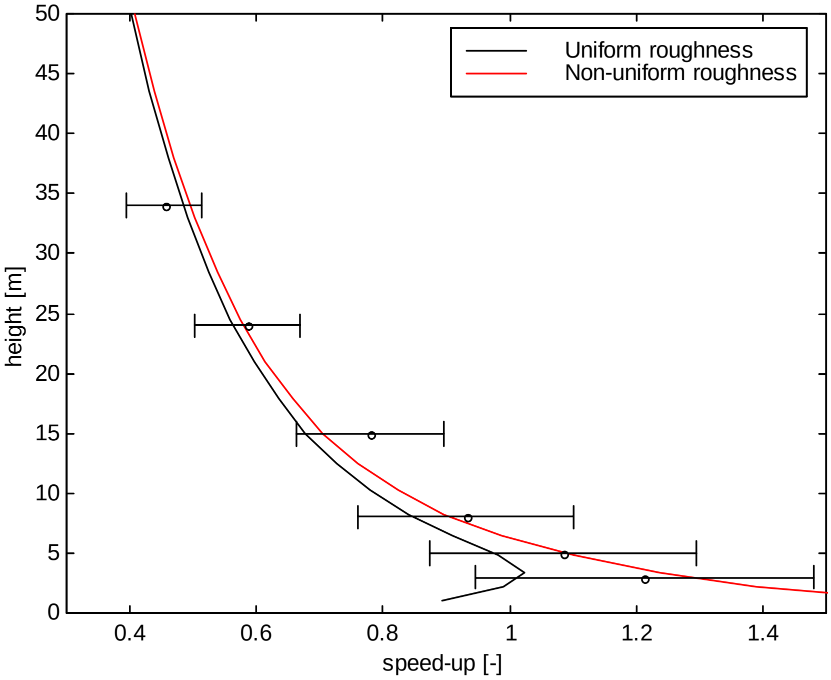

*Figure 66: The speed-up at the hilltop (HT) relative to the reference station (RS) in different heights above ground. Symbols are measurements with uncertainty limits (Taylor and Teunissen, 1985). Non-uniform roughness length simulations (Figure 40) are compared to uniform roughness length simulations ($z_0$=0.03m).*

# 5 Summary and conclusions

The RANS model 3DWind is described and validated in simulations of two test cases. The flow cases used were test case C18 from the ERCOFTAC Classic database and the Askervein hill case. Test case C18 is a 2D hill in a flow channel where the flow medium is water. Experimental measurement data are available together with numerical solutions from different well-proven codes. The Askervein hill case is a full scale wind data measurement campaign, from where the flow condition of the afternoon 3 October 1983 has been chosen for detailed analysis. In addition to measurement results, results from wind tunnel simulations and several numerical simulations are further available for Askervein hill.

The implemented equations of the non-linear 3D flow solver 3DWind seem to calculate both flows in good accordance with available experimental and numerical results. Still, the simulation experience and obtained results show that modelling of recirculation is a difficult task. The flow field is extremely sensitive to the separation point, which is sensitive to most of the other variables. Turbulence model choice, wall function approach, boundary conditions and the grid are factors that influence the separation point. Usually, areas of recirculation are not relevant for wind turbines, but the separation point also influences the highly relevant spot at the hill summit. This is particularly visible at the C18 case, where the hilltop velocity depends on the down stream separation point. This sensitivity is highest close to the ground, but influences the entire wind profile. This separation dependency from different factors indicates that simulation results in complex terrain have to be used with care, and measurements are preferred for supplementary information. Since both cases concern the separation or close to separation aspect, 3DWind should be further validated with a case free from recirculation.

The grid evaluation of both simulations shows that the horizontal resolutions contain minor grid dependence. Simulations from C18 with equal thickness of the first grid cell, gave almost similar results with three different grid resolutions. At Askervein hill a map of two meter contours was used to establish the grid, which ensured a good spatial resolution. The speed-up profiles follow local terrain formations very well. Two different horizontal resolutions are compared, and only minor differences are found between the fine and the coarse grid. This indicates that a limit is already reached, where only minor improvements are expected due to refined horizontal resolution. The resolution advantage of linear models seems no longer present here, even though there are large differences in computational cost for the different simulation models.

There is still some grid dependence in the vertical direction. In the wake along line A in the Askervein hill simulation with decreased vertical resolution, the turbulence kinetic energy is decreased and the speed-up is increased. Both effects are related to each other. Higher turbulence in the wake with high resolution causes more energy to be removed from the mean flow, and lowers velocities. Upstream turbulence level is also increased in the coarse case. This causes lower velocities at the reference station, and this explains some of a present speed-up difference at the hilltop. In the C18 case two grids of the same size, but different thicknesses of the first cell, were found to influence the simulated separation zone largely. This indicates that the found vertical grid dependence mainly is related to the thickness of the first grid cell and grid dependent wall functions.

The C18 case operates with two different types of wall functions. In the direct wall function, the velocity in the first grid cell is set, and in the indirect wall function the wall shear stress is set. Both methods are found to suffer from limitations. The assumption of a logarithmic law deals with both favourable and adverse pressure gradients. Direct wall functions are not capable of good approximations in all conditions, since they do not allow the velocity vectors at the separation point to have opposite direction in the first and the second cell. The indirect wall functions solve this problem and are also able to solve the problem of wall continuity, and give smooth pressure near the ground. Still, the solution is found to be more dependent on the size of the first grid cell. The direct wall function approach was used further in the Askervein hill case.

Five different turbulence models have been involved in this analysis. A one-equation k-l model, three different k-ε models and a Reynolds stress model. The different turbulence models are found to influence the velocities, particularly in the wake of the hill. Turbulence levels upstream of the Askervein hill are found to have large variations depending on the used turbulence model. The RNG k-ε model calculates the lowest turbulence level, and results are at the same level as measurements. The values calculated with the k-l model are almost twice this level. The same order is found in the speed-ups in the wake, which indicates a possible connection between upstream turbulence level and speed-up in the wake. This is not surprising, since recirculation is a phenomenon depending on the turbulence level in the flow field.

Comparing the results between different turbulence models at the C18 case, the results from the RSM simulations do not seem to increase the accuracy. The turbulence is almost isotropic, and only minor differences are seen between the RSM and the k-ε model. The k-ε method is known to estimate too high values for the turbulent kinetic energy in the area near the ground, in front of the hilltop. This departure is solved by the RSM equation set. On the other hand, residual profile comparisons show that RSM results generally have more 'wiggle' in the velocity field than k-ε model results. This is connected to the velocity-pressure coupling connected to the fact that the grid is collocated. The RSM has less numerical diffusion than the k-ε model, since the diffusion terms are directly estimated from the Reynolds stresses, and not proportional to the mean shear. Compared to the RSM reference solution, the 3DWind version seems to have some more diffusion. This is maybe connected to the eddy-viscosity assumption used in the turbulence equations.

The inclusion of a detailed roughness distribution at Askervein hill is not found to improve the numerical results significantly. The most significant difference is the prediction of a hilltop speed-up profile where the speed-up increases towards the ground in accordance with measurements and theoretical considerations. The speed-up level is also found to correspond with measurements, not underpredicted and with a maximum at approximate 3m above ground, as in the uniform roughness simulation.

The analysis has also shown shortcomings and further potential for development of the solver 3DWind. To increase the predictability of the model, the wall function dependence should be further investigated and, if possible, removed. Still large gradients in the first grid cell are difficult to generalize, but different generalized wall functions are available for implementation (Craft et al., 2002) (Utyuzhnikov, 2005). The artificial viscosity should be modified. It should automatically be minimized in areas where it is not necessary and increased in areas where it is required. Overcompensation, which can cause divergence, should be avoided. The grid generation should use non-linear interpolations, and spot height should be evaluated from more than contour crossing in two directions. The model could also have been improved by a more advanced grid generator algorithm for the generation of orthogonal grids in very complex terrain. In the Askervein hill case it would also be interesting to test the stability dependence by adding the buoyancy terms to the equations.

## Acknowledgements

The author wish to give a special thank to Dominique Laurence for kindly correspondence regarding the ERCOFTAC C18 reference simulation. A special thank is also due to Peter Taylor, who kindly made PDF versions of the reports MSRB-84-6 (Taylor and Teunissen, 1985) and MSRB-83-8 (Taylor and Teunissen, 1983) available on the web[3].

---

[3] http://www.yorku.ca/pat/research/Askervein/index.html

## References

Ahrens, C. D. (1994). *”Meteorology Today. An introduction to weather, climate, and the environment”*. Fifth edition. West Publishing Company, Minneapolis.

Almeida, G. P., Durao, D. F. G. & Heitor, M. V. (1993). *“Wake flows behind two-dimensional model hills”*. Experimental Thermal and Fluid Science, 7: 87 – 101.

Alm, L. K. & Nygaard, T. A. (1995). *“Flow over complex terrain estimated by a general purpose Navier-Stokes solver”*. Modelling, identification and control, 16: 169 – 176.

Arya, S. P. (1988).*“Introduction to Micrometeorology”*. International Geophysics Series, Volume 42. Academic Press, Inc, San Diego, California.

Barnard, J. C. (1991). *“An evaluation of three models designed for siting wind turbines in areas of complex terrain”*. Solar Energy, 46: 283 – 294.

Beljaars, A. C. M., Walmsley J. L. & Taylor P. A. (1987). *“A mixed spectral finite-difference model for neutrally stratified boundary-layer flow over roughness changes and topography”*. Boundary-Layer Meteorology, 38: 273 – 303.

Bonnin, J. C., Buchal, T. & Rodi, W. (1995). *“ERCOFTAC Workshop on Data Bases and Testing of Calculation Methods for Turbulent Flows”*. University of Karlsruhe, Germany, 3-7 April 1995. ERCOFTAC Bulletin: 48 – 54.

Bowen, A. J. & Mortensen, N. G. (1996). *”Exploring the limits of WasP the wind atlas analysis and application program”*. European Union Wind Energy Conference, Göteborg, Sweden, 20-24 Mai 1996.

Bredberg, J. (2002). *“Turbulence Modelling for Internal Cooling of Gas-Turbine Blades”*. PhD-thesis. Chalmers University of Technology, Göteborg, Sweden.

Butcher, J. C. (1987). *”The numerical analysis of ordinary differential equations, Runge-Kutta and general linear methods”*. John Wiley & Sons Ltd., Great Britain.

Castro, F. A., Palma, J. M. L. M. & Silva Lopes A. (2003). *“Simulation of the Askervein flow. Part 1: Reynolds averaged Navier-Stokes equations (k-ε turbulence model)”*. Boundary-Layer Meteorology, 107: 501 – 530.

Chow, F. K. & Street, R. L. (2004). *“Evaluation of turbulence models for Large-Eddy simulations of flow over Askervein hill”*. Paper 7.11, 16th Symposium on Boundary Layers and Turbulence, American Meteorological Society.

Chorin, A. J. (1967). A Numerical Method for Solving Incompressible Viscous Flow Problems. In *Computational Fluid Dynamics,* edited by C. K. Chu, AIAA Selected Reprints Series, 4: 12.

Craft, T. J., Gerasimov, A. V., Iacovides, H. & Launder, B. E. (2002). *“Progress in the generalization of wall-function treatments”*. International Journal of Heat and Fluid Flow, 23: 148 – 160.

Dudhia, J., Gill, D., Manning, K., Wang, W., & Bruyere, C. (2005). *“PSU/NCAR Mesoscale Modeling System Tutorial Class Notes and Users' Guide (MM5 Modeling System Version 3)”*. http://www.mmm.ucar.edu/mm5/documents/

Eidsvik, K. J. (2004). *“A System for Wind Power Estimation in Mountainous Terrain. Prediction of Askervein Hill Data”*. Research Article in press at Wind Energy.

Eriksson, L.-E. (1987). *“A finite volume solution technique for the Navier-Stokes equations governing viscous compressible flow”*. HOG Report 1987:102(A). Division of Hydro- and Gas Dynamics, The Norwegian Institute of Technology, Trondheim.

Ferziger, J. H. & Perić, M. (2002). *“Computational Methods for Fluid Dynamics”*. 3rd Edition. Springer-Verlag, Berlin Heidelberg, Germany.

Hirsch, C. (1988). *“Numerical computation of internal and external flows, volume 1”*. John Wiley & Sons, Great Britain.

Hirsch, C. (1990). *“Numerical computation of internal and external flows, volume 2”*. John Wiley & Sons, Great Britain.

Jameson, A., Schmidt, W. & Turkel, E. (1981). *“Numerical simulation of the Euler equations by finite volume methods using Runge-Kutta time stepping schemes”*. AIAA Paper 81-1259, AIAA 5th Computational Fluid Dynamics Conference.

Kim, H. G. & Patel V. C. (2000). *“Test of turbulence models for wind flow over terrain with separation and recirculation”*. Boundary-Layer Meteorology, 94: 5 – 21.

Kim, H. G., Patel, V. C. & Lee, C. M. (2000). *“Numerical simulation of wind flow over hilly terrain”*. Journal of Wind Engineering and Industrial Aerodynamics, 87: 45 – 60.

Knauer, A. and Nyhammer, F. K. (2002). *”Numerical and experimental methods for wind farm site evaluation in complex terrain”*. Conference proceedings Global Windpower 2002, Paris, France, 2-5 April 2002.

Launder, B. E. & Spalding, D. B. (1974). *“The numerical computation of turbulent flows”*. Computer methods in applied mechanics and engineering, 3: 269 – 289.

Laurence et al. (2003) (EU project G1RT-CT-2000-05003). www.qnet-cfd.net. Thematic Area 3, Underlying Flow Regime: Flow separation behind a 2D hill.

Leroy, J. & Gravdahl, A. R. (1999). *“Wind field simulations at Askervein hill”*. Vector, Tønsberg, Norway.

Lopes, A. M. G. (2003). *“WindStation –a software for the simulation of atmospheric flows over complex topography”*. Environmental Modelling & Software 18: 81 – 96.

Mickle, R. E., Cook, N. J., Hoff, A. M., Jensen, N. O., Salmon, A. J., Taylor, P. A., Tetzlaff, G. & Teunissen, H. W. (1988). *“The Askervein Hill project: Vertical profiles of wind and turbulence”*. Boundary-Layer Meteorology, 43: 143 – 169.

Panofsky, H. A. & Dutton, J. A. (1984). *“Atmospheric turbulence. Models and Methods for Engineering Applications”*. John Wiley & Sons, USA.

Patankar, S. V. (1980). *“Numerical heat transfer and fluid flow”*. Series in computational methods in mechanics and thermal sciences. Hemisphere Publ., Washington.

Raithby, G. D., Stubley, G. D. & Taylor, P. A. (1987). *“The Askervein Hill project: A finite control volume prediction of three-dimensional flows over the hill”*. Boundary-Layer Meteorology, 39: 247 – 267.

Rogers, S. E. & Kwak, D. (1991). *“Steady and Unsteady Solutions of the Incompressible Navier-Stokes Equations”*. AIAA Journal, 29: 603 – 610.

Salmon, J. R., Bowen, A. J., Hoff, A. M., Johnson, R., Mickle, R. E., Taylor, P. A., Tetzlaff, G. & Walmsley, J. L. (1988). *“The Askervein Hill project: Mean wind variations at fixed heights above ground”*. Boundary-Layer Meteorology, 43: 247 – 271.

Seinfeld, J. H. & Pandis, S. N. (1998). *“Atmospheric chemistry and physics. From Air Pollution to Climate Change”*. John Wiley & Sons, Inc., USA.

Taylor, P. & Teunissen, H. (1985). *“The Askervein Hill Project: Report on the September/October 1983 Main Field Experiment”*. Report MSRB-84-6, Atmospheric Environment Service, Downsview, Ontario.

Taylor, P. A. & Teunissen, H. W. (1987). *“The Askervein Hill project: Overview and background data”*. Boundary-Layer Meteorology, 39: 15 – 39.

Teunissen, H. W., Shokr, M. E., Bowen, A. J., Wood, C. J. & Green, D. W. R. (1987). *“The Askervein Hill project: Wind-tunnel simulations at three length scales”*. Boundary-Layer Meteorology, 40: 1 – 29.

Troen, I. & Petersen, E. L. (1988). *”Siting of wind turbines”*. European Community Wind Energy Conference, Herning, Denmark, 6-10 June 1988.

Undheim, O. (2003). *”Comparison of turbulence models for wind evaluation in complex terrain”*. Conference proceedings European Wind Energy Conference, Madrid, Spain, 16-19 June 2003.

Undheim, O. (2005). *”2D simulations of terrain effects on atmospheric flow”*. Conference proceedings MekIT’05, Trondheim, Norway, 11-12 May 2005.

Undheim, O., Andersson, H. I. & Berge, E. (2005). *”The Askervein hill case; Some new aspects”*. Paper submitted for journal publication, Kjeller, Norway.

Utaaker, K. (1991). *”Mikro- og lokalmeteorologi. Det atmosfæriske miljø på liten skala”*. Alma Mater Forlag AS, Bergen, Norway.

Utyuzhnikov, S. V. (2005). *“Some new approaches to building and implementation of wall-functions for modeling of near-wall turbulent flows”*. Computers & Fluids, 34: 771 – 784.

Versteeg, H. K. & Malalasekera, W. (1995). *”An introduction to Computational Fluid Dynamics; The Finite Volume Method”*. Prentice Hall, London.

Walmsley, J. L. & Taylor, P. A. (1996). *“Boundary-layer flow over topography: Impacts of the Askervein study”*. Boundary-Layer Meteorology, 78: 291 – 320.

White, F. M. (1991). *“Viscous fluid flow”*. McGraw-Hill series in mechanical engineering. McGraw-Hill, New York.

Wilcox, D. C. (2000). *“Turbulence Modelling for CFD”*. Second Edition. DCW Industries, Inc. California.

Windpower monthly news magazine. Volume 20. No.3. Mars 2004. *“Wind market status”*. Knebel, Denmark.

Øye, I. J. (1996). *”On the aerothermodynamic effects on space vehicles”*. PhD-thesis. Norwegian University of Science and Technology, Trondheim, Norway.

# Appendix A

Profiles of the vertical velocity, the turbulent kinetic energy, the dissipation and some selected profiles from the Reynolds stresses.

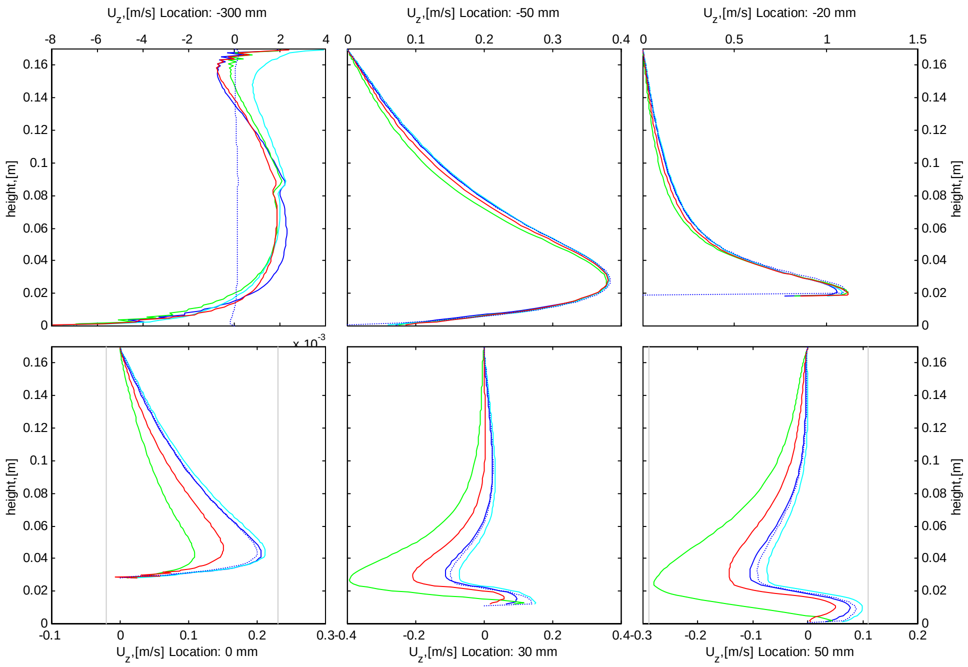

*Figure A.1: The charts show the vertical velocity of the first six profiles. The colour coding is: the k-l model(●), the k-ε model with the indirect wall function approach(●), the k-ε model(●) and the RSM(●). Dashed lines are reference values that correspond to the method of the colour they wear, (▲) are experimental values. The areas within grey lines are plotted and discussed in subsection 3.5.6.*

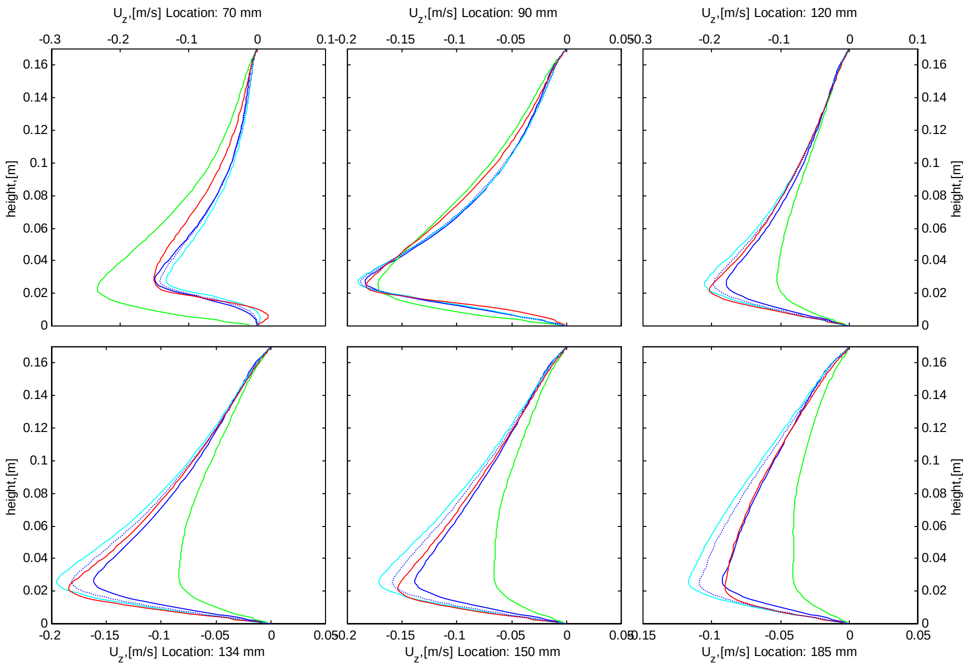

*Figure A.2: The charts show the vertical velocity of the last six profiles. The colour coding is: the k-l model(●), the k-ε model with the indirect wall function approach(●),the k-ε model(●) and the RSM(●). Dashed lines are reference values that correspond to the method of the colour they wear, (▲) are experimental values.*

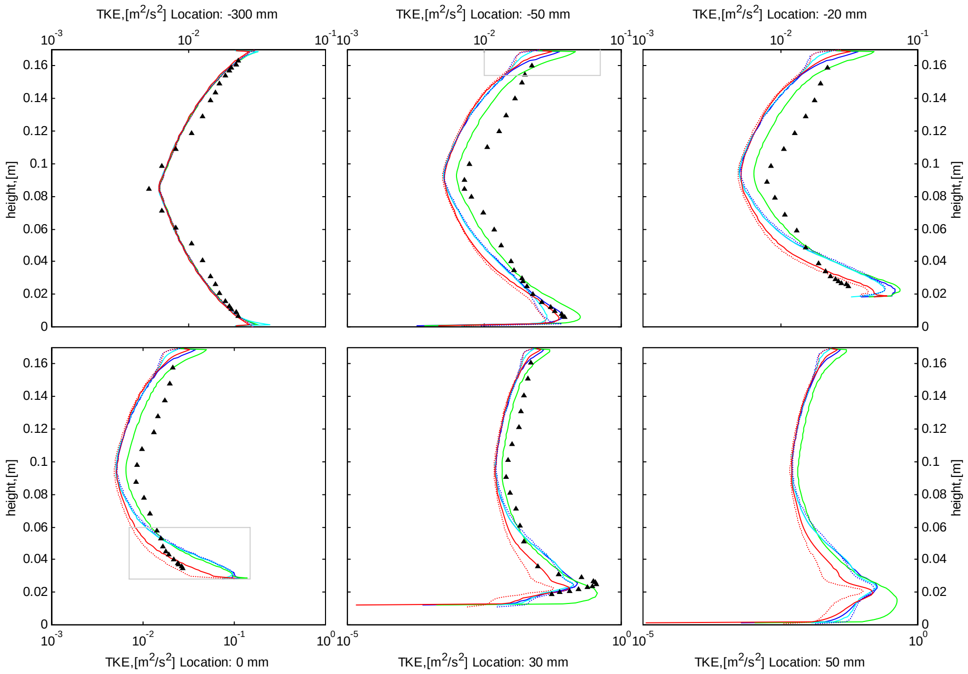

*Figure A.3: The charts show the turbulent kinetic energy k of the first six profiles. The colour coding is: the k-l model(●), the k-ε model with the indirect wall function approach(●), the k-ε model(●) and the RSM(●). Dashed lines are reference values that correspond to the method of the colour they wear, (▲) are experimental values. The areas within grey lines are plotted and discussed in subsection 3.5.6.*

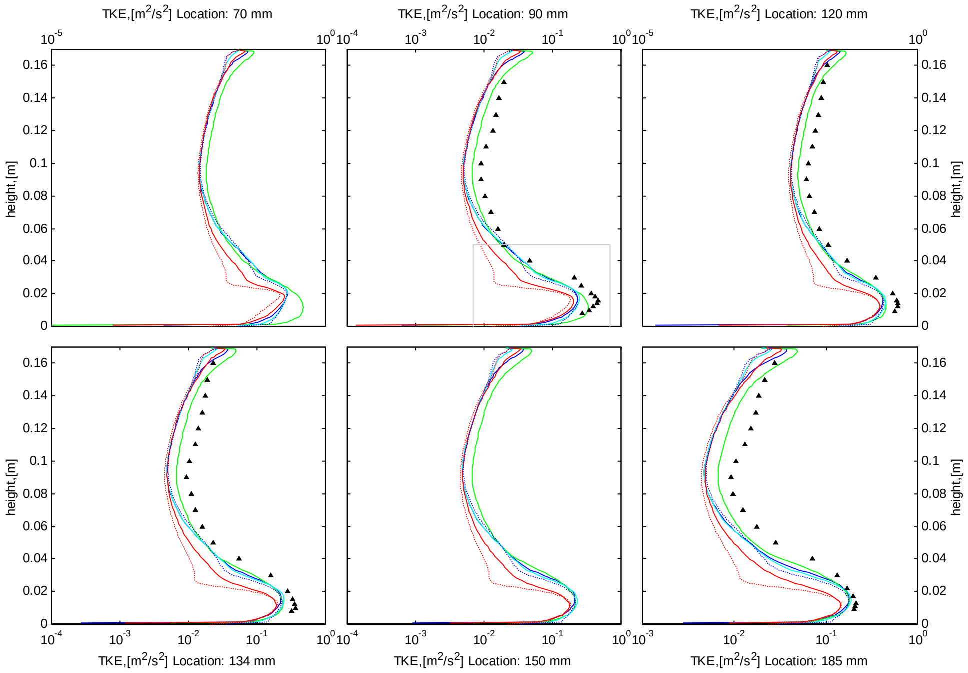

*Figure A.4: The charts show the turbulent kinetic energy k of the last six profiles. The colour coding is: the k-l model(●), the k-ε model with the indirect wall function approach(●), the k-ε model(●) and the RSM(●). Dashed lines are reference values that correspond to the method of the colour they wear, (▲) are experimental values. The area within grey lines is plotted and discussed in subsection 3.5.6.*

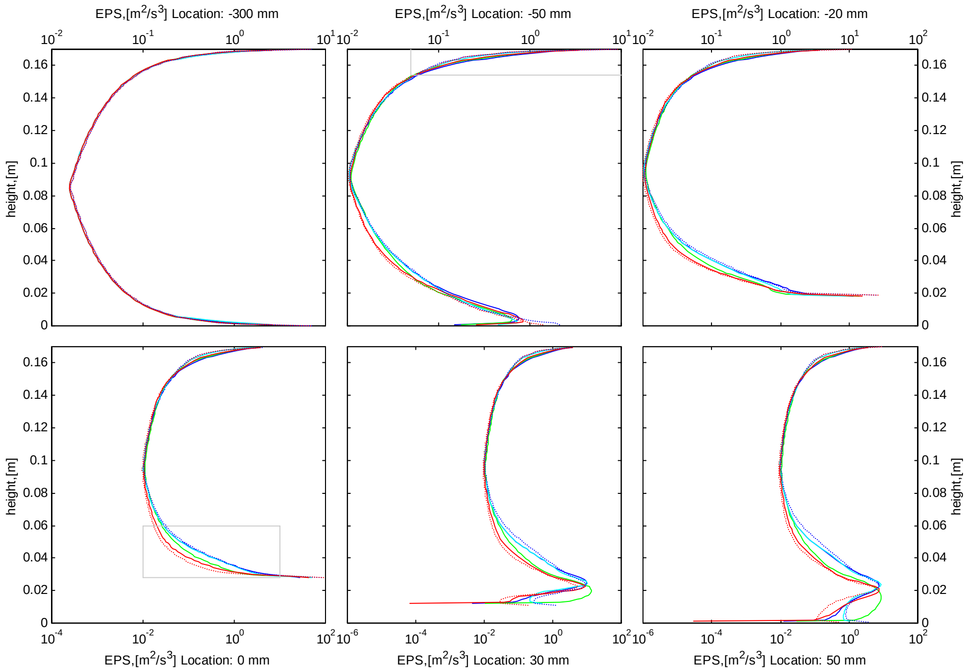

*Figure A.5: The charts show the dissipation rate ε of the turbulent kinetic energy of the first six profiles. The colour coding is: the k-l model(●), the k-ε model with the indirect wall function approach(●), the k-ε model(●) and the RSM(●). Dashed lines are reference values that correspond to the method of the colour they wear, (▲) are experimental values. The areas within grey lines are plotted and discussed in subsection 3.5.6.*

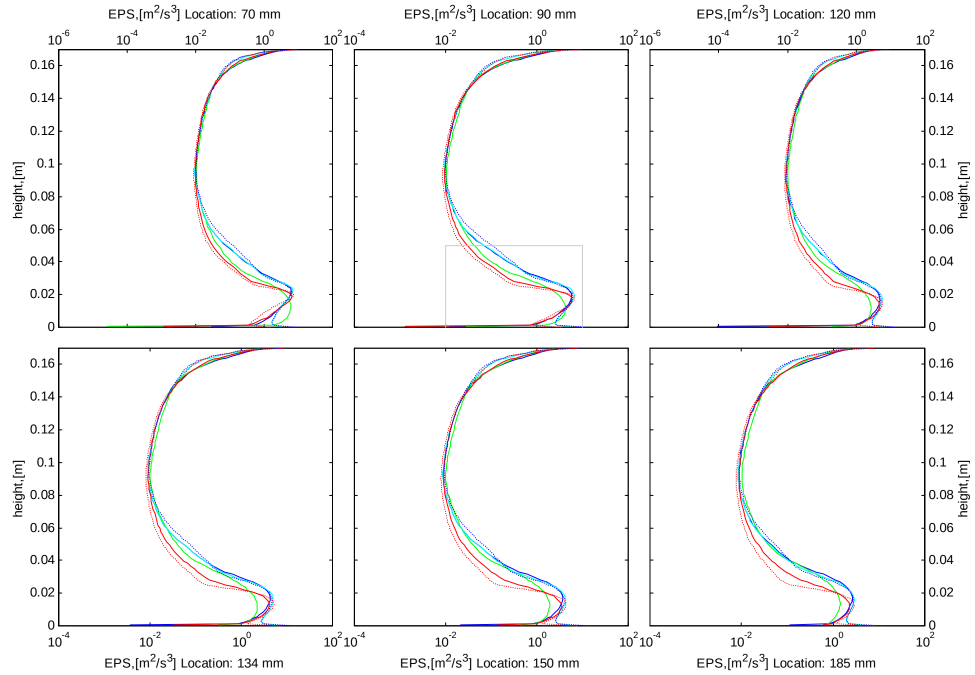

*Figure A.6: The charts show the dissipation rate ε of the turbulent kinetic energy of the first six profiles. The colour coding is: the k-l model(●), the k-ε model with the indirect wall function approach(●), the k-ε model(●) and the RSM(●). Dashed lines are reference values that correspond to the method of the colour they wear, (▲) are experimental values. The area within grey lines is plotted and discussed in subsection 3.5.6.*

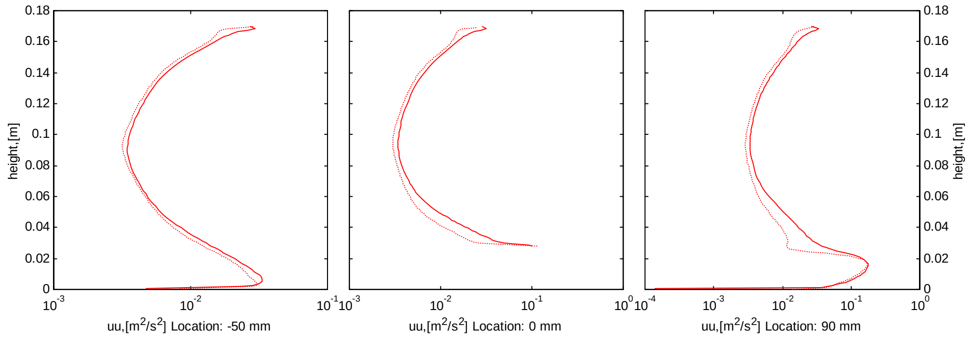

*Figure A.7: The charts show the Reynolds stress $\overline{uu}$ of the profiles at –50mm, 0mm and 90mm. Solid line is the RSM results and dashed line is the RSM reference values.*

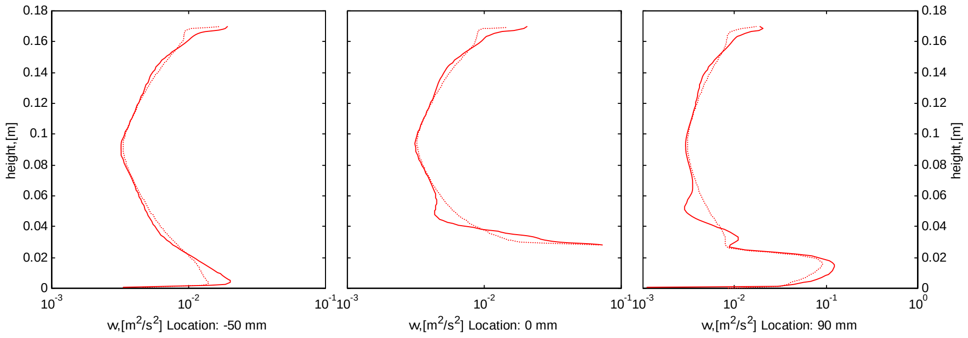

*Figure A.8: The charts show the Reynolds stress $\overline{vv}$ of the profiles at –50mm, 0mm and 90mm. Solid line is the RSM results and dashed line is the RSM reference values. The reason for large spatial oscillations in this particular parameter is related to the fact that differential equations are solved for all other Reynolds stresses, and the turbulent kinetic energy k, while $\overline{vv}$ is calculated from $\overline{vv} = 2k - \overline{uu} - \overline{ww}$.*

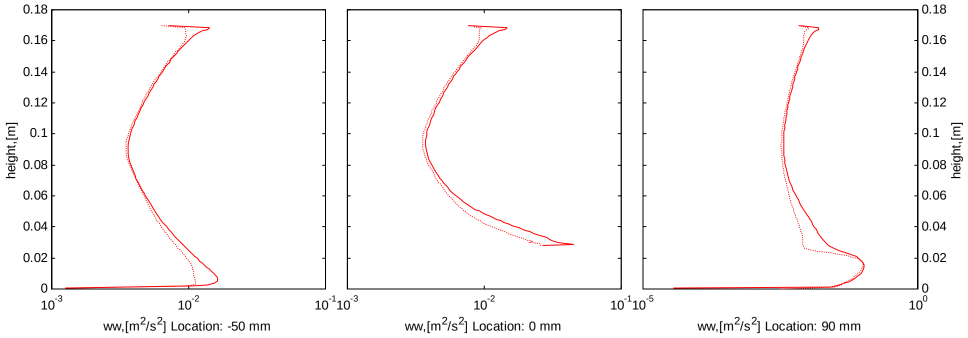

*Figure A.9: The charts show the Reynolds stress $\overline{ww}$ of the profiles at –50mm, 0mm and 90mm. Solid line is the RSM results and dashed line is the RSM reference values.*

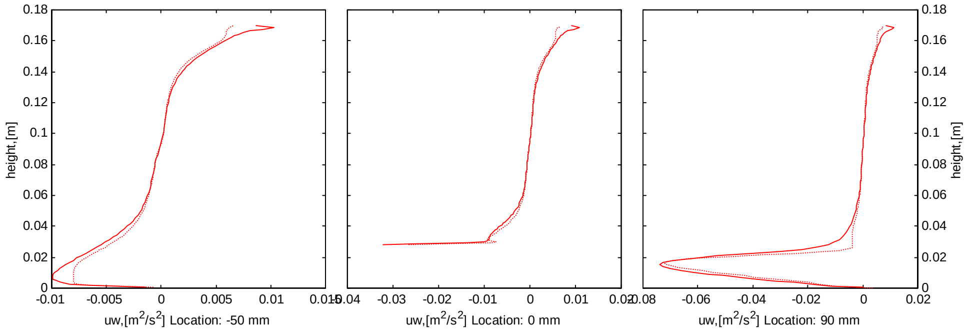

*Figure A.10: The charts show the Reynolds stress $\overline{uw}$ of the profiles at –50mm, 0mm and 90mm. Solid line is the RSM results and dashed line is the RSM reference values.*

# Appendix B

C18 results from simulations with the k-l turbulence model:

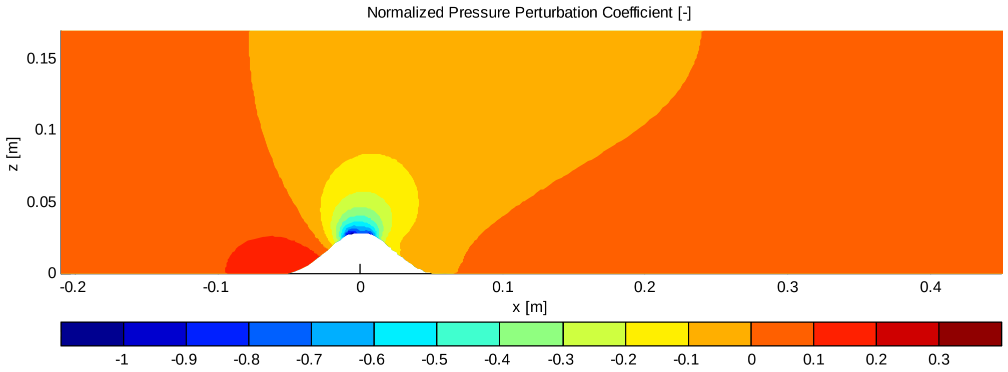

*Figure B.1: A filled contour plot of the effective pressure calculated with the k-l turbulence model.*

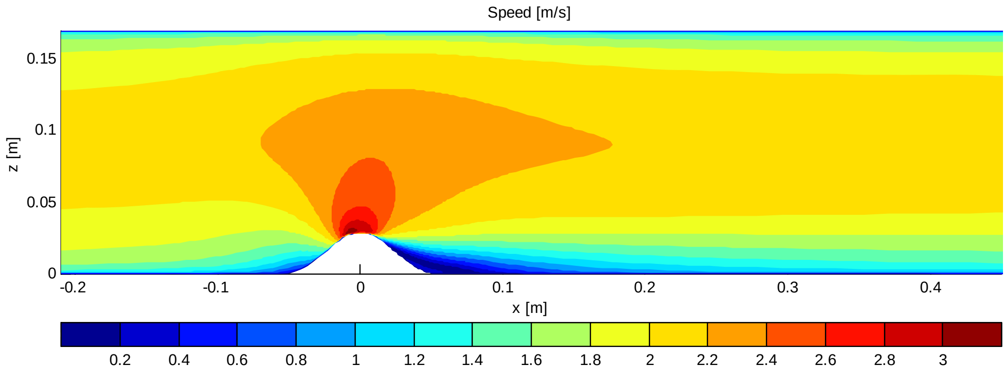

*Figure B.2: A filled contour plot of the absolute velocity calculated with the k-l turbulence model.*

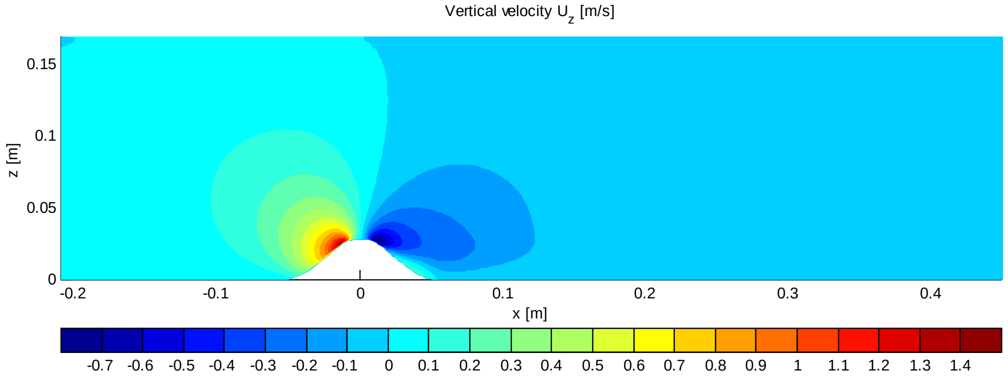

*Figure B.3: A filled contour plot of the vertical velocity calculated with the k-l turbulence model.*

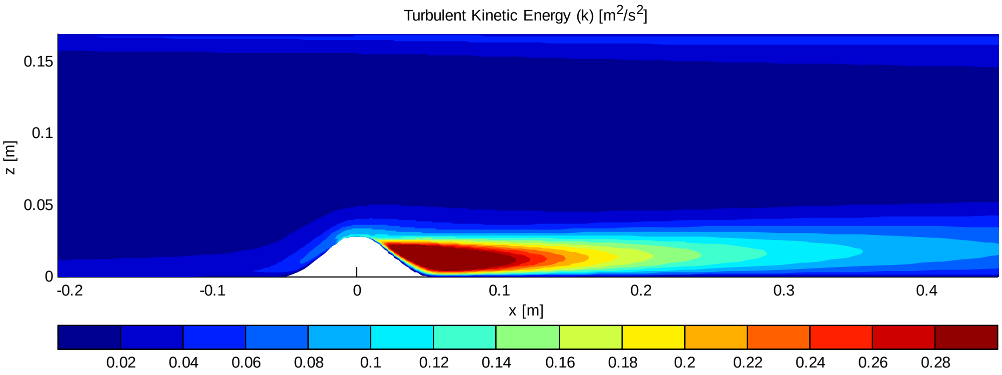

*Figure B.4: A filled contour plot of the turbulent kinetic energy k calculated with the k-l turbulence model.*

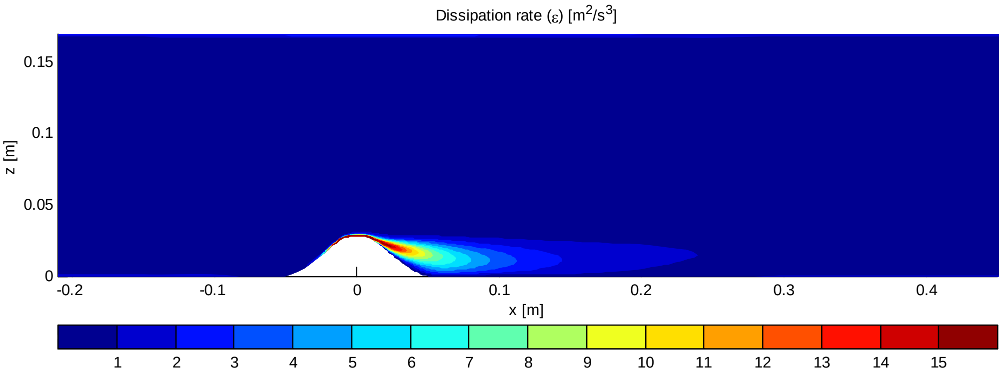

*Figure B.5: A filled contour plot of the dissipation rate ε of the TKE calculated with the k-l turbulence model.*

C18 results from simulations with the k-ε turbulence model:

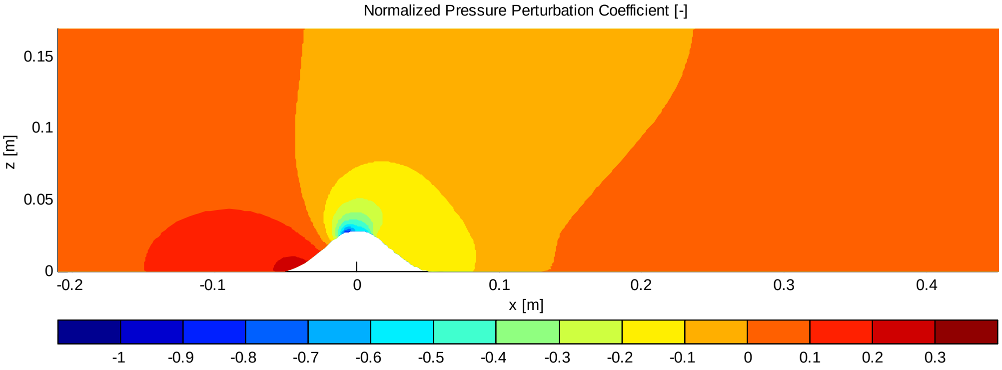

*Figure B.6: A filled contour plot of the effective pressure calculated with the k-ε turbulence model.*

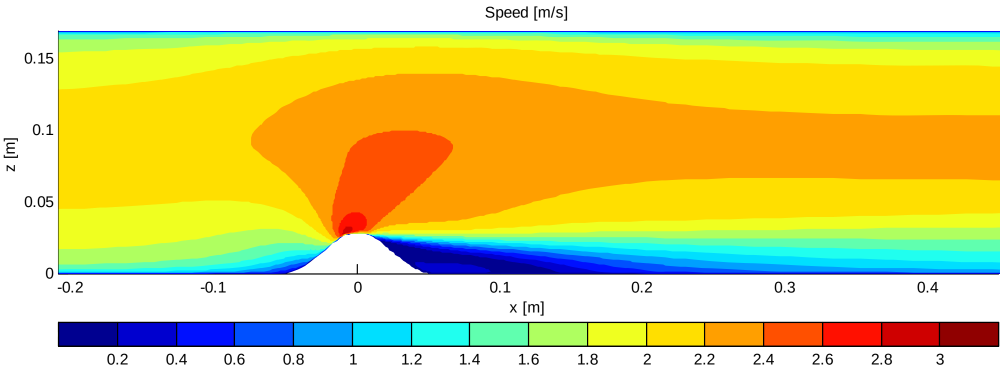

*Figure B.7: A filled contour plot of the absolute velocity calculated with the k-ε turbulence model.*

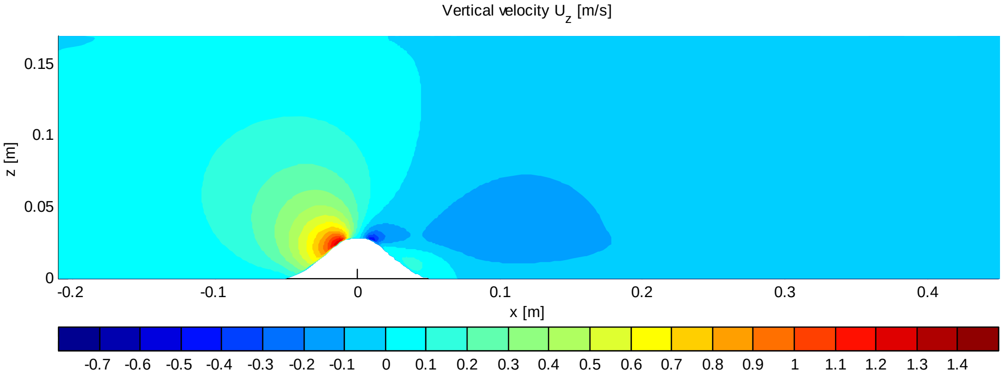

*Figure B.8: A filled contour plot of the vertical velocity calculated with the k-ε turbulence model.*

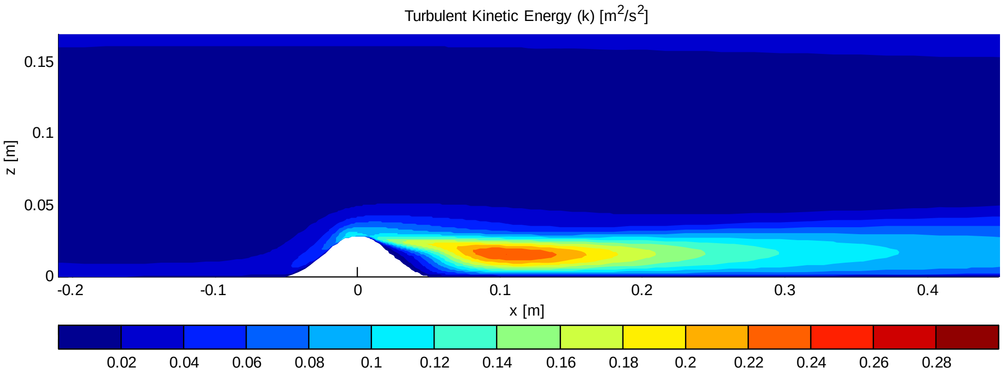

*Figure B.9: A filled contour plot of the turbulent kinetic energy k calculated with the k-ε turbulence model.*

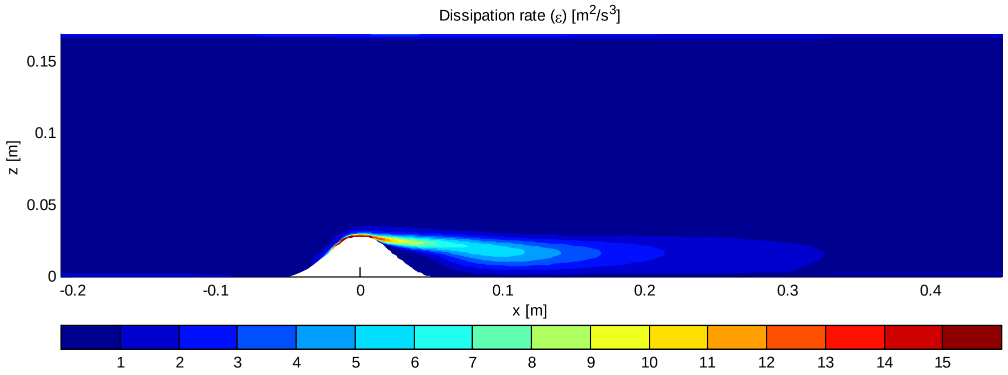

*Figure B.10: A filled contour plot of the dissipation rate ε of TKE calculated with the k-ε turbulence model.*

C18 results from simulations with the RSM:

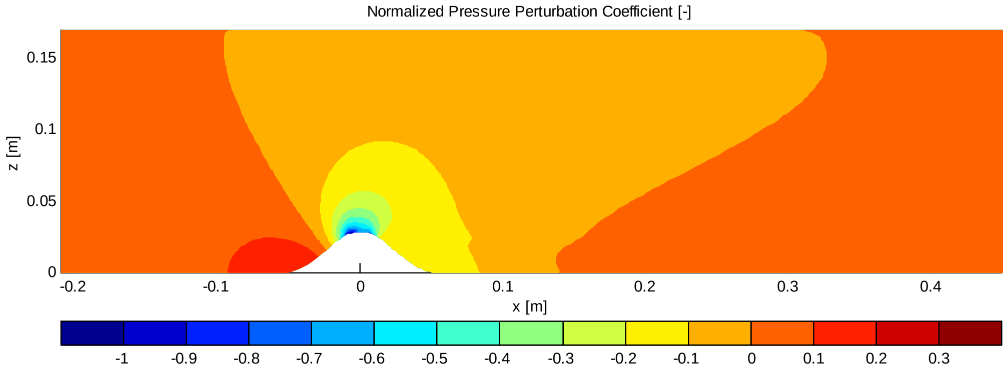

*Figure B.11: A filled contour plot of the effective pressure calculated with the RSM.*

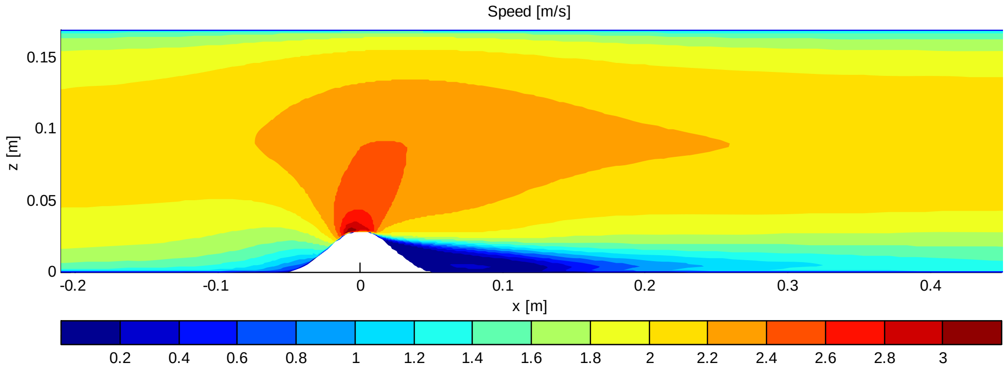

*Figure B.12: A filled contour plot of the absolute velocity calculated with the RSM.*

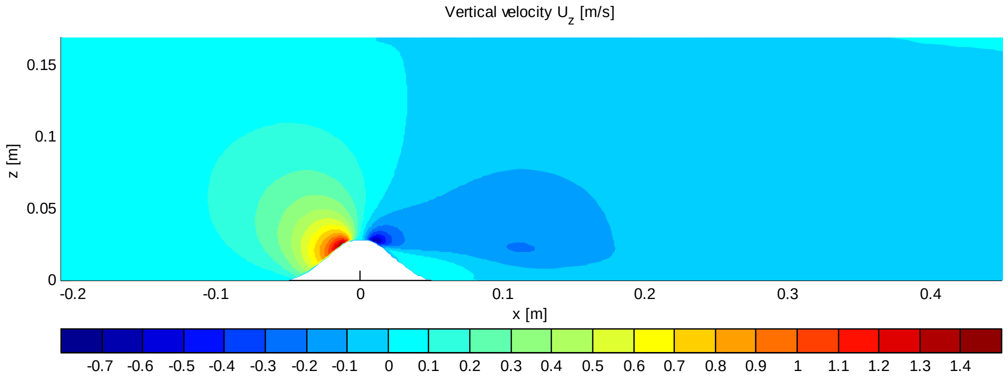

*Figure B.13: A filled contour plot of the vertical velocity calculated with the RSM.*

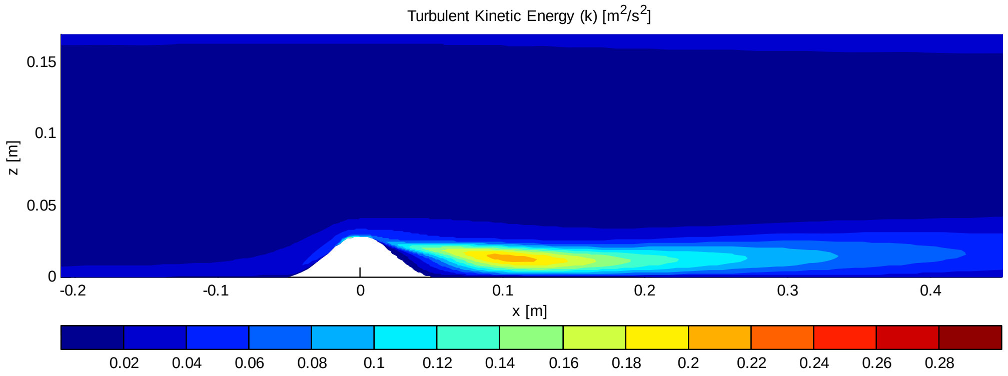

*Figure B.14: A filled contour plot of the turbulent kinetic energy calculated with the RSM.*

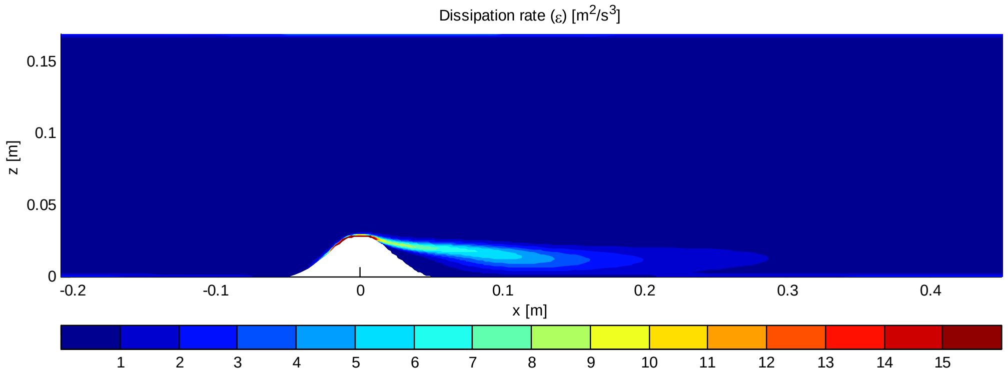

*Figure B.15: A filled contour plot of the dissipation rate ε of the TKE calculated with the RSM.*

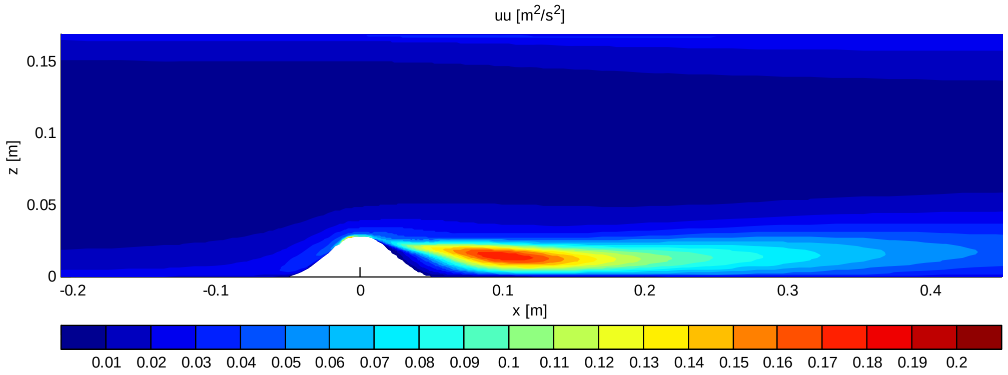

*Figure B.16: A filled contour plot of Reynolds stress* $\overline{uu}$ *calculated with the RSM.*

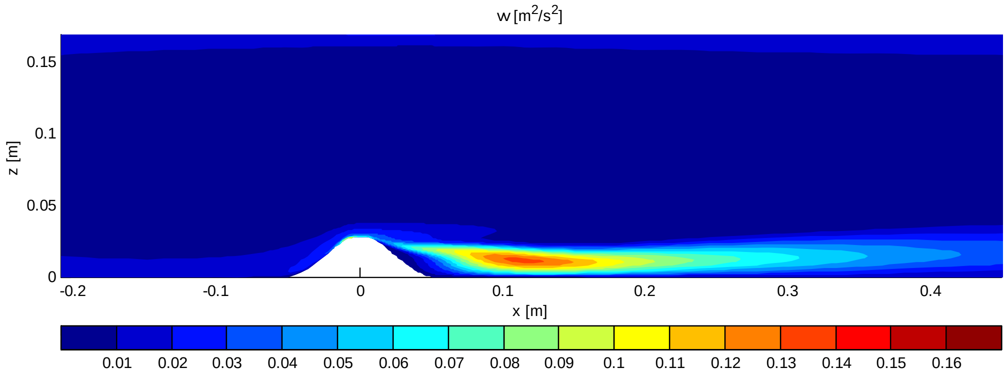

*Figure B.17: A filled contour plot of Reynolds stress* $\overline{vv}$ *calculated with the RSM.*

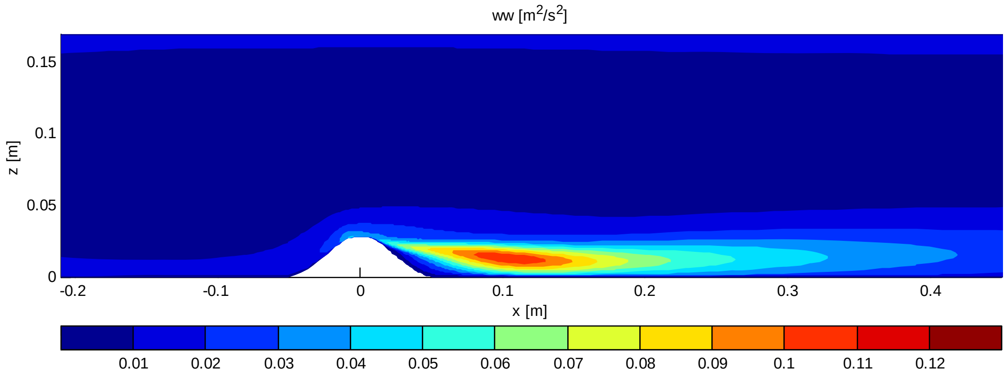

*Figure B.18: A filled contour plot of Reynolds stress* $\overline{ww}$ *calculated with the RSM.*

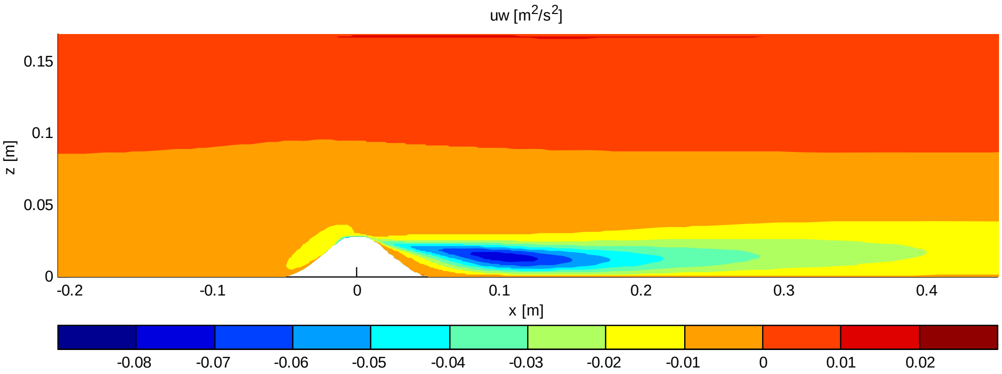

*Figure B.19: A filled contour plot of Reynolds stress* $\overline{uw}$ *calculated with the RSM.*

# Appendix C

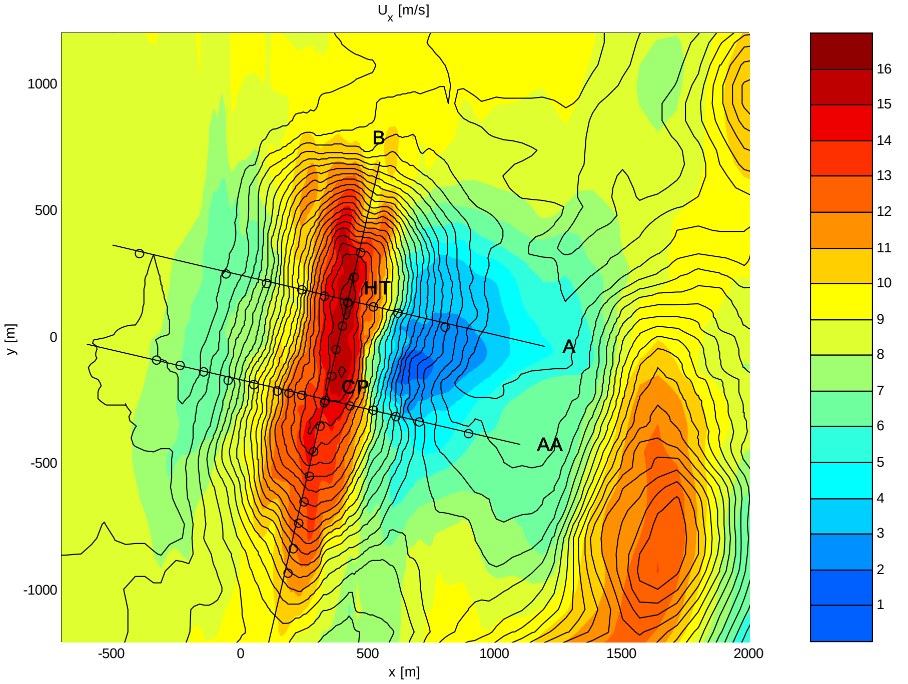

*Figure C.1: A filled contour plot of $U_x$ 10m agl. at Askervein calculated with 3DWind using the RNG turbulence model.*

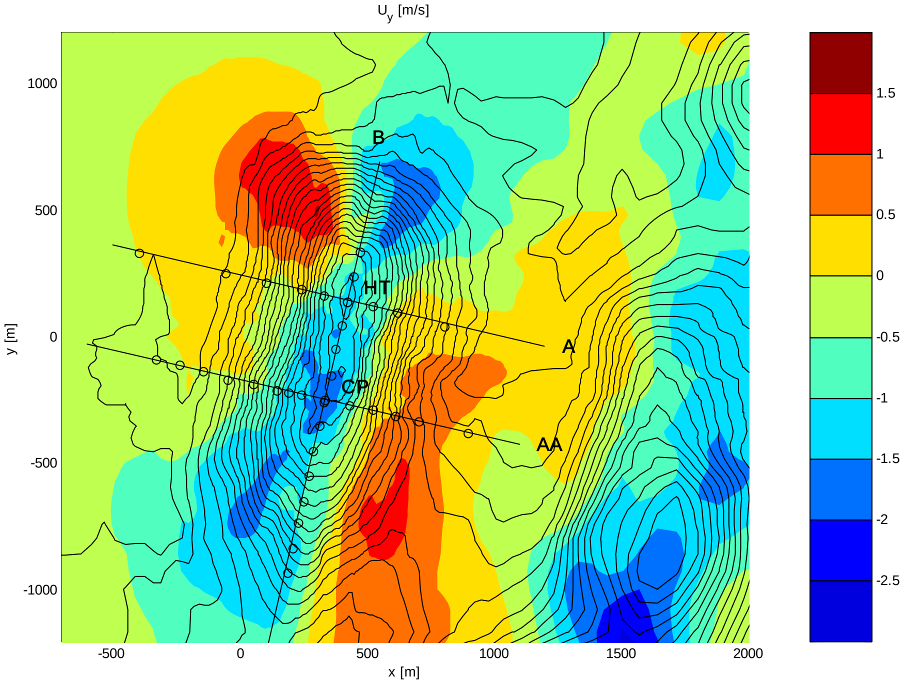

*Figure C.2: A filled contour plot of $U_y$ 10 m agl. at Askervein calculated with 3DWind using the RNG turbulence model.*

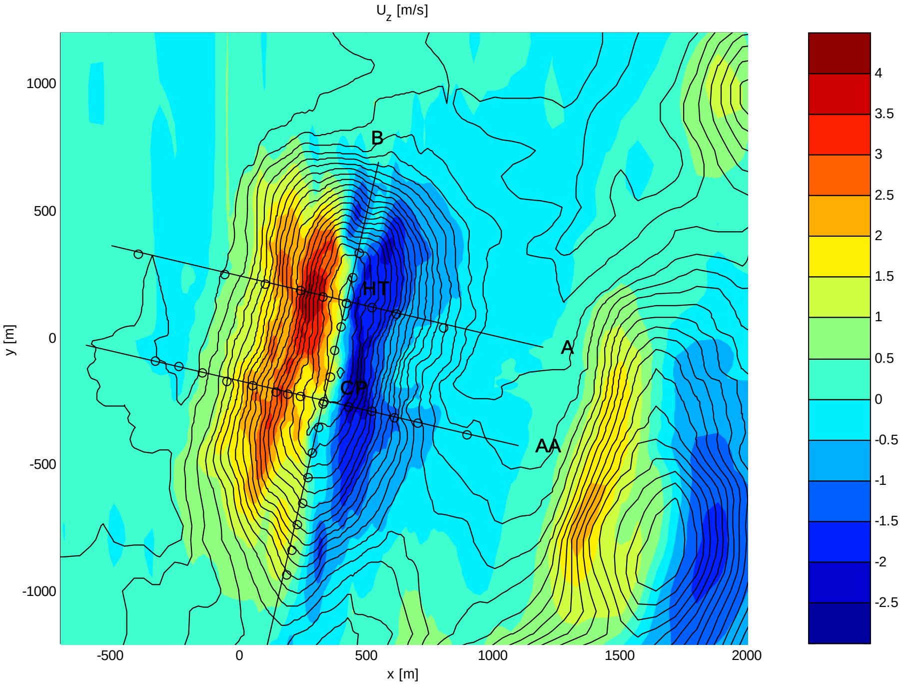

*Figure C.3: A filled contour plot of $U_z$ 10m agl. at Askervein calculated with 3DWind using the RNG turbulence model.*

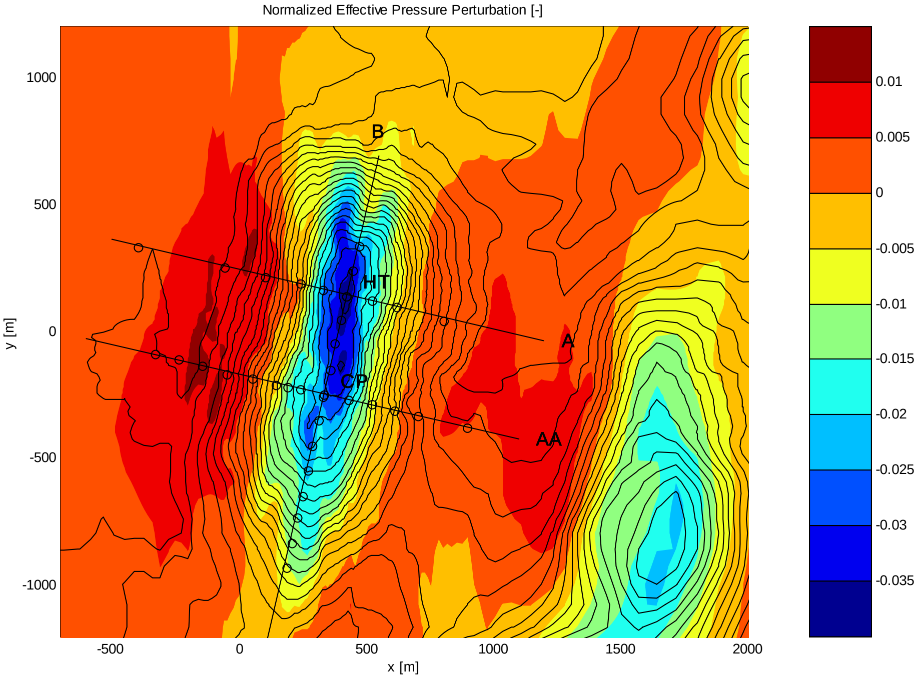

*Figure C.4: A filled contour plot of the effective pressure 10m agl. at Askervein calculated with 3DWind using the RNG turbulence model.*

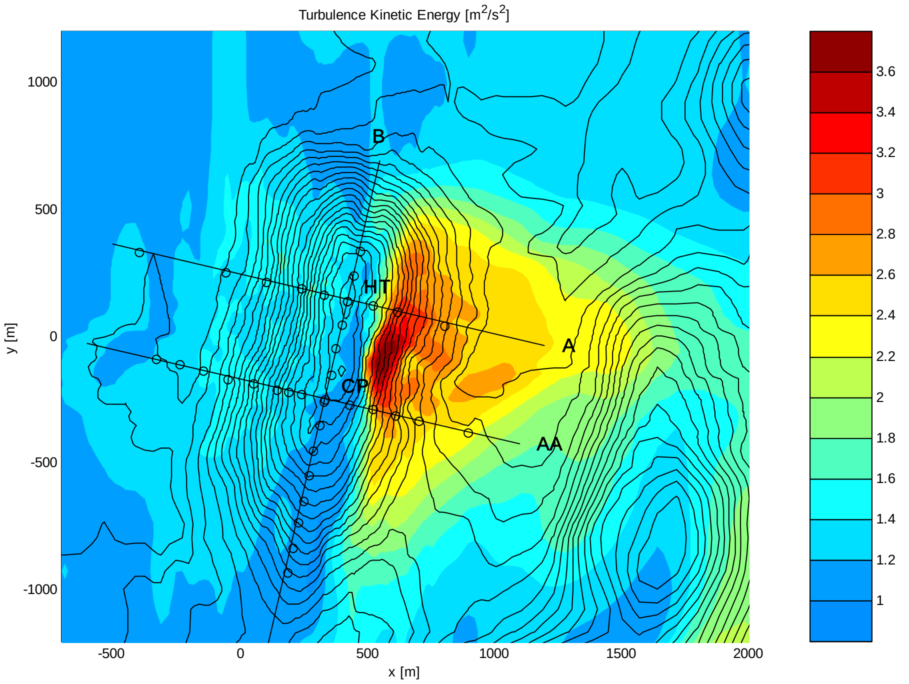

*Figure C.5: A filled contour plot of the turbulent kinetic energy 10m agl. at Askervein calculated with 3DWind using the RNG turbulence model.*

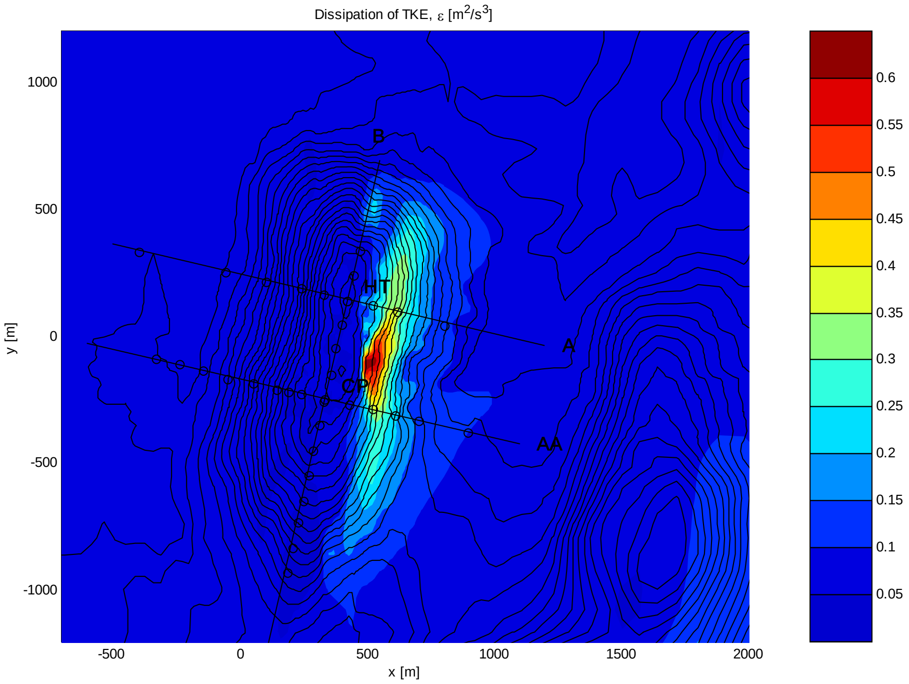

*Figure C.6: A filled contour plot of the dissipation of turbulent kinetic energy (ε) 10m agl. at Askervein calculated with 3DWind using the RNG turbulence model.*

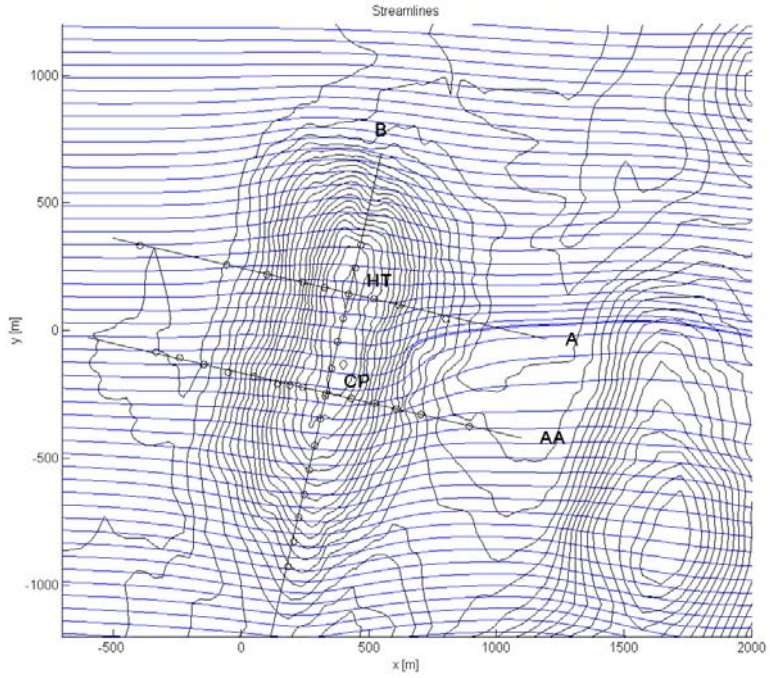

*Figure C.7: A streamline plot 1m agl. at Askervein calculated with 3DWind using the RNG turbulence model.*

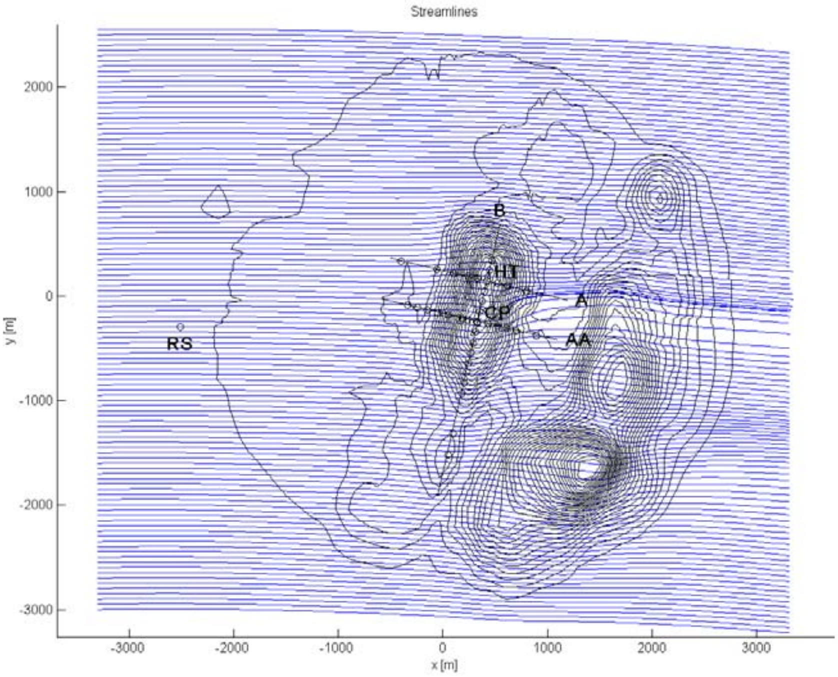

*Figure C.8: A streamline plot 1m agl. at Askervein calculated with 3DWind using the RNG turbulence model. The figure shows the wind flow direction difference between the inflow boundary and the outflow boundary caused by the Coriolis force.*

# Paper 2

## The Askervein hill case; Some new aspects

*Article submitted for journal publication*

# The Askervein hill case; Some new aspects

*O. Undheim*[1]*, H. I. Andersson*[2] *and E. Berge*[3]

[1] Institute for Energy Technology, IFE, Kjeller, [2] Dep Energy and Process Engineering, NTNU, Trondheim, [3] Kjeller Vindteknikk, KVT, Kjeller

## Abstract

The flow solver 3DWind is used to explore new aspects of the Askervein hill flow. Previous works have paid attention to dependencies concerning grid, inflow boundary profile, roughness and turbulence model, in addition to several different linear and non-linear models that have been validated by means of the Askervein hill case.

This analysis focuses on the flow dependency on the inflow direction and the contour intervals of the map, in addition to the regular grid dependence test. The horizontal resolution is found to be fine enough to cause only minor differences compared to a grid where every second node is removed. Still a vertical resolution dependence is encountered, and this is mainly attributed to the wall functions.

Simulations are performed where the wind directions at the reference station are 200°, 205°, 210° and 215°. The smallest direction biases compared to experimental values along a line through the hilltop are found from the directions 200° and 205°. The wind direction variation is also found to increase along the same line moving from 215° to 200° at the reference station. Still at 200° the veering is lower than found in the experimental results, and this is maybe caused by a slightly stable atmosphere.

The map contour interval dependence is found to be particularly high close to the ground on the top of the hill. This is where the speed-up is most important. The differences are decreasing with the height from the ground. At higher levels the speed-ups are smaller and caused by terrain formations with larger scales.

**Keywords**: Askervein hill, atmospheric flow, CFD, direction dependence, map contour interval dependence.

## 1 Introduction

The growing wind power installation and production cause an increased interest in wind flow simulation in wind farm areas. The globally installed wind power capacity increased by 20% during 2004, causing the totally installed capacity to be about 47GW at the end of 2004 (www.ewea.org, 2005). The new installations are often larger wind farms with larger turbines than earlier. Some wind farms have also been located in complex terrain and met with new difficulties caused by higher turbulence levels and a more complex flow field. The larger complexity in the flow field in the wind farm area puts increased demands on the flow modelling and the validation cases.

The Askervein hill case is a large full-scale atmospheric experiment describing relatively complex flow. This is a coastal site containing large speed-ups, roughness dependence and flow recirculation. The flow field have been analysed in detail. There are two reports (Taylor and Teunissen, 1983 and 1985) and three published articles describing the main field experiments and measurements (Taylor and Teunissen, 1987) (Mickle et al., 1988) (Salmon et al., 1988). Four different wind tunnel simulations have also been carried out in two wind tunnels (Teunissen et al., 1987), and a lot of wind flow solvers have been validated by means of the Askervein hill data (Beljaars et al., 1987) (Raithby et al., 1987) (Troen and Petersen, 1988) (Barnard, 1991) (Alm and Nygaard, 1995) (Ayotte, 1997) (Leroy and Gravdahl, 1999) (Kim and Patel, 2000) (Lopes, 2002) (Castro et al., 2003) (Chow and Street, 2004) (Eidsvik, 2004).

In the following we give an overview of results of earlier simulations related to the issues of this paper. One important issue is the comparison of linear and non-linear flow simulation methods. The Navier-Stokes equations contain a non-linear advection term, which is linearized in linear methods to reduce needed computational effort and complexity of the simulation. Raithby et al. (1987) performed the first non-linear simulation of the Askervein hill flow, and the results are compared with a mixed spectral finite difference model by Beljaars et al. (1987). The linear method was found to have a better spatial resolution at a much lower computational cost. This caused a better representation of topographical small-scale variations. On the other hand, the low velocities in the wake of the hill were not captured.

Walmsley and Taylor (1996) also compared linear and non-linear modelling results. One of the conclusions of their article was that linear models are sufficient in conjunction with wind power estimates, since they were performing well both upstream and on the hill summit. However, according to Castro et al. (2003), isolated hills are rarely found in nature and the poor prediction of the flow in the hill's lee-side may affect simulations of the flow around a second hill or a set of hills located further downstream.

This leads to the recirculation issue. At Askervein hill the flow separations tended to be three-dimensional in nature; low speed and high turbulence rather than displaying the reverse flow at the surface, which is typical of two-dimensional separation (Teunissen et al., 1987). The separated region is very sensitive to the presence of any sharp discontinuity in the terrain profile (Arya, 1988), and discontinuities are not present on the modelling scale. Wind tunnel simulations indicate that varying degree of flow separation is directly related to the nature of the roughness on the surface of the hill models (Teunissen et al., 1987). Due to this fact, the originally sought hill was one without flow separation. Still non-linear models are expected to give additional information compared to linear models, which are unable to predict recirculation. Kim and Patel (2000) found that the neighbouring hills behind the Askervein hill had a blocking effect, and therefore caused flow separation. A similar analysis of Castro et al. (2003) concluded that the nearby hills did not affect the flow either at the top or downstream of the Askervein hill.

Even though the non-linear 3D models predict low velocities in the wake of the hill, the turbulence levels in the wake of the hill are too low. This indicates that there is a non-stationary flow field generating turbulence in the wake of the hill (Raithby et al., 1987). Simulations that strengthen this theory have been carried out. Castro et al. (2003) found regular periodic behaviour with periods in the order 3-6min, and Chow and Street (2004) performed LES simulations, and found turbulence quantities at the right order in the wake of the hill.

The upstream velocity profile of Askervein hill has been discussed in different contexts. The shore is present one km west of the reference station, and the internal boundary layer developed over land is expected to be 90m high at the reference station (Mickle et al., 1988). A kink in the logarithmic profile is seen between 30m and 50m, but the profile above indicates an anomalously high roughness length (~1-3m) (Taylor and Teunissen, 1985). According to Mickle et al. (1988), this profile appear to be qualitatively compatible with theoretically predicted profiles for homogeneous terrain with $z_0$=0.03m under barotropic conditions with slightly stable stratification. Both Mickle et al. (1988) and Taylor and Teunissen (1985) concluded that coastal roughness-change effects are not evident and presume that stratification effects tend to mask them.

To account for this non-neutral profile, Ayotte (1997) used optimal control theory to achieve initial profiles that are both similar to the experimental mean velocity measurements in the entire PBL, and such that the mean and turbulent fields were in balance with almost no time dependency. Compared to a pure logarithmic profile, this initial profile gave better predictions of the velocity profiles at both the hilltop and the central point.

The majority of these approaches tend to underestimate the relative speed-up near the ground at the hilltop, even though the relative speed-up values are quite accurate at 10m (Beljaars et al., 1987) (Walmsley and Taylor, 1996) (Kim et al., 2000) (Castro et al., 2003). The only methods that perform quite well the lowermost 3-4m are the non-linear method described by Raithby et al. (1987) and the LES performed by Chow and Street (2004). But according to Castro et al. (2003), the results by Raithby et al. (1987) were fortuitous, and caused by a grid dependent wall function.

Underprediction near the ground was also found in the wind tunnel simulations, where the maximum speed-up was found about 3m above ground at the hilltop (Teunissen et al., 1987). This departs from theoretical considerations suggesting that the maximum speed-up should occur at the surface (Teunissen et al., 1987), which is in accordance with full-scale measurements. In the wind tunnel simulations this is explained by measurement errors very close to the surface of the terrain model (Teunissen et al., 1987).

Mickle et al. (1988) gave some possible reasons for the underprediction. It can be related to the representation of the topography in the model and the turbulence closure hypothesis. The slight stability and the departures of the observed upstream profile from the assumed logarithmic form are other possible causes. It can also be related to variations in the surface roughness of the hill; there is a suspicion that the hilltop area could have been slightly smoother than the upstream terrain. Some projects have performed simulations with decreased roughness on the top of the hill (Castro et al., 2003) (Undheim, 2005). This is seen to improve the relative speed-up profiles between the hilltop and the reference station.

Even though several aspects are treated in the simulations, measurements and discussions, there are still some aspects that need more thorough investigations. The sensitivity to the direction of the inflow wind is one such aspect which will be addressed in this article. Complex flow situations can cause rather large changes in the flow caused by a small wind direction change. Another interesting subject, not earlier evaluated, is the dependency on the available map contour interval. According to Castro et al. (2003), grid refinement causes both a reduced spatial discretization error and improved resolution of the topography, adding surface details that would be otherwise lost. If the grid resolution is finer than the available terrain information, improved resolution of the topography can be achieved by adding more terrain information.

## 2 Model description

The microscale model 3DWind (Alm and Nygaard, 1995) (Knauer and Nyhammer, 2002) (Undheim, 2003) (Undheim, 2005i and ii) solves the incompressible Reynolds Averaged Navier-Stokes equations (RANS), where the averaged mass balance is given by:

$$\frac{\partial U_i}{\partial x_i} = 0 \tag{4}$$

$U_1$, $U_2$ and $U_3$ are the time averaged velocity components. $U_1$ and $U_2$ are the horizontal components, and $U_3$ is the vertical component.

Averaged momentum equations are given by:

$$\frac{\partial U_1}{\partial t} + U_j \frac{\partial U_1}{\partial x_j} - \frac{\partial}{\partial x_j}\left( -\overline{u_1 u_j} + \nu_l \frac{\partial U_1}{\partial x_j} \right) + \frac{1}{\rho}\frac{\partial P}{\partial x_1} - fU_2 = 0 \tag{5}$$

$$\frac{\partial U_2}{\partial t} + U_j \frac{\partial U_2}{\partial x_j} - \frac{\partial}{\partial x_j}\left( -\overline{u_2 u_j} + \nu_l \frac{\partial U_2}{\partial x_j} \right) + \frac{1}{\rho}\frac{\partial P}{\partial x_2} + fU_1 = 0 \tag{6}$$

$$\frac{\partial U_3}{\partial t} + U_j \frac{\partial U_3}{\partial x_j} - \frac{\partial}{\partial x_j}\left( -\overline{u_3 u_j} + \nu_l \frac{\partial U_3}{\partial x_j} \right) + \frac{1}{\rho}\frac{\partial P}{\partial x_3} = 0 \tag{7}$$

where $u_1$, $u_2$ and $u_3$ are velocity fluctuations, $\nu_l$ is the kinematic viscosity, $P$ is the averaged pressure and $f$ is a factor that depends on the rotational speed of the reference frame. This term represents the Coriolis force. According to Taylor and Teunissen (1985) and Mickle et al. (1988) the Coriolis parameter $f$ at Askervein hill is $1.22 \cdot 10^{-4}$s$^{-1}$.

The correlations of the deviations from the mean wind speed $-\overline{u_i u_j}$ are called the Reynolds stresses or second moments. This is a second-order symmetrical tensor that must be parameterized to close the equations. In the eddy-viscosity assumption the Reynolds stresses are expressed by:

$$\overline{u_i u_j} = \frac{2}{3}k\delta_{ij} - \nu_T\left( \frac{\partial U_i}{\partial x_j} + \frac{\partial U_j}{\partial x_i} \right) \tag{8}$$

This is a first order closure (Versteeg and Malalasekera, 1995), where $\nu_T$ is the turbulent viscosity and $k$ is the turbulent kinetic energy. The turbulent quantities are obtained from the following equations:

$$\frac{Dk}{Dt} = \frac{\partial}{\partial x_m}\left(\frac{\nu_T}{\sigma_k}\frac{\partial k}{\partial x_m}\right) + 2\cdot\nu_T\cdot E_{ij}\cdot E_{ij} - \varepsilon \tag{9}$$

$$\frac{D\varepsilon}{Dt} = \frac{\partial}{\partial x_m}\left(\frac{\nu_T}{\sigma_\varepsilon}\frac{\partial \varepsilon}{\partial x_m}\right) + C_{1\varepsilon}\frac{\varepsilon}{k}2\nu_T E_{ij}\cdot E_{ij} - C_{2\varepsilon}\frac{\varepsilon^2}{k} \tag{10}$$

$$\nu_T = C_\mu \frac{k^2}{\varepsilon} \tag{11}$$

ε is the dissipation rate of the turbulent kinetic energy and $E_{ij}$ is the mean strain-rate tensor.

$$E_{ij} = \frac{1}{2}\left(\frac{\partial U_i}{\partial x_j} + \frac{\partial U_j}{\partial x_i}\right) \tag{12}$$

The RNG k-ε values of the constants in these equations are $C_\mu$=0.085, $\sigma_k$=0.7179, $\sigma_\varepsilon$=0.7179, $C_{1\varepsilon}$=1.42-$C_{1R}$ and $C_{2\varepsilon}$=1.68 (Kim and Patel, 2000) (Kim et al., 2000). $C_{1R}$ is defined according to Eqn.13, and $\eta$ in Eqn. 14.

$$C_{1R} = \frac{\eta\left(1 - \frac{\eta}{4.38}\right)}{\left(1 + 0.015\eta^3\right)} \tag{13}$$

$$\eta = \sqrt{2E_{ij}E_{ij}}\frac{k}{\varepsilon} \tag{14}$$

The 3D finite volume method (Versteeg and Malalasekera, 1995) is used in 3DWind. The solution domain is divided into a finite number of cubes in which the values inside each cube are assumed to be constant. The Reynolds Averaged Navier-Stokes equations describe the interaction between the cubes. This collection of cubes is called a mesh, and the grid generator Grid3d makes meshes for use in 3DWind. The meshes are non-orthogonal, terrain following and use grid cell stretching to focus the computational effort to areas of special interest.

The time integration is solved by a second order, explicit, three-stage Runge-Kutta method. Even though the time derivative is included in the equations, realistic transient solutions are not achievable with the model. This is caused by variable time step used to speed up the simulations, and the non-physical Chorin's method used to solve the pressure field (Chorin, 1967) (Hirsch, 1990).

# 3 Simulation

## 3.1 Experimental basis

Askervein hill is located at the southern end of the Outer Hebrides island chain. The hill is essentially elliptical in plan form with a 1 km minor axis, and a 2 km major axis. The case chosen in this analysis was measured 3 October 1983. This is a commonly used dataset, and is generally regarded as the "best" day for data collection of the entire campaign. There were steady, moderate-to-strong winds from 210˚ through most of the day, with an estimated surface geostrophic wind of 22m/s and direction 220º (Taylor and Teunissen, 1985 and 1987).

Computed results are compared to a mean flow run (MF03-D 1400-1700), a turbulence run (TU03-B 1400-1700) and a TALA kite run (TK03 1500-1700). In the mean flow run, measurements were collected by cup anemometers in 10m heights along the three lines A, AA and B (*Figure 1*). All values are relative speed-up factors normalised with the speed at the reference station RS, located about 3km west (upstream) of the hill.

Turbulence results from TU03-B were collected from 3-component propeller anemometers along line A. The turbulence run also contained vertical profiles at both the hilltop and the reference station. Corresponding results are available at 3m, 5m, 8m, 15m, 24m and 34m. The TALA kite run gives the simultaneous velocity at six different heights at the coast, about 1km west of the reference station. Measurement heights are 30m, 48m, 70m, 116m, 178m and 267m. The measurement technique calculates both the velocity and the height where the kite is flown based on the line force, the line angle and the line length. Reference calibration indicates an RMS error near 4% for the ten-minutes values (Taylor and Teunissen, 1985).

The mean wind speed at the reference station was 8.9m/s, and the near surface Richardson number for this period varies from –0.0038 to –0.011. The Richardson number is a dynamic stability parameter. Negative values correspond to instable stratification. Profiles derived from AIRsonde measurements in the heights 50-500m indicate a potential temperature gradient of about 2ºK/km. This indicates a weak stable stratification through the PBL as a whole and a slight instability at the surface (Taylor and Teunissen, 1985), still the approximation of neutrally stratified atmosphere seems to be fairly good ($|Ri|<0.015$) (Taylor and Teunissen, 1987).

The fact that the wind direction during a period will have some variation, also points to a need to perform simulations from nearby directions. This is particularly important in very complex sites, where a modest change in the flow field direction can alter the entire flow field in an area. The Askervein hill is quite regular, and no large effects are expected. Still the orientation of the wake and the valley following tendency might be influenced.

The direction measurements of the mean flow runs are grouped in 5º-groups, and the MF03-D direction is 210º according to Taylor and Teunissen (1987). The 10m mean flow direction value from the same period is 207º according to Table A1.5 in the report by Taylor and Teunissen (1985). The wind direction mean from the TALA kite run from the current period (TK03) was 205º. Direction measurements were also performed through the turbulence run TU03-B. The 10m mean wind direction measurements at RS were 207.9° according to tilted gill uvw anemometers, 207.3° from AES vertical gill uvw anemometers and 211° from sonic anemometers (Taylor and Teunissen, 1985). This is not contradictory, but confirms that the direction estimates contain uncertainty of the order 5°.

## 3.2 Grid

The grid used in the simulations highly influences the results. Both the grid resolution and accuracy of the terrain data are important. Grid A and grid B described by Walmsley and Taylor (1996) have been made available, but it was decided to establish a grid with the grid generator grid3d, which is a part of the modelling system. This is the grid generator used in other projects, and it is interesting to involve it in the validation process. This also made it possible to compare the effect of using 10m contour interval original in the Ordnance Survey map, to the same map digitized to 2m contour interval for the uppermost 80m of the hill, and in front and behind the hill according to *Figure 1*. This digitizing was done based on a detailed map presented in Taylor and Teunissen (1985), using the WAsP map editor.

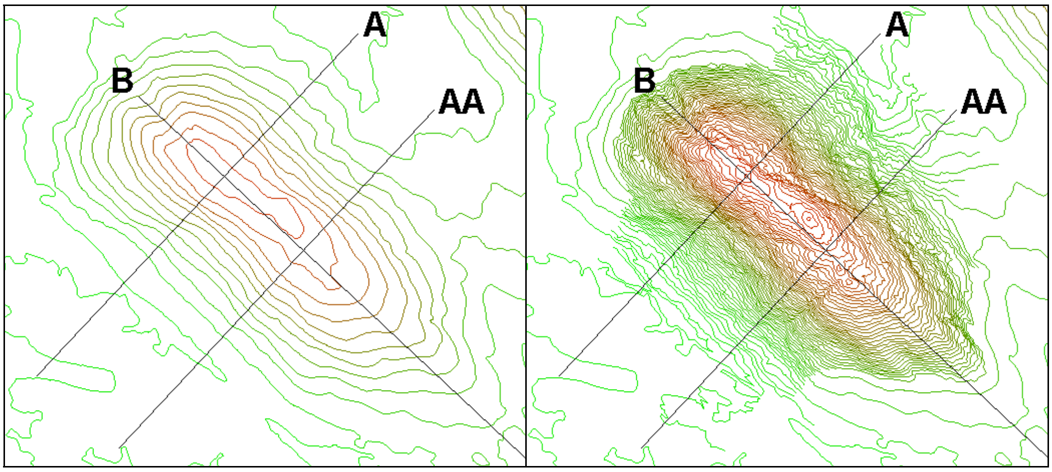

*Figure 1: Map information with 10m contours, and map information digitized manually from 2m contour map (Taylor and Teunissen, 1985).*

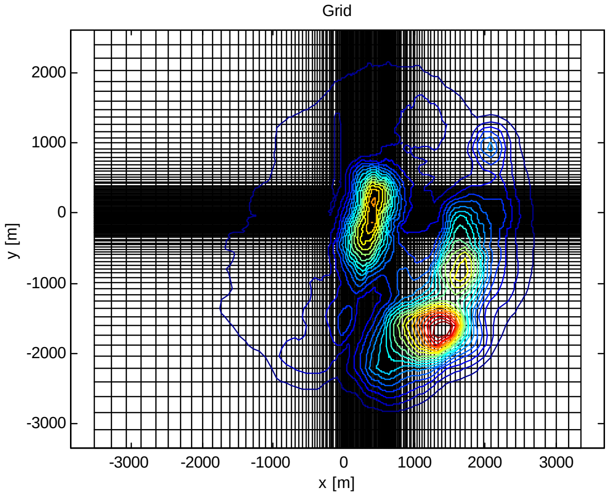

*Figure 2: The horizontal distribution of the grid cells used in the simulations.*

The simulation domain is chosen to include the neighbouring hills behind the Askervein hill, and the grid used in the simulations has a horizontal extension from 4km in front of the hilltop, to 3km behind the hilltop. The width of the domain is about 6km, and the height of the domain is 2000m. The horizontal distribution of the grid cells is visualized in *Figure 2*, and a 3D plot is given in *Figure 3*. The resolution in the centre is $\Delta x$=10m and $\Delta y$=12m. This is constant in a central square of 700mx500m, with a linear increase of 7% in the x-direction and 9% in the y-direction outside this square. The largest cell is 240m in the x-direction and 267m in the y-direction. The height of the first grid cell is 1.0m. With a vertical stretching of 12.1%, the largest vertical extension is 217m. The total amount of grid cells is 162x111x48.

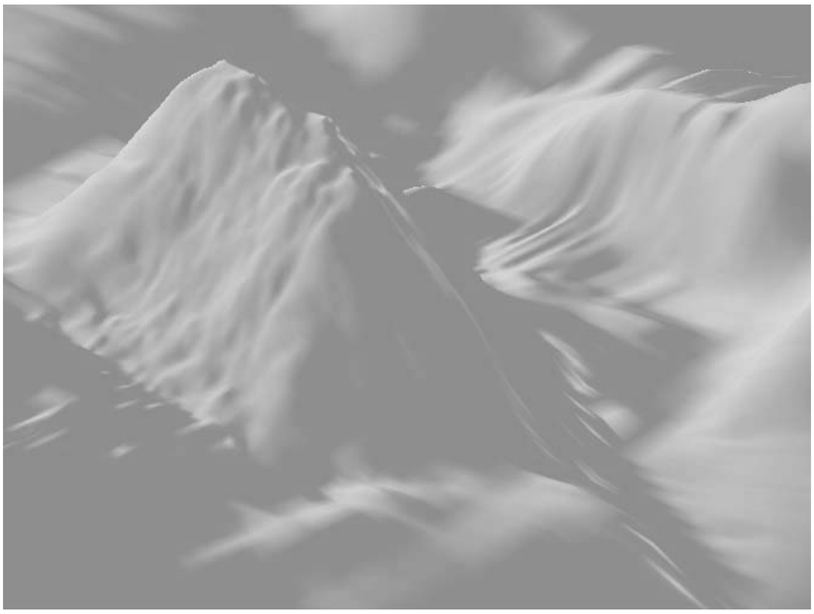

*Figure 3: The Askervein hill, a plot based on the terrain information from the fine grid. Terrain heights are multiplied by five to better show terrain details.*

The height information is first converted to .map format with the WAsP map editor, and the height of the lower vertices of the first cell is interpolated from the contours. The high frequency oscillations of wavelength 2*$\Delta x$ are then removed by a high frequency filter. The height is also gradually smoothed to zero from 2.3km to 3km from the centre of the simulation.

### 3.3 Initial and boundary conditions

A one-dimensional simulation is done to establish a profile over homogeneous conditions. With the roughness length $z_0$=0.03m and the velocity 17m/s in 2000m, the simulated velocity 10m above ground level becomes 8.95m/s. The Coriolis term is present in the equations, and causes 10° turning up to 530m and 20° turning up to 2000m. This profile is used as both inflow boundary condition and initial condition for the entire domain. At the side boundaries there are periodic boundary conditions, and at the outflow boundary there is a zero-gradient (i.e. Neumann) condition. The surface boundary condition is expressed by wall functions, connecting the velocity in the first cell to the roughness and the log law assumption. The top boundary is as a zero-gradient surface in all variables except the vertical velocity, which is defined not to allow any material transport through the boundary. This means a vertical velocity equal to zero at the top boundary.

From this basis, a converged solution is obtained after about 5000 iterations. This corresponds to about 120 hours on a 2.5 GHz processor. A residual smoothing algorithm is used in order to speed-up the simulation (Hirsh, 1990). This algorithm is switched off for the last 2000 iterations. An artificial viscosity term is also added to stabilize the simulation and to smooth the solution (Hirsh, 1990). This converged solution is the basis for further simulations to evaluate the wind inflow direction dependence and the map contour interval dependence.

# 4 Results

## 4.1 General results

Main results of this analysis are obtained from the grid denoted by “fine” in *Figures 4-10*. This is the grid described in the set up section. In order to evaluate the grid dependence of the solution, results are compared to three coarser grids. In the “coarse ij” grid, every second node is removed in the x and y direction in the horizontal plane. The vertical resolution is unchanged. In the “coarse k” grid, every second node is removed in the vertical direction (z), while the horizontal resolution remains unchanged. In the “coarse ijk” grid, every second node is removed in all three directions. This is done to separate grid dependences caused by the horizontal and the vertical resolution.

To evaluate the relative values of the velocity within the domain, the horizontal velocity is interpolated along the three lines A, AA and B. The simulated and measured values are normalized with the horizontal speed in 10m at the reference station. The normalized values are subtracted by one to give the relative speed-up factors caused by the hill. The plotted turbulence kinetic energy along line A is normalized by the squared horizontal speed in 10m at the reference station, while vertical turbulence intensity profiles are defined as: $TI = \sqrt{(4k/3)/(U_1^2 + U_2^2)}$.

Beljaars et al. (1987) argued that the linear methods had a better spatial resolution at a much lower computational cost compared to non-linear methods. This is still true, but with increased computer power, the non-linear 3D simulation in *Figures 4-5* is seen to have the same level of details as the linear simulation in the area ±500m from the hilltop and the centre point. This method is also able to capture the low velocities in the wake of the hill. With exception from estimating too low speed-up values in the wake of the hill along line AA, and the large difference from the points 300m and 500m from the hilltop along line B, the results seem to fit the experimental data very well, both quantitatively and qualitatively.

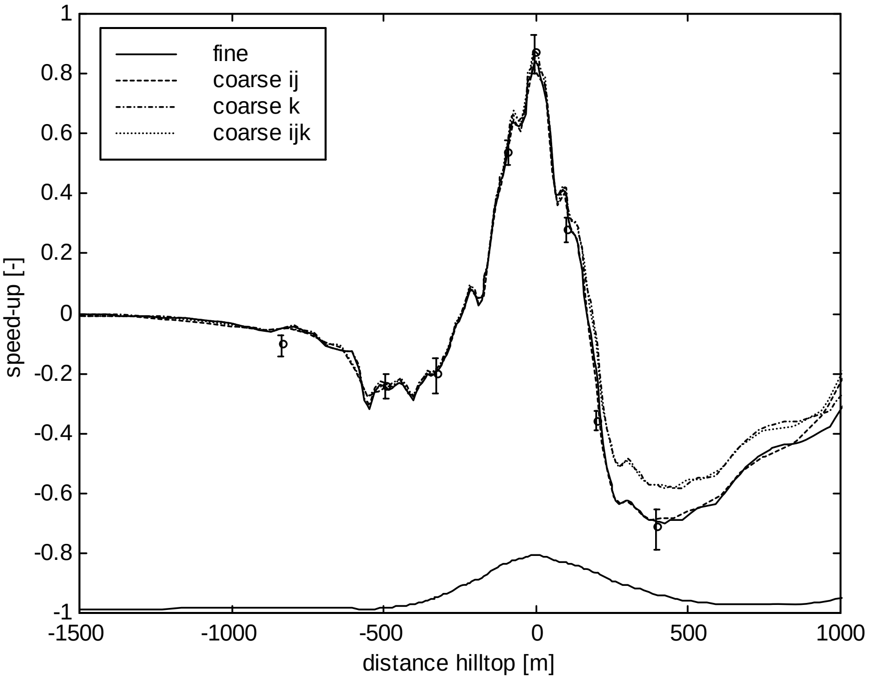

*Figure 4: A grid dependence comparison of relative speed-up along line A. Symbols are measurements with uncertainty limits (Taylor and Teunissen, 1985).*

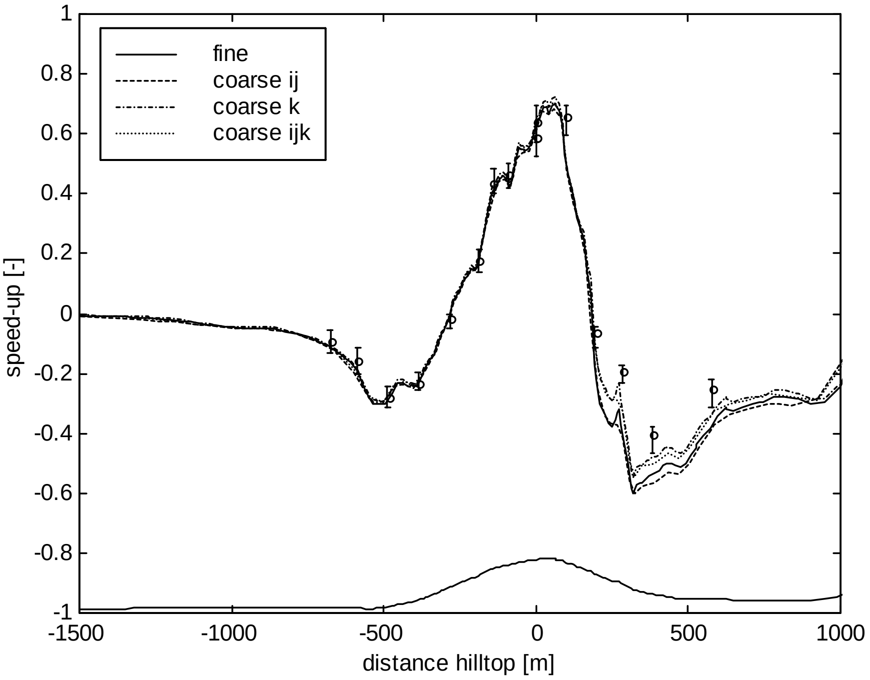

*Figure 5: A grid dependence comparison of relative speed-up along line AA. Symbols are measurements with uncertainty limits (Taylor and Teunissen, 1985).*

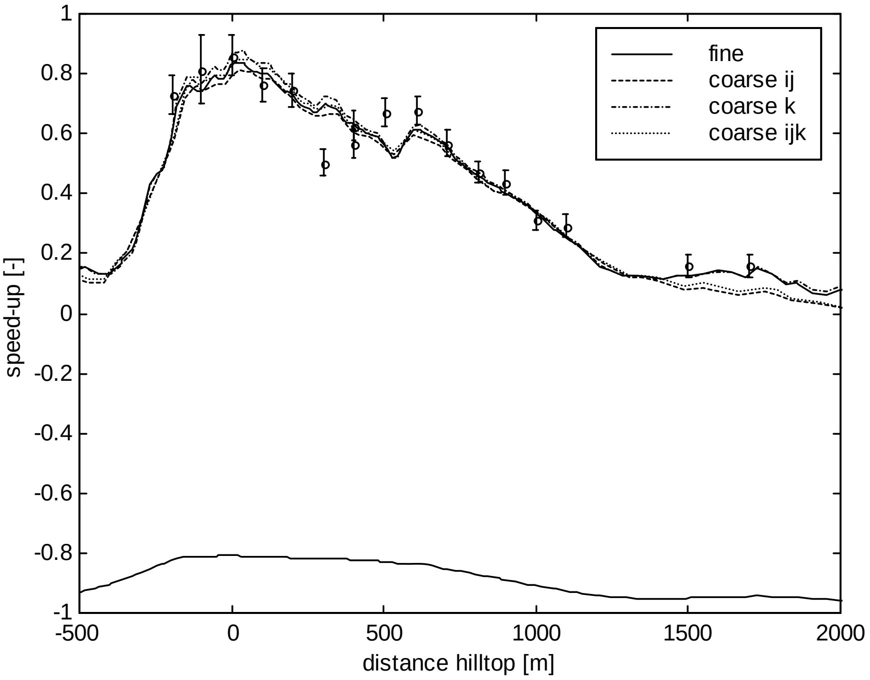

*Figure 6: A grid dependence comparison of relative speed-up along line B. Symbols are measurements with uncertainty limits (Taylor and Teunissen, 1985).*

*Figures 4-6* show that the largest grid dependence is caused by decreased vertical resolution. When the vertical resolution is decreased, the speed-up at the hilltop is slightly increased, and the speed-up behind the hill is higher. The ability to estimate the speed-up values at the two leftmost points at line B, is, on the other hand, related to the horizontal resolution. Good resolution causes the speed-up on this low hill to be captured.

Through the turbulence run TU03-B, also the direction, the vertical velocity and the turbulent kinetic energy were collected along line A. These results are compared with the simulation results from the four grid resolutions. According to Taylor and Teunissen (1985), the wind direction measurements from the TU runs at the hilltop are strongly suspected to have an alignment error. These measurements are therefore replaced by the direction data extracted from the HT Wind monitor strip chart.

*Figure 7* shows that the simulation results are not able to capture the large wind direction variation seen along line A. The four grids calculate almost identical estimates of the direction distribution. The mean direction also tends to be somewhat higher in the simulation results. This topic is further discussed in the subsection exploring the direction dependence.

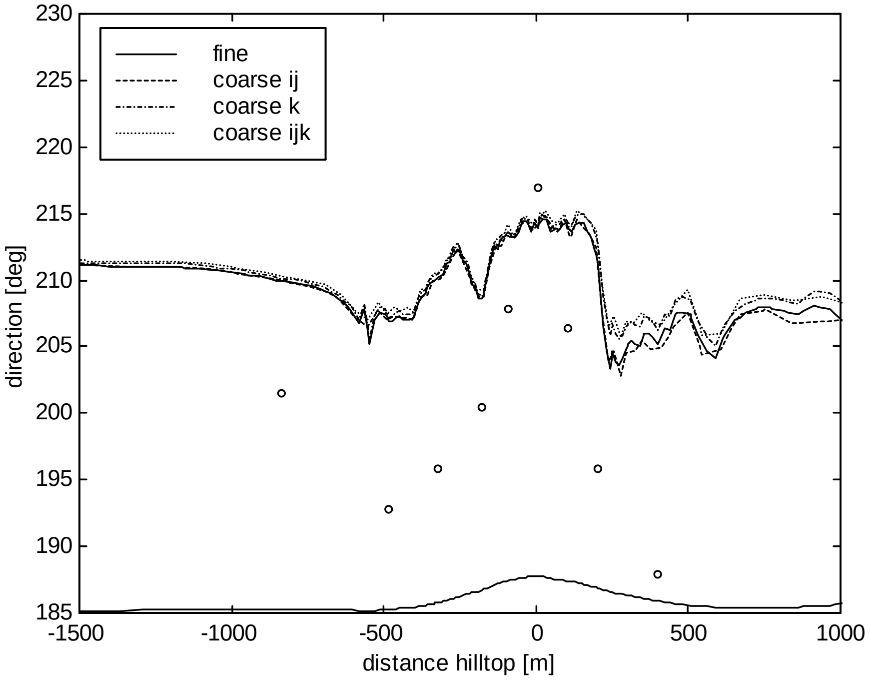

*Figure 7: A grid dependence comparison of direction distributions along line A. Symbols are measurements (Taylor and Teunissen, 1985).*

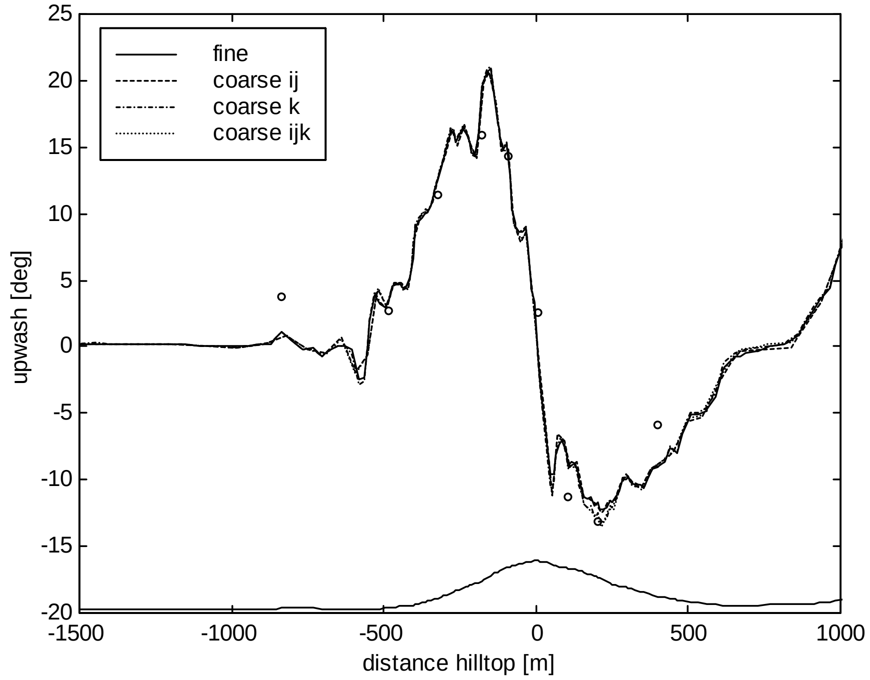

*Figure 8: A grid dependence comparison of the angles between the wind velocity and the horizontal plane along line A. Symbols are measurements (Taylor and Teunissen, 1985).*

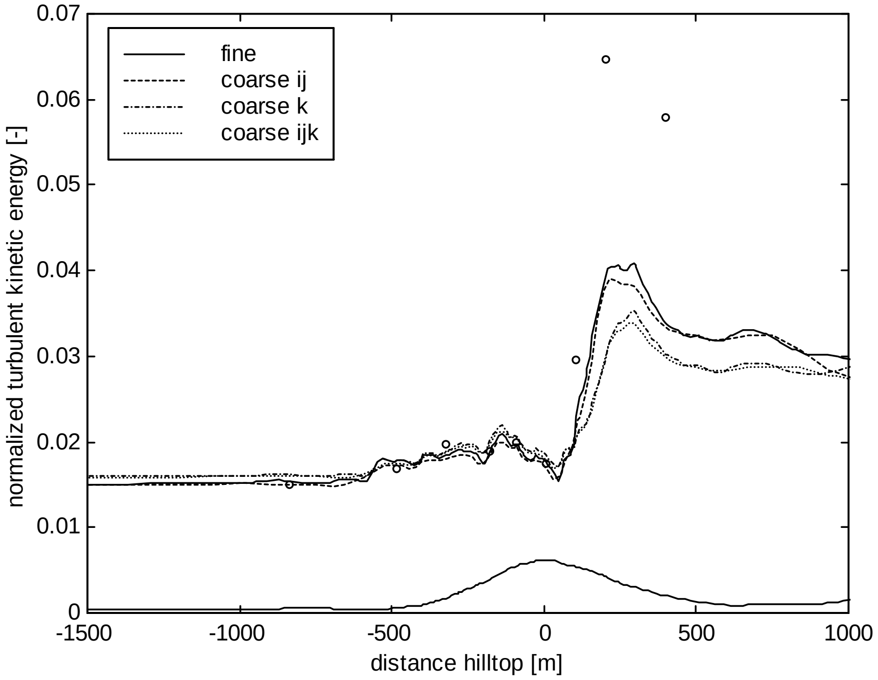

*Figure 9: A grid dependence comparison of the normalized turbulent kinetic energies along line A. Symbols are measurements (Taylor and Teunissen, 1985).*

The angles between the wind velocity and the horizontal plane follow the measurements quite accurately for all grids (*Figure 8*), while the model is seen to underestimate the turbulence levels in the wake of the hill (*Figure 9*). This is in accordance with other similar models (Raithby et al., 1987) (Kim and Patel, 2000) (Castro et al., 2003) (Eidsvik, 2004). Raithby et al. (1987) and Castro et al. (2003) found some higher turbulence values upstream of the hill. Kim and Patel (2000) related this to the turbulence closure with modified constants. These high upstream values are maybe one reason for turbulence values simulated by Castro et al. (2003) to be closer to experimental values in the wake. The fact that the turbulence in the wake from *Figure 9* is higer than corresponding results from Kim and Patel (2000), which used the same turbulence model, is maybe connected to different thickness of the first gridcell. Diminished vertical resolution tends to give a little larger turbulence upstream of the hill, but underestimates the turbulence in the wake of the hill some more than the high vertical resolution grids. Differences in the numerical diffusion may also explain the departure in the turbulence levels in the wake.

The results discussed above illustrate the CFD model's ability to predict wind variations in the horizontal plane. An aspect that also is important in the field of wind engineering is the model's ability to predict the vertical profiles within the area. Measurement profiles exist both at the hilltop and at the reference station. The simulated profiles of both the horizontal wind speed and the turbulence intensities are compared to these profiles.

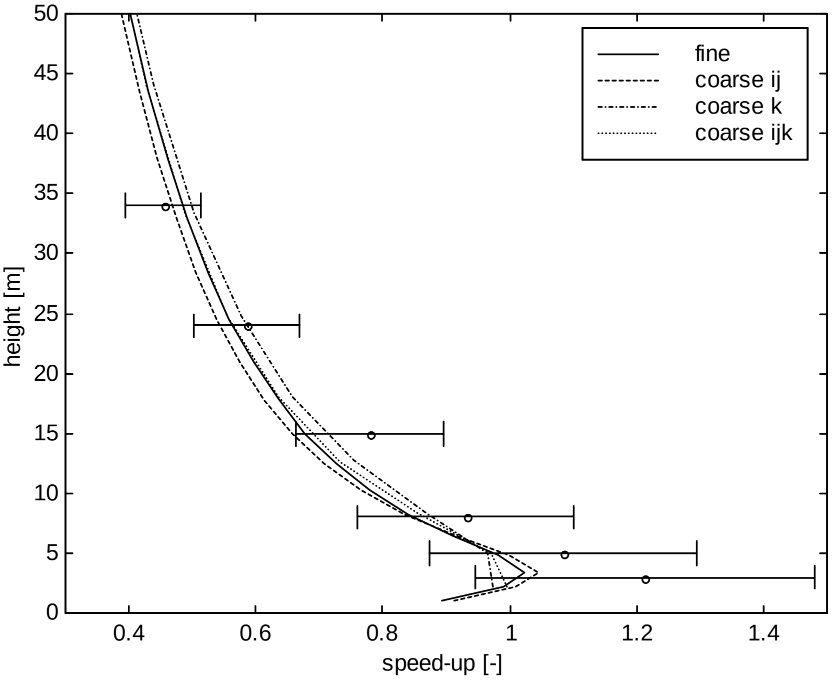

*Figure 10: A grid dependence comparison of the speed-up at the hilltop (HT) relative to the reference station (RS) in different heights above ground. Symbols are measurements with uncertainty limits (Taylor and Teunissen, 1985).*

From *Figure 10* it is seen that decreased resolution in the horizontal plane causes an underestimation above heights of about 7m and an overestimation below, compared to the fine grid. Decreased vertical resolution causes the opposite. These two effects are seen to align each other, and the results from the pure coarse grid are following the results from the fine grid quite well. Generally, all results are within the uncertainty limits, but there is a tendency to overpredict the speed-up above heights of about 30m, while an underprediction is seen below. In accordance with other simulation methods as discussed in the introduction, the maximum speed-ups are found at heights of about 3m and not at the surface.

The tendency to over and under predict the values above and below 30m and the tendency to underpredict the wind veering seen in *Figure 7*, could be connected to the slight stability discussed in the introduction. The atmosphere tends to avoid vertical motions, and this causes higher speed-up near the ground, and more of the flow passing around the hill rather than above. Another possible reason for the differences, that is indirectly dependent on the stability, is the inflow profile represented by the profile at the Reference station seen in *Figure 11.* Near the ground the profile is almost logarithmic, and there is good accordance between the measurements and the simulated results. But above 30m there is a kink, not present in the simulation results. Ayotte (1997) found improved results when the inflow profile was fitted to measurements.

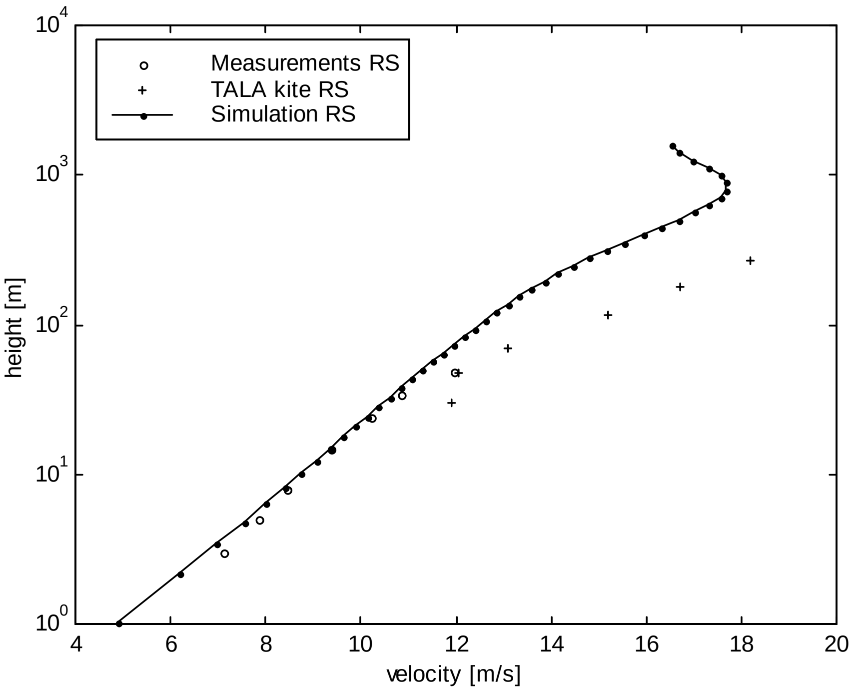

*Figure 11: Semi logarithmic plot of the horizontal velocity profile at the reference station (RS). ○ are measurements from met mast at RS, + are TALA kite measurements by the shore, 1km west of the reference station (Taylor and Teunissen, 1985). The results are from RNG k-ε simulation.*

The turbulence intensity profiles in *Figure 12* are found to depend on the vertical resolution. High resolution causes lower turbulence values, particularly near the ground. Compared to measurements, the turbulence profile at the reference station is quite accurate, while the turbulence profile at the hilltop follows the measurements near the ground and up to a minimum at about 5m. The measurements continue to decrease and have a minimum at about 15m. The difference is already present in the inflow profile. There are two possible explanations for this. One, the decreased amount of cells close to the ground increases the numerical diffusion and causes slightly decreased velocities and increased turbulence near the ground. The other is connected to the wall functions. They are found to be grid dependent, and might have a similar influence on the turbulence and the velocity.

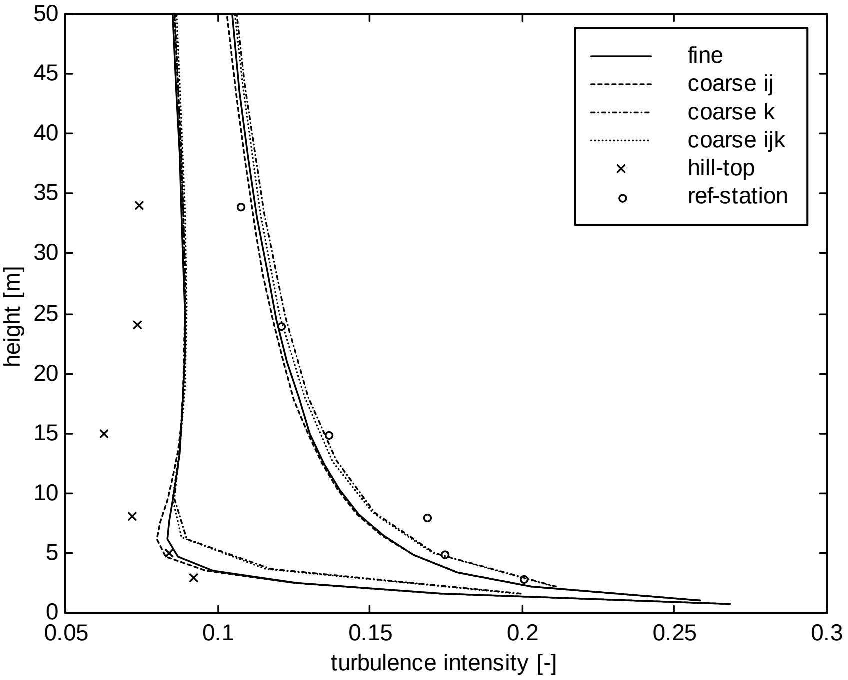

*Figure 12: A grid dependence comparison of the turbulence intensities with different meshes.* X *is the turbulence intensity measurements at the hilltop (HT) and* ○ *is the turbulence intensity measurements at the reference station (RS) (Taylor and Teunissen, 1985).*

## 4.2 Direction dependence

In order to evaluate the direction dependence, simulations are performed where the directions at the reference station are 200°, 205°, 210° and 215°. Streamline plots from 1m height agl. are plotted for the different directions in *Figure 13*. The direction comparisons show only minor differences between the different directions upstream of the hill, and at the hilltop (*Figures 14-15*). Behind the hilltop, there are increasing velocities downstream from the hill along line AA with decreasing inflow direction. Along line AA the best accordance with measurements is found in the 200° simulation. In the wake of the hill downstream along line A, the velocities are firstly slightly higher in the results from the 200° and 215° simulations, and best accordance with measurements are found from the 205° and 210° simulations. Further downstream the velocities increase faster in the results from the 200° and 205° simulations, and the highest values are found from these two directions. In this area there are no measurements to compare with the simulation results.

Flow from 200° yield the smallest slope when the air has to pass the hill (*Figure 13*). From *Figure 16* it is seen that this causes larger direction differences along line A, indicating a little more flow along the valley behind the hill as seen in *Figure 13*. These findings indicate that an inflow condition less perpendicular to the hill gives a reduced wake that is located closer to line A, causing the low values behind the hill along line AA to become a little higher, and closer to measurements. The profile along line A remains almost unchanged, but the less vertical inflow direction causes the speed-up to increase faster behind the wake along line A.

Along line A experimental values span from 188.1° to 217.1°. 217.1° is the hilltop value from the strip chart. This value replaces the original hilltop value of 203.4° (x in *Figure 16*), because of a strongly suspected alignment error (Taylor and Teunissen, 1985). This is mentioned to stress the uncertainty of this value. Simulation results show less turning at the uppermost part of the hill. This is maybe attributed to the stability, but also indicates that the real value was maybe somewhere in between the two values.

The simulations based on the 200° main direction give variations of 24.4° from the maximum angle at the hilltop to minimum angle in the wake. The corresponding values for 205°, 210° and 215° are 20.8°, 15.8° and 12.8°. For comparison, Raithby et. al (1987) and Lopes (2003) found about 17°, and Kim et. al (2000) about 25° direction differences. The LES simulations by Chow and Street (2004) gave variations from 13° to over 20°. These results have all a hilltop value of about 212°. This is somewhere in between the 200° and the 205° case, which had hilltop values of about 210° and 215°. According to *Figure 16*, the 200° and the 205° cases also have the least overall direction biases. This difference is probably partly caused by the Coriolis force, turning the wind between the reference station and the hilltop.

*Figure 17* shows that the normalized turbulence kinetic energies are almost identical, but directions 200° and 205° are seen to decrease faster in the wake. *Figure 18* shows that the speed-up profiles from directions 200° and 205° at the hilltop generally have a little lower values than corresponding profiles from 210° and 215°.

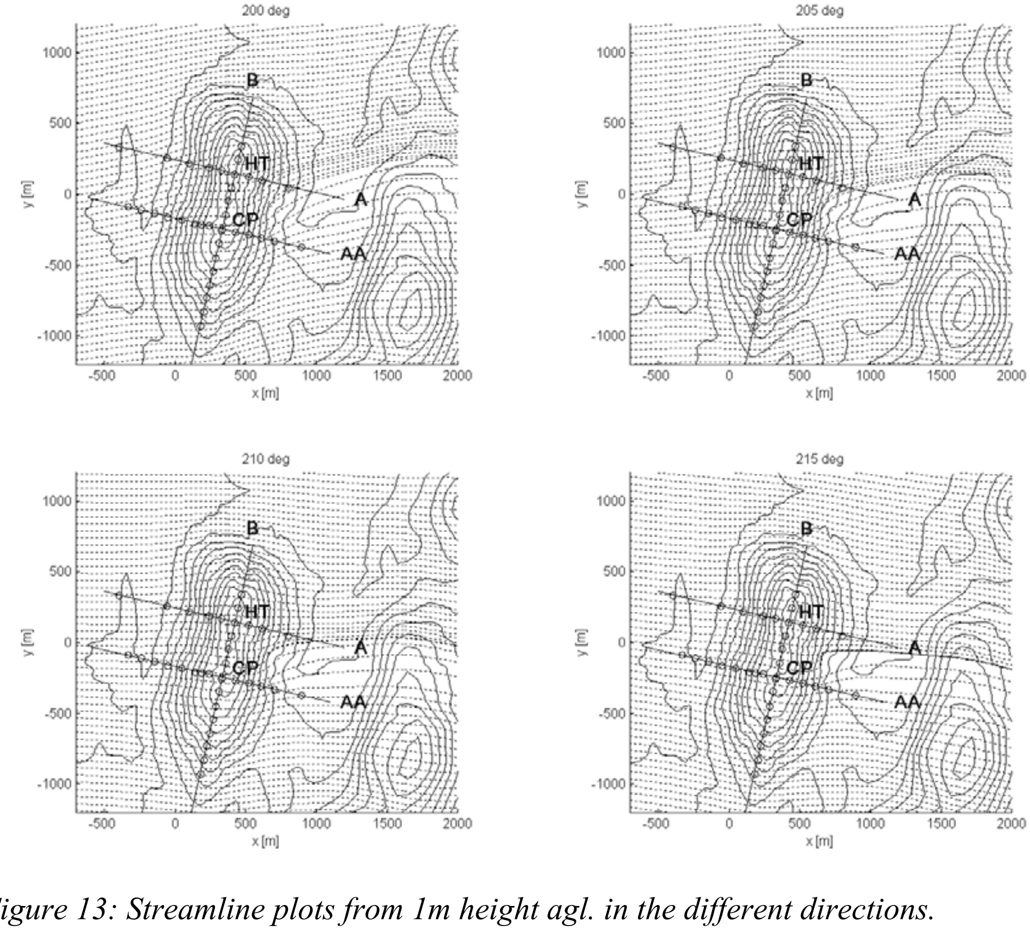

*Figure 13: Streamline plots from 1m height agl. in the different directions.*

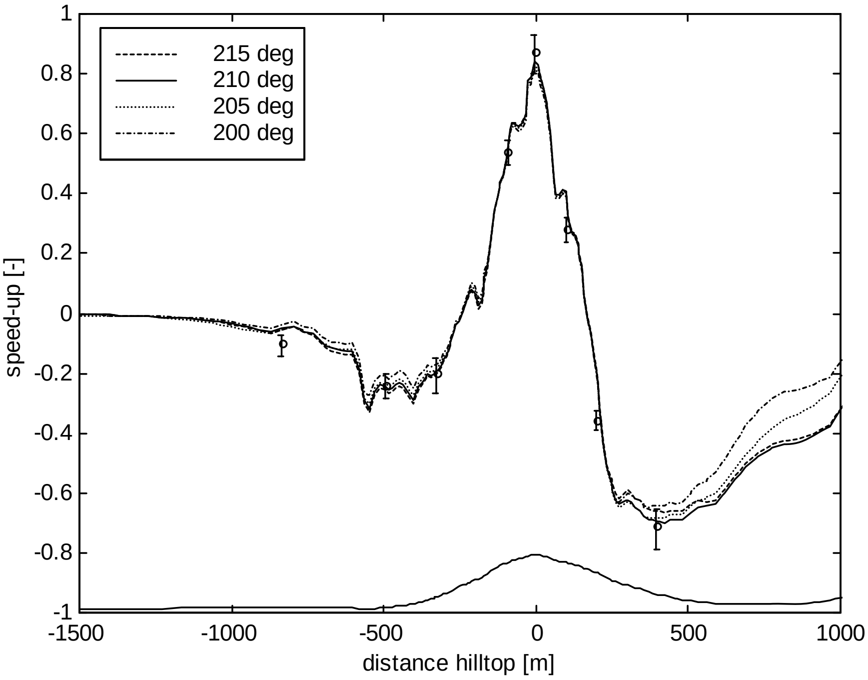

*Figure 14: A direction dependence comparison of relative speed-up along line A. Symbols are measurements with uncertainty limits (Taylor and Teunissen, 1985).*

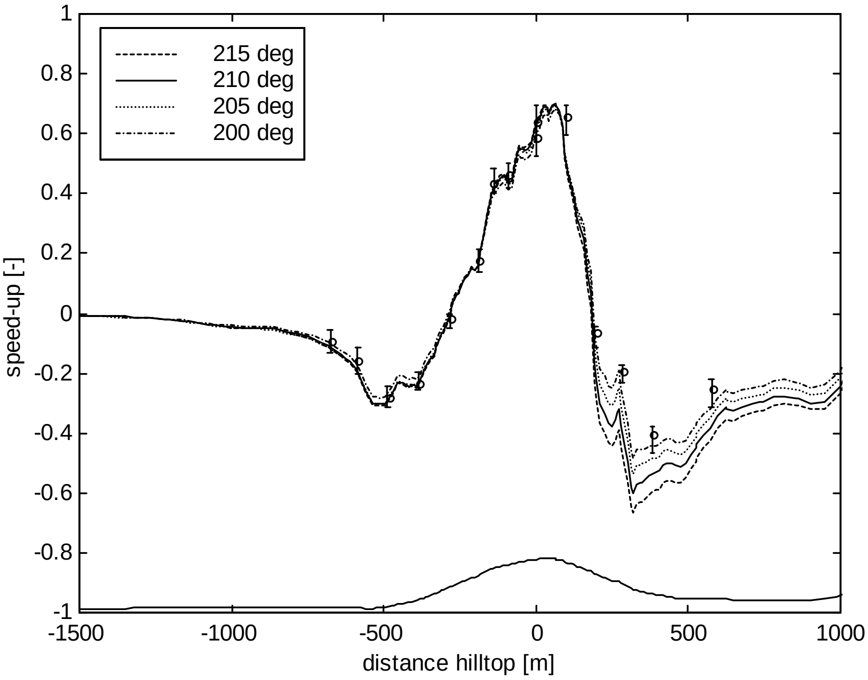

*Figure 15: A direction dependence comparison of relative speed-up along line AA. Symbols are measurements with uncertainty limits (Taylor and Teunissen, 1985).*

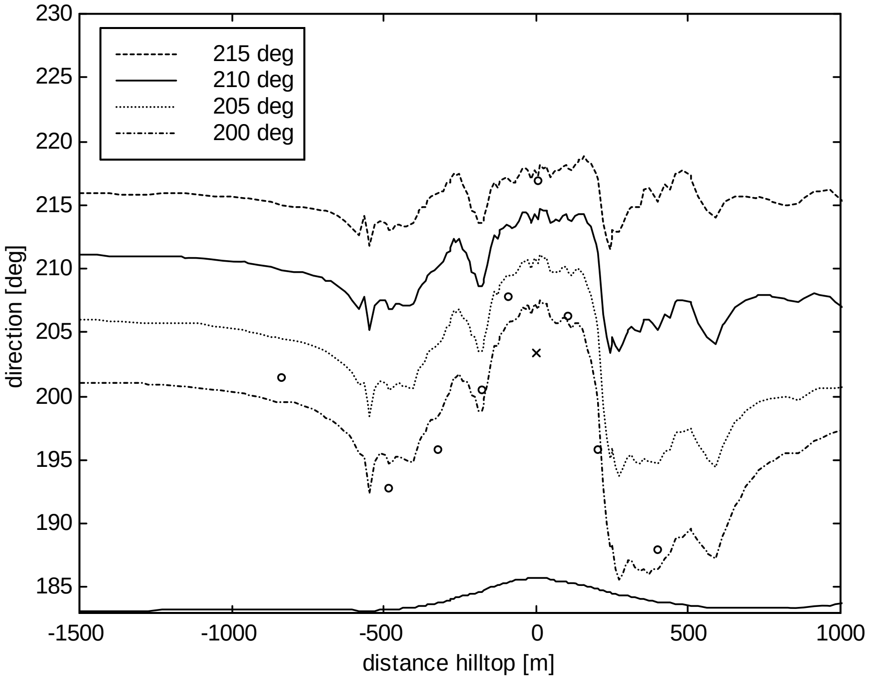

*Figure 16: A direction dependence comparison of direction distributions along line A. Symbols are measurements (Taylor and Teunissen, 1985).*

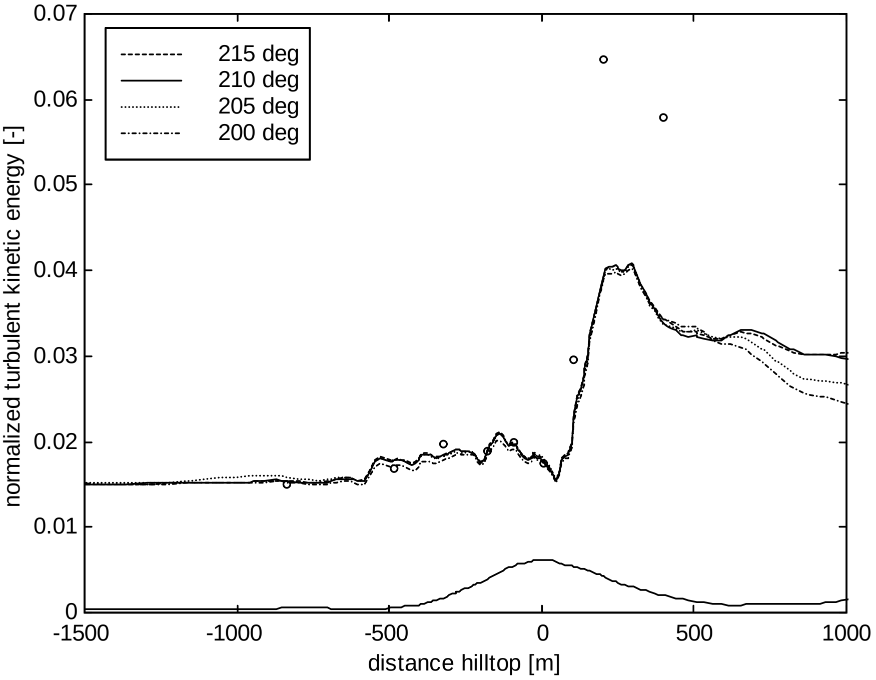

*Figure 17: A direction dependence comparison of the normalized turbulent kinetic energies along line A. Symbols are measurements (Taylor and Teunissen, 1985).*

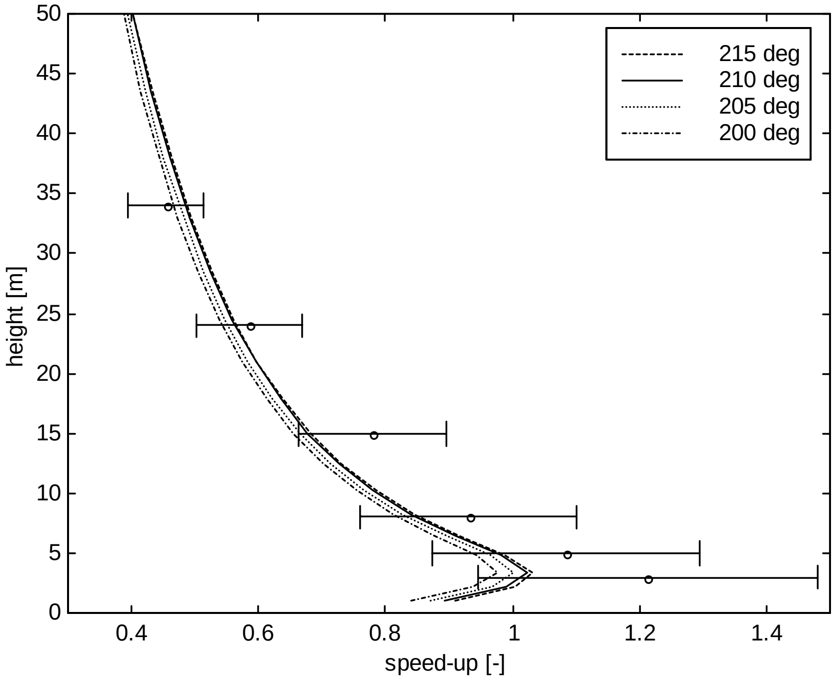

*Figure 18: A direction dependence comparison of the speed-up at the hilltop (HT) relative to the reference station (RS) in different heights above ground. Symbols are measurements with uncertainty limits (Taylor and Teunissen, 1985).*

### 4.3 Map contour interval dependence

The grid-resolution test is relevant to wind power since real sites only have 5-10m resolutions. More detailed digitizing is expensive, but if simulation results are significantly improved it will maybe be advisable. The influence of the local variations at the ground level is reduced with height. This will obviously have an effect at 10m, but it is also interesting to evaluate the differences in 50m, which is the current measurement height in wind power projects, and 80m, the current typical wind turbine hub height. The effect of detailed digitizing is assumed to have a particularly large influence on the hilltop. The 10m equidistance causes the hilltop height to be 120m, while the real height is 126m. This is expected to cause low simulated wind speeds at HT, both through reduced speed-up, particularly near the ground, and the fact that the measurements are collected at a lower level.

When 10m contours are used instead of 2m contours (see *Figure 1*) some terrain information is lost, and this is seen in the speed-up profiles along line A (*Figure 19*) and line B (*Figure 20*). Large differences are, in particular, found on the hilltop. In conjunction with wind power, this is also a critical point. *Figure 20* shows that the errors along the edge of the hilltop are largest in the areas inside the top contour line. This is the case around the hilltop, and at a low hill about 1500m from the hilltop, where the two leftmost measurement points are located. Along line A the direction plot and the plot of the angles between the wind velocity and the horizontal plane showed only minor differences caused by the local terrain differences, and are not shown here. The normalized turbulence intensities from *Figure 21* also show minor differences. The turbulence increase behind the hilltop is located a little more downstream. The turbulence intensities at the hilltop are in *Figure 22* seen to be a little higher with no digitizing. Lower wind velocities mainly cause this.

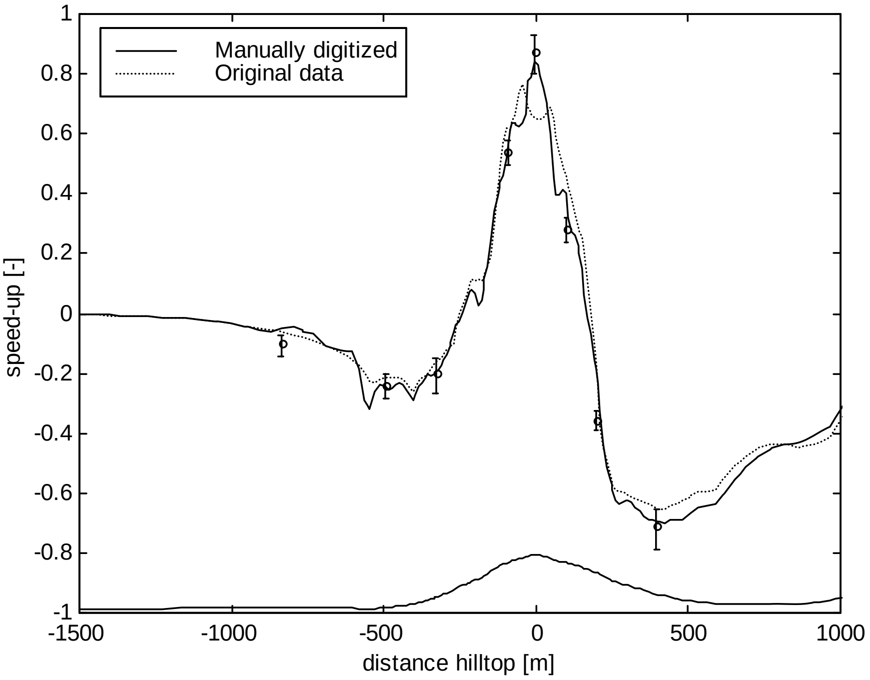

*Figure 19: A digitized terrain dependence comparison of relative speed-up along line A. Symbols are measurements with uncertainty limits (Taylor and Teunissen, 1985).*

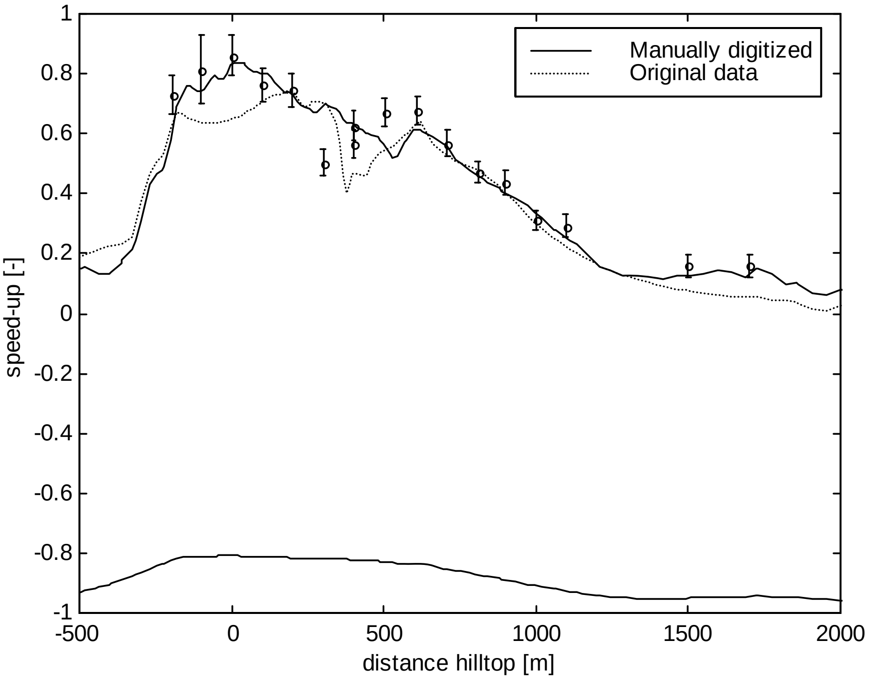

*Figure 20: A digitized terrain dependence comparison of relative speed-up along line B. Symbols are measurements with uncertainty limits (Taylor and Teunissen, 1985).*

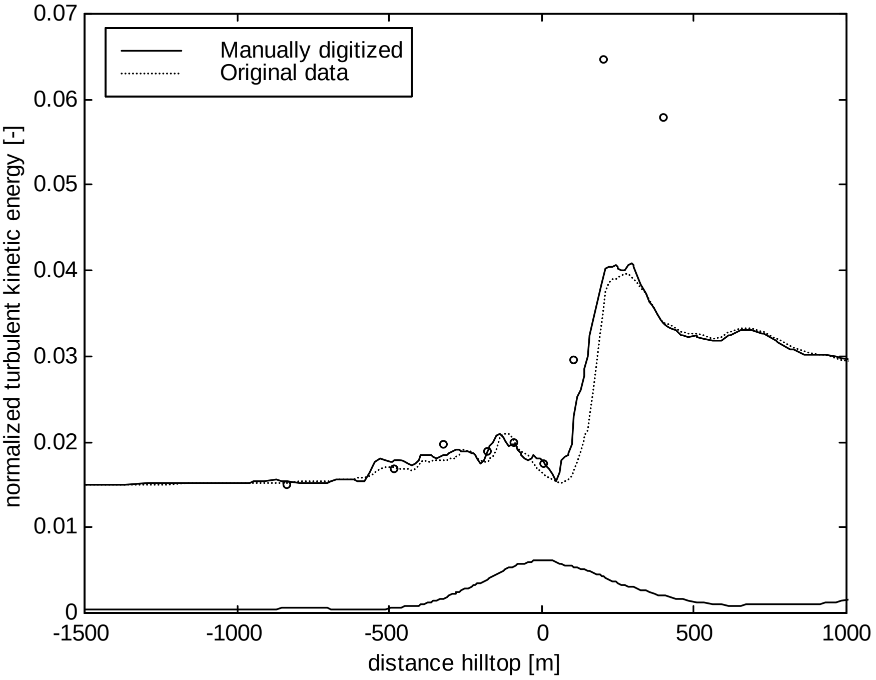

*Figure 21: A digitized terrain dependence comparison of the normalized turbulent kinetic energies along line A. Symbols are measurements (Taylor and Teunissen, 1985).*

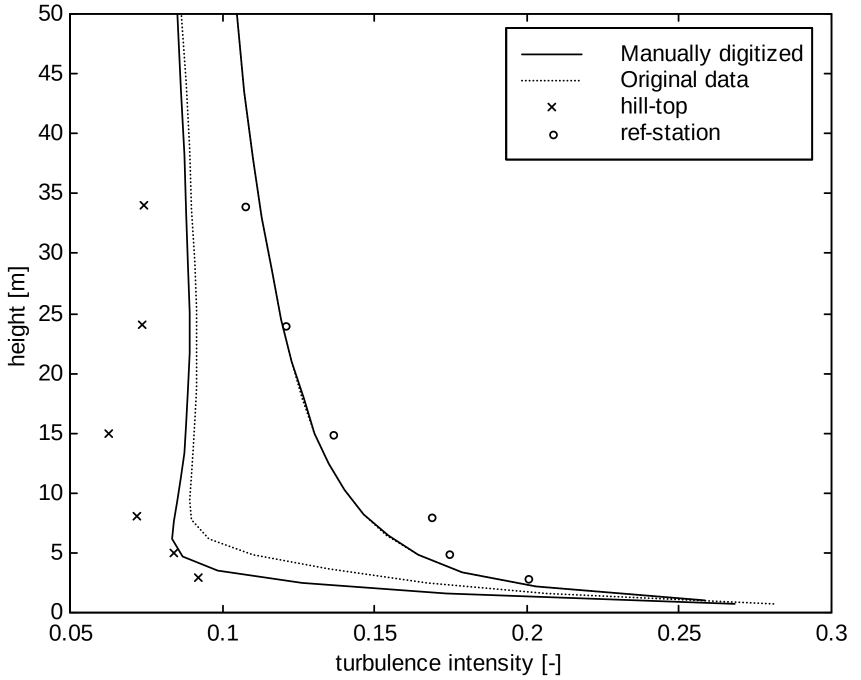

*Figure 22: A digitized terrain dependence comparison of the turbulence intensities.* x *is the turbulence intensity measurements at the hilltop (HT) and* ○ *is the turbulence intensity measurements at the reference station (RS) (Taylor and Teunissen, 1985).*

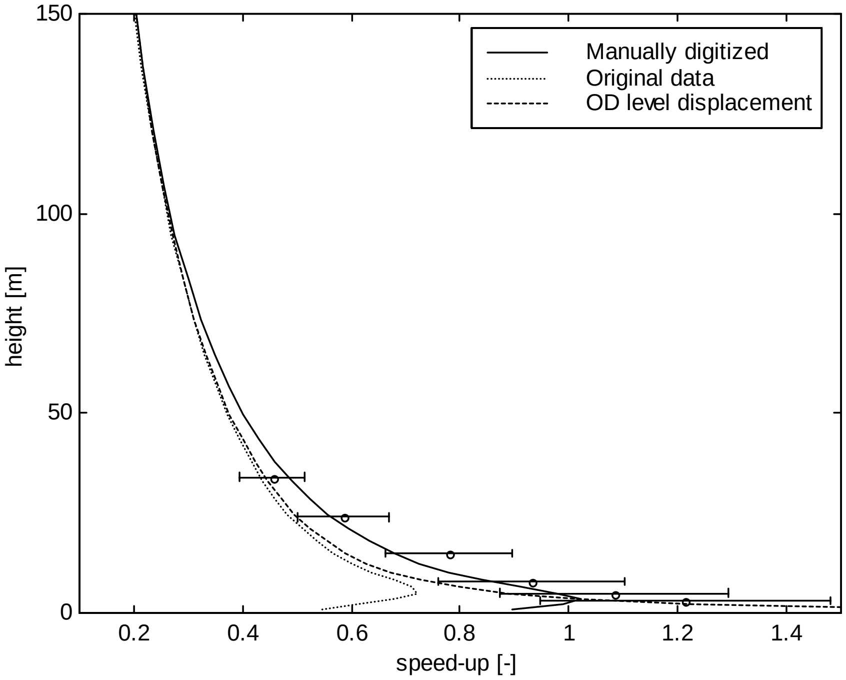

*Figure 23: A digitized terrain dependence comparison of the speed-up at the hilltop (HT) relative to the reference station (RS) in different heights above ground. Symbols are measurements with uncertainty limits (Taylor and Teunissen, 1985).*

From *Figure 23* it is seen that the relative speed-up is further decreased close to the ground in the case of non-digitized terrain. This difference is found to be particularly significant close to the ground. The difference is connected to both lower speed-up and the fact that the location is estimated at a lower altitude. To separate those effects, the results are also compared, where the zero level is set to 4.5m, i.e. the differences between the estimated terrain height from the original terrain data and the manually digitized terrain data. The roughness effect is largest close the ground, so this line is not valid in the area close to the ground, which indicates largest speed-up values at the ground, which is in accordance with the theory.

Assuming that the manually digitized data are closest to the real values, these are used as reference values. Then the original data underestimate the speed-up by 8.1% in 10m, 2.1% in 50m and 0.9% in 80m. 0.9% velocity reduction corresponds to a 2.6% power density reduction. This power density is still not fully available to the wind turbines. For a standard wind turbine of 2-3MW and a site with annual mean velocity in the area 7-9m/s, a power output increase of typically twice the velocity increase is found from the turbine power curve and the velocity distribution function. In this case this corresponds to about 1.8% power output reduction.

The corresponding values with the level displacement are 6.0% in 10m, 1.8% in 50m and 0.8% in 80m. On the other hand, if the data are calibrated towards measurements in 50m, the extrapolation to 80m causes an overestimation of the wind speed in 80m, since the error is less here than in 50m. If the original data are extrapolated from 50m to 80m this causes an overestimation of the estimated velocity in 80m of 1.2%, which corresponds to a production overestimation of 2.4%.

# 5 Conclusions

The flow solver 3DWind is used to analyse the Askervein hill flow. The simulations are non-linear and 3D, with a spatial resolution down to 10m. A map of two meter contours are used to establish the grid, and the speed-up profiles are seen to follow local terrain formations very well. Two different horizontal resolutions are compared, and only minor differences are found between the fine and the coarse grid. This indicates that a limit is reached, where minor improvements are expected due to refined horizontal resolution. The resolution advantage of linear models is then no longer present, even though there are large differences in computational cost.

Grid dependencies in the vertical direction are also encountered. This is probably related to the thickness of the first grid cell, equipped with wall functions. Along line A this causes differences in both the speed-up and the turbulence kinetic energy. Both effects are related to each other. Higher turbulence in the wake with high resolution causes more energy to be removed from the mean flow, and thereby lower velocities. Increased upstream turbulence in the coarse case causes lower velocities at the reference station, and this explains some of the speed-up difference at the hilltop. The vertical resolution is found to be the key issue to the estimated turbulence in the wake of the hill. The coarse horizontal resolution, the direction turning and the grid based on 10m contours show only minor differences in the simulated turbulence level. To increase the predictability of the model, this wall function dependence should be further investigated, and if possibly removed. Still large gradients in the first grid cell are difficult to generalize, but different generalized wall functions are available for implementation (Craft et al., 2002) (Utyuzhnikov, 2005).

The directional dependence is found to be rather small for all variables except the direction. The simulations with 200° and 205° direction at the reference station are found to have least bias compared to experimental values. Other 210° simulations have a direction of about 212° at the hilltop (Raithby et al., 1987) (Kim et al., 2000) (Lopes, 2003) (Chow and Street, 2004). This is in between presented simulations from 200° and 205°, which causes the direction at the hilltop to become respectively 210° and 215°. Some of the difference is probably caused by the Coriolis force, which causes a slight turning towards higher angles.

The 200° direction is found to have most veering along line A, but still less than experimental values. This is maybe related to a measurement error or the slightly stable atmosphere, causing the flow to move around the obstacle rather than passing over. This effect is seen when the fluid parcels do not possess sufficient kinetic energy to overcome the potential energy required for lifting the parcel through the stably density gradient (Arya, 1988). Other possible stability effects are the differing inflow profiles as discussed in the introduction and speed-ups at the hilltop that are overestimated above 30m and underestimated below. Suppressed vertical movements at stable stratification may also cause more of the flow to pass over at lower levels compared to the neutral case.

Grid established from 2m contours instead of 10m contours is seen to have influence on the hilltop results. This influence is particularly high at low levels, with a 8% underestimation in 10m. Moving to 80m, a common hub height of wind turbines, the difference is decreased to 0.9%. This corresponds to a power production difference of about 1.8%. This is within other uncertainties, but can still be important to the margin of profit.

Simulations from Askervein hill are thoroughly analysed, and numerical simulation tools are seen to prescribe most aspects. Still a possible improvement is to account for the non-neutral atmospheric stratification. Recommended further extensions of this model are the implementation of generalized wall functions and testing of the stability dependence by adding the buoyancy terms to the equations.

This analysis is part of Undheims PhD work, where 3DWind has been validated, and a Reynolds Stress Model (RSM) has been implemented. Results from the RSM are presented in the PhD thesis, but the decreased numerical diffusion connected to RSM generally gave poorer results than the two-equation RNG method. Thus the results were not presented in this article (Undheim, 2005ii). Still, the RSM is known to handle buoyancy better than the k-ε model, since buoyancy causes a coupling of the Reynolds stresses and the scalar flux fields ($\overline{u_i\theta}$) (Launder, 1996). The RSM is therefore recommended if buoyancy terms are included.

## Acknowledgements

The authors wish to give a special thank to Peter Taylor, who kindly made PDF versions of the reports MSRB-84-6 (Taylor and Teunissen, 1985) and MSRB-83-8 (Taylor and Teunissen, 1983) available on the web[1]. Thanks are also given to John Walmsley for making some digitized topography and measurement data available and to Fotini Katopodes Chow and Wensong Weng for kindly passing on these data. The authors also wish to thank all other people that joined the first project, and that has contributed to the huge amount of data available of the Askervein hill case.

## References

Alm, L. K. & Nygaard, T. A. (1995). Flow over complex terrain estimated by a general purpose Navier-Stokes solver. *Modeling, identification and control*, 16: 169 – 176.

Arya, S. P. (1988). *Introduction to Micrometeorology*. International Geophysics Series, Volume 42. Academic Press, Inc, San Diego, California.

Ayotte, K. W. (1997). Optimization of upstream profiles in modelled flow over complex terrain. *Boundary-Layer Meteorology*, 83: 285 – 309.

Barnard, J. C. (1991). An evaluation of three models designed for siting wind turbines in areas of complex terrain. *Solar Energy*, 46: 283 – 294.

---

[1] http://www.yorku.ca/pat/research/Askervein/index.html

Beljaars, A. C. M., Walmsley J. L. & Taylor P. A. (1987). A mixed spectral finite-difference model for neutrally stratified boundary-layer flow over roughness changes and topography. *Boundary-Layer Meteorology,* 38: 273 – 303.

Castro, F. A., Palma J. M. L. M. & Lopes A. S. (2003). Simulation of the Askervein flow. Part 1: Reynolds averaged Navier-Stokes equations (k-epsilon turbulence model). *Boundary-Layer Meteorology,* 107: 501 – 530.

Chorin, A. J. (1967). A Numerical Method for Solving Incompressible Viscous Flow Problems. In *Computational Fluid Dynamics,* edited by C. K. Chu, AIAA Selected Reprints Series, 4: 12.

Chow, F. K. & Street, R. L. (2004). Evaluation of turbulence models for Large-Eddy simulations of flow over Askervein hill. Paper 7.11, *16th Symposium on Boundary Layers and Turbulence,* American Meteorological Society.

Craft, T. J., Gerasimov, A. V., Iacovides, H. & Launder, B. E. (2002). Progress in the generalization of wall-function treatments. *International Journal of Heat and Fluid Flow,* 23: 148 – 160.

Eidsvik, K. J. (2004). A System for Wind Power Estimation in Mountainous Terrain. Prediction of Askervein Hill Data. Research Article in press at *Wind Energy.*

Hirsch, C. (1990). *Numerical computation of internal and external flows, volume 2.* John Wiley & Sons, Great Britain.

Kim, H. G. & Patel V. C. (2000). Test of turbulence models for wind flow over terrain with separation and recirculation. *Boundary-Layer Meteorology,* 94: 5 – 21.

Kim, H. G., Patel, V. C. & Lee, C. M. (2000). Numerical simulation of wind flow over hilly terrain. *Journal of Wind Engineering and Industrial Aerodynamics*, 87: 45 – 60.

Knauer, A. & Nyhammer, F. K. (2002). Numerical and experimental methods for wind farm site evaluation in complex terrain. *Conference proceedings Global Windpower 2002,* Paris, France.

Launder, B. E. (1996). "An introduction to single-point closure methodology", In: *Computational Fluid Dynamics,* eds. M. Lesieur, P. Comte & J. Zinn-Justin, pp. 257 – 323, North-Holland.

Leroy, J. & Gravdahl, A. R. (1999). *Wind field simulations at Askervein hill.* Vector, Tønsberg, Norway.

Lopes, A. M. G. (2003). WindStation – a software for the simulation of atmospheric flows over complex topography. *Environmental Modelling & Software,* 18: 81 – 96.

Mickle, R. E., Cook, N. J., Hoff, A. M., Jensen, N. O., Salmon, A. J., Taylor, P. A., Tetzlaff, G. & Teunissen, H. W. (1988). The Askervein Hill project: Vertical profiles of wind and turbulence. *Boundary-Layer Meteorology*, 43: 143 – 169.

Raithby, G. D., Stubley, G. D.  & Taylor, P. A. (1987). The Askervein Hill project: A finite control volume prediction of three-dimensional flows over the hill. *Boundary-Layer Meteorology*, 39: 247 – 267.

Salmon, J. R., Bowen, A. J., Hoff, A. M., Johnson, R., Mickle, R. E., Taylor, P. A., Tetzlaff, G. & Walmsley, J. L. (1988). The Askervein Hill project: Mean wind variations at fixed heights above ground. *Boundary-Layer Meteorology*, 43: 247 – 271.

Taylor, P. & Teunissen, H. (1983). *ASKERVEIN '82: Report on the September/ October 1982 Experiment to Study Boundary-Layer Flow over Askervein, South Uist.* Report MSRB-83-8, Atmospheric Environment Service, Downsview, Ontario.

Taylor, P. & Teunissen, H. (1985). *The Askervein Hill Project: Report on the September/October 1983 Main Field Experiment*. Report MSRB-84-6, Atmospheric Environment Service, Downsview, Ontario.

Taylor, P. A. & Teunissen, H. W. (1987). The Askervein Hill project: Overview and background data. *Boundary-Layer Meteorology,* 39: 15 – 39.

Teunissen, H. W., Shokr, M. E., Bowen, A. J., Wood, C. J. & Green, D. W. R. (1987). The Askervein Hill project: Wind-tunnel simulations at three length scales. *Boundary-Layer Meteorology*, 40: 1 – 29.

Undheim, O. (2003). Comparison of turbulence models for wind evaluation in complex terrain. *Conference proceedings European Wind Energy Conference*, Madrid, Spain.

Undheim, O. (2005i). 2D simulations of terrain effects on atmospheric flow. *Conference Proceedings MekIT'05,* Trondheim, Norway.

Undheim, O. (2005ii). *Description and validation of 3DWind*. Internal report IFE/KR/F-2005/062, Kjeller, Norway.

Utyuzhnikov, S. V. (2005). Some new approaches to building and implementation of wall-functions for modeling of near-wall turbulent flows. *Computers & Fluids,* 34: 771 – 784.

Versteeg, H.K. & Malalasekera, W. (1995). *An Introduction to Computational Fluid Dynamics; The Finite Volume Method*. Prentice Hall, London.

Walmsley, J. L. & Taylor, P. A. (1996). Boundary-layer flow over topography: Impacts of the Askervein study. *Boundary-Layer Meteorology*, 78: 291 – 320.

www.ewea.org. Latest news, Press Release 4 Mars 2005. *Global wind power continues expansion*. Brussels, Belgium.

# Paper 3

## 2D simulations of terrain effects on atmospheric flow

*Conference proceedings MekIT'05*

# 2D simulations of terrain effects on atmospheric flow

*O. Undheim*[1]

[1] Institute for Energy Technology, IFE, N-2027 Kjeller
e-mail: ove.undheim@ife.no

## Abstract

The micro-scale flow solver 3DWind is used in a 2D analysis to investigate both topographical and roughness effects on the wind flow field. This is an important issue in the knowledge of where to locate wind turbines. To illustrate some of the terrain effects, different 2D simulations are carried out. It is seen how the roughness influences the flow developed under uniform conditions, and how the influence of a roughness change spreads upwards in the boundary layer downstream from the roughness change. Escarpments and ridges are represented by 2D topography using four different sine shaped slopes. In the escarpment case the profile development downstream the escarpment plateau is visualized. For the ridge case both the speed-up at the top of the ridge and the reconstruction of the boundary layer profile in the wake of the ridge are visualized. The results from the simulations are compared to equivalent values from empirical equations. The terrain effects are found to have great influence on the flow field and the mean wind conditions in an area. To predict the sum of these non-linear effects, simulations performed by a non-linear flow solver are recommended to supplement measurements.

**Keywords:** atmospheric flow, CFD, terrain effects, wind power

## INTRODUCTION

Power extraction from wind is clean and renewable, and is becoming competitive to most other energy resources. According to Windpower monthly news magazine: “Wind generation prices were in January 2004 almost level with those of fossil fuels and have long since beaten nuclear” (Windpower 1, 2004). Norway has a great energy potential from wind, due to large areas available with high mean wind. There is also a governmental goal that forces the expansion. 10TWh of the Norwegian power production is decided to come from new renewable energy sources within 2010, from which at least 3TWh should be covered by wind power. Today it seems like the entire 10TWh is going to be covered by wind power (Windpower 3, 2004). This is a large expansion, and to minimize the disadvantages connected to all power production the siting of the wind turbines has to be done with care.

The mean wind on a potential wind power site is very important to the economy in the project. The power in the wind is proportional to the cubic wind speed. Norwegian areas with good wind conditions, generally also have complex topography. To predict the flow field on a site, measurements are preferably supplemented with numerical simulations. Such simulations take both the surface friction and the topography’s influence on the wind into account. This is a complicated system, and it is interesting to separate the effects, to see how each factor influences the flow field.

There are different methods to calculate the flow field, and based on these methods, there are a lot of models. Today linear models, not able to predict flow separation, are the most common tools. In the present analysis the non-linear wind flow solver 3DWind is used (Alm and Nygaard, 1995) (Knauer and Nyhammer, 2002) (Undheim, 2003). This model solves the Reynolds Averaged Navier-Stokes equations with the finite volume approach.

## THEORY

### Roughness

Roughness is friction caused by the ground and depends on the land use properties. Water surfaces have low friction and forests have high friction. The friction depends on the size of the elements causing the friction. This is parameterized by a length that represents the ground cover. In neutrally stratified homogeneous flow, the logarithmic law (Eqn.1) is a good estimate of the wind profile near the ground (Arya, 1988).

$$\frac{U(z)}{u_*} = \frac{1}{\kappa}\ln\left(\frac{z}{z_0}\right) \tag{1}$$

In this equation $U(z)$ is the wind velocity in height $z$. $z_0$ is the roughness length, and $\kappa$ is von Karman's constant, an empirical constant of about 0.41. $u_*$ is the friction velocity defined as $u_* = (\tau_0/\rho)^{1/2}$ where $\tau_0$ is the ground shear stress, and $\rho$ is the fluid density. In this analysis some typical roughness lengths are evaluated. The roughness length of water is $10^{-4}$-$10^{-3}$m depending on the wind and the waves on the sea. In this analysis the roughness $10^{-4}$m is used. The roughness length of open farmland with isolated trees and uncut grass is about 0.03m. The roughness lengths of forests vary depending on type of forest, but in this analysis the roughness length representing a forest is chosen to be 0.5m.

A step change in the surface roughness causes a change in the velocity profile of the wind. This change has been extensively studied both experimentally and theoretically (Arya, 1988), and a schematic of the upstream flow and the modified flow due to change in the surface roughness is shown in Fig.1. In this figure, area 1 is the area upstream from the roughness change, and area 2 is the area downstream from the roughness change. The roughness length of area 1 is lower than the roughness length of area 2.

The velocity profile of the approaching flow $U_1(z)$ depends on the roughness length $z_{01}$ and the friction velocity $u_{*1}$ according to Eqn.1. After the roughness change, a modified profile starts to develop within the planetary boundary layer (PBL). This is called the internal boundary layer (IBL). An empirical equation (Eqn.2) of the IBL growth rate is derived based on several field and laboratory observations taken under neutral stability conditions (Arya, 1988).

$$\frac{h_i(x)}{z_{02}} = a_i\left(\frac{x}{z_{02}}\right)^{0.8} \tag{2}$$

In this equation $h_i$ is the height of the internal boundary layer at location $x$, $z_{02}$ is the roughness length after the step change and $a_i$ is an empirical constant between 0.35 and 0.75.

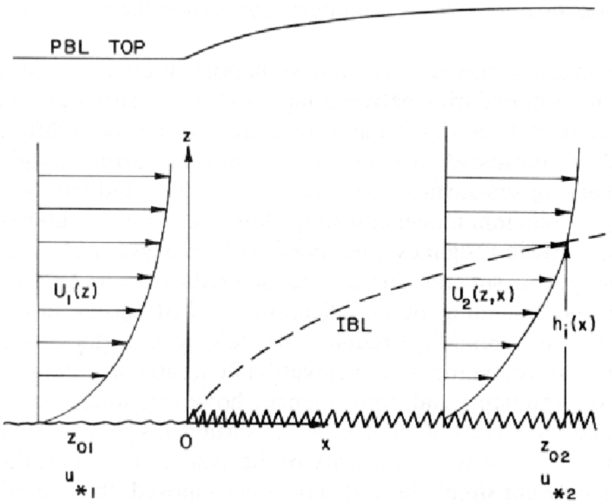

**Fig.1**: Schematic of the internal boundary layer development and wind profile modification following a step change in the surface roughness (Arya, 1988).

The velocity profile development $U_2(z,x)$ follows the logarithmic law (Eqn.1) corresponding to roughness length $z_{02}$ and friction velocity $u_{*_2}$ below and $z_{01}$ and friction velocity $u_{*_1}$ above the IBL.

**Topography**

The wind field is influenced by the topography. The air is a fluid, and the motion can be described by streamlines. To have continuity in the flow field above a hilltop, the streamlines are forced together. This equals an increase of the wind speed. From this increased wind speed, the speed-up factor $\Delta S$ is defined from Eqn.3 and according to Fig.2.

$$v_{tot}(z) = (1 + \Delta S) \cdot v(z) \tag{3}$$

In this equation $v_{tot}(z)$ is the wind velocity in the point, while $v(z)$ is the velocity that would have been in the same point with no speed-up.

The speed-up factor can either be evaluated through detailed numerical simulations described in the model description subsection, or by empirical methods based on experimental results. One empirical method to estimate the speed-up in a given point is described in Lemlin et. al. (1988). Due to the complexity the method is not described in detail in this article, but the maximum speed-up is mainly depending on *H/L*, the ratio between the hill height and the horizontal distance from the hilltop to the upstream point of half the height of the hill according to Fig.2.

Another topographical effect is the separation of the flow in the wake of a hill. The size of the separated region is very sensitive to flow direction and the presence of any sharp discontinuity in the terrain profile (Arya, 1988). Separation may occur if the maximum downwind slope is larger than about 0.2, which corresponds to 11° (Arya, 1988), and according to Bowen and Mortensen (1996) separation is likely to be present at slopes greater than 17°. Behind long, steep ridges the cavity region may extend up to 10 hill heights in the downstream direction, while the cavity for three-dimensional hills is at most a few hill heights long (Arya, 1988). This phenomenon is complex, and it is difficult to give a general empirical formula. Even the most sophisticated flow models have difficulties calculating the separation zone accurately. This is connected to the fact that the separated region is very sensitive to the presence of any sharp discontinuity in the terrain profile (Arya, 1988), and such a terrain formation is usually on a sub grid scale.

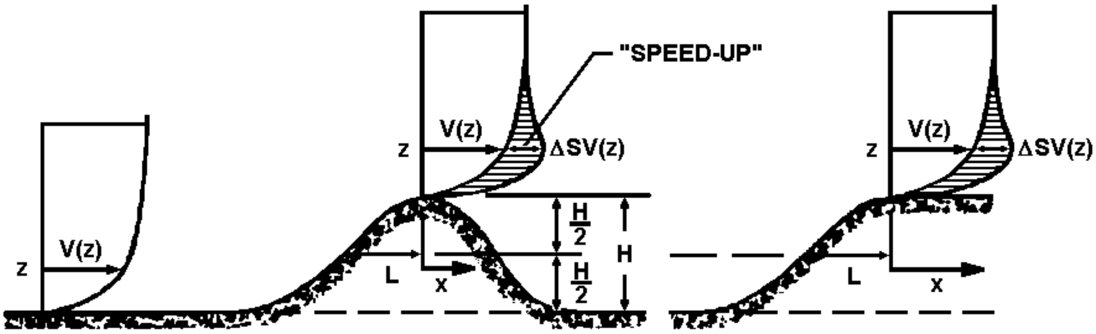

**Fig.2**: A schematic view of the undisturbed profile together with profile with topography induced speed-up caused by a ridge and an escarpment. Important scales in the empirical evaluation of the speed-up are also included (Lemlin et. al., 1988).

Both the empirical method to calculate the speed-up, and the flow solver described in the next section assume a neutral stratification. Strictly neutral stability conditions are rarely encountered in the atmosphere, though near-neutral conditions often occur in conjunction with strong surface geostrophic winds (Arya, 1988). According to Arya (1988), effects of topography on the flow are considerably modified in the presence of stable stratification. Increased stability causes an increased tendency of the fluid to go around rather than over the topography. Pure stability effects like lee waves, rotors and hydraulic jumps also influence both the speed-up on the hilltop and the flow field in the wake of the hill.

## Model description

3DWind solves the incompressible Reynolds Averaged Navier-Stokes equations (RANS), where the averaged mass balance is given by:

$$\frac{\partial U_i}{\partial x_i} = 0 \qquad (4)$$

$U_1$, $U_2$ and $U_3$ are the time averaged velocity components. $U_1$ and $U_2$ are the horizontal components, and $U_3$ is the vertical component.

Averaged momentum equations are given by:

$$\frac{\partial U_1}{\partial t} + U_j \frac{\partial U_1}{\partial x_j} - \frac{\partial}{\partial x_j}\left( -\overline{u_1 u_j} + \nu_l \frac{\partial U_1}{\partial x_j} \right) + \frac{1}{\rho}\frac{\partial P}{\partial x_1} - fU_2 = 0 \qquad (5)$$

$$\frac{\partial U_2}{\partial t}+U_j\frac{\partial U_2}{\partial x_j}-\frac{\partial}{\partial x_j}\left(-\overline{u_2u_j}+\nu_l\frac{\partial U_2}{\partial x_j}\right)+\frac{1}{\rho}\frac{\partial P}{\partial x_2}+fU_1=0 \tag{6}$$

$$\frac{\partial U_3}{\partial t}+U_j\frac{\partial U_3}{\partial x_j}-\frac{\partial}{\partial x_j}\left(-\overline{u_3u_j}+\nu_l\frac{\partial U_3}{\partial x_j}\right)+\frac{1}{\rho}\frac{\partial P}{\partial x_3}=0 \tag{7}$$

$u_1$, $u_2$ and $u_3$ are velocity fluctuations, $\nu_l$ is the kinematic viscosity, $P$ is the averaged pressure and $f$ is a factor that depends on the latitude and the angular velocity of the Earth's rotation. This term represents the Coriolis force, and in this analysis $f$=0.0001s$^{-1}$. Physical values in Norway span from 0.00012s$^{-1}$ in the South to 0.00014s$^{-1}$ in the North.

The correlations of the deviations from the mean wind speed $-\overline{u_iu_j}$ are called the Reynolds stresses or second-moments. This is a second-order symmetrical tensor that must be parameterized to close the equations. In the eddy-viscosity assumption the Reynolds stresses are expressed by:

$$\overline{u_iu_j}=\frac{2}{3}k\delta_{ij}-\nu_T\left(\frac{\partial U_i}{\partial x_j}+\frac{\partial U_j}{\partial x_i}\right) \tag{8}$$

This is a first order closure (Versteeg and Malalasekera, 1995), where $\nu_T$ is the turbulent viscosity and $k$ is the turbulent kinetic energy. In this analysis $k$ is estimated by a two-equation $k$-$\varepsilon$ model, defined by Eqn.9, 10 and 11.

$$\frac{Dk}{Dt}=\frac{\partial}{\partial x_m}\left(\frac{\nu_T}{\sigma_k}\frac{\partial k}{\partial x_m}\right)+2\cdot\nu_T\cdot E_{ij}\cdot E_{ij}-\varepsilon \tag{9}$$

$$\frac{D\varepsilon}{Dt}=\frac{\partial}{\partial x_m}\left(\frac{\nu_T}{\sigma_\varepsilon}\frac{\partial \varepsilon}{\partial x_m}\right)+C_{1\varepsilon}\frac{\varepsilon}{k}2\nu_T E_{ij}\cdot E_{ij}-C_{2\varepsilon}\frac{\varepsilon^2}{k} \tag{10}$$

$$\nu_T=C_\mu\frac{k^2}{\varepsilon} \tag{11}$$

ε is the dissipation rate of the turbulent kinetic energy. Atmospheric values of the constants in these equations are $C_\mu$=0.0324, $\sigma_k$=1.00, $\sigma_\varepsilon$=1.85, $C_{1\varepsilon}$=1.44 and $C_{2\varepsilon}$=1.92. (Raithby et al, 1987)(Alm and Nygaard, 1995). $E_{ij}$ is the mean strain-rate tensor.

$$E_{ij}=\frac{1}{2}\left(\frac{\partial U_i}{\partial x_j}+\frac{\partial U_j}{\partial x_i}\right) \tag{12}$$

The 3D finite volume method (Versteeg and Malalasekera, 1995) is used in 3DWind. This method divides the solution domain in a finite number of cubes, in which the values inside each cube are assumed to be constant. The Reynolds Averaged Navier-Stokes equations describe the interaction between the cubes. This collection of cubes is called a mesh, and the grid generator Grid3d makes meshes for use in 3DWind. The meshes are non-orthogonal, terrain following and use grid cell stretching to focus the computational effort to areas of special interest (Undheim, 2005).

The time integration is solved by an explicit, three stage Runge-Kutta method (Øye, 1996). Even though the time derivative is included in the equations, transient solutions are not achievable with the model. This is caused by variable time step length used to speed the simulations, and the non-physical Chorin's method used to solve the pressure field (Chorin, 1967) (Hirsch, 1990).

## SIMULATION

To illustrate the main 2D terrain effects, several 2D simulations are performed. These simulations investigate different physical effects separately, and help to understand what to be aware of when a wind farm is planned and designed. It should also be mentioned that the flow field is non-linear, and a super position principle will probably not work when adding different effects. Even though some quantitative considerations are done based on the simulation results, these should be used with care. It is quite easy to get a qualitative view of the flow field, but micro-scale atmospheric flows are transient and depend on scales ranging from $10^{-3}$ to $10^{3}$ m and $10^{-4}$ to $10^{2}$ s (Arya, 1988) (Versteeg and Malalasekera, 1995) (Ahrens, 1994). This wide range is not resolvable, and the needed parameterizations and the stationary inflow condition introduce uncertainties. The 2D approach is also a simplification of the 3D flow field, since the turbulence field is always three-dimensional.

Throughout the results, the increased power density in the air caused by the speed-up is sometimes included. This power density increase is still not fully available to the wind turbines. For a standard wind turbine of 2-3MW and a site with annual mean velocity in the area 7-9m/s, a power output increase of typically twice the velocity increase is found from the turbine power curve and the velocity distribution function. The corresponding power density increase is about three times the velocity increase. This means that if the velocity is increased by 10%, the power output is increased by 20% and the power density is increased by 30%. This is a linearisation and should not be used in cases of large differences.

### Set up

#### *Grid*

The simulation is two dimensional with 158x60 mesh cells. The 2D approach is chosen to limit the computational effort, since minor transverse gradients are expected for the given terrain. Compared to a 3D simulation the only difference is that there is only one mesh cell in the transverse direction. The domain height is 2km, and the domain length is 7.5km. The height of the first mesh cell is 5m, and the vertical mesh cell stretching is 5%. Horizontally, the cell size in the central area is 10m. Outside this area there is a cell stretching of 8%, up to the maximum cell size of 100m.

#### *Initial conditions and boundary conditions*

The initial condition and the inflow boundary condition are calculated from a 1D simulation with a geostrophic wind of 15m/s. This means that the value at the upper cell is 15m/s in the 1D simulation. The ground boundary condition is expressed by wall functions in both the 1D and the 2D simulations. The velocity values in the mesh cell adjacent to the ground are estimated according to Eqn.1. This assumption is assumed to be valid up to the second cell. The wall functions of the turbulent quantities are according to Versteeg and Malalasekera (1995). There are periodic boundary conditions at the sides. The top and outflow boundary have a zero gradient condition in the 2D simulation.

## Results and discussion

Throughout the visualisations, the green profile is a reference profile, showing the wind profile that would be present at the same location in the case of flat topography and a uniform roughness with a roughness length of 0.03m, in this analysis called farmland.

### *Roughness influence*

Focusing on the roughness influence on the flow field, the first aspect to evaluate is how the profile changes downstream a roughness change. It is interesting to quantify the IBL propagation, and compare it with corresponding results calculated from Eqn.2. A common situation in the siting of wind turbines is the roughness change from sea to land, since the wind turbines are often located in coastal areas. When the flow develops over sea and propagates past a roughness change to farmland, Eqn.2 predicts that the IBL height propagation will be in the order 1m pr 10-20m. From the simulation results illustrated in Fig.3, the IBL height propagation is found to be 1m pr 13-30m. As indicated in Fig.1, the IBL height propagation is found to be fast in the beginning, and then slows down, as the IBL gets thicker. This is connected to the fact that the friction causes largest turbulence close to the ground. 1m pr 13m is the result from the first 200m, and 1m pr 30m is the result from the first 4km.

From Fig.3 it is seen that the IBL reaches 130m 4km from the roughness change. This means that 4km from the shore a turbine (with hub height 80m and a rotor diameter of 80m) would be entirely within the IBL. It may look like the favourable wind condition caused by low roughness is no longer present. But as seen in Fig.4, where the profiles are compared to results with the same background geostrophic wind with a uniform roughness of 0.03m, most of the energy from the sea roughness condition is still present within the area swept out by the turbine. At the shore, the mean wind at hub height is 12.9m/s. This is 1.6m/s larger than the corresponding velocity at uniform farmland condition. This means 14% higher velocity and 47% higher power density in the air. 4km from the roughness change, the velocity is still increased by 13% compared to a uniform farmland condition. This corresponds to an increased power density in the air of 43%. Even though the profile 4km from the shore is changed according to the new roughness up to 130m, it is still the long time effect of the previous roughness that is most important to the mean wind condition. It should be mentioned though that the wind shear within the area swept by the turbine is increased, and this will increase the fatigue load.

To compare with the distance needed to achieve a uniform farmland wind profile, Eqn.2 is used in the limiting case where the internal boundary layer equals the planetary boundary layer. If the planetary boundary layer is assumed to be 1km thick, uniform farmland condition is achieved in the range from 20-50km downstream.

Another interesting aspect locating a wind farm is the influence of an area of high roughness. It might be a village or a forest. How will these regions of high roughness influence the wind profile in the vicinity? To visualize this Fig.5 shows the profile development downstream from a 2km long forest in an area of farmland. The results are compared to the situation with no forest (green profile in Fig.5). At the end of the forest, the speed close to the ground is slowed down. At hub height the wind speed is almost unchanged, causing a higher wind shear over the swept area. Increased wind shear is present up to 4km from the forest. As the distance to the forest increase, the vertical location of reduced velocity caused by the forest propagate upwards. This is a situation with two different internal boundary layers. The first caused by the roughness change from farmland to forest and the second caused by the roughness change from forest to farmland 2km later. At 4km the velocity just above ground is almost the same as before the forest. The vertical location of reduced wind velocity is here in the area swept by the turbine, and the speed is reduced by 2% at hub height. This corresponds to a reduced power density in the air of 6%.

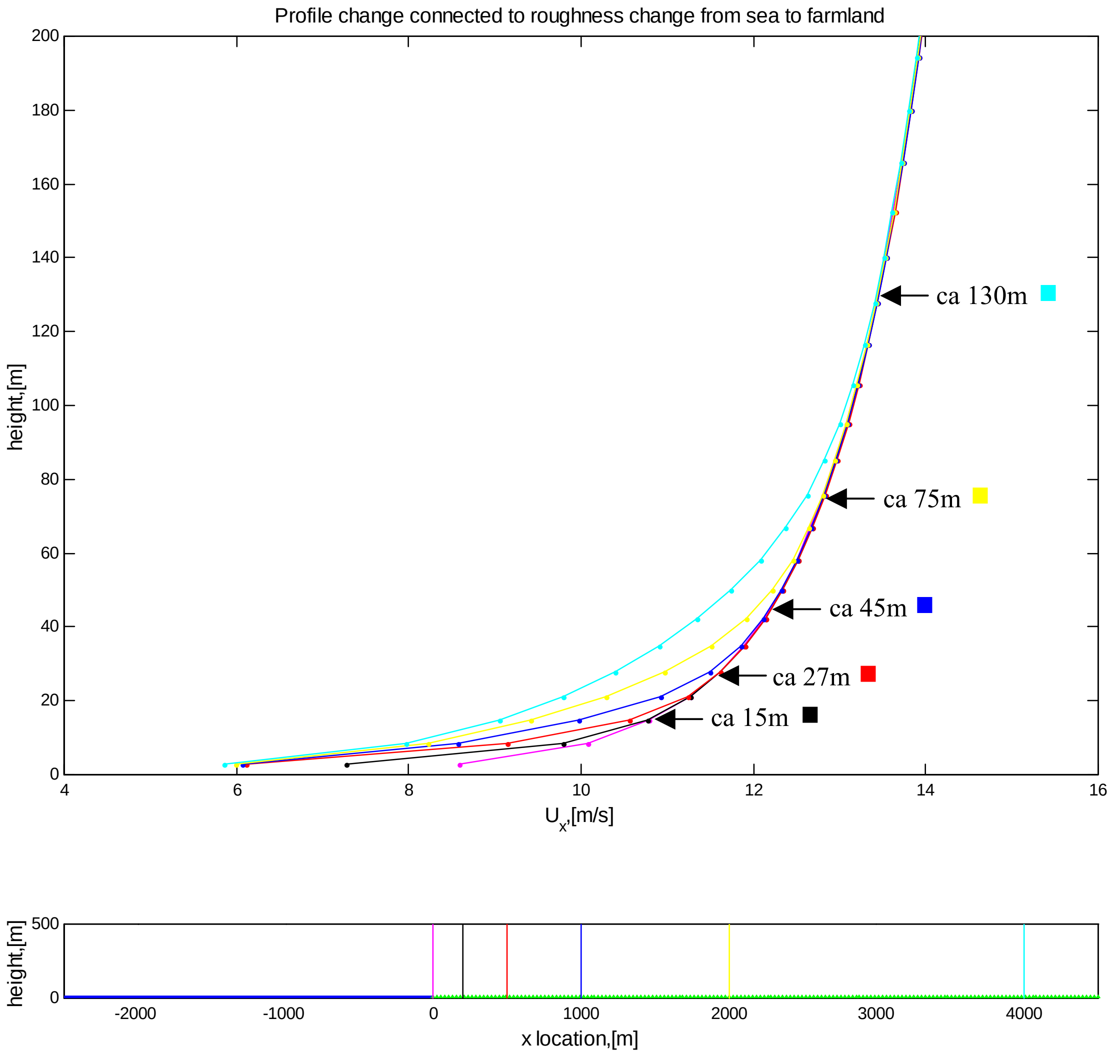

**Fig.3**: Wind profiles the first 200m from ground, showing how the profiles changes downstream from a roughness change. The lower diagram shows the location of each profile in the upper diagram. The flow comes from left, and is developed under uniform sea condition ($z_0$=0.0001m, blue colour coding in the lower diagram) and reaches farmland ($z_0$=0.03m, green colour coding in the lower diagram). The IBL height at each location is indicated in the upper diagram.

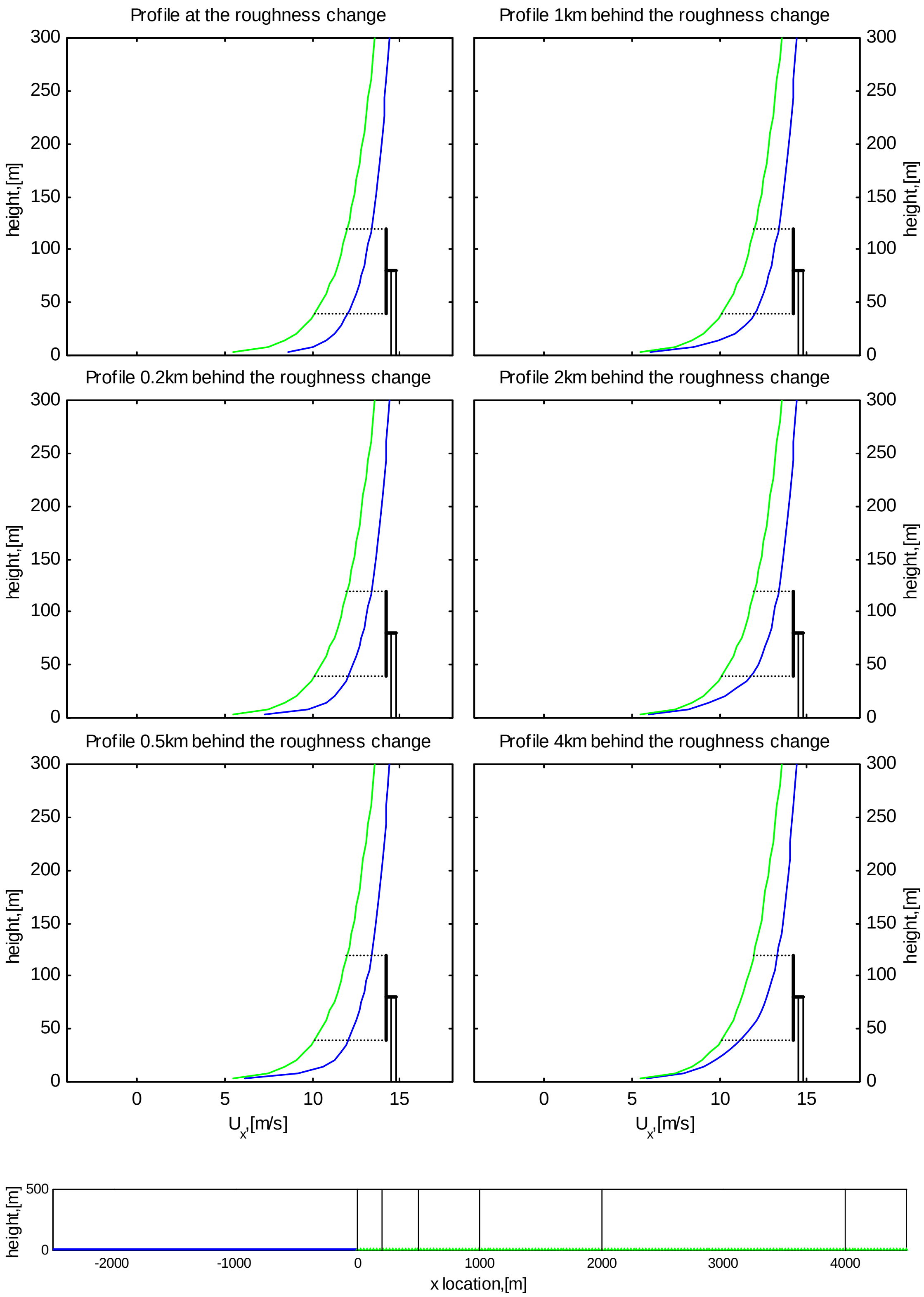

**Fig.4**: The same situation as visualized in Fig.3, but in this figure the profile in each location (🟦) is compared to the corresponding profile under uniform farmland condition (🟩) ($z_0$=0.03m). The lower diagram shows the location of each blue profile in the upper diagram. The flow comes from left, and is developed under uniform sea condition ($z_0$=0.0001m, blue colour coding in the lower diagram) and reaches farmland ($z_0$=0.03m, green colour coding in the lower diagram).

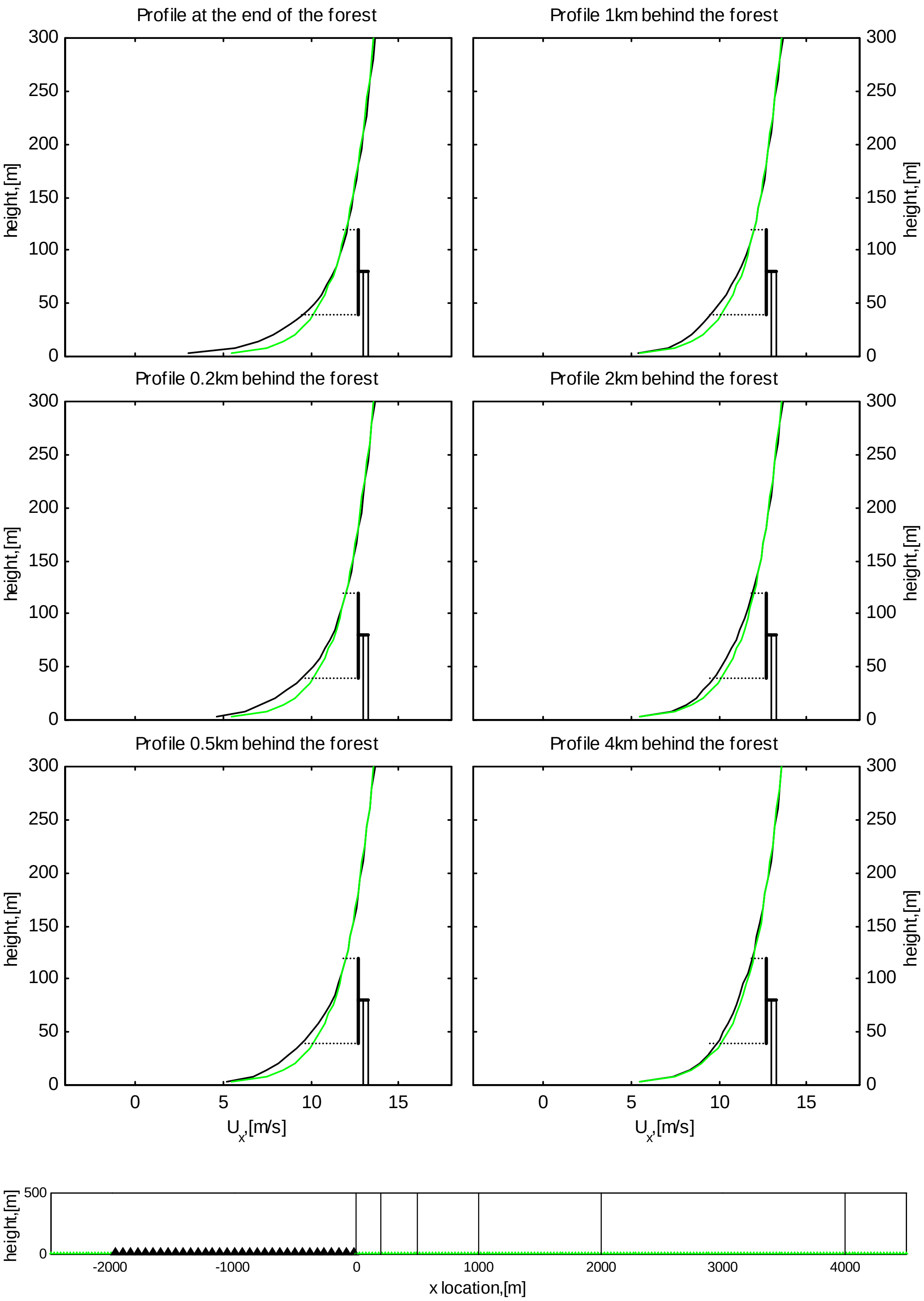

**Fig.5**: The lower diagram shows the location of each black profile in the upper diagram. The flow comes from left, and is developed under uniform farmland condition ($z_0$=0.03m, green colour coding in the lower diagram), then it reaches a 2km long forest ($z_0$=0.5m, black colour coding in the lower diagram) and comes back into farmland. The black profiles visualize the profile development behind the forest, and are compared to the corresponding green profile developed under uniform farmland condition ($z_0$=0.03m).

*Topography influence*

Before presenting the influence of the topography from the simulation results, a description of the topographical conditions has to be given. Geometries that enhance the average wind speeds can mainly be divided in 3 categories as shown in Fig.6; hills, ridges and escarpments. Most wind-exposed locations are somehow a combination of these major geometries. The flow has the ability to go around a hill. This is a 3D effect, which is not evaluated in these 2D simulations. The ridge and the escarpment are easily represented with a 2D representation, and evaluated in this analysis.

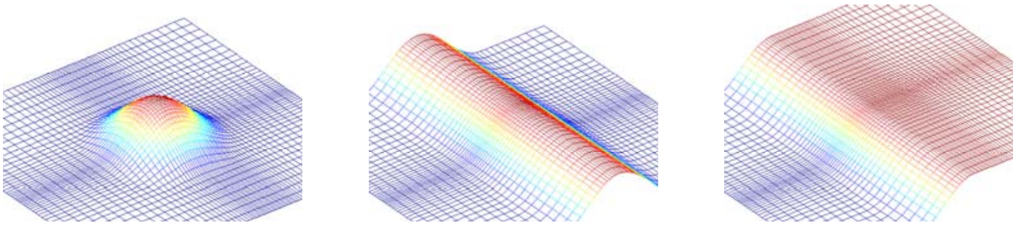

**Fig.6**: A visualisation of the three major geometries, which improve the wind conditions. The first is a hill, the second is a ridge and the third is an escarpment.

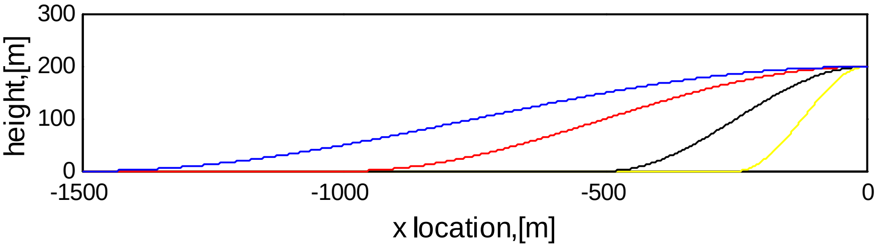

**Fig.7**: A visualisation of the four different sine shaped ascents used in the simulation. The height of the hill is 200m, and the steepest slope of each hill is: blue 8.4°, red 12°, black 24° and yellow 42°.

A second property of the geometry is the slope and the shape of the ascent. As shown in Fig.7 this simulation uses four different sine shaped ascents. Blue is 8.4°, which corresponds to 14%, and is on the same level as the steepest roads in Norway. To compare, the Oslofjord tunnel is 7%. Red is 12° and black is 24°. Yellow is 42°. To compare, the landing slope at Holmenkollen is 38°. This is a steep slope, but still quite common in the Norwegian mountains.

The first visualisations of the simulations in Fig.8 show the profile development the first 4km downstream the plateau on the top of an escarpment. Immediately on the escarpment top, the largest speed-up factors are found for the steepest slopes. The speed-up for the red profile corresponding to 12° is 29%. The corresponding result using the empirical formula described by Lemlin et. al. (1988) is 30%. A velocity increase of 30% corresponds to a power density increase of 120%. This shows that speed-up effects are extremely important in wind farm design. Moving inwards, the speed-up effect is gradually decreased. After 0.5km the speed-up effect of all the slopes are almost equal. The speed-up at 12° is 18%, and the corresponding result using the empirical formula is 12%. Further downwind the situation is reversed, and the gentlest slope gives the largest speed-up. After 4km the speed-up at 12º is 8%. This corresponds to 26% power density increase. The corresponding result using the empirical formula is here 1%. The agreement between the simulation and the empirical formula is good close to the hill, but become poorer inward the plateau. There are probably different reasons for this. One source of error is the 2D approach, which tends to be too slow to neutralize differences that occur in the flow field. Another reason can be the fact that 4km is quite far from the escarpment edge, and probably outside the optimum range of the empirical formula.

For the last group of simulation the profiles of the speed-up on the top of some ridges are visualized together with the profile development in the wake behind the ridges. One interesting aspect is whether a given slope gives recirculation or not. At the top of the ridge, it is no longer the steepest slope that gives the largest speed-up. The largest speed-up is found with 12º slope, and is 38% in 80m. The corresponding result with the empirical formula is 53%. 38% is calculated speed-up with the empirical formula in the corresponding 3D hill case. This is lower due to the 3D effects. In the wake of the ridge, separation is found for the three steepest slopes, and only the profile of the gentlest slope is fully reconstructed 4km behind the ridge. After 4km the speed-up with 42º is -42%, with 24º is -26% and with 12º is -13%. As discussed earlier these values would probably not be that large in a 3D flow, which would cause a better mixing.

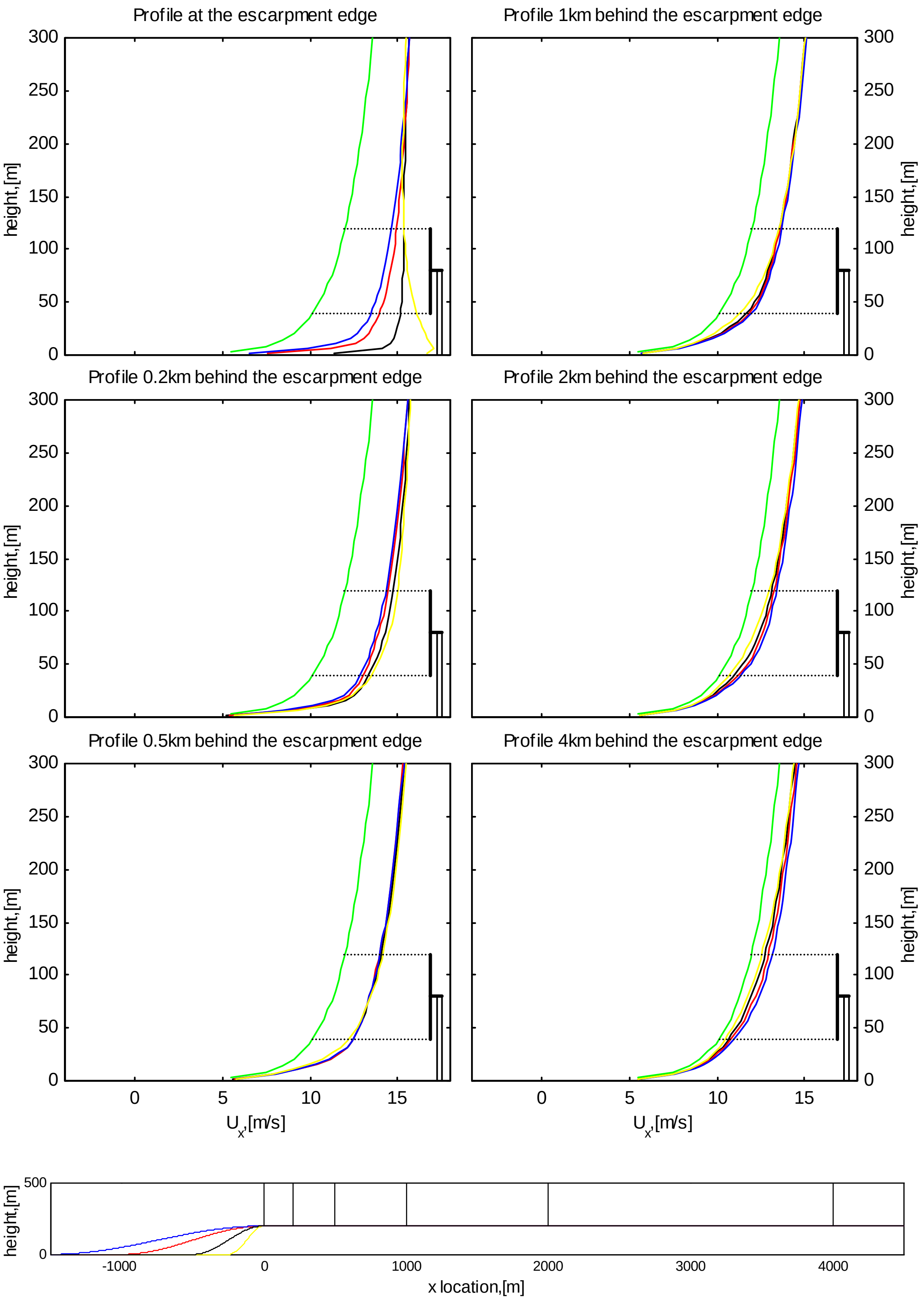

**Fig.8**: The lower diagram shows the location of each profile in the upper diagram. The flow comes from left and reaches escarpments of four different slopes. The upper diagram illustrates how the profiles corresponding to the different slopes develop inward the plateau. The profiles are compared to the corresponding green profile developed under a flat condition. All simulations operate with a uniform roughness length of 0.03m.

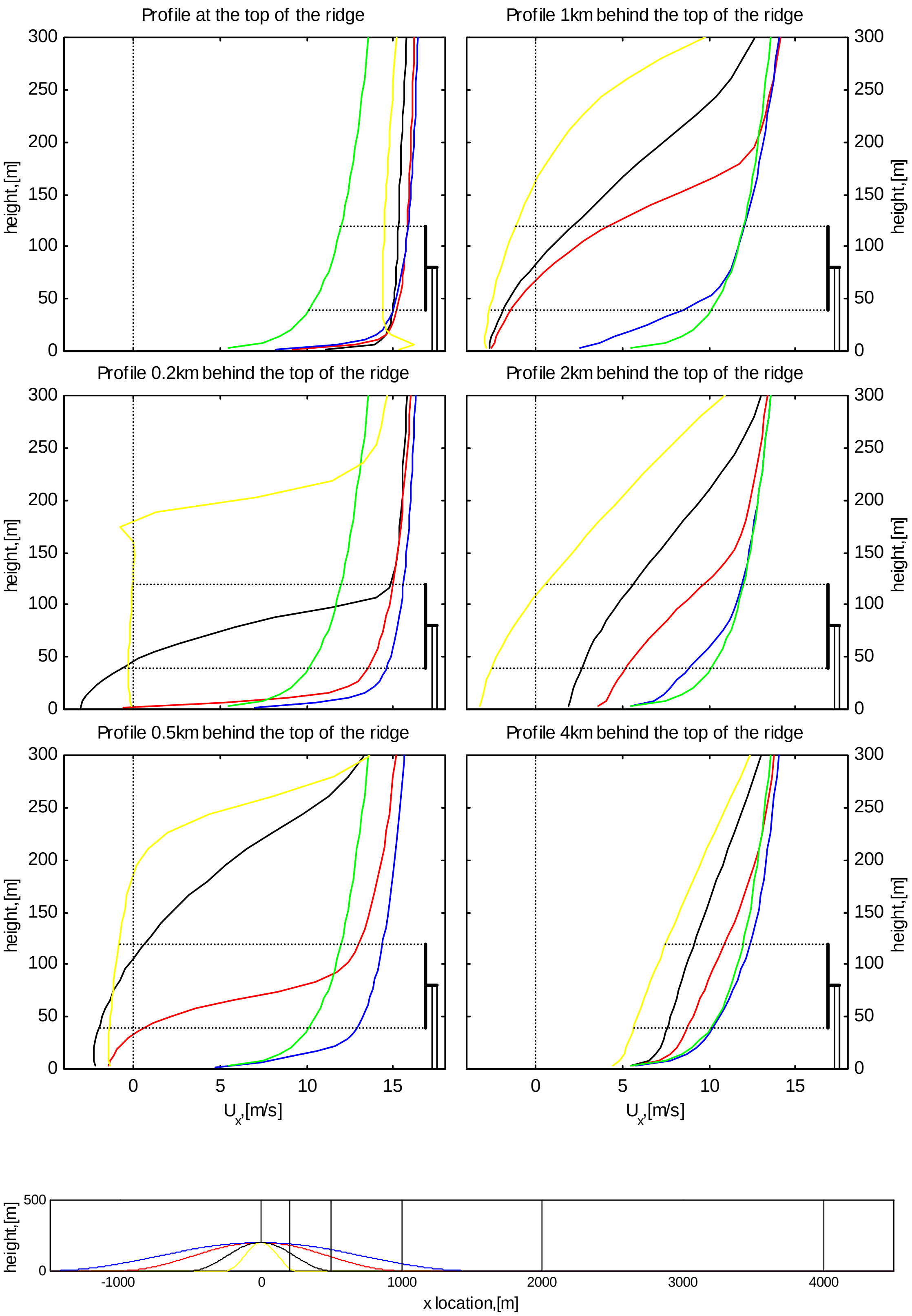

**Fig.9**: The lower diagram shows the location of each profile in the upper diagram. The flow comes from left and reaches ridges of four different slopes. The upper diagram illustrates how the profiles corresponding to the different slopes are at the top of the ridge, and how they develop in the wake of the ridge. The profiles are compared to the corresponding green profile developed under a flat condition. All simulations operate with a uniform roughness length of 0.03m.

## CONCLUSIONS

The roughness influence is found to be important to high wind velocities found in coastal areas. At a typical coastal roughness length, it is seen that within the first 4km from the shore in downwind direction, the wind velocity is increased by 13-14% in 80m compared to a similar non-coastal area. A forest is found to decrease the mean velocity. At a simulation with a 2km long forest in farmland, the wind velocity 4km downstream from the forest is 2% lower in 80m than a similar site with no forest.

Enhanced wind velocities were also found at escarpments and ridges. At an escarpment of 12° slope and 200m height, the speed-up in 80m is found to be 29% on the escarpment edge and 8% 4km downstream on the plateau. In the corresponding ridge simulation, the speed-up on the top was 38%, with reduced velocities in the wake of the ridge. Steep slopes gave large separation zones, and highly reduced velocities in the wake, while the gentlest slope of 8.4° gave no recirculation and minimal reduction of the velocity in the wake.

Terrain effects are found to influence the mean wind velocity level. If the annual mean velocity is increased by 10%, the annual power production is typically increased by 20%. This shows that the estimated annual power production is very sensitive to errors in the estimated annual mean wind speed. In an area of complex terrain, it is difficult to predict the sum of the terrain effects, since they are non-linear. Addition of the different effects can still be valuable information as preliminary estimates, but in an extended analysis measurements should always be performed within the area of interest to avoid biases. Based on the measurements, a non-linear flow solver adds the terrain effects to give a detailed annual mean wind prediction for the entire area.

In short the siting of wind turbines are recommended in areas on top of hills, ridges and escarpments with low roughness in the main wind directions. Gentle slopes are important upstream to avoid flow separation, which causes high turbulence and low mean velocities.

## Acknowledgements

This work has been funded by The Norwegian Research Council and Statkraft SF through the KMB[1] "Development of Norwegian wind power technology".

---

[1] Competence project with user participation

## REFERENCES

Alm L K & Nygaard T A (1995). Flow over complex terrain estimated by a general purpose Navier-Stokes solver. *Modeling, identification and control*, vol 16, pp 169 – 176.

Ahrens C D (1994). *Meteorology Today. An introduction to weather, climate, and the environment.* Fifth edition. West Publishing Company, Minneapolis.

Arya S P (1988). *Introduction to Micrometeorology*. International Geophysics Series, Volume 42. Academic Press, Inc, San Diego, California.

Bowen A J & Mortensen N G (1996). Exploring the limits of WasP the wind atlas analysis and application program. *European Union Wind Energy Conference*, Göteborg, Sweden.

Chorin A J (1967). A Numerical Method for Solving Incompressible Viscous Flow Problems. In *Computational Fluid Dynamics,* edited by C. K. Chu, AIAA Selected Reprints Series, vol 4, p 12.

Hirsch C (1990). *Numerical computation of internal and external flows, volume 2.* John Wiley & Sons, Great Britain.

Knauer A and Nyhammer F K (2002). Numerical and experimental methods for wind farm site evaluation in complex terrain. *Conference proceedings Global Windpower 2002*, Paris, France.

Lemlin D R, Surry D & Davenport A G (1988). Simple approximations for wind speed-up over hills. *Journal of Wind Engineering and Industrial Aerodynamics*, vol 28, pp 117 – 127.

Raithby G D, Stubley G D & Taylor P A (1987). The Askervein Hill project: A finite control volume prediction of three-dimensional flows over the hill. *Boundary-Layer Meteorology*, vol 39, pp 247 – 267.

Undheim O (2003). Comparison of turbulence models for wind evaluation in complex terrain. *Conference proceedings European Wind Energy Conference*, Madrid, Spain.

Undheim O (2005). *Description and validation of 3DWind.* Internal report IFE/KR/F-2005/062, Kjeller, Norway.

Versteeg H K & Malalasekera W (1995). *An introduction to Computational Fluid Dynamics; The Finite Volume Method.* Prentice Hall, London.

Windpower monthly news magazine. Volume 20. No.1. January 2004. *Becoming respectable in serious circles*. Knebel, Denmark.

Windpower monthly news magazine. Volume 20. No.3. Mars 2004. *Wind market status*. Knebel, Denmark.

Øye I J (1996). *On the aerothermodynamic effects on space vehicles.* PhD-thesis. Norwegian University of Science and Technology, Trondheim, Norway.

# Paper 4

## Comparison of turbulence models for wind evaluation in complex terrain

*Conference proceedings EWEC 2003*

# COMPARISON OF TURBULENCE MODELS FOR WIND EVALUATION IN COMPLEX TERRAIN

Ove Undheim
Institutt for energiteknikk
P.O.Box 40, N-2007 Kjeller, Norway
Phone: +47 63 80 61 83
Fax: +47 63 81 29 05
e-mail: ove.undheim@ife.no
web-site: www.ife.no

**ABSTRACT:** The non-linear Navier-Stokes solver 3DWind has been used for the simulation of wind in complex terrain. A hilly island at the west coast of central Norway has been investigated. Simulations were carried out with three different turbulence models, the mixing length, a k-l and a k-ε model. The results were compared with measured data and simulation results from the linearized model WA$^S$P. The wind fields from 3DWind and WA$^S$P differ especially in the vicinity of steep edges. Overestimation of the windspeed in WA$^S$P at steep edges is likely to be the case. The resulting differences in wind fields result in differences in optimal wind turbine positioning.

## 1 INTRODUCTION

Complex terrain has large influence on wind flow development. The presence of speed-up at hilltops is beneficial; on the other hand turbulence in complex terrain can represent a serious fatigue load on wind turbines. To assess the wind flow conditions in complex terrain, numerical methods are very useful.

Non-linearized Navier-Stokes solvers seem most suitable for the investigation of wind flow in complex terrain, allowing simulation of turbulence and complex wind flow phenomena. Turbulence is present in complex terrain and influences other flow phenomena in various degrees. To assess the performance of different turbulence models, a comparison analysis of the mixing length, the k-l and the k-ε turbulence models was carried out with the CFD-model 3DWind. Through improved modelling of the turbulence in the flow fields, wind maps will be improved too, allowing a more effective identification of wind park positions and park design.

For purposes of comparison, additional simulations with the linearized model WA$^S$P are carried out. Simulations were based on wind fields from the island of Hitra, where measurement data were available and kindly provided by STATKRAFT SF.

## 2 MODEL DESCRIPTION

The numerical model 3DWind [1] is a Navier-Stokes solver for simulation of turbulent, non-neutral and non-hydrostatic microscale flows. The purpose of 3DWind is to identify the influence of complex terrain on the wind field development.

The model solves the Reynolds Averaged Navier-Stokes equations (RANS), where the averaged mass balance is given by:

$$\frac{\partial \rho}{\partial t} + \frac{\partial}{\partial x_i}\left(\rho U_i\right) = 0 \qquad (1)$$

$U_1$, $U_2$ and $U_3$ are the time averaged velocity components, and $\rho$ is the density.

Averaged momentum equations are given by:

$$\frac{\partial U_i}{\partial t} + U_j \frac{\partial U_i}{\partial x_j} - \frac{\partial}{\partial x_j}\left( -\overline{u_i u_j} + \nu_l \frac{\partial U_i}{\partial x_j} \right) + \frac{1}{\rho}\frac{\partial p}{\partial x_i} = 0 \qquad (2)$$

$u_1$, $u_2$ and $u_3$ are velocity fluctuations. The Reynolds stresses $\overline{u_i u_j}$ represent the turbulence, and must be modelled to close the equations. In this model the Reynolds stresses are approximated by the following expression:

$$\overline{u_i u_j} = \frac{2}{3} k \delta_{ij} - \nu_T \left( \frac{\partial U_i}{\partial x_j} + \frac{\partial U_j}{\partial x_i} \right) \qquad (3)$$

This assumption come from K-theory, and $\nu_T$ is the turbulent viscosity. Available turbulence models for the estimation of the turbulent viscosity in 3DWind are the mixing length model, a one-equation k-l model and a two-equation k-ε model.

The grid generator Grid3d makes grids for use in 3DWind. Grid3d generates both a one-dimensional grid used for estimation of boundary conditions, and a three dimensional grid for the full simulation. The grid is not orthogonal. In the grid generator there are options for both linear and nonlinear stretching of the gridcells. The non-linear stretching is based on the arctan function, and enables a larger central area with good resolution.

Simulations with 3DWind require fully described vertical profiles at the inflow boundary. An one-dimensional simulation develops this. At the upper boundary at 5 km a boundary wind speed of 30m/s is used. At the ground the wind speed is 0m/s while a wall function connected to the roughness sets the velocity in the first grid cell above ground. There are periodic boundary conditions both in x and y directions. One-dimensional profiles are also used as initial condition all over the domain.

In the 3D analysis a no gradient boundary condition is assumed at the outflow boundary. Periodic conditions are enforced at the side boundaries, while the surface boundary is expressed by wall functions. A friction free solid wall interprets the upper boundary. This is a reasonable assumption when the domain height is more than 10 times the level differences at the surface boundary.

One simulation is made for each of the 12 directions. Based on directional mean wind and directional distribution calculated from measurements, a mean wind map is calculated for each measuring site inside the domain. If there is more than one measuring site, the maps for each site are interpolated to make one common wind map representative for the whole area.

Measured turbulence intensities (TI) are compared to TIs simulated from 3DWind. TIs from 3DWind are computed with the equation [2]:

$$TI = \frac{\left(\frac{2}{3}k\right)^{1/2}}{U} \tag{4}$$

$k$ is the turbulent kinetic energy, and $U$ is the mean wind. Equation for estimation of turbulence intensities based on the measurements is [3]:

$$TI = \frac{\sigma}{U} \tag{5}$$

In this equation $\sigma$ is the standard deviation of the measured wind speed. To make sure that the wind field is neutral, only measurements with velocities above 6m/s are basis for TI estimates.

WA$^S$P is a linear flow model developed at RISØ. Fore further information about the model, it is referred to the European Wind Atlas [4].

## 3 THE HITRA PROJECT

Hitra is an island in the Norwegian county Sør-Trøndelag. The total area of the island is 565km$^2$. Eldsfjellet is a hill formation at the island, where the hill shapes are expected to create local speed-up of the wind from several directions.

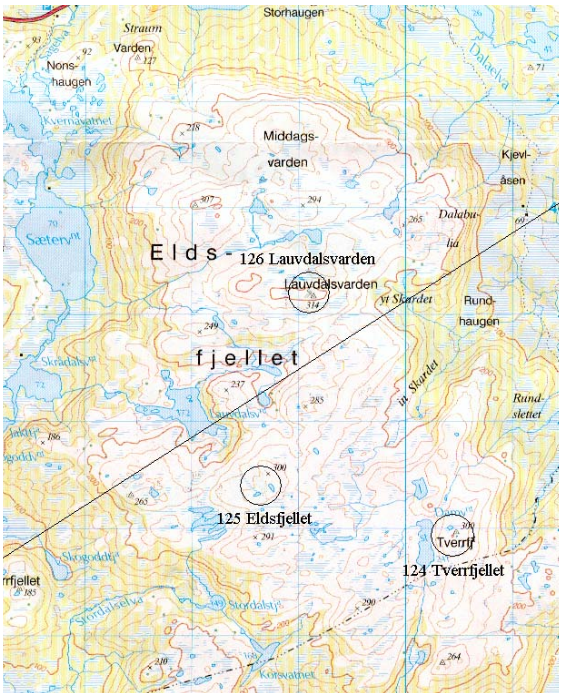

*Figure 1: Map that includes central parts of the computed area. The three measuring sites are marked with circles. The crossover line is the vertical slice that is investigated with respect to wind profiles and turbulence development. The sides of the squares are 1km.*

### 3.1 MEASUREMENTS

Measurements are collected from the three sites Tverrfjellet, Eldsfjellet and Lauvdalsvarden (Figure 1). The three 50m masts were equipped with cup anemometers and wind vanes. This analysis is based on measurements from one year (14.10.98 to 13.10.99). Icing periods have been removed from the data material.

A wind rose is shown for the measuring site at Eldsfjellet (Figure 2). The main wind direction is from the sector with centre at 240°, but also the sector with centre at 120° is a common direction. Calculated mean winds at the sites for this particular year are 7.83m/s at Tverrfjellet, 7.64m/s at Eldsfjellet and 8.06m/s at Lauvdalsvarden. The measurements are calibrated for sheltering effects from both the lightning rod and the mast top [5].

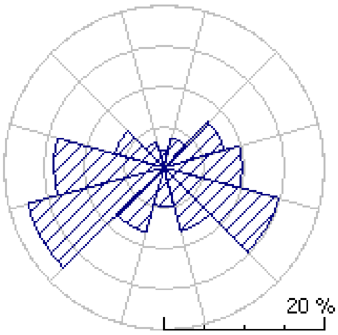

*Figure 2: Wind rose that shows the direction distribution.*

## 3.2 NUMERICAL INVESTIGATION

The non-linear grid stretching is used for the Hitra site. The horizontal grid distance is 55m in the centre of the domain. For a radius of 3km the cell sizes are 200m. This radius covers the most interesting area. Smoothing starts at 6km, where the cell sizes are 530m. The area plotted on the figures constitutes 12% of the total domain, but contain 50% of the cells. The total domain has a volume of 20x20x5km$^3$, and contains 90x90x48 gridcells. The ground layer of the grid is shown in Figure 3.

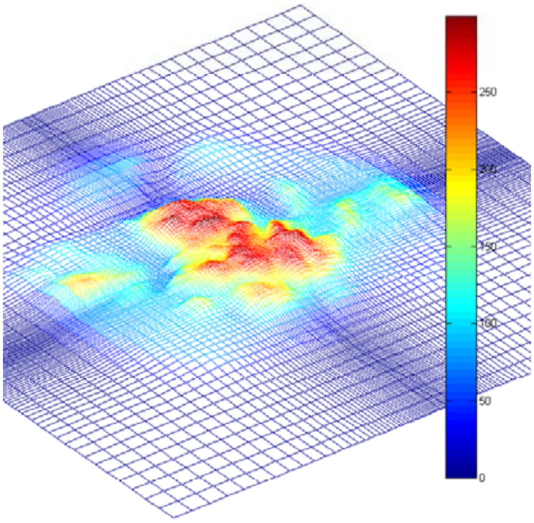

*Figure 3: Grid used for simulations with 3DWind.*

Vertical resolution is given by a cell height of 10m at ground, increasing linearly to 380m at 5000m heights. This is for the sea level. The stretching from ground to 600m is varying to fit the topography.

There have been two one-dimensional simulations for the Hitra project. Vertical profiles are simulated for the roughnesses 0.001m and 0.03m. The results from the simulations are shown in Figure 4. These profiles are not meant to represent real atmospheric profiles, which are quite different. They are boundary conditions of the model where only the first few hundred meters are of interest, and neutral conditions are assumed. There is sea at the inflow boundary for the sectors 120° to 210°. From the other directions the wind originates from land areas.

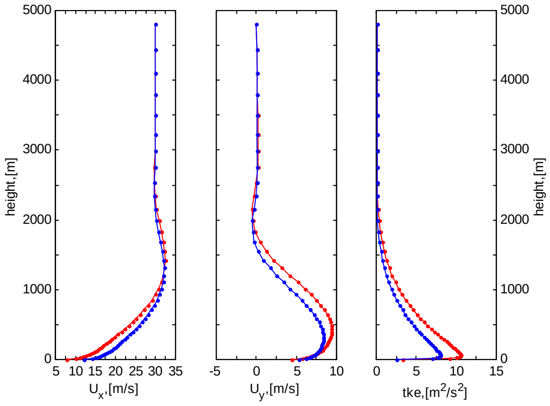

*Figure 4: Profiles based on one-dimensional simulations. Red illustrates roughness 0.03m, and blue illustrates roughness 0.001m.*

The three dimensional simulation was carried out on a 2.53 GHz computer. Time spent on each simulation was 60 hours. Simulated results are then obtained for all the three different turbulence models.

Simulation results from 240° are used to evaluate the model's ability to estimate turbulence intensities. 240° is chosen because this is the main wind direction. The uncertainty of the measured turbulence intensity is linked to the number of observations. Measured turbulence intensities for the measuring sites are compared with simulated turbulence intensities for the same locations. This is done for both the mixing length model, the k-l model and the k-ε model. The measured TIs are computed from measurements with direction in the interval 235°-245°.

WA$^S$P simulations are based on the same measurements as 3DWind. The computational domains are though somewhat different. This is connected to 3DWind's need for smoothing the topography to zero some distance to the boundaries. The domain used in WA$^S$P has the size 14x14km$^2$, and consists of 425x425 square gridcells. The sides of the gridcells are 33m, which means a better resolution than 3DWind.

The assumed roughness ($z_0$) in both the 3DWind simulation and the WA$^s$P simulation is 0.001m for water surfaces. Over land $z_0$ is set to 0.03m. This is a simplification, but in central parts of the domain, it seems to be a fairly good approximation. Estimated mean wind maps for each measuring site is converted to a common map using the same method as described for 3DWind.

## 3.3 RESULTS AND DISCUSSION

Figure 5 and 6 show the simulated mean wind map worked out by WA$^S$P and 3DWind. The differences are not large and would probably not cause big differences in the decision process to locate the turbines. Still there is a tendency that WA$^S$P estimates the areas of highest wind speed conditions to be located closer to the edges of steep terrain. The wind conditions are further estimated to be higher in the valleys for WA$^S$P than for 3DWind.

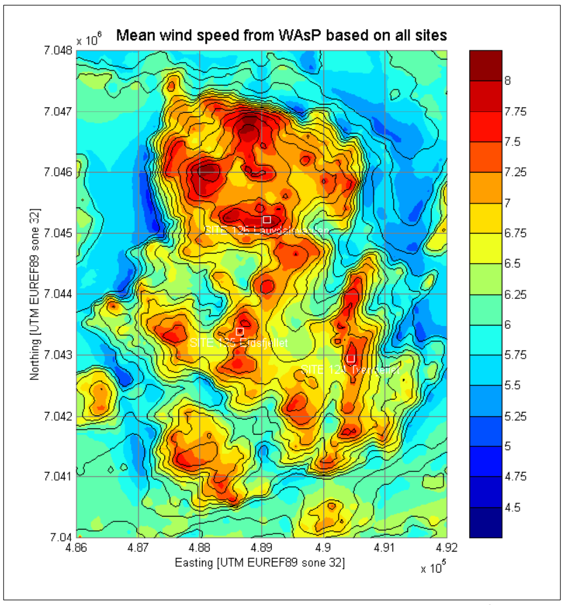

*Figure 5: Mean wind map worked out by WA$^s$P.*

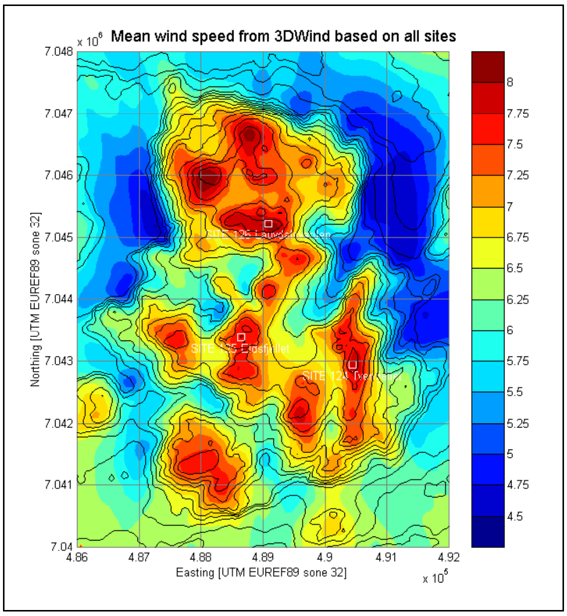

*Figure 6: Mean wind map worked out by 3DWind. Results based on the k-l turbulence model.*

The local effects of the topography are most visible in the WA$^S$P charts. This is due to model differences, but also connected to WA$^S$P having better resolution. Another important difference between the models is the level difference in the valleys. For both models the results are interpolated to coincide with measurements at the measuring sites. All the measuring sites are located at almost equally exposed positions and good wind conditions. Therefore WA$^S$P does a fairly good interpolation between the measuring sites, but has a tendency to simulate too high wind speeds in the valleys. The differences between 3DWind and WA$^S$P (Table 1) would probably have been bigger if there were measurements in the valleys too.

Based on each measuring site, the wind conditions at the other sites have been modelled by means of both 3DWind and WA$^S$P. The results are given in Table 1.

| **Tverrfjellet** | **k-ε** | **k-l** | **mixing** | **WAsP** | **Measure** |
|---|---|---|---|---|---|
| Eldsfjellet | **-2.79 %** | **-2.58 %** | **-2.92 %** | **-4.68 %** | **7.64** |
| Lauvdalsvarden | **-3.66 %** | **-2.69 %** | **-3.36 %** | **-5.59 %** | **8.06** |

| **Eldsfjellet** | **k-ε** | **k-l** | **mixing** | **WAsP** | **Measure** |
|---|---|---|---|---|---|
| Tverrfjellet | **2.91 %** | **2.59 %** | **3.02 %** | **3.92 %** | **7.83** |
| Lauvdalsvarden | **-2.01 %** | **-1.21 %** | **-1.54 %** | **-2.51 %** | **8.06** |

| **Lauvdalsvarden** | **k-ε** | **k-l** | **mixing** | **WAsP** | **Measure** |
|---|---|---|---|---|---|
| Tverrfjellet | **3.70 %** | **2.39 %** | **3.32 %** | **6.04 %** | **7.83** |
| Eldsfjellet | **0.76 %** | **-0.23 %** | **0.35 %** | **1.60 %** | **7.64** |

*Table 1: This table show the result for the estimation of mean wind at one measuring point based on one of the two other stations.*

From Table 1 the mean deviation with 3DWind is 2.6% with the k-ε model, 1.9% with the k-l model, 2.4% with the mixing length model, and the mean deviation with WA$^S$P is 4.1%. Results from the k-l model are presented in Figure 6-8, while results from mixing and k-ε are contained in appendices for comparison. In the mean wind maps the differences between the three turbulence models are small, and there are no general trends.

The simulation for the vertical wind in 50m is shown in Figure 7. A turbine manufacturer recommends locating wind turbines at a maximum flow inclination of 5° on an average [6]. From Figure 6 and 7 it is seen that for the locations with the highest mean wind, the angles of the velocity are below the recommended limit. If turbine locations are decided based on WA$^S$P results there could be a conflict between good locations and high vertical wind speed (Figure 5 and 7). This is caused by WA$^S$Ps tendency to calculate high wind speeds in the vicinity of steep edges.

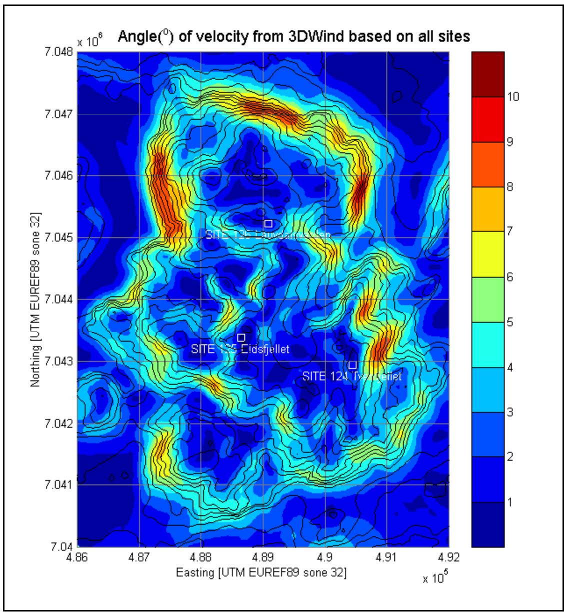

*Figure 7: Average flow inclination in height 50m agl. Based on simulation result from 3DWind, with the k-l turbulence model.*

The distribution of the turbulence intensity is given in Figure 8. Results are calculated on basis of calculated TI for the 12 directions, and the knowledge of the direction distribution. TI is assumed to be a constant not connected to velocity for velocities above 6m/s. Results from simulations with the k-l model (Figure 8) are similar to results from the mixing length model (Figure A4). The k-ε model shows the same pattern, but the level is higher (Figure A2). This indicates that some parameters in the k-ε model should have been adjusted.

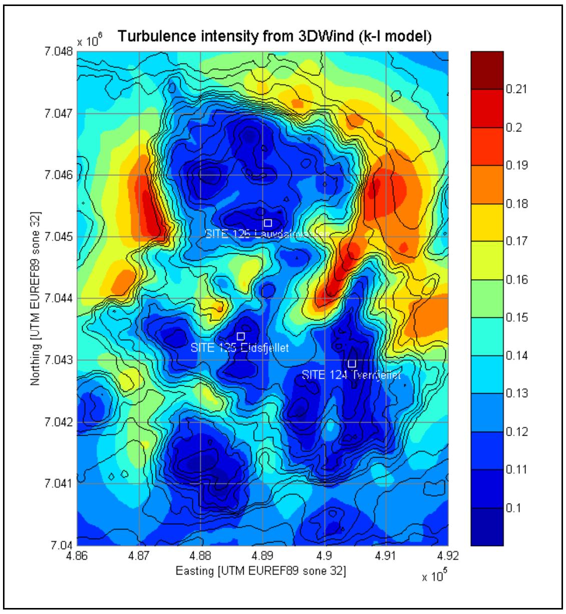

*Figure 8: Mean turbulence intensity. Results based on the k-l turbulence model.*

Table 2 and 3 show the measured and the simulated turbulence intensities for wind direction 240°. Compared to the measured turbulence intensities, the simulated turbulence intensities are higher. The k-ε model is actually quite far from the measured level. On the other hand, the k-ε model estimates the differences between the measuring sites better than the k-l model and the mixing length model. In addition to numerical error, the turbulence model deviations can be connected to the assumption of $z_0$=0.03m onshore, which is a simplification.

| | |
|---|---|
| Tverrfjellet (124) | 0.080 |
| Eldsfjellet (125) | 0.100 |
| Lauvdalsvarden (126) | 0.087 |

*Table 2: Turbulence intensities calculated for the measuring sites based on measurements.*

| | k-ε | k-l | mixing |
|---|---|---|---|
| Tverrfjellet | 0.154 | 0.104 | 0.108 |
| Eldsfjellet | 0.162 | 0.103 | 0.109 |
| Lauvdalsvarden | 0.150 | 0.095 | 0.102 |

*Table 3: Turbulence intensities simulated for the different turbulence models in 3DWind.*

A vertical analysis has been performed for the line indicated in Figure 1. The wind direction is 240°, following the given line from left to right. Estimated results are visualized in Figure 9, 10 and 11. Results are based on 3DWind simulations with the k-ε turbulence model.

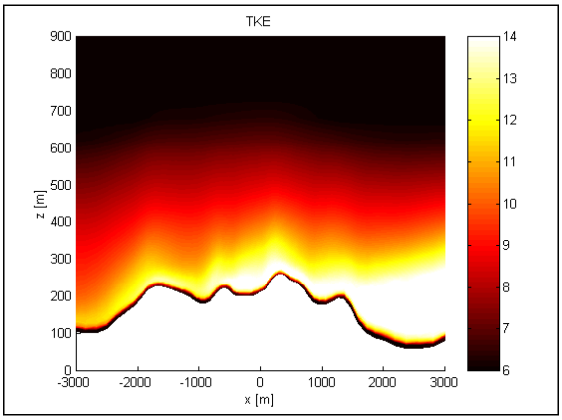

*Figure 9: Turbulence development in the vertical slice shown in Figure 1. Wind direction from 240°.*

Figure 9 show that the turbulence is gradually increasing as the wind passes the hills. It is thus preferable to avoid upwind disturbances.

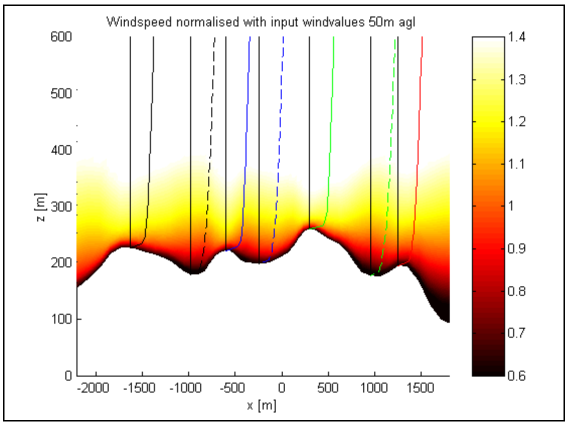

*Figure 10: Normalized wind speed. Wind profiles are plotted to show the locations of the profiles in Figure 11.*

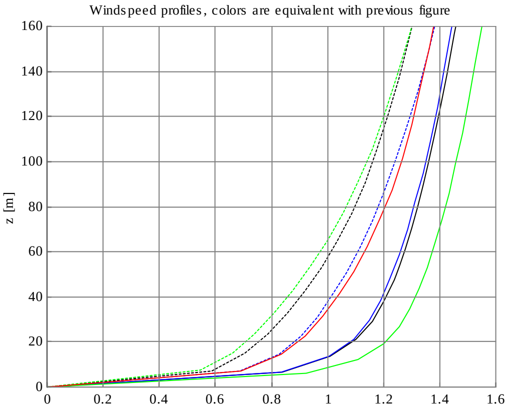

*Figure 11: Wind profiles on sites illustrated in Figure 10 (normalized to input velocity 50m agl).*

The vertical profiles in Figure 10 and 11 can be used to estimate velocity in nacelle height. Extra expenses are considerable when the height of measuring mast exceeds 50m. The Norwegian national aviation authorities require light signals for masts taller than 50m. For the best-exposed location (green line) the relative velocity in 50m is 1.35 compared to 1.42 in 80m (typical nacelle height). This equals an increase of 5.5%. Both values are normalized with inflow boundary condition 50m above ground level.

## 5 SUMMARY AND CONCLUSION

3DWind seems to calculate the wind field better than WA$^S$P at this particular case at Hitra. Calculated mean deviation with 3DWind (mean for all three turbulence models) are found to be 2.3%, compared to 4.1% for WA$^S$P. Still the capabilities of improved turbulence calculations are present, and might cause the difference to increase. Compared to 3DWind, WA$^S$P also simulates higher velocities in the valleys and higher velocities in the vicinity of steep edges. Due to lack of measurements in these regions this cannot be verified in this case, but most likely WA$^S$P gives too high wind speeds in valleys and near edges. The turbulence intensities are simulated for the three measuring sites by the three different turbulence models. The measured differences are best captured by the k-ε model, but the k-l model has the best level estimates. The k-l turbulence model is for this case found to be the best performing turbulence model for the 3DWind simulations. An activity to validate the turbulence modelling is started on a theoretical case. This is the C18 case from the ERCOFTAC classic database [7]. Another aspect is verification of the simulated vertical profiles. Wind speed data are available in 10m, 30m and 50m. Good estimates of wind speed at nacelle height are crucial, and the estimated wind shear is also important.

## REFERENCES

[1]: Knauer, A. and Nyhammer, F.K. Numerical and experimental methods for wind farm site evaluation in complex terrain. Proceedings of the Global Windpower 2002, Paris.

[2]: An introduction to computational fluid dynamics. Versteeg, H K and Malalasekera, W. 1995.

[3]: Introduction to micrometeorology. Pal Arya, S. Academic press, San Diego, California, 1988

[4]: Troen, I. and Petersen, E.L. (1989). European Wind Atlas. ISBN 87-550-1482-8. Risø National Laboratory, Roskilde. 656 pp.

[5]: Preliminary internal report from Kjeller Vindteknikk KVT/FKN/2003/001

[6]: Bonus 2MW Siting and Installation,1999.

[7]: http://cfd.me.umist. ac.uk/ercoftac/

# APPENDIX

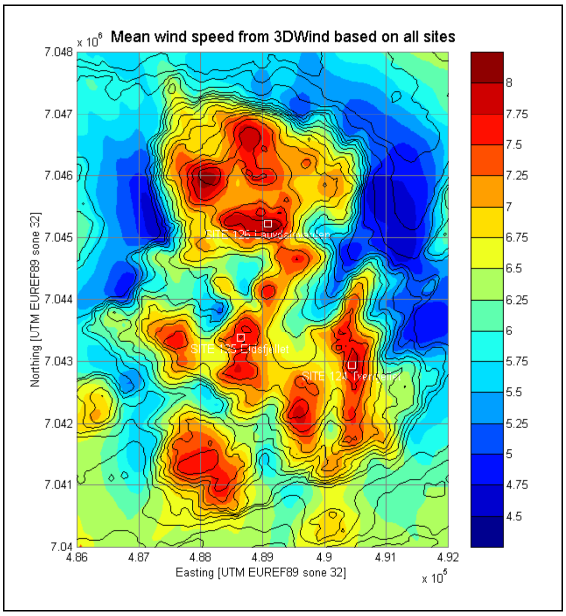

*Figure A1: Mean wind map worked out by 3DWind. Results based on the k-ε turbulence model.*

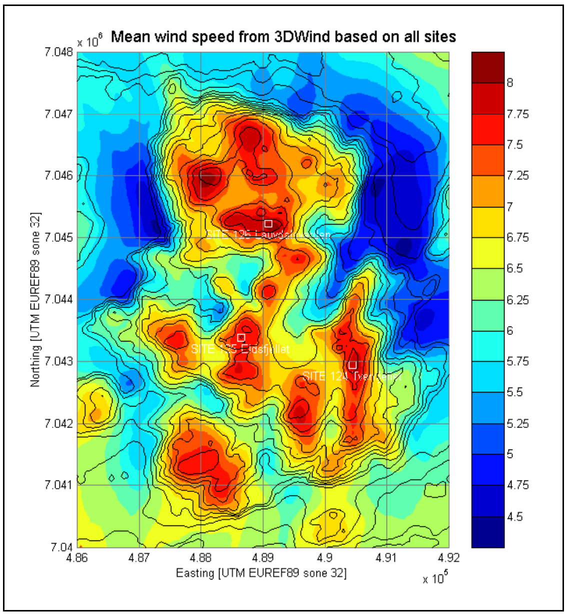

*Figure A3: Mean wind map worked out by 3DWind. Results based on the mixing length model.*

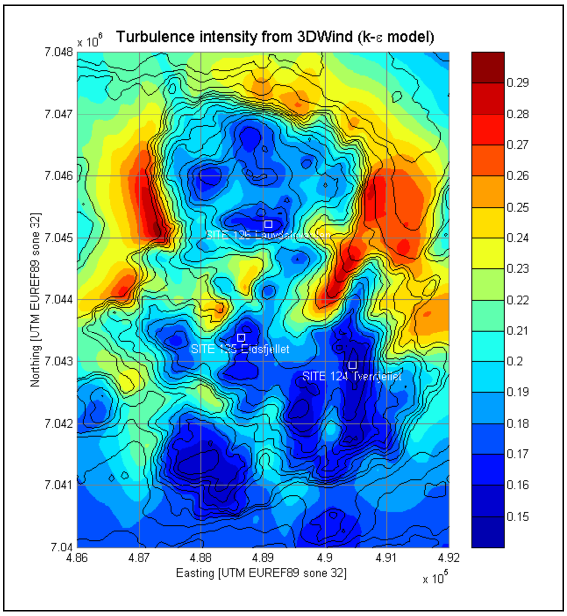

*Figure A2: Map of the turbulence intensity worked out by 3DWind. Results based on the k-ε turbulence model.*

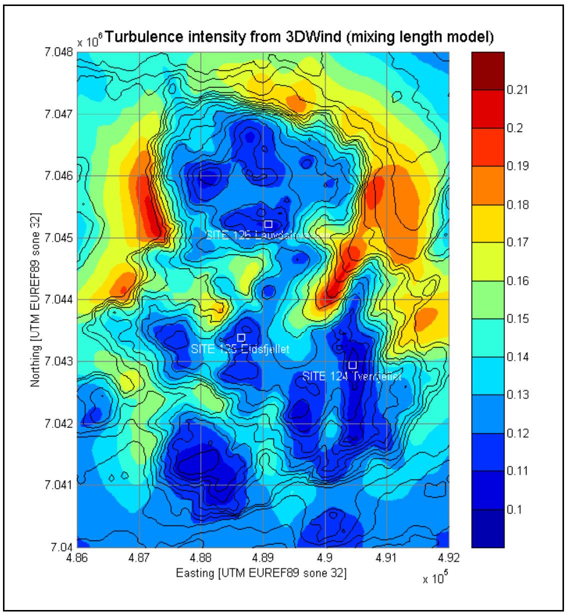

*Figure A4: Map of the turbulence intensity worked out by 3DWind. Results based on the mixing length model.*